Extending the Record of Time-Variable Gravity
by Combining GRACE and Conventional Tracking Data

by

Matthieu J. Talpe

B.S., Planetary Sciences,
Massachusetts Institute of Technology, Cambridge, MA, 2011

M.S., Planetary Sciences,
Massachusetts Institute of Technology, Cambridge, MA, 2012

M.S., Aerospace Engineering Sciences,
University of Colorado Boulder, Boulder, CO, 2015

A thesis submitted to the

Faculty of the Graduate School of the

University of Colorado in partial fulfillment

of the requirements for the degree of

Doctor of Philosophy

Department of Aerospace Engineering Sciences

2017

This thesis entitled:
Extending the Record of Time-Variable Gravity
by Combining GRACE and Conventional Tracking Data
written by Matthieu J. Talpe
has been approved for the Department of Aerospace Engineering Sciences

_____
R. Steven Nerem

_____
Frank G. Lemoine

_____
Jeffrey Thayer

_____
Robert R. Leben

_____
Kristy Tiampo

Date _____

The final copy of this thesis has been examined by the signatories, and we find that both the content and the form meet acceptable presentation standards of scholarly work in the above mentioned discipline.

Talpe, Matthieu J. (Ph.D., Aerospace Engineering Sciences)

Extending the Record of Time-Variable Gravity

   by Combining GRACE and Conventional Tracking Data

Thesis directed by Prof. R. Steven Nerem

The Gravity Recovery and Climate Experiment (GRACE) mission has provided invaluable insight on the behavior of mass redistribution on the surface of the Earth since its launch in March 2002. GRACE measures the range between its two satellites to obtain a new, high-resolution, global gravity field of the Earth every month. This dissertation presents the first record of high-resolution time-variable gravity that extends to the 1990s. This gravity reconstruction is obtained by combining GRACE with gravity solutions generated from conventional tracking of satellites that start in November 1992. These tracking observations originate from two ground-based systems, Satellite Laser Ranging (SLR) and Doppler Orbitography and Radiopositioning Integrated by Satellites (DORIS). The statistical framework for the reconstructions of the two fields can be described in three major steps. First, high-resolution spatial patterns are obtained from a Principal Component Analysis (PCA) decomposition of GRACE gravity coefficients. In the second step, the top four patterns are used as the model relating the SLR/DORIS coefficients to their temporal modulation, which are solved for in a Least Squares Adjustment. Lastly, the full patterns and their temporal modulation are linearly combined to form gravity fields that span the SLR/DORIS time frame and therefore add a decade of perspective before GRACE. An error budget is also designed to quantify the influence of assumptions made in the reconstruction. The primary scientific goal was to add perspective on the behavior of polar ice sheet melt in the 1990s. The second goal was to extend the record of terrestrial water storage. One last application examined the possibility of using this technique as a way to bridge the upcoming multi-month gap between GRACE and its successor mission, GRACE Follow-On.

Dedication

To Prof. John Wahr and Prof. George Born, because this thesis is a direct result of their trailblazing work in satellite geodesy and precise orbit determination.

John was one of the main reasons I decided to attend the University of Colorado Boulder to study geodesy. The few interactions I had with him – whether as a student in his office, as a reader of his work, or in the audience at one of his talks – were special.

Acknowledgements

I would first and foremost like thank Prof. Steve Nerem. He was the only professor I reached out to after my undergrad years because I was certain that I wanted to study geodesy in an aerospace context. His constant support, technical advice, and ability to connect to the big picture were invaluable in helping me develop as a student and researcher. It is amazing how often his high-level advice and intuition turned out to be 100% right.

Members of my committee include Prof. Kristy Tiampo, Prof. Bob Leben, Prof. Jeffrey Thayer, and Dr. Frank Lemoine. I am especially grateful for Dr. Frank Lemoine's mentorship, especially during the summers of 2014 and 2015 while at Goddard Space Flight Center in his office. I learned an immense amount with him about real-world orbit determination packages. Dr. Doug Chinn, Dr. Terry Sabaka were also very helpful while at GSFC. I would also like to thank Dr. Felix Landerer who welcomed me at JPL in the summer of 2014.

It was nice to witness the Nerem research group at CU grow throughout the years and become the supportive research group that it is now. I would especially like to single out Michael Croteau and Ryan Hardy, with whom I have had the pleasure to study throughout most of my time at CU. David Wiese and Emily Pilinski, Steve's previous students, were also very helpful.

I am indebted to the NASA MEaSUREs and Cryosphere programs, and NASA Earth and Space Science Fellowship for their funding. I also thank the Fulbright commission for supporting my year in Munich at the Deutsches Geodätisches Forschungsinstitut. Combining strong geodesy culture in Germany with a lifelong dream to spend a year in Munich made for what was probably the most memorable year of my life. When it came down to business (well, geodesy), Prof. Michael

Schmidt, Dr. Verena Lieb, and Dr. Mathis Blofeld were very helpful. I also spent a productive week in August 2016 in Bern with Dr. Andrea Maier and Prof. Adrian Jäggi.

Conferences always brought about new perspectives and productive conversations. One of the best outcome was meeting Prof. Ehsan Forootan, whose knowledge of PCA and geodesy has been beyond helpful. In Bonn, Dr. Roelof Rietbroek and Prof. Jürgen Kusche welcomed me in 2004 and shared useful insights in this reconstruction process.

The Ann and H.J. Smead Department of Aerospace Engineering Sciences is truly incredible and I will advertise them throughout my career. I found the classes to be exceptional, especially the Stat OD courses with Prof. Parker and Prof. McMahon; the GPS classes with Prof. Axelrad and Prof. Larson; the attitude dynamics class with Prof. Schaub; and the satellite geodesy class with Steve. I am also grateful for additional training; namely, the JPL Planetary Science Summer School in the summer 2014 at JPL; the Autumn Gravity school in the fall 2016 in Bonn, Germany; the Svali PhD School in Greenland in the summer 2015.

Time at work would not be as productive without a minimum of fun and so there are many people to acknowledge: friends from the CU Aerospace Department; the CU triathlon team, the TEDxCU community, Munich, the Boulder Stammtisch and CU German club, conferences, previous life chapters, etc. You know who you are.

Thank you to the people who proofread my dissertation, especially Eileen Lagman from the Graduate Writing Support program at CU.

I will end this acknowledgement by thanking my family and parents, whose support on both sides of the Atlantic is without equal and can not properly be articulated. I would not be here without you and this dissertation is as much mine as it is yours.

Contents

Chapter

Tables

Table

Figures

Figure

Chapter 1

Introduction

1.1   Introductory Remarks

The acceleration due to the force of gravity on the surface of the Earth is widely known in physics classes as 9.8 m/s^2. It is less known how and why the true value deviates from this approximation. It is even less appreciated how and why these deviations change as a function of time. In this dissertation, the temporal changes in the latter digits of this gravity value are used to study the Earth's constantly evolving system. Namely, the changes in the Earth's ice sheets, water cycle, and oceans have garnered particular interest since the March 2002 launch of a space mission dedicated to detect these small gravity changes: the Gravity Recovery and Climate Experiment (GRACE) mission.

But while this mission has arguably revolutionized the scientific understanding of surface mass redistribution since 2002, is there a way to leverage other data before the launch of GRACE? **The main hypothesis of this dissertation is that the global gravity fields from the GRACE mission can be extended into a longer record using complementary conventional data of satellite tracking.** As such, there are two main outcomes to this dissertation. First, a novel statistical framework to combine two time-variable gravity fields of varying time span and spatial resolution is developed along with an approach to quantify the errors that arise in this framework. Second, this framework is used to reconstruct a new, high-resolution, global, time-variable gravity field starting in 1992 using GRACE and complementary satellite tracking data. The combination of the two datasets hinges on adjusting, in a least-squares sense, spatial patterns from a Principal

Component Analysis of GRACE on the complementary satellite tracking data. Because of the uniqueness and novelty of this approach, a number of design and modeling possibilities are explored along with the accompanying error budget. These reconstructed fields provide an opportunity to answer questions pertaining to the Earth system before 2002: Were the polar ice sheets losing mass in the 1990s at a lower rate than during the GRACE time frame? Figure 1.1 illustrates the potential benefit of the extended time series from reconstructed global gravity fields. Has the behavior of terrestrial water and its relationship to global mean sea level changed since the 1990s? Furthermore, can the reconstructed gravity fields bridge the upcoming gap between GRACE and its successor mission GRACE Follow-On?
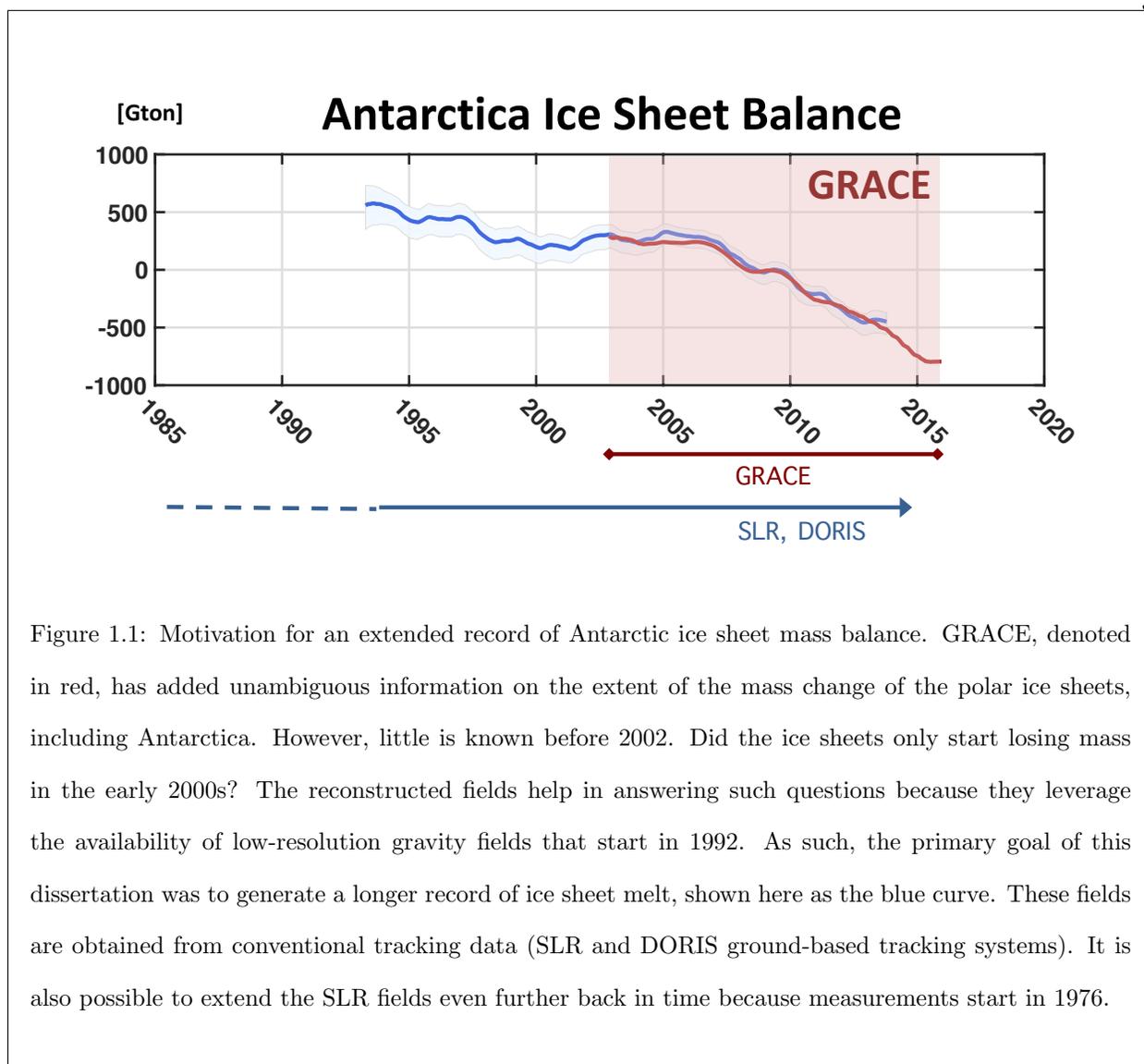
Figure 1.1: Motivation for an extended record of Antarctic ice sheet mass balance. GRACE, denoted in red, has added unambiguous information on the extent of the mass change of the polar ice sheets, including Antarctica. However, little is known before 2002. Did the ice sheets only start losing mass in the early 2000s? The reconstructed fields help in answering such questions because they leverage the availability of low-resolution gravity fields that start in 1992. As such, the primary goal of this dissertation was to generate a longer record of ice sheet melt, shown here as the blue curve. These fields are obtained from conventional tracking data (SLR and DORIS ground-based tracking systems). It is also possible to extend the SLR fields even further back in time because measurements start in 1976.

A number of studies have already investigated the use of conventional satellite tracking data as a basis to detect and interpret time-variable gravity signals before GRACE. *Cox and Chao* (2002), *Nerem and Wahr* (2011), and *Cheng et al.* (2013) have shown that time series of J_2 estimates, where J_2 is the zonal coefficient describing the oblateness of the Earth, provide a reliable metric to measure the combined contribution of the Greenland and Antarctic ice sheet balance. *Morrow et al.* (2013) argue, however, that the next even zonal coefficient J_4 provides a metric of even higher reliability because of smaller contamination from other signals, such as the Glacial Isostatic Adjustment (GIA), the 18.6-year solid Earth body tide, and core-mantle coupling. Fields up to

degree four (spatial resolution of 5,000 km) have been released in various centers (*Cheng et al.*, 2011; *Matsuo et al.*, 2013). In particulary, *Matsuo et al.* (2013) employed these data to conclusively detect mass change in Greenland, but the findings were greatly limited by the noise from the low-resolution fields. While other studies sought to combine the two types of fields (GRACE and conventional tracking data) at the normal equation level (e.g., *Haberkorn et al.* (2014)) for only low degree and order coefficients, this study combines the final products including all available Stokes coefficients.

Furthermore, while such reconstruction of gravity fields has never been undertaken before, the oceanography and altimetry communities have successfully reconstructed longer time series of sea level using various datasets (sea level pressure, temperature, tide gauges) and the high resolution information of sea level from satellite altimeters (*Kaplan et al.*, 2000; *Chambers et al.*, 2002; *Church et al.*, 2004; *Hamlington et al.*, 2011). The dissertation utilizes a similar approach by fusing datasets of varying time lengths and spatial resolution, but does not rely on sources of data other than global time-variable gravity fields derived from tracking observations of satellites.

A short overview of the rich history of geodesy is first given in Section 1.2. Section 1.3 describes the recent advancements from satellite geodesy and how this dissertation utilizes three different techniques that are at the heart of satellite geodesy. The GRACE mission is presented in Section 1.4 and its contributions to geodesy and geophysics summarized in Section 1.5; these contributions are important to understand because the reconstructed fields seek to contribute in a similar manner, but over a time frame before the GRACE mission. Finally, the explicit advancements derived from this dissertation are listed in Section 1.6, as well as a brief description of each chapter.

1.2   Historical Background

A brief overview of the history of geodesy is presented here. *Vaníček and Krakiwsky* (1986) define four periods: historical beginnings, scientific beginnings, the mapping period, and the modern era. Some major examples and figures are described to illustrate each period. Lastly, the

connections between the modern era of geodesy and the themes of this dissertation are presented.

J. Wahr (p. 2, 1986) remarked that "Geodesy has a reasonable claim to being the oldest branch of geophysics." The word *geodesy* finds its origin in the ancient Greek word meaning "division of the earth." The earliest known efforts in addressing fundamental questions (e.g., is the Earth flat?) come from ancient Greece: Aristotle posited a spherical earth; Erathostenes, in one of the most famous empirical experiments in Antiquity, estimated the circumference of the Earth around 240 BC using the shadows cast in wells by the mid-day sun and the distance between them; Ptolemy compiled the first set of geodetic works and as such attempted to standardize cartography, i.e., the making of maps [Section 1.1. in *Vallado* (2007)]. Concurrently, mathematical fields such as geometry and trigonometry were formally developing throughout the Hellenistic world, and then passed along to the Islamic world between the sixth and twelfth centuries (*O'Leary*, 1948).

The push for global exploration and the Enlightenment period opened an era of rapid development in geodesy in fifteenth and sixteenth century Europe. Columbus' accidental discovery of a new continent and Magellan's first Earth-circumnavigating expedition are two examples of voyages that motivated technological advancement in navigation and time-keeping. Mercator created the first set of comprehensive and mathematically rigorous global maps; Huygens first used the pendulum as a mechanical device designed to accurately keep track of time [Section 1.1 in *Misra and Enge* (2011)]. The scope of geodetic projects became larger and made the financial backing by national institutions necessary. The Longitude Prizes, for example, were funded by the British Parliament to reward advances in ability to measure longitude while at sea – ultimately many of these Prizes were given to British clockmaker John Harrison, who invented the first clocks reliable enough to be used at sea (*Sobel*, 1995). The Enlightenment also brought about a number of mathematical breakthroughs, of which Newton's formulation of gravity in *Principia* in 1687 is perhaps the most famous. In this work, Newton postulated that the Earth was oblate, i.e., larger at the equator than at the poles. The French Academy of Sciences financed two expeditions to Peru and Lapland to determine the non-sphericity of the Earth (*Hoare*, 2005) and ultimately confirmed Newton's intuition – the Earth is indeed flatter by approximately 21 km.

Further practical developments in geodesy enabled the surveying of large swaths of unchartered territories. In particular, surveying was improved by the combination of Snell's triangulation techniques (whereby trigonometric principles enable quick calculation of distances between two points) with the newfound portability of surveying instruments such as theodolites. The quest to map India and the tallest Himalayan peaks, led by British Col. George Everest (*Keay*, 2000), was a well-documented surveying endeavor. This mapping period also witnessed the refinements of mathematical tools: Gauss's definition of the geoid (the surface of equal gravitational potential that best fits the mean sea surface) and least-squares methods, Legendre's use of polynomials, Laplace's theory of tides and work in probability, etc. With this evolution in the practical and theoretical worlds, a number of geodesy concepts were further reinforced in the context of geophysics. Airy and Pratt were the first to describe the relationship between topography and gravity; Eötvös defined gravity gradients. At the end of this mapping period early in the twentieth century, continental-wide datums were first put in place. This globalization was also visible on an organizational level: the IUGG (International Union of Geodesy and Geophysics) and its geodesy branch (IAG, International Association of Geodesy) were created in 1919, along with AGU (American Geophysical Union) – three organizations that play dominant roles in connecting global geodetic efforts.

World War II and the Cold War were the impetus for paradigm shifts in observational geodesy. The launch of Earth-orbiting satellites, the development of microelectronics, and the ability to track electromagnetic waves allowed geodesists to study the Earth at unprecedented scales. To make sense of these new types of observations from space, analytical approaches to satellite-based geodesy were developed by *Kaula* (1966). Furthermore, new standards were put in place: the Very Large Baseline Interferometry (VLBI) system and its tracking of quasars provided an opportunity to first define an inertial coordinate frame; the US Air Force's Global Positioning System (GPS) allowed for global, standardized, and precise measurements of time and position. National space agencies deployed scores of geodesy-focused satellites; due to their position in space, satellites are particularly effective at quantifying the static and time-variable components of the gravity fields (see Section 1.3). Specifically, the Gravity Recovery And Climate Experiment (GRACE) mission

(see Section 1.4) connects gravity measurements to a number of other geophysical disciplines (see Section 1.5).

All in all, the modern era witnessed an orders-of-magnitude increase in the volume, precision, and accuracy of global geodetic measurements. This data-rich environment warrants novel techniques to combine different data types. **This dissertation expands on this theme because it seeks to utilize the wealth of data from three specific satellite geodesy techniques in order to form a unifying set of time-variable global gravity fields.** With this overview of geodesy in mind, the following section further defines the field of satellite geodesy.

1.3   Satellite Geodesy and Time-Variable Gravity

The gravity field of the Earth can be measured using different techniques. Satellite geodesy offers unique advantages compared to gravimetric techniques based on the surface of the Earth, such as static gravimetry and "moving" gravimetry. First, static gravimeters are mechanical devices designed to measure either the absolute value of gravity or a value relative to a reference. The absolute gravimeters are especially powerful as they can achieve μGal-level accuracy[1]. Relative gravimeters are useful in that they require less time to perform measurements and are therefore better suited for surveying. Superconducting relative gravimeters also provides high-precision measurements on the order of nGal – it is important to note that this high precision does not equate to high accuracy (i.e., close to a true value), hence the requirement for a reference. However accurate and precise they are, the need to transport and reset static gravimetry devices for each new measurement is a severe hindrance to the achievement of large spatial sampling. This issue is mitigated with "moving" gravimetry. Despite its lower precision on the order of mGal (*McLeish and Ferguson*, 2016), this technique is a more cost-effective and powerful tool for regional studies. Examples of airborne gravimetry include Operation IceBridge over the polar caps from the National Aeronautics and Space Administration (NASA) (*Koenig*, 2010), as well as the GRAV-D program established by

---

[1] One Gal corresponds to an acceleration of 1 cm/s^2. 1 μGal is equivalent to 3 mm of elevation difference (*Nerem et al.*, 1995).

the National Ocean and Atmospheric Administration (NOAA) to determine a geoid-based vertical datum for North America (*Johnson*, 2009). However, airborne and ship-borne geodesy provide solutions that are neither global nor easily repeated. To address the lack of global perspective at repeated intervals, one must turn to satellites.

Due to the high-altitude, periodic nature of their motion, satellites are inherently powerful vantage points. The Laser GEOdynamics Satellite-1 (LAGEOS-1), launched on 4 May 1976, is one of the first satellites solely dedicated to geodetic purposes. It consists of a 60-cm wide cannonball-like satellite orbiting the Earth at an altitude of 5,900 km. Its retroreflectors, arranged in a sphere to optimize the return of a signal back to its origin, enable high-precision passive tracking from an Earth-based ranging system called the Satellite Laser Ranging (SLR). SLR tracking stations are deployed throughout the world (see further details in Section 3.3.1). The tracking of satellites is an essential process of satellite geodesy known as orbit determination (OD) because it yields information on the inhomogeneities of Earth's gravity field. Since LAGEOS-1, more cannonball-like satellites and a slew of more complex satellites have been launched. In particular, SeaSAT (NASA), Geosat (US Navy), Europe Remote Sensing-1 (ERS-1), and ERS-2 (European Space Agency (ESA)) paved the way for consistent improvement in OD. Ultimately, orbit determination centers were able to determine the position of satellites in space to within one cm. The advent of the Doppler Orbitography and Radiopositioning Integrated by Satellite (DORIS), a second successful global tracking system, was another important development (see Section 3.3.1). This allowed for the development of altimetry-focused satellites initiated by NASA and the French space agency, Centre National D'Études Spatiales (CNES), in 1993 with the launch of TOPEX/POSEIDON. Soon following were Jason-1, Jason-2, and Jason-3 in January 2016.

After satellite altimetry became an operational technique in the 1990s, satellite gravity would follow in the 2000s. The CHAllenging Minisatellite Payload (CHAMP) from the German space agency, Deutsches Zentrum für Luft- und Raumfahrt (DLR), was a multi-disciplinary mission that measured the Earth's gravity field over 10 years (July 2000 – September 2010). Its GPS track-ing data allowed for a time-variable gravity field of degree and order four, equivalent to a half-

wavelength spatial resolution of approximately 5,000 km, distributed on a monthly basis (*Reigber et al.*, 2005). ESA's Gravity field and steady-state Ocean Circulation Experiment (GOCE) employed three orthogonal pairs of accelerometers to form a high-precision gradiometer. This enabled the measurement of the Earth's gravity gradients. Moreover, GOCE's low altitude of 250 km facilitated the detection of the finer gravity features that are otherwise attenuated at higher altitudes. The final result of this 2009–2013 mission was a geoid with spatial resolution of less than 100 km and vertical accuracy of 2-3 cm (*van der Meijde et al.*, 2013).

GOCE provided a high-resolution global geoid; CHAMP showed that time-variable component of Earth's long wavelength gravity were detectable from space-based measurements; the GRACE mission complements both. As such, the GRACE mission has profoundly marked the field of satellite geodesy; it rendered observations that before would have been considered extraordinary, now merely routine; it has unraveled connections between various geophysical phenomena; and GRACE has provided a view of the Earth System that is forever changed. The reconstructed gravity fields of this dissertation are generated using tracking data from SLR and DORIS, which are currently used to form a gravity field that extends back to the early 1990s, as complements to this unique GRACE information. In the next section, the GRACE mission and its measurements are further explained.

1.4   The GRACE Mission

The Gravity Recovery And Climate Experiment (GRACE) mission consists of two satellites, GRACE-A and GRACE-B, orbiting the Earth. The mission is operated by NASA and the German space agency DLR, was selected under the NASA Earth System Science Pathfinder program in March 1997, cost approximately $450 million, and was launched on 17 March 2002 from the Plesetsk Cosmodrome in Russia. The planned lifetime of the mission was five years but it has exceeded this amount by over ten years and continues to collect data. As of February 2017, it is expected that the GRACE mission will finally end in June or July 2017, with the spacecraft disintegrating upon re-entry in the upper layers of the atmosphere at high speeds (*Webb et al.*, 2016).

The orbit of the two satellites is near-circular ($e = 0.001$), near-polar ($i = 89.5°$), and has an orbit of 91 min (*Tapley et al.*, 2004a). The initial altitude of the GRACE satellites was 500 km and it has steadily drifted to below 400 km. GRACE-A and GRACE-B are on the same orbital plane and are separated by 170–220 km along track. In other words, this means that one satellite is always chasing the other in their free-fall around the Earth – hence their nickname, Tom and Jerry.

The primary goal of the GRACE mission is to measure inhomogeneities in the Earth's gravity field. It does so by measuring the distance between the two satellites. This distance changes in time because the two satellites are far enough from each other that they are subject to different forces. A number of these forces, called non-conservative, are unrelated to gravity and include solar radiation pressure, atmospheric drag, etc. But a portion of theses forces are due to the slight changes in gravity between the two satellites. To best disentangle these two types of forces operating on the spacecraft (non-conservative vs. Earth gravity), four main subsystems were specifically designed (*Tapley et al.*, 2004a).

First, the K-band ranging (KBR) system measures the range and range-rate between the two spacecraft. The signal is dual-one-way range in K- and Ka-band phase, which allows for the removal of ionospheric errors. The range accuracy achieved is one μm (*Tapley et al.*, 2004a) and range-rate accuracy 0.5 μm/s (*Ditmar and Xianglin*, 2008). Second, the GPS trackers and Ultra Stable Oscillator (USO) tag the timing of all signals on-board the spacecraft (*Dunn et al.*, 2003). The GPS trackers are also a key subsystem to enable OD, along with an SLR retroreflector. Third, the accelerometers identify the non-conservative forces that act on the spacecraft. Inside the accelerometer, an electrostatically suspended proof mass is centered between capacitor plates (*Touboul et al.*, 1999); the motion of this mass and the voltage needed to maintain its position highlight these non-conservative forces and enable their measurement. Fourth, the attitude control and magnetic actuators co-locate and control this center of mass and accelerometer proof mass (*Watkins and Bettadpur*, 2000). The attitude is given by star trackers that orient the spacecraft in an inertial reference frame by noting the position of stars (*Watkins and Bettadpur*, 2000). In

summary, the main GRACE data product is the changes in range and range-rate between its two satellites measured by the KBR subsystem. These changes in range and range-rate are filtered to remove non-conservative forces, which are identified by the accelerometer and attitude subsystems and linked in time via the GPS and USO subsystem. What is left from this process are the KBR residuals, in which gravity information is found.

Three research centers are officially tasked with the transformation of these KBR data into more accessible, level-2 data: global gravity fields with a spatial resolution of approximately 330 km (*Tapley et al.*, 2004a). The three research centers are the Center for Space Research (CSR) at the University of Texas – Austin, TX, GeoForschungsZentrum (GFZ) in Potsdam, Germany, and the Jet Propulsion Laboratory (JPL) in Pasadena, CA. Today, global gravity fields are defined as sets of coefficients that each describe the amplitude of distinct, global, independent basis functions. These functions are called spherical harmonics and the coefficients can be referred to as Stokes coefficients (see Section 2.2). In addition to Stokes coefficients, it is possible to use the level-1 data to directly infer mass changes in customized regions defined as "mass concentrations", or mascons. Mascons are even more accessible and readily visible[2] than spherical harmonics and their associated Stokes coefficients. These gravity fields are commonly distributed on a monthly basis, although some centers have experimented with shorter time periods – even daily updates, such as at the University of Graz, Austria (*Klinger et al.*, 2016).

In summary, the GRACE mission was specifically designed to measure the changes in inter-satellite range and range-rate, while accounting for the influence of non-conservative forces. This information is used to generate high-resolution global gravity fields on a monthly basis; the differences in monthly fields illustrate the time dependency of Earth's gravity field. The two advantages of these GRACE global gravity fields – their high-resolution and time-dependency – have enabled the scientific community to make advances in a number of geophysics disciplines, which are summarized in the following section.

---

[2] See http://ccar.colorado.edu/grace/.

1.5   Applications of GRACE to Geophysics

Because many geophysical phenomena lead to changes in the gravitational field of the Earth, GRACE observations are used in a number of different investigations. Since the delivery of the first global gravity field from GRACE in April 2002, new activities have been made possible (e.g., unambiguous drought monitoring, see Section 1.5.2) and existing models have been improved (e.g., global ocean models, see Section 1.5.3). GRACE is therefore at the heart of many geophysical disciplines. The main product of this dissertation is a set of reconstructed gravity fields that seek to provide a similarly informative view of various geophysical fields over the time periods that are not covered by GRACE. It is therefore important to understand the context of these geophysical disciplines that have been most advanced by time-variable gravity data from the GRACE mission: glaciology, hydrology, oceanography, and solid Earth. An overview of these disciplines and their connection to GRACE observations is provided in the following sections.

1.5.1   Glaciology

The change in the mass of glaciers and polar ice sheets is one of the largest geophysical signals seen by GRACE. In particular, the sheer size and magnitude of the ice melting in Greenland and West Antarctica dwarfs other long-period signals. Because of the influence of this melt on sea level rise and their potential in affecting society, they have garnered much attention. Indeed, the Greenland and Antarctic ice sheet store enough frozen water to raise the global sea level by approximately 6 and 60 meters, respectively; mountain glaciers in Alaska, Europe, the Himalaya, the Andes, and Patagonia would also raise sea level by several meters if they were to melt entirely (*Church et al.*, 2013). While no climate model would ever suggest such catastrophic sea level rise in the foreseeable future (100-yr time frame), even a few decimeters of global sea level rise is a major cause of concern.

The mass loss of polar ice sheets has been observed since the early years of the GRACE mission (*Velicogna and Wahr*, 2006a; *Ramillien et al.*, 2006) using a basin-averaging method (*Swenson and*

Wahr, 2002) and pre-defined mass concentrations called mascons (*Luthcke et al.*, 2006). *Velicogna and Wahr* (2006a) determine that heavy mass loss is concentrated in West Antarctica. *Wouters et al.* (2008) show that mass loss in Greenland is concentrated in the peripheral glaciers along the southeastern and northwestern coasts; *Velicogna and Wahr* (2006b) suggest that the Greenland ice sheet responds quickly to climate perturbations. Follow-up studies have confirmed that this mass loss is not limited to the first years of GRACE (*Luthcke et al.*, 2013; *Velicogna et al.*, 2014). Observations of ice melt are also applicable throughout the world (*Gardner et al.*, 2013) including glaciers in Patagonia (*Chen et al.*, 2007), and Alaska (*Tamisiea et al.*, 2005; *Luthcke et al.*, 2008). Nowadays, the mass balance of the polar ice sheets determined by GRACE is monitored on an operational basis and made publicly available on website such as the NASA Climate page[3] , ESA Climate Change Initiative[4] , and Technische Universität Dresden[5] .

As such, recent studies have also focused on refining techniques and assessing their limits. *Velicogna and Wahr* (2013) assess the limitations of GRACE-based methods and show that Greenland and Antarctica are influenced differently by various error sources; *Bonin and Chambers* (2013) seek to further define errors from the signal leakage that is inherent to the basin-averaging method (*Swenson and Wahr*, 2002). *Wouters et al.* (2013) discuss the limitation in assigning certain statistics to the mass loss curves that are temporally limited; in particular, the computation of an acceleration term is still challenging given the short GRACE time series. *Schrama and Wouters* (2011) investigate the signal partition in different basins in and near Greenland, including over the Canadian Archipelago, i.e., Ellesmere Island, Baffin Island, Iceland, and Svalbard. *Harig and Simons* (2012) address the limitation of a spherical harmonic kernel approach and employ Slepian functions to concentrate the energy of the global signal in specific areas, which is impossible for spherical harmonics (*Schmidt et al.*, 2008). *Xu et al.* (2015) implement new constraint equations to optimize the inversion of GRACE level-2 data onto separate drainage systems.

Because GRACE-based methods still show disagreement, independent geodetic techniques

---

[3] http://climate.nasa.gov/vital-signs/land-ice/
[4] http://esa-icesheets-cci.org/
[5] https://data1.geo.tu-dresden.de/

are used for validation purposes. *Cazenave* (2006) use radar altimetry in addition to GRACE to estimate a consistent measure of mass change over both ice sheets. *Sutterley et al.* (2014) is an example of a regional study that used different geodetic techniques to validate mass change in the Antarctic peninsula. *Rignot et al.* (2011) validate GRACE-based results with mass balance results from an input-output method, whereby ice discharge data are subtracted from surface mass balance[6] to obtain mass balance. Finally, reconciled estimates are pursued to better disentangle disagreements between various techniques, as is done in *Shepherd et al.* (2012) for polar ice sheet mass balance and *Gardner et al.* (2013) for glaciers.

The GRACE data and their limitations are now well documented and integrated in scientific applications. Is there a way to extend this before the launch in 2002? Were the polar ice sheets already losing mass at such rates in the 1990s? Do the polar ice sheets experience inter-annual variations that are not detectable using only GRACE? *Rignot et al.* (2011) use radar altimetry to show that the Antarctic ice sheet is more sensitive to regional variations in mass change than the Greenland over the 1990s, but that the Greenland ice sheet experienced significant mass gain between 1995 and 1997. Can reconstructed time-variable gravity confirm this behavior? Furthermore, could reconstructed fields detect major changes in behavior of the polar ice sheets during a gap between GRACE and GRACE Follow-On?

1.5.2   Hydrology

The motion of water on land is a prime signal for the GRACE mission. The global water cycle entails exchange of water mass between the continents, the atmosphere, and bodies of water such as lakes, seas, and oceans. The fact that GRACE measures the entire water column (i.e., the sum of groundwater, soil moisture, snow, surface water, ice, etc.) separates it from *in-situ* hydrologic data which are typically limited to one layer of the water column. The first results were published shortly after the launch; *Tapley et al.* (2004a), *Crowley et al.* (2006) show meaningful mass change

---

[6] Surface mass balance is defined as the difference between the accumulation and ablation of snow. This process is analogous to precipitation minus evaporation for water.

in the Amazon and in the Congo, respectively.

Humphrey et al. (2016) give a recent overview of the assessment of global terrestrial water storage (TWS) and its variability for inter-annual, seasonal, sub-seasonal signals. Such an overview showed that TWS relate to atmospheric drivers, thereby enabling the use of these data for hydrological forcing. Moreover, large-scale single events are well-constrained by GRACE. The Australia event of 2011, in which the Australian land mass retained enough water to slow the ongoing global sea level, is investigated in *Fasullo et al.* (2013) and *Boening et al.* (2012). By virtue of its ability to capture changes throughout the water column, GRACE has also become a more reliable indicator than other land-based instruments, which can only monitor certain layers of the water column. The Texas drought of 2011, for example, was well isolated by GRACE (*Long et al.*, 2013). *Famiglietti and Rodell* (2013) illustrate the applications of GRACE product in improving the management of regional groundwater reserves.

Beyond the use of GRACE data alone, GRACE data are assimilated into hydrological models as a way of constraining them. Hydrological models include GLDAS (*Rodell et al.*, 2004). *Eicker et al.* (2014) assimilate GRACE data into an advanced global land data assimilation system (Water-GAP Global Hydrology Model) via an Ensemble Kalman Filter and showed that these assimilation procedures are improved with GRACE data.

What about the temporal behavior of TWS? *Reager et al.* (2016) determine that changes in TWS have slowed climate-driven rise in sea level: an additional 3,200±900 Gt of water have been stored on land since 2002, offsetting sea level change by 0.71±0.20 mm. Once again, extending the GRACE time record prior to 2002 would shed more light on this effect: has TWS been accumulating mass in the 1990s? Furthermore, reconstructed gravity fields could also be assimilated in global hydrological models, as proposed by Prof. E. Forootan in a 2017 Natural Environment Research Council (NERC, United Kingdom) proposal [*personal communication with E. Forootan, 2017*].

1.5.3   Oceanography

The time-variable gravity signal from the ocean is smaller in magnitude than in hydrology and glaciology. Yet, contributions from GRACE are particularly useful because of its unique ability to directly detect mass change.

While altimetry satellites detect changes in height of the oceans, they are unable to disentangle the two components that influence global sea level rise: the changes due to added heat and the subsequent thermal expansion of water (called steric) vs. the changes due to added mass (called eustatic). Instead, GRACE provides a direct measure of this eustatic component, driven mostly by the melt of land glaciers and polar ice sheets (*Chambers et al.*, 2010; *Chambers and Bonin*, 2012). *Johnson and Chambers* (2013) show that this mass changes contributes almost 2 mm/year of the total sea level trend seen over the GRACE time period of nearly 3 mm/year and that regional patterns of ocean mass change vary annually by up to 4 cm.

Beyond spatial variations over a decade, *Quinn and Ponte* (2012) demonstrate that GRACE products can be used to detect barotropic changes in large-scale ocean variability at high frequency (down to 14-day periods). Barotropic means that the ocean bottom pressure (OBP) detected by GRACE are related to changes in deep ocean currents. As such, *Landerer et al.* (2015), for example, use GRACE data to measure changes in the North Atlantic Meridional Ocean Circulation; *Makowski et al.* (2015) show that the transport variability of the Antarctic Circumpolar Current (ACC) over the southern Indian Ocean is significantly different than previously known. Combining GRACE data with other data over regional areas, such as satellite altimetry and/or floats, allows for regional sea budget studies. *Kleinherenbrink et al.* (2016) demonstrate that the sea level budget in the North Atlantic Ocean can be closed using all those different types of data. *Kusche et al.* (2014) apply a similar approach of sea level budget closing to the Bay of Bengal. Another application of GRACE in oceanography is in constraining and validating global barotropic ocean tide models (*Stammer and et al.*, 2014). Reducing the errors of tide models ultimately improves the process of precise orbit determination (POD) because tide models are removed from *a priori* gravity models.

However, the reconstructed fields are not expected to add much knowledge prior to GRACE because their noise is likely larger than the signal in oceanography.

1.5.4 Solid Earth

Variability in the distribution of Earth's mass is also affected by variability in the crust of the Earth. Two phenomena operate at time scales that are applicable to GRACE: isostatic adjustment and earthquakes.

Isostatic adjustment is the viscoelastic response of the Earth's crust to variability in mass loading; it is analogous to the slow rebounding of a sponge once extra mass has suddenly been removed after lying on top of it. To properly interpret GRACE-based gravity signal such as ice sheet mass change, it is essential to constrain the extent of any isostatic adjustment. In particular, the crust of the Earth is still rebounding from the melting of major continental ice sheets created during the Last Glacial Maximum (LGM) approximately 20,000 years ago. This effect is known as the Global Isostatic Adjustment (GIA), sometimes referred to as Post-Glacial Rebound (PGR). Two of the most visible examples of GIA can be found in the Hudson Bay and in Scandinavia, where GPS stations record upward motion of up to 10 mm/yr (*Milne et al.*, 2001). Current efforts to determining a GIA model are still plagued with large errors and, therefore, inhibit properly estimating mass changes in Antarctica.

GIA consists of two main inputs: the ice loading history and the Earth's viscosity profile. ICE-6G is an example of global ice loading histories (*Peltier et al.*, 2015), while *Ivins et al.* (2013); *Whitehouse et al.* (2012a) provide a regional model of ice loading history in Antarctica, called IJ05_R2 and W12a, respectively. Furthermore, the Earth's viscosity profile is still not very well constrained.

As opposed to GIA, which operates over thousands of years, earthquakes have a time-variable gravity signature that is near instantaneous. Two examples of earthquakes large enough to be detected by GRACE mission are the 2004 Sumatra earthquake (*Han et al.*, 2006) and the 2011 Tohoku-Oki earthquake (*Wang et al.*, 2012). In this dissertation, only the GIA effects are taken

into account.

While reconstructed fields based on GRACE data are not expected to add directly to solid Earth research, it is vital to take into account at least GIA effects. Because these effects are effectively linear over decades in nature, they are easily extended to the time frames that span beyond GRACE.

1.5.5   Miscellaneous

Because of the inherent multi-disciplinary nature of time-variable gravity, it is possible to combine various data types and recover signal for different geophysical fields. *Wu et al.* (2012), *Wu and Heflin* (2015) show that a number of geodetic methods can be used to derive results for polar ice sheets using GPS, OBP, SLR, and GRACE. Other general geodetic purposes include investigating time-variability of the Earth's geocenter (*Wu et al.*, 2012), polar motion (*Chen et al.*, 2013; *Adhikari and Ivins*, 2016), and oblateness (*Nerem and Wahr*, 2011; *Cheng et al.*, 2013).

1.6   Contributions of this Dissertation: Executive Summary

The motivation for this dissertation originated in a proposal named "Reconstruction of Temporal Gravity Variations Prior to and After the GRACE Mission: Towards a Gravity Climate Data Record" and submitted in response to the NASA call NNH10ZDA001N-GRACE. The proposal outlined the basic building blocks of the reconstruction approach and referenced the availability of complementary time-variable gravity solutions from the Goddard Space Flight Center (GSFC). This dissertation implemented the reconstruction, explored different avenues that sought to improve the process, and applied the reconstructed fields.

Chapter 2 develops the theory behind the spherical harmonic representation of global gravity fields and the main techniques used in this dissertation. Namely, the reconstruction process uses two main steps: Principal Component Analysis (PCA) and a Least Squares Adjustment (LSA). Other techniques common to GRACE are presented. In particular, the section on PCA presents possibilities for future research.

Chapter 3 defines the data used in this work, namely, the two types of time-variable gravity solutions. The GRACE data are first presented along with commonly-applied corrections. A major focus of this chapter is the definition of the time-variable gravity solutions that are generated from the conventional tracking data. As such, the two ground-based systems from which the tracking data are obtained are defined. Moreover, the constellation of satellites tracked is described. Furthermore, the three different time-variable gravity field solutions that are based on these tracking systems are described. In particular, the GSFC solution is discussed in great detail. The quantification of the contribution of certain DORIS satellites to the solutions as well as in the creation of a longer time series of C_{20} is presented. Two of the solutions are compared to GRACE – the last solution does not extend much further before the GRACE time period and therefore does not feature extensively in this dissertation. A comparison between the two main solutions were presented at the ESA Living Planet Symposium (*Talpe et al.*, 2016a).

Chapter 4 presents the development of a statistical framework for this combination method (interchangeably referred to as reconstruction). The combination process is best described in three steps. First, the high-resolution GRACE fields are decomposed via Principal Component Analysis in their EOFs, which are the spatial patterns. Second, the top four EOFs were fit via Least-Squares onto the SLR/DORIS fields to obtain the temporal modulation of each spatial pattern. Third, the four EOFs from the first step and associated PCs from the second step are combined linearly to form the reconstructed gravity fields. The peculiarities of the reconstruction process and major design decisions are described in detail and were presented at AGU and EGU conferences (*Talpe et al.*, 2013, 2014). For example, the input matrix that is used as input in the PCA process in the first step was composed of spherical harmonics coefficients and not grid cells, as is commonly done. This decision required the need for a new weighting scheme, which was determined empirically as $1/l$, where l reflects the degree of the coefficients. A second example of design decision pertained to truncating the resolution of the GRACE fields in the LSA process in order to match the resolution of the SLR/DORIS fields. One last example is the assumption that the modes are stationary, i.e., constant beyond the GRACE time period. Moreover, the error budget from this statistical

framework and its associated assumption is developed and three main error sources are addressed and quantified for specific regional cases – Greenland and Antarctica. A large part of this work was published in the Journal of Geodesy (*Talpe et al.*, 2017).

Chapter 5 shows the main scientific application of the reconstructions: a longer time series of mass change of the Greenland and Antarctic ice sheets. The results are validated against other methods that are independent of time-variable gravity, including an Input-Output Model that is computed for the purpose of this dissertation. This was a direct result of participation at the 2015 Climate Days conference (*Talpe et al.*, 2015a). The main conclusions from this study is that Greenland was losing mass at a much lower rate in the 1990s than over the GRACE time frame. Furthermore, the reconstruction showed an episode of mass loss and gain over the 1998–2002 period that is not seen in other models. Finally, Antarctica appeared to have melted in the 1990s at about half the rate of afterwards, while also neither gaining nor losing significant mass between 1998 and 2002. This work was published in Journal of Geodesy (*Talpe et al.*, 2017) and will hopefully be included in the second version of an inter-method comparison exercise seeking to combine all possible estimates of mass change in the cyrosphere (*Shepherd et al.*, 2012).

Chapter 6 presents another scientific application: quantifying the contribution of terrestrial basins to sea level rise before the GRACE mission. A similar approach to the one developed Chapter 5 is employed, but to different regions, and, therefore, sheds light on the performance of the reconstructions while also providing a different method for validation – models of hydrologic mass changes instead of cryospheric mass changes. While the reconstruction lacks some important inputs, namely, geocenter coefficients, the study suggests that the non-ice sheet areas were not contributing much to sea level in the 1990s. This work was the basis of a poster at AGU 2016 (*Talpe et al.*, 2016b).

Chapter 7 discusses an application of the reconstructed fields in mitigating the future gap between GRACE and GRACE Follow-On. In particular, the influence of gaps in GRACE-like data on the final reconstructions was examined and it is shown that the top three modes are not strongly affected by gaps, suggesting that this technique is robust to bridge gaps, but not

necessarily in detecting meaningful short-term regional time-variable gravity changes. This study was presented at AGU 2015 (*Talpe et al.*, 2015b).

Lastly, Chapter 8 provides a summary of the dissertation and an outlook on possible avenues for future research. Applications such as Precise Orbit Determination in the 1990s are briefly discussed. Also enumerated are improvements to the statistical framework in which large datasets describing the same geophysical products are combined. Indeed, this reconstruction method is not limited to time-variable gravity fields.

Owing to the fact that this work is entirely concerned with gravity fields, the following chapter describes their nature in more detail, along with the general mathematical techniques used throughout this dissertation.

Chapter 2

Theory

2.1   Overview

This chapter introduces the mathematical background of the techniques of this dissertation. First, Section 2.2 derives and describes the spherical harmonics that are the analytical representations of global gravity fields. Second, Section 2.3 develops the tool used to extract the dominant spatial patterns from the GRACE data, Principal Component Analysis, and several alternatives. Finally, Section 2.4 discusses three analysis techniques: Least Squares Adjustment, regional mass computation from global gravity fields, and full matrix error propagation.

2.2   Derivation and Use of Spherical Harmonics

The gravitational potential of the Earth V can be expressed analytically in a spherical coordinate frame as a superposition of functions,

$$V(r, \phi, \lambda) = \frac{GM}{r} \left[\sum_{l=0}^{l_{max}} \sum_{m=0}^{l} \left(\frac{r_E}{r} \right)^l \tilde{P}_{lm}(\sin(\phi)) \left(\tilde{C}_{lm} \cos(m\lambda) + \tilde{S}_{lm} \sin(m\lambda) \right) \right]. \qquad (2.1)$$

In this section, the terms of this expression are defined and an overview of the derivation of this equation is presented. But first, why is an analytical representation of gravity fields necessary? Why not just provide empirically-derived values of the force of gravity on predefined grids? An analytical expression is necessary because (1) it is easily scalable into whatever resolution desired and (2) it is differentiable and aptly manipulated in conjunction with other well-defined concepts relevant in satellite geodesy, such as Love numbers. Love numbers describe how the crust of the Earth

responds to loading on its surface and are distributed in this spherical harmonics representation (*Wahr et al.*, 1998).

There are many steps to the derivation of Eq. 2.1, which belongs to a general field call potential theory. First, the force of gravity and its associated potential are defined in Section 2.2.1. Second, Laplace's equation is introduced in the context of gravity fields and its solutions derived in Section 2.2.2. The solutions to Laplace's equation are the spherical harmonics that represent the gravity fields analytically. *Kaula* (1966), *Wahr* (1986), *Hofmann-Wellenhof and Moritz* (2005), and *Jekeli* (2009) give proper rigor, a fuller context, and further details such as setting up the boundary-value problem, the non-uniqueness of gravity fields, etc. The notation used here is adopted from *Kaula* (1966). Third, illustrations are provided to help visualize the physical meaning of these spherical harmonics and their associated coefficients in Section 2.2.3. Lastly, Section 2.2.4 describes how spherical harmonics can be used to compute a geoid and changes in surface mass density, which is vital for this dissertation.

2.2.1   Gravitational Force and Potential

The force of gravity describes the force that inherently arises in the presence of mass. In Newtonian physics, the force of gravity $\mathbf{F_g}$ exerted between two particles is expressed as

$$\mathbf{F_g} = G \frac{m_1 m_2}{|\mathbf{r}|^2} \hat{\mathbf{r}}, \tag{2.2}$$

where $\mathbf{r}$ describes the vector between the two masses and $\hat{\mathbf{r}}$ its normalized version, m_1 and m_2 the mass of the two particles, and G the gravitational constant with an approximate value of 6.67×10^{-11} m^{3}s^{-2}kg^{-1}. This force of gravity $\mathbf{F_g}$ is a vector quantity.

The potential of a gravity field from one particle V_1 and from an ensemble of n particles V is defined as

$$V_1 = G \frac{m_1}{r_1}, \tag{2.3}$$

$$V = G \sum_{i=1}^{n} \frac{m_i}{r_i}, \tag{2.4}$$

respectively, where r_i is the distance to the particle of mass m_i ($r_i = |\mathbf{r}_i|$). When the number of particles becomes large ($n \to \infty$) and their mass becomes infinitesimally small ($m \to dm$), the summation becomes an integral. Furthermore, when the mass elements aggregate to form a solid body of varying density ρ, the mass elements dm are replaced by ρdV. Both the density profile ρ and the distance r are dependent on the position $\mathbf{p}$, so the integral over the volume of the body $\mathcal{V}$ becomes

$$V = G \int_{\mathcal{V}} \frac{\rho(\mathbf{p})}{r(\mathbf{p})} dV. \tag{2.5}$$

For the applications of this dissertation, what is ultimately sought is this density profile $\rho(\mathbf{p})$ because it contains the gravity information. But there is no way to solve or even measure this density profile $\rho(\mathbf{p})$. The second derivatives of the potential are the key components of this derivation, and it can be shown that they satisfy Laplace's equation. Laplace's equation states that outside of this body, the Laplacian of the potential is zero,

$$\Delta V = 0, \tag{2.6}$$

where the Laplacian operator Δ (sometimes written ∇^2) refers to the sum of the partials with respect to a certain set of coordinates.

2.2.2   Solving Laplace's Equation

In this section, the solution to Laplace's equation are derived in three steps: (1) a full evaluation of Laplace's equation in spherical coordinates, (2) a separation of variables that enables systematically solving each term-based expression, and (3) the normalization of the final expression.

First, Laplace's equation is expanded in spherical harmonics. In rectangular coordinates, Laplace's equation is expressed as

$$\Delta = \frac{\partial}{\partial x^2} + \frac{\partial}{\partial y^2} + \frac{\partial}{\partial z^2}. \tag{2.7}$$

Spherical coordinates are, however, better suited given the geometry of the Earth. As such, r is

the distance from the origin, ϕ is the latitude, and λ is the longitude measured eastward, and

$$x = r\cos(\phi)\cos(\lambda),$$

$$y = r\cos(\phi)\sin(\lambda),$$ (2.8)

$$z = r\sin(\phi).$$

The derivation of each partial in terms of spherical harmonics is not shown here, but the resulting expression in spherical coordinates is

$$r^2 \Delta V = \frac{\partial}{\partial r}\left(r^2 \frac{\partial V}{\partial r}\right) + \frac{1}{\cos(\phi)}\frac{\partial}{\partial \phi}\left(\cos(\phi)\frac{\partial V}{\partial \phi}\right) + \frac{1}{\cos^2(\phi)}\frac{\partial^2 V}{\partial \lambda^2}.$$ (2.9)

The second step of this derivation involves solving Laplace's equation, i.e., finding an analytical solution for the potential V as a function of r, ϕ, and λ. It is assumed that this solution has a separate function for each parameter:

$$V = R(r)\Phi(\phi)\Lambda(\lambda).$$ (2.10)

Each term in Eq. 2.7 is replaced by using the expressions in Eq. 2.10, divided by V, and total derivatives are used instead of partials in order to finally obtain

$$\frac{1}{R}\frac{d}{dr}\left(r^2\frac{dR}{dr}\right) + \frac{1}{\Phi\cos(\phi)}\frac{d}{d\phi}\left(\cos(\phi)\frac{d\Phi}{d\phi}\right) + \frac{1}{\Lambda\cos^2(\phi)}\frac{d^2\Lambda}{d\lambda^2} = 0.$$ (2.11)

One notes that the first term with respect to the term R is independent of the two other terms since they do not contain any reference to the variable r. In other words, the derivative of the first term is constant, and it is convenient (with hindsight!) to equate this constant to $l(l+1)$, where l is an integer. Multiplying both this by R and re-arranging the terms leads to

$$r^2\frac{d^2 R}{dr^2} + 2r\frac{dR}{dr} - l(l+1)R = 0.$$ (2.12)

After more convenient re-arranging and knowledge of the general solution of this particular differential equation, one notes that R takes the form r^k. A full possible solution is thus given by

$$R(r) = Ar^l + Br^{-l-1},$$ (2.13)

where A and B are arbitrary constants. Since the potential of interest for applications pertaining to gravity goes to zero as $r \to \infty$, one can set $A = 0$ and B is set to 1. Therefore,

$$R(r) = \frac{1}{r^{l+1}}.$$

(2.14)

Now that the $R(r)$ portion of Eq. 2.11 has been solved for, the $\Lambda(\lambda)$ portion is examined. This last term of Eq. 2.11 is simplified by multiplying the full equation with $\cos^2(\phi)$. Furthermore, using similar logic as for the $R(r)$, one sees that this term only depends on Λ, so it must be constant and hindsight allows one to set it equal to $-m^2$, where m is an integer, and

$$\frac{1}{\Lambda} \frac{d^2\Lambda}{d\lambda^2} = -m^2.$$

(2.15)

This equation is a harmonic oscillator. A well-defined solution is therefore

$$\Lambda(\lambda) = C \cos(m\lambda) + S \sin(m\lambda),$$

(2.16)

where C and S are once again arbitrary constants that, unlike with the constants A and B for the derivation of $R(r)$, do not have an intuitive value and will be dealt with later.

The derivation of the $\Phi(\phi)$ portion is particularly tedious and difficult to succinctly summarize, so only the major steps are highlighted. It is worth noting that a dependence on l and m arises and that the derivation comes to a point where Legendre's equation manifests itself. The solution to this equation is a power series that contains l and m in the coefficients T_{lmt} associated with each one of the power series,

$$T_{lmt} = \frac{(-1)^t(2l-2t)!}{2^l t!(l-t)!(l-m-2t)!},$$

(2.17)

where the non-negative integer t appears in the derivation and is constrained by $t \leq (l-m)/2$. Furthermore, the power series are defined as the associated Legendre function:

$$\Phi(\phi) = P_{lm}(\sin(\phi)) = \cos^m(\phi) \sum_{t=0}^{k} T_{lmt} \sin^{l-m-2t}(\phi).$$

(2.18)

To find the full form of V from Eq. 2.10, one must combine Eqs. 2.14, 2.16, 2.18. The combination of 2.16 and 2.18 leads to the term S_{lmi} called surface spherical harmonics.

$$V(r, \phi, \lambda) = R(r)\Phi(\phi)\Lambda(\lambda) \tag{2.19}$$

$$= \frac{1}{r^{l+1}} P_{lm}(\sin(\phi)) \left(C \cos(m\lambda) + S \sin(m\lambda)\right) \tag{2.20}$$

$$= \frac{1}{r^{l+1}} S_{lmi}. \tag{2.21}$$

The third step is to use one important property of theses surface spherical harmonics: their orthogonality,

$$\int_{\text{sphere}} S_{lmi} S_{hkj} d\sigma = 0 \quad \text{if} \quad l \neq h \quad \text{or} \quad m \neq k \quad \text{or} \quad i \neq j. \tag{2.22}$$

Equivalently,

$$\int_{\text{sphere}} S_{lmi}^2 d\sigma = 4\pi \left[\frac{(l+m)!}{(l-m)!(2l+1)(2-\delta_{0m})} \right], \tag{2.23}$$

This means that each surface spherical harmonic changes in magnitude with respect to l and m; it is more convenient to normalize them:

$$\tilde{S}_{lmi} = \left[\frac{(l-m)!(2l+1)(2-\delta_{0m})}{(l+m)!} \right]^{1/2} S_{lmi}. \tag{2.24}$$

This normalization is applied to the associated Legendre functions and the C and S coefficients, so that V,

$$V(r, \phi, \lambda) = \frac{1}{r^{l+1}} \sum_{l=0}^{\infty} \sum_{m=0}^{l} \tilde{P}_{lm}(\sin(\phi)) \left(\tilde{C}_{lm} \cos(m\lambda) + \tilde{S}_{lm} \sin(m\lambda) \right). \tag{2.25}$$

The superposition arises from the fact that each l and m spherical harmonic contributes to the total potential V. The integer m is constrained following $m < l$. With some re-arranging, assigning a practical limit to the upper value of l (l_{max}), and including the terms GM and r_E to set this potential expression in the right dimensions, the expression becomes what was presented at the beginning of this section:

$$V(r, \phi, \lambda) = \frac{GM}{r} \left[\sum_{l=0}^{l_{max}} \sum_{m=0}^{l} \left(\frac{r_E}{r} \right)^l \tilde{P}_{lm}(\sin(\phi)) \left(\tilde{C}_{lm} \cos(m\lambda) + \tilde{S}_{lm} \sin(m\lambda) \right) \right], \tag{2.26}$$

where r_E is the average radius of the Earth, M its mass, and G the gravitational constant.

In summary, Eq. 2.26 contains normalized spherical harmonics $\tilde{P}_{lm}$, which are the basis functions on a sphere, and the normalized $\tilde{C}_{lm}$ and $\tilde{S}_{lm}$ coefficients, called the Stokes coefficients and that provide the amplitude for each spherical harmonic. The subscripts l and m are the degree and order, respectively. This summation representation of the potential V is analogous to how a Fourier series decompose a 2-D time series in an infinite number of sinusoidal functions of different periods, each weighted by their own coefficient.

The next section provides illustrations of these spherical harmonics and their dependence on the integers l and m.

2.2.3   Illustration of Spherical Harmonics Fields

The spherical harmonics can be categorized as either zonals, tesserals, or sectorals (see Figure 2.1). Zonal harmonics are when the order is 0 ($m = 0$) and the harmonics show $l+1$ latitudinal bands. There are only C_{l0}-type zonals, because S_{l0} is undefined since the sin term disappears when $m = 0$. Zonals are sometimes expressed as J_l, where $J_l = -\sqrt{2l+1}C_{l0}$. Sectoral harmonics are when the order is equal to the degree ($l = m$) and the harmonics show $2m$ longitudinal sectors. Tesseral harmonics are the remaining cases ($m \neq 0$, $l \neq m$) and the harmonics show checkered patterns with $l+1$ latitudinal zeros and $2m$ longitudinal zeros.
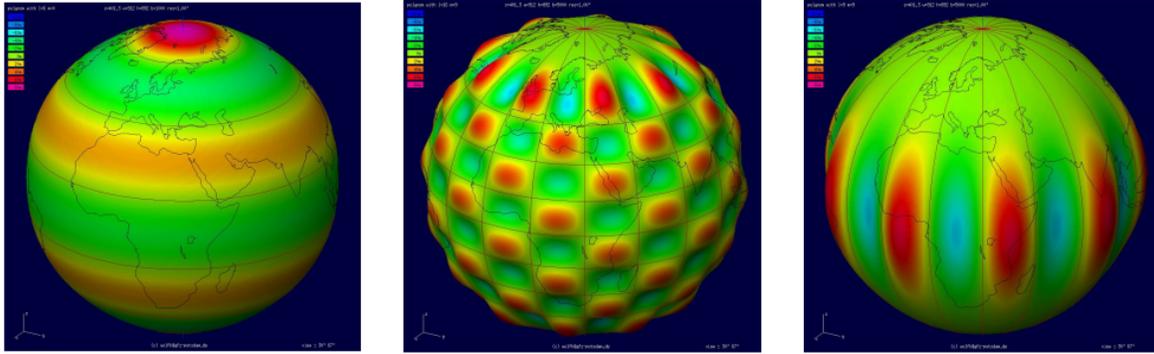
Figure 2.1: Illustration of spherical harmonics: zonals, tesserals, and sectorals. The leftmost figure depicts a zonal where $l = 6$ and $m = 0$; the middle figure a tesseral with $l = 16$ and $m = 9$; the rightmost a sectoral where $l = 9$ and $m = 9$. A full gravity field is a summation of such functions; each spherical harmonic function defined by its degree l and order m is weighted by Stokes coefficients C_{lm} and S_{lm}. The image is taken from `http://icgem.gfz-potsdam.de/ICGEM/potato/gravity-field-tutorial.pdf`.

Finally, it is worth noting that a field with a higher maximum degree l_{max} yields a field with finer spatial structures. A simple rule of thumb relating the spatial scale of a gravity field and the maximum degree l_{max} of its spherical harmonic representation is given as:

$$\lambda = \frac{20,000}{l_{max}}, \tag{2.27}$$

where λ is the spatial resolution of the gravity field in kilometers.

2.2.4 Computing Geoid and Surface Mass Density

How are spherical harmonic fields and their associated normalized Stokes coefficients $\tilde{C}_{lm}$ and $\tilde{S}_{lm}$ related to useful geodetic metrics, such as the geoid and surface mass density? Eq. 2.26 illustrates the link with the potential V.

First, the link between the spherical harmonic representation of the potential in Eq. 2.26 to the geoid height $N(\phi, \lambda)$ is similarly computed, in that the spherical harmonic functions remain

the same, but the units change, so that the dependence on r disappears,

$$N(\phi, \lambda) = a \left[\sum_{l=0}^{l_{max}} \sum_{m=0}^{l} \tilde{P}_{lm}(\sin(\phi)) \left(\tilde{C}_{lm} \cos(m\lambda) + \tilde{S}_{lm} \sin(m\lambda) \right) \right]. \tag{2.28}$$

Furthermore, it is worth noting that in time-variable gravity studies, the inherent topic of interest is changes in geoid, referred to as $\Delta N(\phi, \lambda)$, compared to a reference geoid $N(\phi, \lambda)$. This reference geoid is typically a mean geoid over a certain time frame. The changes in the geoid can also be expressed as the changes in the Stokes coefficients compared to an average value of Stokes coefficient, i.e., $\Delta C_{lm} = C_{lm} - \bar{C}_{lm}$ and $\Delta S_{lm} = S_{lm} - \bar{S}_{lm}$. It is henceforth assumed that (1) the tilde symbolizing the normalization discussed previously is removed and (2) the time dependency is never explicitly written but still present, i.e., $\Delta \tilde{C}_{lm}(t) = \Delta C_{lm}$. Given these assumptions, the changes in geoid are expressed as

$$\boxed{\Delta N(\phi, \lambda) = a \sum_{l=0}^{l_{max}} \sum_{m=0}^{l} \tilde{P}_{lm}(\sin(\phi)) \left(\Delta C_{lm} \cos(m\lambda) + \Delta S_{lm} \sin(m\lambda) \right)}. \tag{2.29}$$

Second, the link between the spherical harmonic representation of the potential in Eq. 2.26 to the surface mass density $\sigma(\phi, \lambda)$ (and/or its changes $\Delta \sigma(\phi, \lambda)$) is derived on p. 30,207 of *Wahr et al.* (1998). The essence of the derivation involves finding the contribution of (1) a surface mass density expression $\sigma(\phi, \lambda)$ in addition to (2) the subsequent deformation of the crust, to each Stokes coefficients C_{lm} and S_{lm}. The direct gravitational attraction of the surface mass density is expressed as

$$\left\{ \begin{array}{c} \Delta C_{lm} \\ \Delta S_{lm} \end{array} \right\}_{surf} = \frac{3}{4\pi a \rho_{ave}(2l+1)} \int \Delta \sigma(\phi, \lambda) \tilde{P}_{lm}(\sin(\phi)) \times \left\{ \begin{array}{c} \cos(m\lambda) \\ \sin(m\lambda) \end{array} \right\} \sin(\phi) d\phi d\lambda, \tag{2.30}$$

where ρ_{ave} is the average density of the Earth and approximately 5,500 kg/m^3. The equivalent "indirect" gravitational attraction, which is akin to finding the direct gravitational attraction of the deformed Earth, is expressed as

$$\left\{ \begin{array}{c} \Delta C_{lm} \\ \Delta S_{lm} \end{array} \right\}_{earth} = \frac{3k_l}{4\pi a \rho_{ave}(2l+1)} \int \Delta \sigma(\phi, \lambda) \tilde{P}_{lm}(\sin(\phi)) \times \left\{ \begin{array}{c} \cos(m\lambda) \\ \sin(m\lambda) \end{array} \right\} \sin(\phi) d\phi d\lambda. \tag{2.31}$$

The one difference between the two expressions is the presence of the term k_l in the numerator. The k_l represent the Love number associated with each degree l. Love numbers describe the response of the Earth to surface loading; three different flavors of Love numbers exist and relate various mechanical properties of the Earth, but the focus here is on the "k" flavor because it pertains to potentials. The value of the Love numbers is given in *Han and Wahr* (1995).

Now that individual expressions for the Stokes coefficients have been established given the two contributors (surface mass load and associated gravitational changes), the full expression for $\Delta\sigma(\phi, \lambda)$ is established. It is worth noting that all references to surface mass density changes are expressed in "equivalent water height," meaning that the units of height represent the layer of water needed to reflect the gravitational change. Hence,

$$\Delta\sigma(\phi, \lambda) = a\rho_w \sum_{l=0}^{l_{max}} \sum_{m=0}^{l} \tilde{P}_{lm}(\sin(\phi)) \times \left(\Delta\hat{C}_{lm}\cos(m\lambda) + \Delta\hat{S}_{lm}\sin(m\lambda)\right). \qquad (2.32)$$

It is possible to find the coefficients from the surface density itself. In other words,

$$\left\{ \begin{array}{c} \Delta\hat{C}_{lm} \\ \Delta\hat{S}_{lm} \end{array} \right\} = \frac{1}{4\pi a\rho_w} \int \Delta\sigma(\phi, \lambda)\tilde{P}_{lm}(\sin(\phi)) \times \left\{ \begin{array}{c} \cos(m\lambda) \\ \sin(m\lambda) \end{array} \right\} \sin(\phi)d\phi d\lambda, \qquad (2.33)$$

so that setting the sum of Eq. 2.30 and Eq. 2.31 to Eq. 2.33 yields the following relationship:

$$\left\{ \begin{array}{c} \Delta\hat{C}_{lm} \\ \Delta\hat{S}_{lm} \end{array} \right\} = \frac{\rho_{ave}(2l+1)}{3\rho_w(1+k_l)} \left\{ \begin{array}{c} \Delta C_{lm} \\ \Delta S_{lm} \end{array} \right\}, \qquad (2.34)$$

and, ultimately from Eq. 2.32,

$$\Delta\sigma(\phi, \lambda) = \frac{a\rho_{ave}}{3} \sum_{l=0}^{l_{max}} \sum_{m=0}^{l} \tilde{P}_{lm}(\sin(\phi)) \left(\frac{2l+1}{1+k_l}\right) \times \left(\Delta C_{lm}\cos(m\lambda) + \Delta S_{lm}\sin(m\lambda)\right). \qquad (2.35)$$

The illustration of a single distinct global gravity field as a map of geoid or equivalent water height, or thickness (EWT), is pervasive throughout this dissertation. It is, however, crucial to note that EWT maps do no offer physically meaningful representations of internal gravitational processes (*Chao*, 2016). Furthermore, the assumption that mass change happens at the surface is limited, but this error is too small to be considered in this dissertation work.

2.3 Principal Component Analysis (PCA)

This section presents PCA, the technique that decomposes the GRACE fields into a set of basis functions, allowing for the combination of GRACE and SLR/DORIS fields (see Chapter 4). The original intent of PCA is not a combination of the two different fields, but rather the general decomposition of a large dataset. PCA is defined in Section 2.3.1 and derived in Section 2.3.2. Section 2.3.3 discusses alternative versions of PCA that might be relevant applications for this study.

2.3.1 General Definition

The fundamental idea of PCA is to reduce the dimensionality of a large dataset (*Preisendorfer*, 1988). In simple terms, PCA extracts the main spatial patterns and their associated temporal behavior from a geophysical dataset so that it can mostly be explained using those few main patterns modulated in time. The expression "patterns" is used interchangeably with "modes," "basis functions," and "Empirical Orthogonal Functions" (EOFs). The expression "Principal Component" (PC) refers to the temporal modulation of each spatial pattern. In general mathematical terms, the PCA decomposition of a dataset with spatial and temporal dependence $\mathbf{D}(\theta, \phi, t)$ entails a separation of EOFs $\mathbf{x_k}(\theta, \phi)$ and their individual amplitude $\mathbf{a_k}(t)$, where k is a distinct mode. The original dataset can be approximated by a linear combination of the EOFs and their PCs:

$$\mathbf{D}(\theta, \phi, t) \approx \mathbf{a_1}(t)\mathbf{x_1}(\theta, \phi) + \mathbf{a_2}(t)\mathbf{x_2}(\theta, \phi) + \ldots + \mathbf{a_{N_{modes}}}(t)\mathbf{x_{N_{modes}}}(\theta, \phi) \tag{2.36}$$

$$\approx \sum_{k=1}^{N_m} \mathbf{a_k}(t)\mathbf{x_k}(\theta, \phi), \tag{2.37}$$

where N_{modes} is the number of modes used. The first modes capture the most information of the original dataset and every additional mode until N_{modes} adds less and less to the reconstruction of

the original dataset $\mathbf{D}$. As such, the following relationships hold true:

$$\text{WRMS}\left[\mathbf{D}(\theta, \phi, t) - \mathbf{a_1}(t)\mathbf{x_1}(\theta, \phi)\right] < \text{WRMS}\left[\mathbf{D}(\theta, \phi, t) - \mathbf{a_2}(t)\mathbf{x_2}(\theta, \phi)\right], \tag{2.38}$$

$$\text{WRMS}\left[\mathbf{D}(\theta, \phi, t) - \sum_{k=1}^{2} \mathbf{a_k}(t)x_k(\theta, \phi)\right] > \text{WRMS}\left[\mathbf{D}(\theta, \phi, t) - \sum_{k=1}^{3} \mathbf{a_k}(t)\mathbf{x_k}(\theta, \phi)\right], \tag{2.39}$$

where WRMS is the weighted root mean square of a dataset and scales with the difference between the two fields, such that an WRMS value of zero would mean that the two fields are exactly the same. The first relationship shows that the full first mode $(\mathbf{a_1}(t)\mathbf{x_1}(\theta, \phi))$ captures more of the original data $\mathbf{D}(\theta, \phi, t)$ than the full second $(\mathbf{a_2}(t)\mathbf{x_2}(\theta, \phi))$. The second relationship indicates the summation of a higher number of modes (3 versus 2) captures more information from the data $\mathbf{D}(\theta, \phi, t)$. It is worth noting that in the PCA decomposition, the "information" criterion that determines how to distribute the modes is based on the variance of the original data. Section 2.3.2 develops this choice of information criterion in more rigorous terms.

This simple overview illustrates three important points about PCA: (1) the original data can be approximated by a linear combination of modes (also known as patterns or EOFs) and their associated modulating amplitudes (also known as PCs); (2) the first modes are the most important because they capture the most variance of the original data; (3) each pattern is uncorrelated and, therefore, orthogonal, which enables (1). PCA has previously been applied to time-variable gravity studies; *Wouters and Schrama* (2007) used PCA to filter noise from GRACE signal. In the next section, a derivation of PCA is provided, along with a more mathematical definition of the modes and their associated amplitudes.

2.3.2   Derivation of Decomposition and Reconstruction

The first step is to assume a general dataset of geophysical parameters, whether it be a weekly set of global sea level measurements, a grid of air temperatures over a city delivered every six hours, or global coefficients that describe time-variable gravity every month, etc. At each time interval $i = [1, \ldots, M]$, a time series $\mathbf{x}_i$ is provided, where $\mathbf{x}_i$ is a column vector of size $N \times 1$. A

data matrix $\mathbf{X_0}$ is designed by aggregating all time series,

$$\mathbf{X_0} = \begin{bmatrix} x_{1,1} & x_{1,2} & \cdots & x_{1,M} \\ x_{2,1} & x_{2,2} & \cdots & x_{2,M} \\ \vdots & \vdots & \ddots & \vdots \\ x_{N,1} & x_{N,2} & \cdots & x_{N,M} \end{bmatrix}. \tag{2.40}$$

The data matrix is centered, i.e., the mean is removed:

$$\mathbf{X}_{cent} = \mathbf{X_0} - \texttt{repmat}[\bar{\mathbf{x}}, 1, \texttt{M}], \tag{2.41}$$

where $\bar{\mathbf{x}}$ is the mean of $\mathbf{X_0}$ and of size $N \times 1$. Furthermore, the data must be assigned equal weighting:

$$\mathbf{X} = \mathbf{X}_{cent} \times \texttt{repmat}[\mathbf{d}, 1, \texttt{M}], \tag{2.42}$$

where $\mathbf{d}$ is a weighting vector of size $N \times 1$. For example, when regular spatial grids (e.g., a global map with resolution $1° \times 1°$, or $360 \times 180 \times M$) are used as input, they must be weighted by the cosine of the latitude, otherwise the amount of information contained in the data matrix would be biased towards the information in the polar areas. In this example,

$$\mathbf{d} = \begin{bmatrix} \cos(\theta_1) \\ \vdots \\ \cos(\theta_N) \end{bmatrix}, \tag{2.43}$$

where θ is the latitude corresponding to the location of each grid point.

The auto-covariance matrix $\mathbf{C}$ of the centered and properly weighted data matrix $\mathbf{X}$ is built:

$$\mathbf{C} = \frac{1}{n-1}\mathbf{X}^T\mathbf{X}. \tag{2.44}$$

The goal of the PCA process is to find a vector $\mathbf{s}_1$ that rotates the data in such a way as to maximize the variance,

$$\begin{aligned} \text{var}(\mathbf{X}\mathbf{s}_1) &= \frac{1}{n-1}(\mathbf{X}\mathbf{s}_1)^T(\mathbf{X}\mathbf{s}_1) \\ &= \frac{1}{n-1}\mathbf{s}_1^T\mathbf{X}^T\mathbf{X}\mathbf{s}_1 \\ &= \mathbf{s}_1^T\mathbf{C}\mathbf{s}_1. \end{aligned} \tag{2.45}$$

Without constraint, one could simply select $\mathbf{s}_1$ to be large. However, the normalization $\mathbf{s}^T\mathbf{s} = 1$ constrains the problem (*Jolliffe*, 2002). The method of Lagrange multipliers is pursued, such that the following expression is maximized,

$$\mathbf{s}_1^T\mathbf{C}\mathbf{s}_1 - \lambda\left(\mathbf{s}_1^T\mathbf{s}_1 - 1\right), \tag{2.46}$$

where λ is a Lagrange multiplier. The maximization procedure involves equating the derivative with respect to $\mathbf{s}_1$ as zero,

$$\frac{d}{d\mathbf{s}_1}\left(\mathbf{s}_1^T\mathbf{C}\mathbf{s}_1 - \lambda\left(\mathbf{s}_1^T\mathbf{s}_1 - 1\right)\right) = 0 \tag{2.47}$$

$$\mathbf{C}\mathbf{s}_1 - \lambda\mathbf{s}_1 = 0 \tag{2.48}$$

$$\mathbf{C}\mathbf{s}_1 = \lambda\mathbf{s}_1. \tag{2.49}$$

This is now an eigenvalue problem with $\mathbf{s}_1$ as its eigenvector and λ_1 as its eigenvalue. The eigenvector $\mathbf{s}_1$ represents the first EOF. The second EOF $\mathbf{s}_2$ is still subject to the normalization constraint $\mathbf{s}_2^T\mathbf{s}_2 = 1$, but also the additional constraint of being uncorrelated with the first eigenvector, so $\mathbf{s}_1^T\mathbf{s}_2 = 0$. The same Lagrange multiplier procedure as for $\mathbf{s}_1$ is applied for determining $\mathbf{s}_2$:

$$\mathbf{s}_2^T\mathbf{C}\mathbf{s}_2 - \lambda\left(\mathbf{s}_2^T\mathbf{s}_2 - 1\right) - \phi\mathbf{s}_2^T\mathbf{s}_2 = 0, \tag{2.50}$$

where ϕ is a new Lagrange multiplier. Differentiating by $\mathbf{s}_2$ and multiplying both sides by $\mathbf{s}_1^T$ yields the following relationship

$$\mathbf{s}_1^T\mathbf{C}\mathbf{s}_2 - \mathbf{s}_1^T\lambda\mathbf{s}_2 - \phi\mathbf{s}_1^T\mathbf{s}_2 = 0. \tag{2.51}$$

By virtue of the correlation constraint between $\mathbf{s}_1$ and $\mathbf{s}_2$, this expression becomes

$$\phi\mathbf{s}_1^T\mathbf{s}_2 = 0, \tag{2.52}$$

so $\phi = 0$ and the original equation that was maximized (Eq. 2.50) becomes

$$\mathbf{s}_2^T\mathbf{C}\mathbf{s}_2 - \mathbf{s}_2^T\lambda\mathbf{s}_2 = 0. \tag{2.53}$$

Once again, this is an eigenvalue problem with $\mathbf{s}_2$ as the eigenvector and λ_2 as the eigenvalue. $\mathbf{s}_2$ is the second eigenvector. A similar procedure involving Lagrange multipliers and correlation constraints can be used to find the remaining eigenvectors.

The eigenvectors, or EOFs, $\mathbf{s_k}$ are orthogonal by nature, so $\mathbf{s}_k \cdot \mathbf{s}_l = 0$ with $k \neq l$. The variance explained by each eigenvector $\mathbf{s_k}$ is defined as the ratio of the eigenvalue and the sum of all eigenvalues $(\lambda_k / \sum_{i=1}^{N_{max}} \lambda_i)$. Since matrix operations are more convenient than individual vectors, all EOFs can be stacked in an EOF matrix $\mathbf{S}$ of size $N \times N_{modes}$:

$$\mathbf{S} = [\mathbf{s}_1, \mathbf{s}_2, \cdots, \mathbf{s}_{N_{modes}}]. \tag{2.54}$$

The process of finding PCA can be solved for using a simple eigenvalue decomposition, but more mathematically efficient methods are also available and straight-forward to implement, such as Singular Value Decomposition (SVD).

The projection of each eigenvector onto the original data yields a parameter that is called Principal Component (PC). PCs describes the evolution in time of each EOF.

$$\mathbf{p}_1 = \mathbf{s}_1^T \mathbf{X}, \tag{2.55}$$

and so $\mathbf{p}_1$ is of size $1 \times M$. Similarly, the PCs can be stacked in a matrix of size $N_{modes} \times M$:

$$\mathbf{P} = \begin{bmatrix} \mathbf{p}_1 \\ \vdots \\ \mathbf{p}_{N_{modes}} \end{bmatrix}. \tag{2.56}$$

The linear combination of the modes with their amplitudes yields a matrix $\mathbf{X}_{rec}$ of size $N \times M$ that is approximately equal to the original data matrix $\mathbf{X}$,

$$\mathbf{X}_{rec} = \mathbf{SP} \tag{2.57}$$

$$\mathbf{X} \approx \mathbf{SP}. \tag{2.58}$$

This expression is similar to Eq. 2.36, but in matrix notation.

A more thorough description of PCA is given in *von Storch and Zwiers* (1999), *Jolliffe* (2002) and *Hannachi* (2007). Historically, *Lorenz* (1956) describe one of the first uses in meteorology and

it has been extended since to a number of geophysical fields. While PCA is effective in capturing the important modes from a dataset, it suffers from two main disadvantages. First, PCA relies only on the mean and variance of the original data. Second, the variance is considered stationary, i.e., constant in time. The next section describes several possible alternatives for the PCA procedure designed to mitigate these two disadvantages.

2.3.3   Alternative Versions of PCA: REOF, CEOF, ICA, etc.

In this section, alternative versions of PCA are briefly presented: Rotated EOF (REOF), Independent Component Analysis (ICA), Complex EOF (CEOF), Extended EOF (EEOF), Cyclo-stationary (CSEOF), and Complex ICA (CICA). *Forootan* (2015) provide a comprehensive description of each technique and case studies of their applicability with GRACE fields. This section focuses on the relation of each PCA alternative with (1) the stationarity assumption and (2) the different levels of statistical information captured in the input data.

Stationarity means that the input information (e.g., a covariance) and the output EOFs are assumed constant in time. However, this assumption is not only physically incorrect for geophysical applications, since geophysical processes are non-deterministic, but also reduces the interpretability of the modes. For instance, modes from a regular PCA on sea level data, i.e., will not disentangle the El Niño-Southern Oscillation (ENSO) mode as well as when an alternative PCA approach is applied (*Hamlington et al.*, 2011). Regular PCA, REOFs, and ICA assume stationary data. CEOF, EEOF, CSEOF, and CICA mitigate the stationarity assumption by incorporating lagged information.

Decompositions are based on different levels of statistical information. By definition, the covariance provides information on data up to the second cumulant (second-order statistical moments, i.e., the mean and variance). As such, the usage of a covariance implies that the probability distribution of data follows a Gaussian distribution. Higher-order cumulants include, for example, the third-order (skewness) and fourth-order (kurtosis) statistical moments. The usage of higher-order cumulants is only relevant for data that are not Gaussian, since Gaussian distributions would

yield higher-order cumulants that are zero. Regular PCA, CEOF, CSEOF, and EEOF hinge only on the covariance, while REOF, ICA, and CICA make use of higher-order cumulants.

Table 2.1 summarizes the different decomposition techniques and the following paragraphs discuss each type of decomposition.

Table 2.1: Choice of statistical decomposition for GRACE-based basis functions.

Name	Stat.	Cumulants	Note
EOF	Yes	Second order	noted for ease-of-use; yields orthogonal functions
REOF	Yes	Higher order	enhances EOF interpretability; requires rotation criterion
ICA	Yes	Higher order	yields independent functions; requires independence criterion
CEOF	No	Second order	data matrix uses imaginary portion
CSEOF	No	Second order	data matrix uses lagged time information
EEOF	No	Second order	data matrix uses lagged time information
CICA	No	Higher order	data matrix uses imaginary portion

Rotated EOF (REOF) stem from the original set of EOFs and does not seek to either alleviate the stationarity assumption or add higher-order cumulants. Rather, the rotation aims to translate the EOFs into a simpler, more localized structure, so that they become more physically interpretable, i.e., associate modes with more physically meaningful natural patterns. As such, the REOF procedure relaxes the orthogonality constraint of the EOFs. The mathematical step is a multiplication of the EOF matrix presented in the previous section, $\mathbf{S}$, by a rotation matrix $\mathbf{U}$, in order to obtain a modified EOF matrix $\mathbf{R}$:

$$\mathbf{R} = \mathbf{SU}. \tag{2.59}$$

The rotation matrix is determined by the maximization of a function $f(\mathbf{SU})$. *Richman* (1986) describes five main criteria, but here the focus is on the orthogonal "Varimax" criterion, described as

$$\max\left(\sum_{k=1}^{N_m}\left[p\sum_{j=1}^{p} r_{ij}^4 - \left(\sum_{j=1}^{p} r_{jk}^2\right)^2\right]\right), \tag{2.60}$$

where r_{ij} are the elements of the matrix $\mathbf{R}$ and N_m is the number of modes (*Kaiser*, 1958). Varimax is pre-programmed into MATLAB as `rotatefactors`. In essence, a rotation of the leading EOFs

using the Varimax criterion seeks to accentuate the contrast of this subset of EOFs – the largest EOF becomes larger and the smallest EOF becomes smaller (*Hannachi*, 2007).

ICA is obtained by relying on higher-order cumulants, but also assumes that this statistical information is stationary. The ICA method can be used to improve the extraction of the deterministic components of observed geophysical signals because its aim is to separate modes into statistically independent signals, instead of orthogonal with the PCA approach. In particular, *Forootan and Kusche* (2013) show that ICA algorithm based on diagonalization of fourth-order cumulants is able to separate a mix of trend and sinusoidal signals. Furthermore, *Boergens et al.* (2014) note that extensions of ICA methods, based on maximizing entropy and not just using the fourth-order cumulants, are more effective than PCA in recovering mass change from GRACE fields in North America and, specifically, disentangling hydrologic signal from a trend signal. In a regular PCA approach, such signals would be typically "mixed." The mathematical derivation behind ICA is not presented in this dissertation because ICA is not employed.

A more general description of the PCA method is called the Extended EOF. This technique includes lagged temporal information to deal with non-stationarity assumptions, such that the data matrix becomes

$$
\mathbf{X_0} = \begin{bmatrix} x_{1,1} & \cdots & x_{1,p} & x_{2,1} & \cdots & x_{2,p} & \cdots & x_{M,1} & \cdots & x_{M,p} \\ x_{2,1} & \cdots & x_{2,p} & x_{3,1} & \cdots & x_{3,p} & \cdots & x_{M+1,1} & \cdots & x_{M+1,p} \\ \vdots & \ddots & \vdots & \vdots & \ddots & \vdots & \ddots & \vdots & \ddots & \vdots \\ x_{n-M+1,1} & \cdots & x_{n-M+1,p} & x_{n-M+2,1} & \cdots & x_{n-M+2,p} & \cdots & x_{n,1} & \cdots & x_{n,p} \end{bmatrix},
$$

$$(2.61)$$

with M being the temporal lag (*Forootan*, 2015). The EEOF procedure is mathematically equivalent to Multichannel Singular Spectrum Analysis (MSSA), except that MSSA uses a wider array of time-lag options (*Boergens et al.*, 2014). *Rangelova et al.* (2012) show that MSSA is superior to PCA in extracting non-periodic modulated signals of ocean mass change from GRACE measurements.

Complex EOFs (CEOF) hinge on the summation of the data matrix, so that the variance $\mathbf{C}$

becomes

$$\mathbf{X}_C = \mathbf{X} + i\mathbf{X}_M \tag{2.62}$$

$$\mathbf{C} = \frac{1}{n-1}\mathbf{X}_C^{*T}\mathbf{X}_C \tag{2.63}$$

where (*) is the complex transpose and M represents a time lag. The output will be real-valued PCs with two sets of EOFs – the real and imaginary versions. Similarly to EEOF and MSSA, CEOF is a more suitable way to decompose geophysical data that have an underlying periodic behavior of poorly-established frequencies. An extension of the CEOF is the Hilbert-CEOF, which contain information on the first derivative of the time series.

Cyclo-stationary EOFs (CSEOF) follow in the same vein as the EEOF in that they are superior than conventional EOFs in extracting dominant patterns that have distinct, but not well-established, periodicities (*Kim et al.*, 2015). Each CSEOF carries temporal information in such a way that one unique mode will actually possess several EOFs. *Hamlington et al.* (2011) note that the usage of 1-yr nested periods, where the nested period is the constraining period and its value usually based on a priori understanding of the system, on a CSEOF of sea level is much more effective in extracting the ENSO mode than regular PCA.

Lastly, an extension of the ICA method that can alleviate the stationarity assumption is Complex ICA (CICA). Similarly to ICA, CICA depends on higher-order cumulants and, similarly to CEOF, includes the complex version of the input data matrix that allows for the decomposition to take into account extraneous variability.

All in all, a number of alternatives to a regular PCA decomposition are available and mitigate current issues with PCA, namely the stationarity assumption and the dependence on only two statistical moments, i.e., the mean and variance. While existing literature have noted the advantages of REOF, ICA, EEOF, MSSA, CSEOF, CEOF, and CICA, this dissertation will focus on the REOF. These procedures, however, present potential future decomposition methods for GRACE-based basis functions that have so far extended the scope of this dissertation.

Finally, this section addresses the possibility of using (1) GRACE-free basis functions and

(2) regional basis functions instead of global basis functions, as shown in Figure 2.2. First, modes that do not depend on GRACE are forced and customized for the application, i.e., drawing the outlines of continents (*Bonin and Chambers*, 2016). It is also important to note that the total sum of the kernels must yield a full global map. Second, it is possible to concentrate the information in regional modes called Radial Basis Functions (RBFs) (*Schmidt et al.*, 2007; *Schmeer et al.*, 2012). The mathematical development of such functions is, at the moment, far beyond the scope of this dissertation. Section 4.3.2 discuss their relevance for this dissertation.

Figure 2.2: Choice of basis functions.
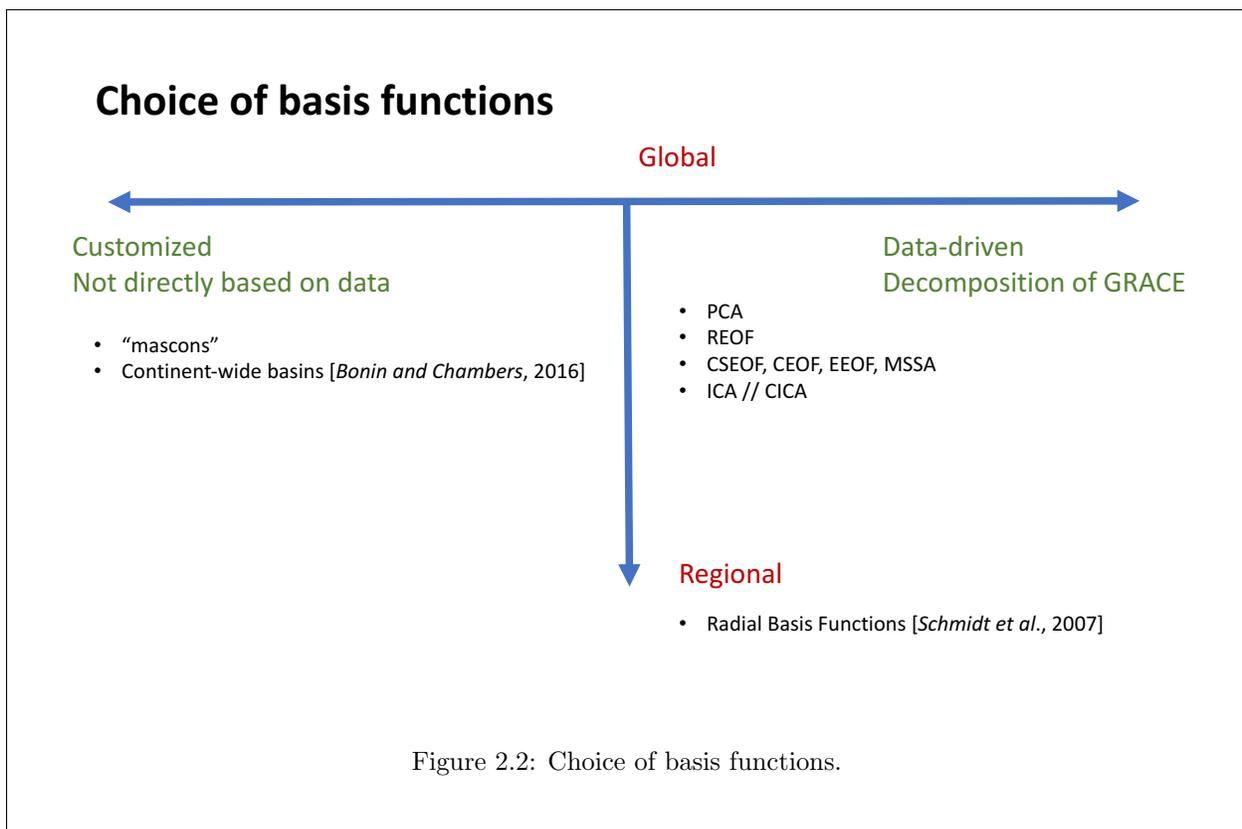
2.4 Analysis Techniques

Three main tools are used in this dissertation and this section provides overviews of their mathematical foundation.

2.4.1 Least Squares Adjustment

The Least Squares Adjustment (LSA) process seeks to estimate a state with parameters $\mathbf{x}$ given observations $\mathbf{y}$, and a model $\mathbf{H}$ that linearly relates the state parameters to the observations.

$$\mathbf{y} = \mathbf{Hx} + \epsilon, \tag{2.64}$$

where ϵ represents the residuals between the observations and estimated observations. The state parameter vector $\mathbf{x}$ is of size $N \times 1$, the observation and residuals vectors $\mathbf{y}$ and ϵ of size $M \times 1$. A covariance $\mathbf{P_y}$ (size $M \times M$) represents the uncertainty in the observations; the diagonal terms capture the variance for each observation and the off-diagonal terms capture the cross-correlations between observations.

The best estimate of $\hat{\mathbf{x}}$ is based on a cost function $J(\mathbf{x})$ that minimizes the sum of the squares of the residuals. In other words, the following function is minimized.

$$
\begin{aligned}
J(\mathbf{x}) &= \frac{1}{2}\epsilon^T \epsilon \\
&= \frac{1}{2}\left(\mathbf{y} - \mathbf{Hx}\right)^T \mathbf{W}\left(\mathbf{y} - \mathbf{Hx}\right),
\end{aligned}
\tag{2.65}
$$

where $\mathbf{W} = \mathbf{P_y}^{-1}$ is the weighting matrix of the observations. By virtue of minimizing this cost function, the derivative is taken and set to zero (a few step are skipped, please see Appendix B in *Tapley et al.* (2004b)), and, ultimately, an expression for the best state estimate $\hat{\mathbf{x}}$ is derived:

$$
\begin{aligned}
\frac{\partial J(\mathbf{x})}{\partial \mathbf{x}} &= 0 = -\left(\mathbf{y} - \mathbf{Hx}\right)^T \mathbf{WH} \\
\mathbf{H}^T \mathbf{WHx} &= \mathbf{H}^T \mathbf{Wy} \\
\hat{\mathbf{x}} &= \left(\mathbf{H}^T \mathbf{WH}\right)^{-1} \mathbf{H}^T \mathbf{Wy}.
\end{aligned}
\tag{2.66}
$$

The resulting covariance matrix of the state parameters is $\mathbf{P_x} = \left(\mathbf{H}^T \mathbf{WH}\right)^{-1}$. When the mapping between the state parameters and the observations is linear, as in Eq. 2.64, there is no need to iterate the process.

2.4.2 Regional Mass Computation

How is surface mass change in a specific basin computed using gravity fields? *Swenson and Wahr* (2002) provide a technique called throughout this dissertation basin-averaging technique. The main steps of this technique include defining a kernel for the region of interest and convolving the kernel with the gravity fields. The kernel is first based on a grid representation $\theta(\phi, \lambda)$, where

$$\theta(\phi, \lambda) \begin{cases} = 1 & \text{when inside the basin} \\ \\ = 0 & \text{when outside the basin} \end{cases} \tag{2.67}$$

The Stokes coefficients are obtained from the grid representation of a kernel via the following relationship,

$$\left\{ \begin{array}{c} \vartheta_{lm}^{c} \\ \\ \vartheta_{lm}^{s} \end{array} \right\} = \int \theta(\phi, \lambda) \bar{P}_{lm}(\sin(\phi)) \left\{ \begin{array}{c} \cos(m\lambda) \\ \\ \sin(m\lambda) \end{array} \right\} d\Omega. \tag{2.68}$$

The convolution of this kernel with a surface mass density function yields the average surface mass density change $\bar{\sigma}_r$ in the region of interest,

$$\bar{\sigma}_r = \frac{a\rho_E}{3\Omega_r} \sum_{l=0}^{\infty} \sum_{m=0}^{l} \frac{2l+1}{1+k_l} \left(\vartheta_{lm}^{c} \Delta C_{lm} + \vartheta_{lm}^{s} \Delta S_{lm} \right). \tag{2.69}$$

The conversion from average surface mass density change to mass change involves accounting for the area of the kernel and the density of water. In practice, the summation can not reach ∞, but rather, a maximum degree l_{max}. This truncation yields a ringing artifact known as the Gibbs phenomenon. To alleviate the spurious mass change signal, a scale factor is computed and represents the leakage that is inherent to the Gibbs phenomenon. The computation follows Eqs. 3-4 in *Longuevergne et al.* (2010). Further sources of error from mass change computations over Greenland and Antarctica are examined in *Velicogna and Wahr* (2013).

2.4.3 Full Matrix Error Propagation

This section derives the error propagation of a gravity field with its associated covariance matrix to applications relevant in this dissertation, namely, errors in global fields of Equivalent Water Thickness (EWT) maps and time series of mass change.

A general explanation for error propagation is first given. A function $f(x_i)$ has variables x_i that each have a certain variance $\sigma_{x_i}^2$. If the errors are uncorrelated, the error E_f of the function $f(x_i)$ can defined as follows:

$$E_f = \sqrt{\sum_i \left(\frac{\partial f}{\partial x_i}^2 \sigma_{x_i}^2 \right)} \tag{2.70}$$

However, when correlations between errors exist, one must take into account the off-diagonal terms and matrix notation is necessary,

$$\mathbf{P}_f = \mathbf{Q}\mathbf{P}\mathbf{Q}^T \tag{2.71}$$

where $\mathbf{Q}$ contains the partials of f with respect to x_i. In the case of uncorrelated errors, $\mathbf{P}$ is simply a diagonal matrix of $\sigma_{x_i}^2$ and the resulting $\mathbf{P}_f$ matrix is a diagonal matrix of σ_f^2. However, when the errors are correlated, the off-diagonal terms $\mathbf{P}_f$ are non-zero. Another important remark is that the errors are evidently independent of the variables x_i.

The following paragraphs explain how this matrix notation can be applied for gravity fields. Specifically, the linearization of the geoid computation is addressed. In the case of a gravity field

with $l = 2$, a geoid is computed as follows,

$$\mathbf{N}(\theta, \lambda) = a \sum_{l=2}^{2} \sum_{l=0}^{l} P_{lm}(\sin(\theta)) \times (C_{lm}\cos(m\lambda) + (S_{lm}\sin(m\lambda))) \tag{2.72}$$

$$= a[P_{20}(\sin(\theta))[C_{20}] + P_{21}(\sin(\theta))[C_{21}\cos(\lambda) + S_{21}\sin(\lambda)] \cdots \tag{2.73}$$

$$\cdots + P_{22}(\sin(\theta))[C_{22}\cos(2\lambda) + S_{22}\sin(2\lambda)] \tag{2.74}$$

$$= a \begin{bmatrix} P_{20}(s\theta) & P_{21}(s\theta)c\lambda & P_{21}(s\theta)s\lambda & P_{22}(s\theta)c2\lambda & P_{22}(s\theta)s2\lambda \end{bmatrix} \begin{bmatrix} C_{20} \\ C_{21} \\ S_{21} \\ C_{22} \\ S_{22} \end{bmatrix} \tag{2.75}$$

$$= a \begin{bmatrix} P_{20}(s\theta) & P_{21}(s\theta)c\lambda & P_{22}(s\theta)c2\lambda & P_{21}(s\theta)s\lambda & P_{22}(s\theta)s2\lambda \end{bmatrix} \begin{bmatrix} C_{20} \\ C_{21} \\ C_{22} \\ S_{21} \\ S_{22} \end{bmatrix} \tag{2.76}$$

More generally, for a field up to degree L:

$$\mathbf{N}(\theta, \lambda) = a \begin{bmatrix} P_{20}(s\theta) & P_{21}(s\theta)c\lambda & \cdots & P_{LL}(s\theta)cL\lambda & P_{21}(s\theta)s\lambda & \cdots & P_{LL}(s\theta)sL\lambda \end{bmatrix} \begin{bmatrix} C_{20} \\ C_{21} \\ \vdots \\ C_{LL} \\ S_{21} \\ \vdots \\ S_{LL} \end{bmatrix} \tag{2.77}$$

$$= \begin{bmatrix} \frac{\partial N(\theta, \lambda)}{\partial B_{lm}} \end{bmatrix} [B_{lm}] \tag{2.78}$$

$$= \mathbf{A}_G(\theta, \lambda)\mathbf{B}_{lm} \tag{2.79}$$

$\mathbf{A}_G$ contains the spatial information and the partials of the geoid with respect to the coefficients, which are contained in $\mathbf{B}_{lm}$. For only particular point θ_s, λ_s, $\mathbf{A}_G$ has dimensions of $1 \times N_c$ (where N_c is the number of coefficients). For a full field, e.g., 180×360 (64800) points, $\mathbf{A}_G$ would have dimensions of $64800 \times N_c$. By definition, the covariance matrix of the geoid map $\mathbf{P}_G$ is therefore

$$\boxed{\mathbf{P}_G = \mathbf{A}_G \mathbf{P} \mathbf{A}_G^T} \qquad (2.80)$$

and has a size 64800×64800. $\mathbf{P}$ is a matrix of size $N_c \times N_c$ that contains information on the errors of the coefficients.

For the case of an Equivalent Water Thickness (EWT) map, the same procedure is applied as for the geoid map, but the $\mathbf{A}$ matrix is different in that it contains the EWT-specific constants, i.e., ρ_{ave} and degree-specific adjustment with love numbers k_l,

$$\Delta\sigma(\phi, \lambda) = \frac{a\rho_{ave}}{3} \sum_{l=0}^{l_{max}} \sum_{m=0}^{l} \tilde{P}_{lm}(\sin(\phi)) \left(\frac{2l+1}{1+k_l}\right) \times (\Delta C_{lm} \cos(m\lambda) + \Delta S_{lm} \sin(m\lambda)) \qquad (2.81)$$

$$= \mathbf{A}_{EWT}(\theta, \lambda) \mathbf{B}_{lm}. \qquad (2.82)$$

The covariance matrix of the EWT map is simply

$$\boxed{\mathbf{P}_{EWT} = \mathbf{A}_{EWT} \mathbf{P} \mathbf{A}_{EWT}^T}. \qquad (2.83)$$

Finally, the full matrix propagation for regional mass change follows the same principles and the differences once again are contained in the partials matrix $\mathbf{A}_M$ that is built using Eq. 2.69.

Chapter 3

Data: Time-Variable Gravity Solutions

3.1   Overview

Chapter 1 underlined the motivation for combining GRACE and SLR/DORIS solutions and Chapter 2 presented the theory behind the nature of the global gravity data, namely, the spherical harmonic coefficients in Section 2.2. As such, this chapter presents the gravity solutions[1] that form the backbone of this dissertation. Section 3.2 introduces the GRACE inter-satellite solutions and several GRACE-specific corrections that are important for this study. Section 3.3 describes the longer time-variable gravity solutions that originate from tracking observations collected by the ground-based SLR and/or DORIS systems. The various estimation strategies implemented by different research centers are discussed, as well as post-processing approaches designed in this dissertation to ensure that the GRACE and SLR/DORIS solutions are compatible for the combination presented in Chapter 4. Lastly, Section 3.4 investigates and illustrates comparisons between two types of solutions, those from ground-based tracking measurements, GSFC and DGFI, and those from inter-satellite tracking measurements, GRACE.

---

[1] In satellite geodesy, the word "solutions" entails that the data, whether from inter-satellite ranging or ground-based tracking, are used as observations in a gravity inversion problem. A subset of the solution parameter space represents the gravity field coefficients presented in Chapter 2, hence the use of the word "solution." However, for geophysical applications, the global gravity fields can be referred to instead as gravity "data" or even "products." In this chapter, the word solution is preferably used especially when referring to the non-GRACE gravity fields.

3.2   Gravity Solutions from GRACE Inter-Satellite Tracking Data

GRACE solutions originate from the latest processing of GRACE data from the Center for Space Research (CSR) at UT-Austin (*Bettadpur*, 2012). They are also made available by the Jet Propulsion Laboratory (JPL) (*Watkins and Yuan*, 2014) and the GeoForschungsZentrum (GFZ) (*Dahle et al.*, 2013). These three official processing centers have reached the fifth release (RL05) of the solutions and have made them available at `podaac-ftp.jpl.nasa.gov/allData/grace/`. It is important to note that new iterations are frequently released due to ongoing improvements in processing strategies and/or new background models. GFZ, for instance, released the RL05a version, which does not fix arc specific parameters compared to RL05 in order to address trend differences with CSR. Furthermore, additional centers provide GRACE-based solutions of time-variable gravity, such as Groupe de Recherche de Géodésie Spatiale (GRGS) (*Bruinsma et al.*, 2010) and Institute of Geodesy in Graz (*Mayer-Gürr et al.*, 2016). For the sake of this dissertation, the CSR solutions were mostly used – differences between the CSR, JPL, and GFZ solutions were negligible. Future approaches could simply apply an arithmetic mean of the three solutions, as shown in *Sakumura et al.* (2014). In summary, the GRACE solutions provide a complete d/o 60 field, or 3,717 coefficients, released almost monthly since April 2002, as shown in Figure 3.1. Recent issues with GRACE batteries have reduced the frequency of the delivery. Covariances are also available but not needed in this dissertation.
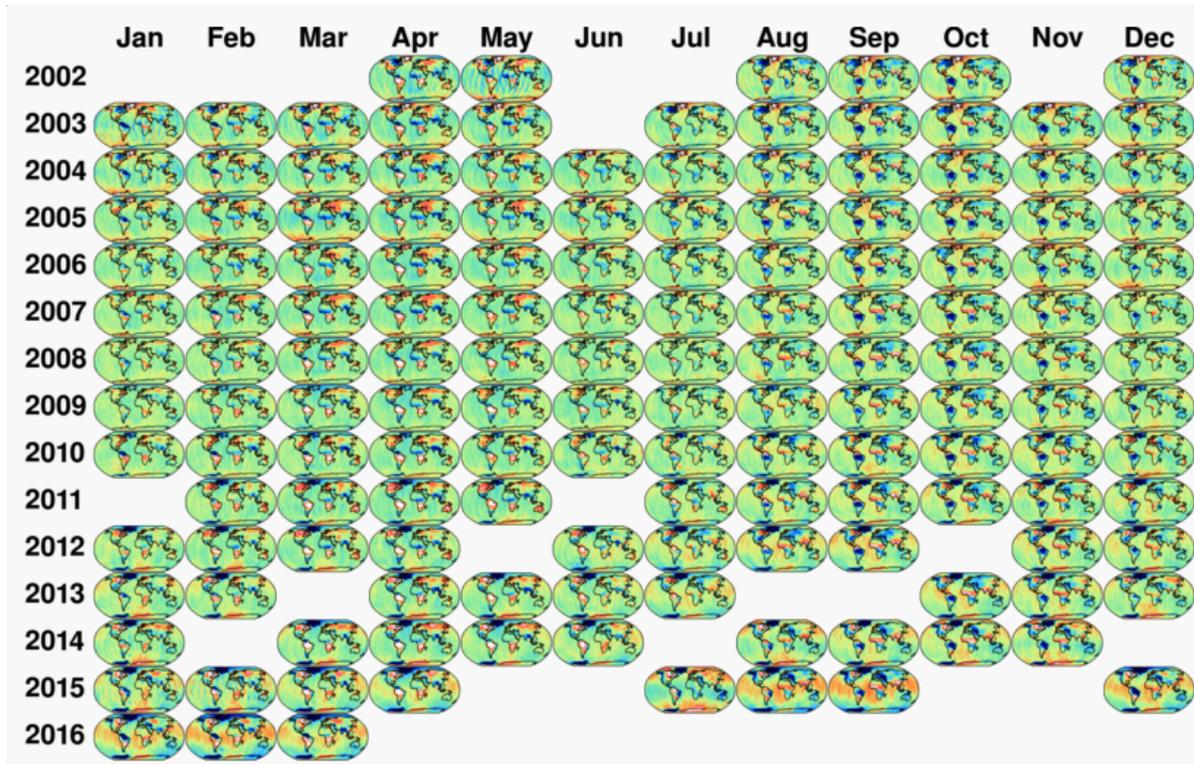
Figure 3.1: Frequency of GRACE product delivery as of April 2016. The frequency has decreased over time due to GRACE battery issues, which have forced the spacecraft to occasionally power down for extended periods of time. This image was taken from https://www.tugraz.at/institute/ifg/downloads/gravity-field-models/itsg-grace2016/.

Corrections to the GRACE solutions are needed and implemented for further geophysical applications; the four most common ones are described: destriping, smoothing, pole tide correction, and C_{20} replacement.

First, the GRACE solutions are contaminated by significant and artificial north-south stripes. They are due to the higher sensitivity of GRACE inter-satellite observations in the along-track direction and limitations in existing processing strategies to fully take into account such sensitivity (*Kusche et al.*, 2009). These stripes are indicative of correlations between gravity coefficients at higher orders, so *Swenson and Wahr* (2006) apply a post-processing "destriping" algorithm that identifies individual correlations and smoothens them via a polynomial fit. It is shown that this

approach does not degrade geophysically-meaningful signal. DDK1, DDK2, and DDK3 are alternative destriping algorithms that rely on covariance information and only differ in their smoothing radius, with DDK3 having the smallest radius of 660 km (*Kusche et al.*, 2009). Both algorithms are accepted in the community and the *Swenson and Wahr* (2006) is used here.

Second, a smoothing filter is applied to the GRACE solutions. The smoothing filter is a Gaussian averaging function in the spectral domain that attenuates the higher degrees (*Jekeli*, 1981). Indeed, the noise in the GRACE solutions increases after degree 30 and so the filter seeks to smoothen out the contribution from the noise. The spatial scale of this filter, known as the half width of the Gaussian averaging function, is selected to be 300 km. This is a commonly used scale.

Third, the C_{21} and S_{21} trends are corrected as recommended by *Wahr et al.* (2015). While GRACE processing centers are able to remove the majority of the pole tide signal captured in the C_{21} and S_{21} time series, they do not take into account long-period signals. Pole tide reflects the tidal response of the oceans and the Earth to polar motion. Polar motion represents the influence of the changes in the mass distribution of the Earth on the motion of its rotation axis.

Lastly, the C_{20} values are replaced by an SLR-based solution (*Cheng et al.*, 2011), because the GRACE K-band measurements are inherently not well predisposed to measure long-wavelength variations, but also because of aliasing from the S_2 tides (*Chen et al.*, 2009).

These four corrections yield GRACE solutions that are apt for geophysical interpretation. Another type of GRACE solution is used for consistency checks. Mascons provide an accessible and easily interpretable solution built directly from GRACE inter-satellite range and range-rate observations. In other words, mascons do not concern themselves with spherical harmonics, but rather mass changes in pre-defined regions. In particular, the mascon solution from GSFC (*Luthcke et al.*, 2013) and JPL (*Watkins et al.*, 2015) have been integrated in the interactive data visualization tool designed at the Colorado Center for Astrodynamics Research[2] . These mascon solutions were occasionally used to ensure the consistency with spherical harmonic solutions from the GRACE products.

---

[2] http://ccar.colorado.edu/grace

In summary, the data provided by inter-satellite-tracking of the GRACE mission and their necessary corrections enable the generation of a global gravity field of high spatial resolution. The following section presents solutions that are derived from ground-based tracking of satellites.

3.3 Gravity Solutions from Ground-Based Tracking Data

Independent gravity solutions produced by ground-based tracking data of satellites have their own advantage compared to GRACE. Namely, these independent solutions do not depend on a single system and are resilient to the failure of one satellite. They are therefore (1) able to continue producing data in the foreseeable future, while GRACE will not survive the summer 2017, and (2) provide data before GRACE. Additionally, these solutions are robust and reliable for the long-wavelength features of the gravity field of the Earth. Section 3.3.1 describes the two tracking systems. The two systems are used to track an evolving constellation of satellites, discussed in Section 3.3.2. Sections 3.3.3 and 3.3.4 are dedicated to time-variable gravity solutions determined by different research centers; Section 3.3.3 goes in much greater detail in explaining the nature and temporal behavior of the time-variable gravity solutions and covariances from one particular center, GSFC.

3.3.1 Satellite Tracking Systems: SLR and DORIS

The two main ground-based tracking systems are described in this section. They both generate observations, namely range and relative velocity, that are eventually used to compute time-variable gravity solutions.

First, the Satellite Laser Ranging (SLR) system provides two-way tracking and near-global coverage of satellites from a network of ground stations (*Pearlman et al.*, 2002). The SLR system was first initiated in 1964 with the launch of the Beacon-B satellite and has since regularly added ground stations and satellites to its system. The station telescopes transmit an ultrashort Nd:YAG (neodymium yttrium aluminium garnet) laser pulse typically operating at 532 nm wavelength (*Tapley et al.*, 2004b) and that are aimed at satellites equipped with passive retroreflectors. The

retroreflectors are designed to make the angle of incidence of the incoming pulse match the angle of incidence of the return pulse, i.e., the signal returns directly to the ground station. A time-of-flight (TOF) counter measures the timing of the departing and return pulse Δt with a precision of down to 30 ps (*Appleby et al.*, 2016). The distance between the station and the retroreflector is hence computed and constitutes the basic measurement type of the SLR system: a range measurement ρ,

$$\rho \approx c\left(\frac{\Delta t}{2}\right) + \rho_{corr.}, \tag{3.1}$$

where c is the speed of light and $\rho_{corr.}$ reflect the range corrections needed. *Otsubo et al.* (2015) remark that the precision of raw range measurements reaches 1 mm, but the accuracy depends on the corrections. Corrections to the range measurement $\rho_{corr.}$ include bias in station coordinates (up to several cms in extreme cases), satellite signature effects (which represent the temporal spread of the returned optical pulse up to 1 cm), center-of-mass corrections (which reflect the difference between the surface of the satellite, where the pulse is reflected, and its center-of-mass) (*Otsubo et al.*, 2015), etc. One salient issue with estimating station coordinates biases is that the errors can be absorbed in other parameters during the estimation process.

Furthermore, the diversity in the nature and stability of the instruments used throughout the global network yields an globally inhomogeneous set of systematic errors. *Appleby et al.* (2016) assess these errors and find that the Herstmonceux station measurements contained a systematic bias of up to 1 cm in TOF counter measurements before it was upgraded in 2007. This bias is likely present in a number of other counters. Instrument inconsistencies are especially visible between the NASA SLR network and the remaining ground stations. These inconsistencies can be mitigated with an empirically-based weighting scheme. The Yarragadee station in Western Australia, for example, is a reference ground station and its data is accordingly more heavily weighted.

The primary advantage of the SLR technique is that the satellites are passive so that no power is required from the satellite. However, this also means that the ground stations are required to have large mechanical instruments to follow the satellites in the sky. Due to the complexity of the

system, tracking stations generally require human maintenance and building space, which reduces cost-effectiveness and inhibits the ability of the network to grow and operate in geographically-constraining environments. For instance, the coverage is dense in Europe, but poor at higher latitudes and clearly lacking in the Pacific and over the South Pole area, as illustrated in Fig 3.2. Furthermore, SLR is weather-dependent because the laser operates in the optical wavelength and is therefore hindered by cloud cover.

Figure 3.2: Map of Satellite Laser Ranging (SLR) ground network. The density of stations is significantly higher in the northern hemisphere, especially in Europe. This unbalanced distribution limits the coverage over the polar areas, especially over Antarctica. This image is from the International Laser Ranging Service (ILRS) website: `https://ilrs.cddis.eosdis.nasa.gov/`.

In summary, the SLR ground network provides range measurements of satellites equipped with retroreflector down to the 1-mm level, but corrections degrade the measurements to the 1-cm level, in an RMS sense. The logistical requirement to carry several instruments in ground stations results in a global network of uneven quality and, therefore, a multitude of correction files. Furthermore, the issue of station biases is still problematic as the errors contaminate the estimation

of global gravity solutions.

The Doppler Orbitography and Radiopositioning Integrated by Satellite (DORIS) system is a one-way, global tracking system composed of stations deployed throughout the world and acquired its first tracking data in March 1990 (*Tavernier et al.*, 2006). DORIS ground-based instruments are transmitting radio beacons and the satellites have receivers that track the radio signal from each beacon. The main observable is therefore a relative velocity that stems from a Doppler shift, $f_r - f_t$, where the relationship between the two is described as

$$f_r \approx \left(1 + \frac{\Delta v}{c}\right) f_t, \tag{3.2}$$

where f_r is the received frequency by the DORIS satellites, f_t the transmitter frequency from the ground-based radio beacons, Δv is the relative velocity, and c is the speed of light. The Doppler shift reflects the frequency shift that arises with the presence of relative speed between the transmitter and receiver on-board the spacecraft.

The two transmitted frequencies are 401.25 MHz and 2036.25 MHz. The dual-frequency approach allows for ionospheric corrections and renders the DORIS system independent of optical hindrances such as cloud cover – unlike SLR. The newest DGXX instruments can track up to seven beacons simultaneously and the whole system, which includes ultra-stable oscillators and a DORIS antenna, have on-board navigation capability: the velocity accuracy reaches 0.5 mm/s and the system delivers 1-10 cm orbit accuracy (*Tapley et al.*, 2004b).

Furthermore, the transmitting radio beacons require no directionality, meaning that they are easy to maintain, generally independent of human presence, and only require a stable power source. As such, the network has been expanded and the coverage is now nearly uniform throughout the world, as seen in Fig. 3.3. The majority of satellites with DORIS receivers are continually covered, except Cryosat-2 and HY-2A, which have a few gaps in coverage over the Pacific.

The one drawback of the DORIS system is that the tracking payload on-board the satellites is somewhat complex because it comprises of a radio receiver, antenna, and ultra stable oscillator. The complexity of the payload is apparent in DORIS measurement processing because dependencies

on corrections arise, such applying a phase law for the Starec and Alcatel antennae (*Lemoine et al.*, 2016). Unlike with the GRACE spacecraft, non-conservative forces (e.g., solar radiation pressure, atmospheric drag, etc.) can not be computed and removed using onboard accelerometers, so the processing of DORIS observations is highly dependent on high-fidelity models.

Unlike with the SLR system, the technological evolution of the instruments mostly affects the satellite payload and not the ground network. Furthermore, only about a dozen satellites operate DORIS payloads, and so it is much easier to keep track of updates in DORIS observations than, for example, when applying biases for all the SLR ground stations while taking into account each of the stations' instrument specs and corrections. However, DORIS satellites are shaped like typical spacecraft, unlike the cannonball-like SLR satellites, so they require complex shape models to remove non-conservative accelerations.

Figure 3.3: Map of Doppler Orbitography and Radiopositioning Integrated by Satellite (DORIS) ground network. The coverage is very well distributed in both hemispheres; the only area with sub-par coverage is the North Pacific. This image is from the International Doris Service (IDS) website: http://ids-doris.org/.

In summary, the DORIS tracking system provides Doppler shift measurements reflecting the relative velocity between a satellite and the ground station(s) tracked by its antenna with an accuracy of 0.5 mm/s. The DORIS ground network provides excellent coverage of satellites, but POD of the satellites is dependent on high-fidelity models.

Finally, it is worth noting that GPS tracking data (also known as "high-low" satellite-to-satellite tracking data, hl-SST) have been shown to be highly effective orbit determination tools. The network provided by the GPS satellites is always visible from Low Earth Orbit (LEO) satellites and the tracking payload on-board satellites only consists of geodetic receivers. Time-variable gravity solutions can be generated and utilized in scientific applications, as was done by the University of Luxembourg (*Weigelt et al.*, 2013), but since these GPS data are not used in this dissertation work, further descriptions are not included. Furthermore, existing hl-SST solutions are temporally limited to the early 2000s, which therefore does not complement the GRACE time series well.

In this section, the two main geodetic tracking systems, SLR and DORIS, have been described. In the next section, the constellation of satellites monitored and tracked by these two systems is discussed.

3.3.2   Description of Satellite Constellation

Satellite constellations have two distinct advantages over GRACE and/or any individual satellite with regards to generating time-variable, global gravity solutions. First, the flow of tracking information from a satellite constellation is resilient to inevitable instrument failure by virtue of the distributed nature of a constellation. Second, the diverse orbits in a satellite constellation minimize correlations between the estimated global parameters. Combining satellite information at the normal equation level is common to all three research centers that produced solutions used here. Differences between the center solutions arise from (1) the choice of satellite used and (2) various modeling and estimation standards, as outlined in Sections 3.3.3, 3.3.4.1, 3.3.4.2 and summarized in Table 3.1.

In the following paragraphs, the advantages of certain satellite types and orbits are discussed.

Table 3.1: Temporal and orbital characteristics of satellites tracked. Each satellite is tracked by up to three systems: Satellite Laser Ranging (SLR), Doppler Orbitography Radiopositioning Integrated by Satellite (DORIS), and/or Global Positioning System (GPS) – although only data from the first two systems are used. Satellites provide unique information because of their distinct orbital configuration. The orbital configuration is rigorously and fully represented by six orbital elements, but here only the two most relevant (altitude and inclination) are shown. Most satellites have near-zero eccentricities, except for Starlette ($e = 0.0206$). The different time spans also highlight the redundancy of a constellation, in that it is assured to continue generating tracking data even if one satellite fails. This is an advantage compared to the GRACE mission. Three different centers generate solutions: Goddard Space Flight Center (GSFC), Deutsches Geodätisches Forschungsinstitut (DGFI), and Astronomisches Institut Universität Bern (AIUB). More information can be found at https://ilrs.cddis.eosdis.nasa.gov/missions/satellite_missions/current_missions/index.html.

Name	Date[1]	Altitude [km]	Inclination [°]	Tracking system	GSFC	DGFI	AIUB
Beacon-C (NASA)	Apr. 1965 – pres.	927	41	SLR	✓		✓
Starlette (CNES)	Jan. 1976 – pres.	800–1,100	30	SLR	✓	✓	✓
LAGEOS-1 (NASA)	July 1976 – pres.	5,850	110	SLR	✓	✓	✓
Ajisai (JAXA[2])	Aug. 1983 – pres.	1,485	50	SLR	✓	✓	✓
Etalon-1 (Ros.[3])	Jan. 1989 – pres.	19,105	65	SLR	✓	✓	
Etalon-2 (Ros.)	May 1989 – pres.	19,135	65	SLR	✓	✓	
SPOT-2 (CNES)	Jan. 1990 – July 2009	832	98.7	DORIS	✓		
TOPEX/Poseidon (NASA/CNES)	Aug. 1992 – Jan. 2006	1,336	66	SLR, DORIS	✓		
LAGEOS-2 (NASA)	Oct. 1992 – pres.	5,625	53	SLR	✓	✓	✓
Stella (CNES)	Sept. 1993 – pres.	815	99	SLR	✓	✓	✓
SPOT-3 (CNES)	Sept. 1993 – Nov. 1997	832	98.7	DORIS	✓		
SPOT-4 (CNES)	March 1998 – July 2013	832	98.7	DORIS	✓		
WESTPAC (Ros.)	July 1998 – pres.	835	98	SLR	✓		
Jason-1 (NASA/CNES)	Dec. 2001 – July 2013	1,336	66	SLR, DORIS	✓	✓	
SPOT-5 (CNES)	May 2002 – March 2015	832	98.7	DORIS	✓		
ENVISAT (ESA)	March 2002 – April 2012	773	98.4	SLR, DORIS	✓	✓	
Larets (Ros.)	Nov. 2003 – pres.	691	98.2	SLR	✓		✓
Jason-2 (NASA/NOAA/CNES)	June 2008 – pres.	1,336	66	SLR, DORIS	✓	✓	
BLITS (Ros.)	Sept. 2009 – April 2013	826	98.6	SLR	✓	✓	✓
Cryosat-2 (ESA)	Apr. 2010 – pres.	725	92	DORIS	✓		
HY-2A (CNSA[4])	Oct. 2011 – pres.	971	99.4	SLR, DORIS	✓		
LARES (ASI[5])	Feb. 2012 – pres.	1,450	69.5	SLR	✓	✓	✓

[1] The date designates initial data tracking or, when not available, the launch date.
[2] JAXA = Japanese Space Agency.
[3] Ros. = Roscosmos State Corporation.
[4] CNSA = China National Space Administration.
[5] ASI = Italian space agency.

The high-altitude satellites such as Etalon-1, -2, LAGEOS-1, -2, are affected neither by smaller features of the Earth's gravity field nor atmospheric drag, so they provide robust estimates of the longer wavelength features. Etalon-1 and -2, by virtue of their high altitude of nearly 20,000 km, have an orbit resonance of spherical harmonic order two, while LAGEOS-1 and -2 have an orbit resonance near order six and seven, respectively. Most other satellites orbiting at altitudes closer to 800 km have resonances[3] at orders 12-15, which is therefore not relevant for this study because the solutions do not extend past d/o six. A resonances translates to higher sensitivity to harmonics of this order, so their information carries more weight in the normal equations at the resonating orders (*Kaula*, 1966). Satellites orbiting at higher inclinations, e.g., HY-2A and LAGEOS-1, are especially sensitive to the zonal coefficients. Sun-synchronous orbits, such as for SPOT and Envisat, lead to high correlation with estimated solar radiation pressure and show sensitivity to degree-two sectorals C_{22} and S_{22}. Furthermore, *Sośnica et al.* (2015) report aliasing by diurnal and semi-diurnal tides. The shape of cannonball-like satellites (most SLR-only spacecraft) is well modeled because they are close to perfectly spherical, so the effect of atmospheric drag is reliably removed. Additionally, such satellites are typically designed to have low area-to-mass ratios, which simplifies their drag behavior. On the other hand, more complicated satellite shapes, such as for the Jason altimetry satellites, yield more complex drag behavior. Maneuvers for such satellites also induce necessary corrections and render the tracking information less reliable. Moreover, twin satellite formations, such as LAGEOS 1+2, Etalon 1+2, and Stella+Starlette series, in which each satellite is designed similarly but placed in different orbits, provide similar observations with time-variable discrepancies that can be traced almost directly to inhomogeneities in the gravitational field.

The estimation process involves accumulating each satellite's contribution into normal equations across regular time intervals, e.g., seven-day arcs. This approach is flexible because it allows for the addition and/or removal of satellites when necessary. At the weekly level, satellites that undergo large maneuvers are excluded from contributing to the weekly arcs. Once the normal

---

[3] The resonance period can be determined from the ratio of the mean motion ($\dot{\omega} + \dot{M}$) and the sum of the rate of the ascending node and the Earth's rotation ($\dot{\Omega} + \dot{\Theta}$) (*Kaula*, 1966)

equations are accumulated, an inversion is applied via Cholesky decomposition to solve for the designated parameter space. Broadly speaking, there are two types of parameters: arc and global parameters. On one hand, arc parameters are only relevant to the specific arcs and are expected to change in time, such as satellite position, velocity, etc. They are therefore estimated locally and the normal equations are modified accordingly. On the other hand, global parameters are expected to remain constant through the arc and are only estimated once; they include spherical harmonics coefficients. As part of the requirements of the work presented in this dissertation, it is also crucial for the solutions to be delivered with covariance information, otherwise the solutions can not be used for the reconstruction process. The covariance contains information on the errors and correlations between all the estimated parameters, including of course spherical harmonic co-efficients. Of particular interest in the estimation process is the choice of parameters, for example with regards to daily empirical acceleration terms. *Bloßfeld et al.* (2015) notes that "if atmospheric drag scaling coefficients are estimated, no empirical accelerations which are parametrized as daily offsets in along-track direction are estimated." *Lemoine et al.* (2016) remarks that the cross-track once-per-revolution (OPR) empirical accelerations are adjusted per arc instead of per day. Furthermore, Envisat and DORIS satellites located at altitudes near 800 km have such parameters estimated every 30 min to hour, particularly near the solar max. These choices are important because judiciously-selected parameters will properly disentangle gravity information from non-conservative force, whereas poorly-chosen parameters will absorb gravity information.

The number of coefficients for a "full" field is $(n+1)^2 - 4$ when the geocenter terms (i.e., C_{10}, C_{11}, and S_{11}) are nor accounted for. It is important to note that the work in this dissertation does not use geocenter terms, which represent the offset between the center-of-mass and center-of-figure of the Earth. A "full" field represents a field in which each set of degrees has a full number of orders, so a full field of degree and order (d/o) 5 will have 32 coefficients. This is not always the case, because the ability to estimate a coefficient of a certain degree and order does not mean that all orders within the same degree will be solvable, despite the fact that they have the same spatial fingerprint.

In summary, this section has described the advantages of a constellation of satellites when solving for time-variable gravity solutions. A constellation is composed of an evolving number of satellites in a variety of orbits, which allows for better sampling of a gravity field, unlike with a single satellite, such as the GRACE mission. The LAGEOS satellites, for instance, yield a unique set of observations by virtue of their high altitude, as compared to TOPEX/Poseidon, which is much lower and detects the smaller structures of the gravity field. Finally, the choice of parametrization of the estimation process is influenced by a number of considerations, such as the use of empirical accelerations. The following section explores in detail the solution produced by GSFC.

3.3.3   GSFC Solutions

In this section, a thorough description of the time-variable gravity solutions produced by the Goddard Space Flight Center (GSFC). First, the description pertains to the motivation, followed by the models and parametrization, the gravity coefficients themselves, their associated covariance, and, finally, an examination of the influence of the contribution of DORIS satellites and an extended time series of C_{20}.

The distinct feature of the GSFC solutions is the combination of DORIS tracking data with SLR tracking data. This new solution was motivated by (1) an ITRF realization update, from ITRF2008 to ITRF2014 (*Lemoine et al.*, 2016) using reprocessed DORIS data and (2) an improvement in the OD of altimetry satellites that depend on DORIS (*Lemoine et al.*, 2010). The current version of the time-variable gravity solution, named `gswcd26`, is the result of incremental refinements and incorporates advancements in force modeling and measurement models, as well as an evolving satellite coverage. The Supplemental Information from *Lemoine et al.* (2016) describes the advancements in the processing over time; *Bail et al.* (2010) discuss the `gscwd10` solution developed for the realization of ITRF2008; Table 2 in *Lemoine et al.* (2014) also tracks the refinments.

Figure 3.4 depicts the evolution in the number of observations as a function of time for the GSFC solution. The major changes are traced to the changes in DORIS observations. Indeed, the tracked satellite constellation contains three DORIS satellites over 1994–1996 until it loses SPOT-3,

to two satellites over 1996 to mid-1998 until it adds SPOT-4, to three satellites again over mid-1998 to mid-2002, and then finally five satellites from mid-2002 to mid-2008 when Envisat and SPOT-5 are included [*personal communication with F. Lemoine, 2017*]. Furthermore, the record of Jason-1 observations is short because the IDS Analysis Working Group recommended to only include Jason-1 data in the absence of TOPEX or Jason-2. Indeed, the Jason-1 DORIS oscillator was severely perturbed by passaged through the SAA (South Atlantic Anomaly), requiring a corrective model for the oscillator (*Lemoine and Capdeville*, 2006).

Figure 3.4: Evolving number of tracking observations in the GSFC constellation. The number generally increases due to the growing number of satellites and ground stations. The solution starts in 1992 with the launch of the TOPEX/Poseidon altimetry mission and coincides with the expansion of the DORIS system. The drop in the number of observations in 2012, for example, is due to the termination of the Envisat mission, but the main reason behind the changes in observations is the evolution of the DORIS constellation. The timeline of each mission and its receiver system are also illustrated and color-coded by tracking type. Furthermore, the newer DORIS satellites have receivers that can track more than one beacon – up to seven for the DGXX receivers on Jason-2 and Cryosat-2.

The estimation process is applied with GSFC's Orbit Determination and Geodetic Parameter Estimation software (GEODYN) (*Pavlis et al.*, 2015). Tracking data from 21 satellites are used. The force modeling is summarized below, but the full version is given in Table 1 of *Lemoine et al.*

(2014). For example, the static gravity model used was GOCO2s (*Goiginger et al.*, 2011) along with a d/o four time-variable gravity component and the d/o 60, 6-hr, ECMWF atmospheric model. The SLR station coordinates are given by SLRF2008 with modified bias modeling and the DORIS station coordinates are DPOD2008. The ocean tides and loading are from GOT4.8; the solid earth tides IERS2003; the mean pole model IERS2010. Satellite-specific macro models are combined with quaternion data and attitude models to take into account spacecraft orientation and solar radiation pressure.

In the latest version `gswcd26`, 33 Stokes coefficients and their associated covariances are estimated. Figure 3.5 depicts a few coefficients. The solution starts in November 1992 and ends in April 2014. The arcs of data span seven days, so the solutions are provided on a weekly basis. C_{50} was not estimated because it was heavily correlated with C_{30}; C_{61} and S_{61} were adjusted because their signal could be separated from the other even-degree, order-one Stokes coefficients. The weighting for each observations were determined through an iterative process; the information content of the solution varies in time and requires manual maintenance. *Lemoine et al.* (2006) state that, for example, SPOT satellites perturbed the C_{31} solution, so that this information was down-weighted by a factor of 10. *Lemoine et al.* (2014) report that Envisat information contributed positively to the overall solution starting in June 2002 and that polar orbiting satellites (Stella, Westpac, Larets) are important in determining the C_{40} zonal coefficient; the jump in October 1993 is directly due to the addition of Stella and SPOT-3 in the satellite constellation (see top left plot in Figure 3.5). Furthermore, the inclusion of LARES starting in February 2012 leads to a jump in C_{51}. It is also important to note that an emphasis on the interpretation of the behavior of single coefficients is limited by the fact that they are correlated; it is therefore more appropriate to focus on the summation of the contributions from all coefficients, for example by examining global gravity maps.

Figure 3.5: Several GSFC coefficients, denoted in blue with the 1-σ envelope shown in gray, compared to GRACE, denoted in red. The focus of this plot is not the comparison against GRACE, but the illustration of artifacts in the SLR/DORIS solutions from GSFC. For example, the jump in C_{51} in 2012 is traced back to LARES and Envisat, while the early behavior of C_{40} is due to the addition of Stella and SPOT-3 observations to the solution. On the other hand, the C_{22} and S_{42} time series do no show spurious signal.

The information from the coefficients is tied to the information contained in the covariance. Figure 3.6 illustrates covariance information. The graphs on the top row show two specific cases for the correlation and variance information, with mean values of the time series are depicted as solid lines and associated one standard deviation as dashed lines. First, the correlations are illustrated. The top left graph shows the time-dependent correlation for two sets of coefficients: (1) C_{22} and C_{30}, which have a low mean correlation value and high variability, and (2) C_{32} and C_{40}, which have a high mean correlation value and low variability. On one hand, this means that C_{32} and C_{40} are poorly separated, regardless of changes in the constellation or processing. On the other hand, the correlation between C_{22} and C_{30} is consistently low, despite the high variability due to the evolution of the constellation. These observations for the two cases are also visible in the middle row of Figure 3.6, which contain the matrix plots representative of mean and standard deviation for all correlation time series. As such, this matrix is 33 by 33 because there are 33 coefficients. The

colors for each case seen on the top left plot correspond to the color of the arrows that designate the rows and columns of interest. Second, the variance are illustrated. The top right graph shows how the variance of two coefficients evolve. The variance of S_{54} has a high value and high variability, whereas the variance C_{42} has low value and low variability. This means that C_{42} is well adjusted, unlike S_{54}. The bottom row provides an overview of the standard deviation (i.e., the square root of the variance value) for all coefficients, with the mean value on the left and standard deviation, representative of variability in time, on the right. The left side of the pyramids contains the C coefficients, while the right side contains the S coefficients. It is clear that higher degree terms and C_{22} have higher variance and that the degree five and order four coefficients vary most in time.

Figure 3.6: Interpreting covariance information from the GSFC SLR/DORIS solution. See text for further explanation.
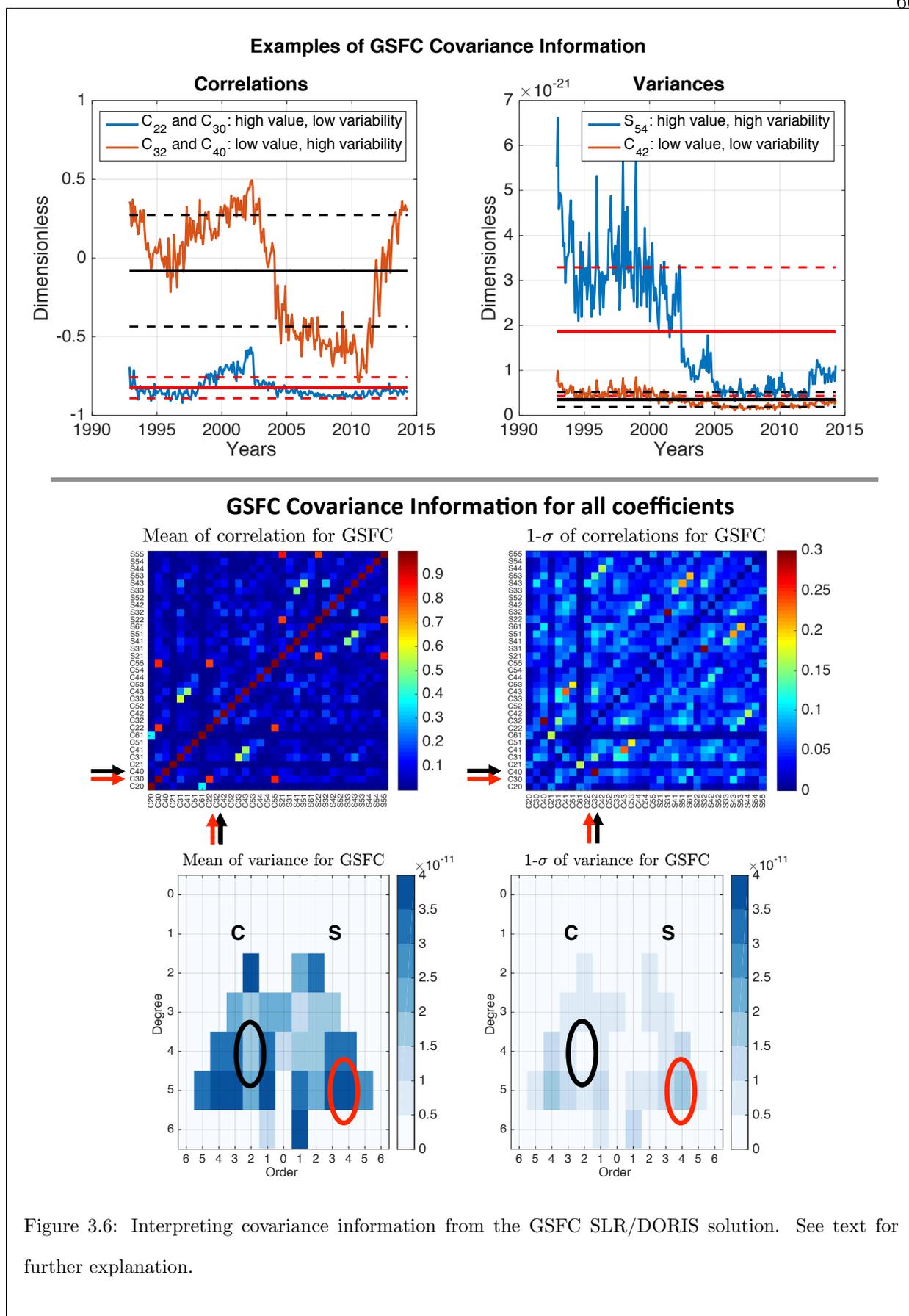
What is the influence of particular satellites on the solution? In particular, what is the influence of DORIS satellites to the GSFC solution? As such, four types of constellations were defined:

1. SLR-only satellites

2. SLR satellites + subset of DORIS satellites: the SPOT satellites (SPOT-2, -3, -4, and -5)

3. SLR satellites + another subset of DORIS satellites: the altimetry satellites (TOPEX/Poseidon, Jason-1, and -2)

4. SLR satellites + all DORIS satellites: the altimetry and SPOT satellites

The variance and correlations of the four types of solutions were examined in Figure 3.8 and Figure 3.7, respectively. A clear contribution from the addition of the DORIS satellites to the SLR constellation is their ability to resolve higher degree ($l > 4$) coefficients. In other words, the GSFC SLR-only parameter space only contains 21 global gravity coefficients, but adding DORIS satellites enables the solution to grow to 33 coefficients. Furthermore, it is clear from Figure 3.8 that the variance is in average reduced with DORIS satellites. The altimetry satellites lower the variance of 21 similar coefficients by approximately 27% while the SPOT satellites lower the variance by about 9%. This is likely due to the added geometry from altimetry satellites; in contrast, all SPOT satellites are in similar sun-synchronous orbital configuration as SLR satellites Stella and Blits. Nonetheless, the contribution from both sets of DORIS satellites together exceeds the sum of the individual contribution from each subset of DORIS satellites.

Why not start even earlier than November 1992? While low-resolution SLR solutions are available starting in 1976 with the launch of LAGEOS-1, the solutions used here commence in November 1992 because only then can full solutions larger than degree two be estimated. Expanding the spherical harmonic time series backwards would require a new processing strategy to accommodate for (1) a different, time-evolving satellite constellation and (2) challenges in the SLR data quality.
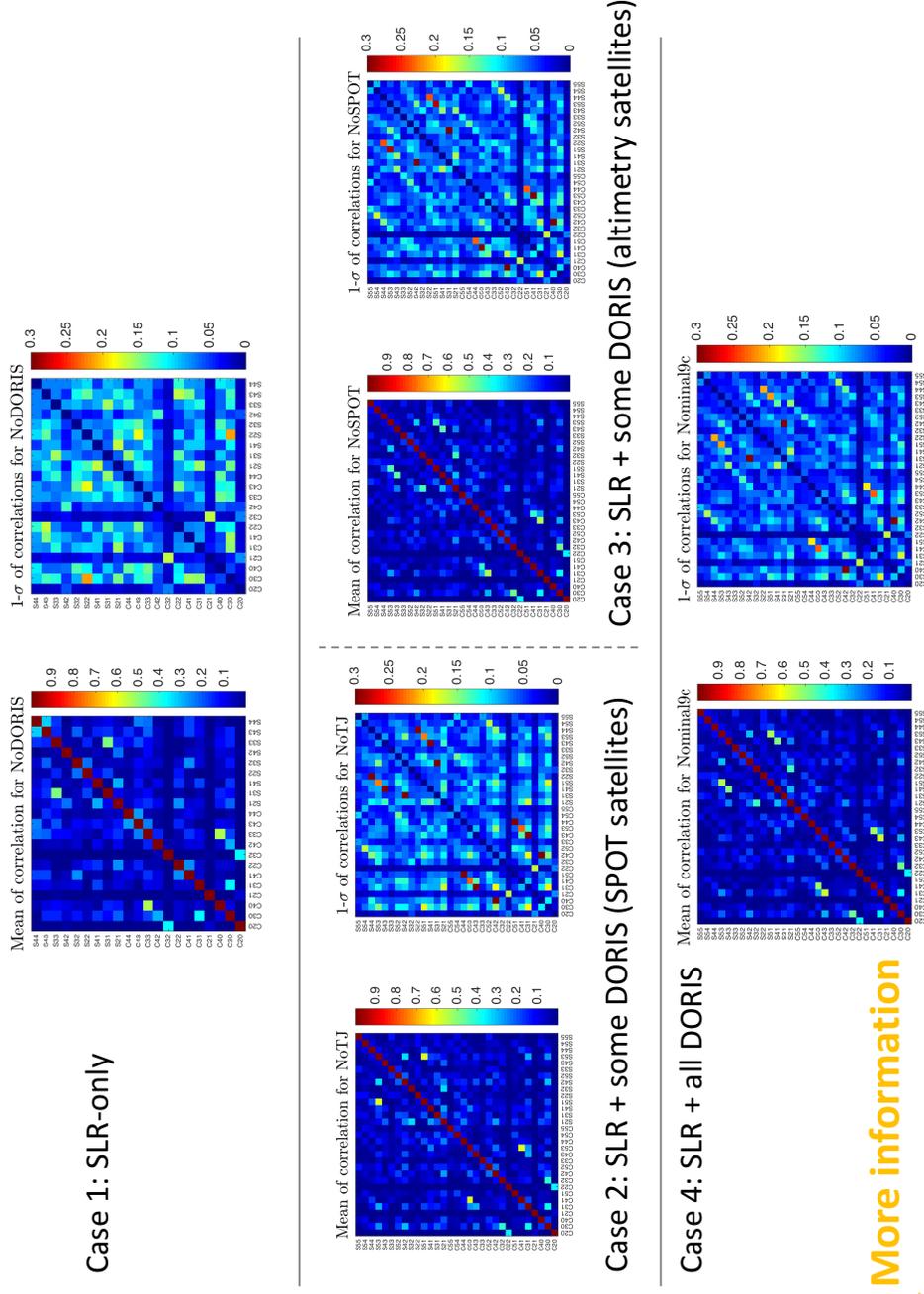
Figure 3.7: Error correlation of GSFC solutions as a function of constellation. The `Nominal9c` case, shown in the bottom right, has the lower variability in the correlation matrix. The case where DORIS contributions were removed, shown in the top left, illustrates how important DORIS is, because the solution is limited to 21 coefficients instead of 33. The cases without SPOT or TOPEX/Poseidon+Jason satellites only influence a few individual coefficient correlations.
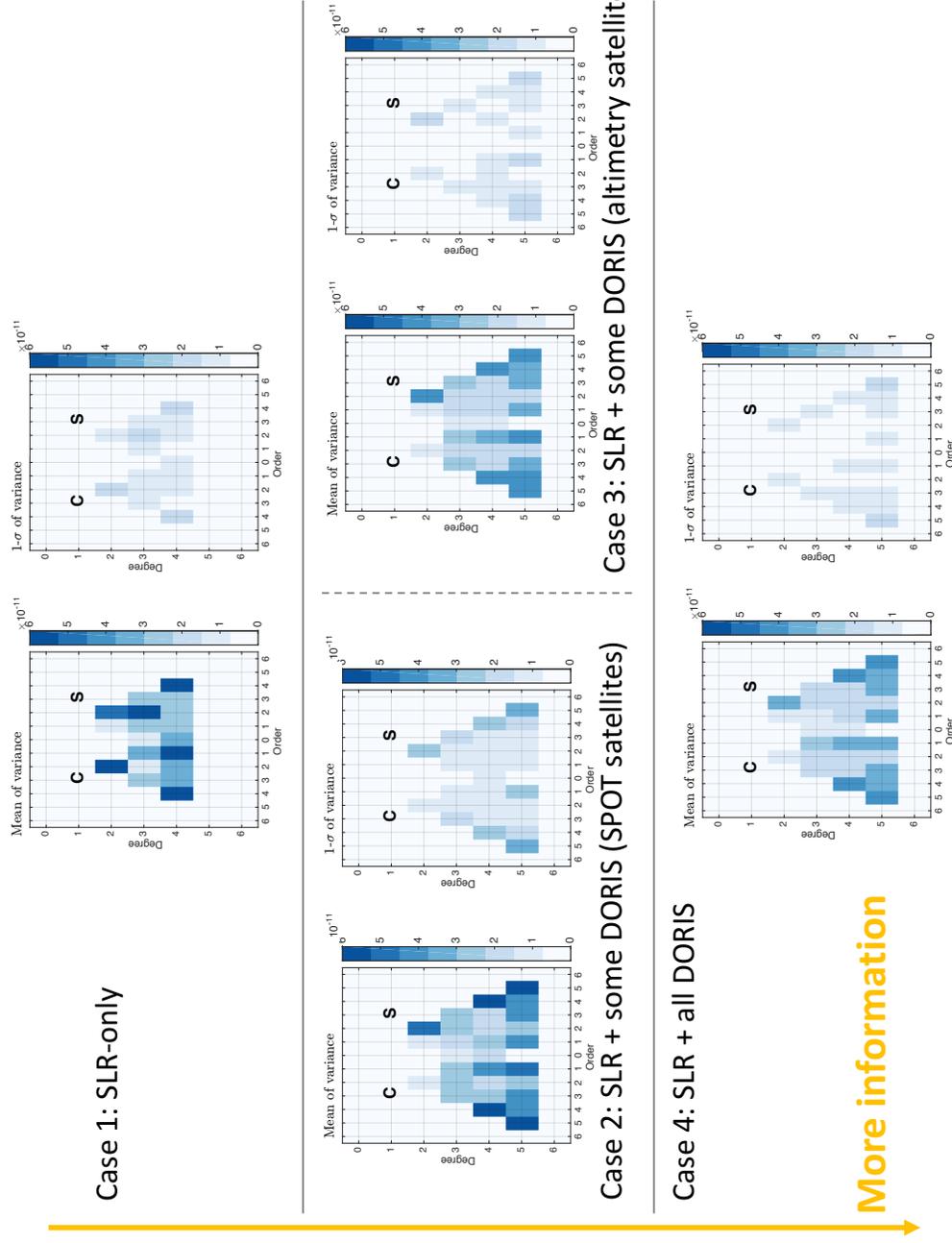
Figure 3.8: Error variance of GSFC solutions as a function of constellation. Once again, it is evident the Nominal9c has the best performance, meaning that the mean of the variances are the smallest. The case without DORIS satellites presents notably large variance values, especially for C_{22}.

However, a C_{20} time series was extended back to 1979 using SLR tracking data of LAGEOS-1. This extension was based on previous work and already stabilized arc data, but updated using new processes, new observation corrections files (e.g., taking into account the distance between where the laser reflects and the center-of-mass of the satellite), and station coordinates. The solution compared well with an existing time series from CSR after 1983, except that the amplitude of the seasonal signals are smaller, as seen in Figure 3.9. This discrepancy is likely due to the addition of the atmospheric background model to the CSR time series. The CSR solution included more tracking data than only LAGEOS-1: LAGEOS-2, Ajisai, Stella, and Starlette were added. This indicates that using only LAGEOS-1 is sufficient for a reliable C_{20} metric, but not prior to 1983, when an improved solution would require more satellites.
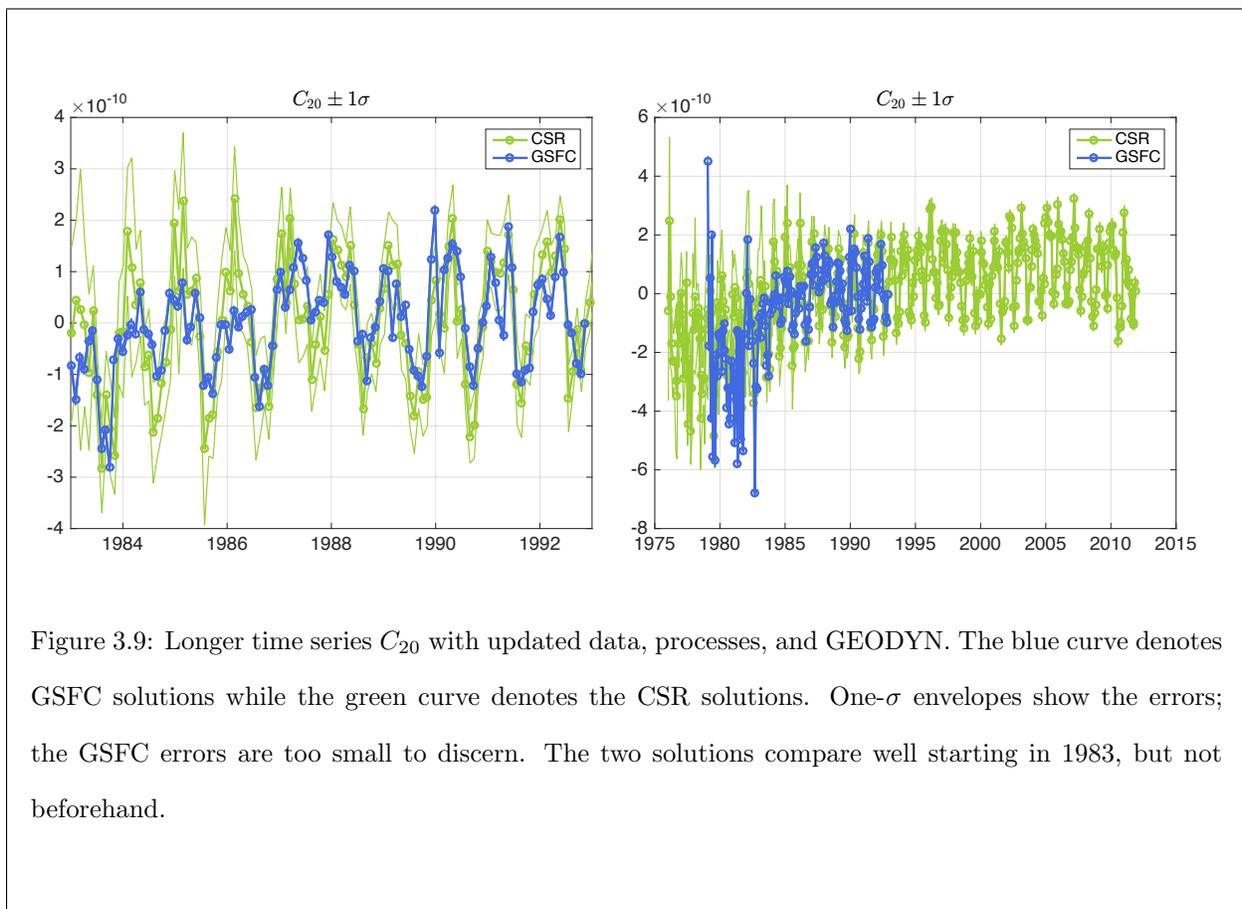
Figure 3.9: Longer time series C_{20} with updated data, processes, and GEODYN. The blue curve denotes GSFC solutions while the green curve denotes the CSR solutions. One-σ envelopes show the errors; the GSFC errors are too small to discern. The two solutions compare well starting in 1983, but not beforehand.

All in all, this section provided more background and detailed information on one particular

solution, from GSFC, derived by tracking a suite of satellites. In the following sections, additional solutions are briefly discussed.

3.3.4 Additional Solutions

3.3.4.1 DGFI Solution

The Deutsches Geodätisches Forschungsinstitut (DGFI) computes its own time-variable gravity solution using only SLR data (*Bloßfeld et al.*, 2015). The primary motivation was to provide an assessment of geophysical phenomena, such as the mass-related excitation functions, as well as C_{20}-induced differences in Antarctica ice mass loss, complementary to the findings from the GRACE mission. The estimation process is done with DGFI Orbit and Geodetic parameter estimation Software (DOGS). Table A.1 summarizes the background models used, but it is worth noting that this study used iterative variance component estimation to weight the different normal equations (see Eq.1-3 in *Bloßfeld et al.* (2015)). See Table 5 in *Bloßfeld et al.* (2015) for a summary of the parametrization chosen. A number of constellations were tested, from two-satellite constellation to ten-satellite constellation, and the larger constellation yielded a solution with the smallest correlation between the estimated C_{20} and the right ascension of the ascending node of the single solution formed by LAGEOS-1.

3.3.4.2 AIUB Solution

The Astronomisches Institut Universität Bern (AIUB) has provided time-variable gravity solutions for a variety of space missions. *Sośnica et al.* (2015) show a time-variable gravity solution using an SLR-based satellite constellation and the Bernese GNSS software (*Dach et al.*, 2007). As with DGFI, the primary aim for this endeavor was geophysical studies, but it also raises the possibility of bridging a potential gap between GRACE and GRACE Follow-On. Their solutions were validated by comparing seasonal variations of GRACE solutions. Solving for a full solution up to d/o 10 was attempted but deemed not possible unless regularization was employed. Three main limitations were outlined: deficiencies in background models (particularly the S_2 tidal alias),

deficiencies in non-gravitational perturbations such as solar radiation pressure, or correlations between coefficients C_{30} and C_{50}. The arcs span ten days but the solutions are distributed monthly. As for background models, the IERS 2010 conventions were followed and AOD RL05 has been used for de-aliasing. Table 2 in *Sośnica et al.* (2015) shows the parametrization. Once-per-revolution empirical orbit parameters in along-track are estimates that absorb mismodelled albedo and solar radiation pressure. Table 3 in *Sośnica et al.* (2015) summarizes the differences between GRACE and SLR missions and gravity solutions. The limiting factor of the AIUB solution in the context of this dissertation is their current time span, because they are limited to March 2002. Hence, they are only used in this dissertation as ways of comparison over the 2002 – 2014 time interval.

Four additional solutions of time-variable gravity based on SLR or DORIS are briefly mentioned here. First, CSR provides a wealth of data. *Cheng et al.* (2013) show, for example, that five satellites are enough to measure a longer time series of C_{20}, as shown in Figure 3.9. Furthermore, *Ries and Cheng* (2014) report existing correlations between C_{21} and C_{61}, but also that a solution of at least d/o 7 is needed in order to detect continental signal. While their solutions are used throughout the community, the lack of covariance information inhibits further usage in this dissertation. Second, the Space Research Institute at the Austrian Academy of Science has built a framework for SLR-based gravity solutions (*Maier et al.*, 2012)[4] . Third, *Cerri et al.* (2013) show that utilizing DORIS measurements alone is enough to generate judiciously located mascons. Lastly, *Matsuo et al.* (2013) use their own SLR-based processing to detect Greenland mass change in the 1990s. However, none of the latter three solutions are publicly available.

3.3.4.3   Processing to Ensure Consistency

To ensure the validity of the combination of GRACE and SLR and/or DORIS gravity solutions, it is essential that the gravity solutions are processed similarly. In particular, the SLR and/or DORIS solutions undergo a number of steps in order to be consistent and, therefore, comparable. Four major examples include ensuring that the discrepancies that arise by using different a_e (the

---

[4] See `http://geodesy.iwf.oeaw.ac.at/d_slr_monthly.html#gcoef`

equatorial radius) values used in the estimation process are normalized, interpolating the solutions onto similar time steps, re-arranging covariances, and standardizing the signal contained in the time-variable gravity solutions by adding atmosphere signal when necessary.

First, the coefficients are normalized according to their equatorial radius, as noted in *Gruber et al.* (2006):

$$
\left\{ \begin{array}{c} C_{lm}^{norm.} \\ S_{lm}^{norm.} \end{array} \right\} = \left(\frac{a_e^{field}}{a_e^{GRACE}} \right)^l \left\{ \begin{array}{c} C_{lm}^{unnorm.} \\ S_{lm}^{unnorm.} \end{array} \right\}.
\tag{3.3}
$$

For example, the GRACE equatorial value is 6378.13646 m, whereas the AIUB value is 6378.137 m. The ratio is 1.0000000847, which has a notable influence on the time-variable component of C_{20}. At degrees larger than $l > 3$, this ratio goes to zero and is therefore negligible.

Second, the global weekly solutions are binned and averaged into monthly solutions. Their associated covariances are averaged into one monthly covariance as follows,

$$
\mathbf{P_{month}} = \left[\sum_{k=1}^{N_{weeks}} \mathbf{P_k^{-1}} \right]^{-1},
\tag{3.4}
$$

where N_{weeks} is the number of weeks depending on the month (four or five). The error that accompanies the approximation that some months are 28 days or 35 days is considered too small to matter for the scope of this study.

Third, the covariances are re-arranged to ensure that the format is comparable. The GSFC covariances, used here as a standard, are ordered by order and type, i.e., a degree three solution would have the following order: C_{20}-C_{30}-C_{21}-C_{31}-C_{22}-C_{32}-C_{33}-S_{21}-S_{31}-S_{22}-S_{32}-S_{33}. Other covariances might be originally ordered by degree: C_{20}-C_{21}-C_{22}-S_{21}-S_{22}-C_{30}-C_{31}-C_{32}-C_{33}-S_{31}-S_{32}-S_{33}.

Lastly, the atmospheric signal is removed from the AIUB solution to ensure that the signal is consistent with the signal from DGFI and GSFC. For the latter two solutions, this atmospheric signal was left out of the solution, while the AIUB post-processing added AOD products back.

In summary, all original solutions stemming from conventional tracking data undergo a streamlined pre-processing check that ensures that they are composed of the same type of signal. As such, the combination process with GRACE data is not biased by discrepancies between

the solutions from GSFC, DGFI, and AIUB. In the following section, these normalized solutions are compared to GRACE.

The processing strategies are presented in Appendix A. Assessing the differences between the three different centers is beyond the scope of this study. However, there is an ongoing effort to merge different processing centers' strategies under the helm of the European Gravity Service for Improved Emergency Management (EGSIEM). Ultimately, while the IERS already provides a set of conventions (*Petit and Luzum*, 2010), the processing decisions of the various solutions will converge to an even more consistent set of standards.

Finally, it is important to note that some non-GRACE-specific post-processing corrections that occur with GRACE solutions, as described in Section 3.2, also take place with SLR solutions. This means that all coefficients are de-seasoned by removing a least-squares fit of annual and semi-annual cycles. Furthermore, the means of each coefficient over the GRACE time frame are removed. Finally, they are smoothed by twelve months and the first and last six months are hence discarded.

3.4   Comparisons and Comments

Section 3.2 described the GRACE solutions and Section 3.3 introduced the solutions generated using ground-based tracking observations. Finally, Section 3.4 investigates the differences between the solutions.

The correlations between coefficients are mitigated when the information from all the coefficients is added together, i.e., when global maps of Equivalent Water Thickness (EWT) are evaluated. One way to examine the maps without showing every month is to compute and compare their trend, as done in Figure 3.10 for the GSFC and DGFI solutions over two time frames. To first order, the two trend maps show a much higher agreement than the comparison of the coefficients would suggest. There are slight discrepancies, for example, over the Pacific ocean and East Antarctica.

Trend of GSFC solution, EWT [cm/yr]
10/92 to 03/14

04/02 to 03/14

Trend of DGFI solution, EWT [cm/yr]
01/93 to 04/15

04/02 to 04/15
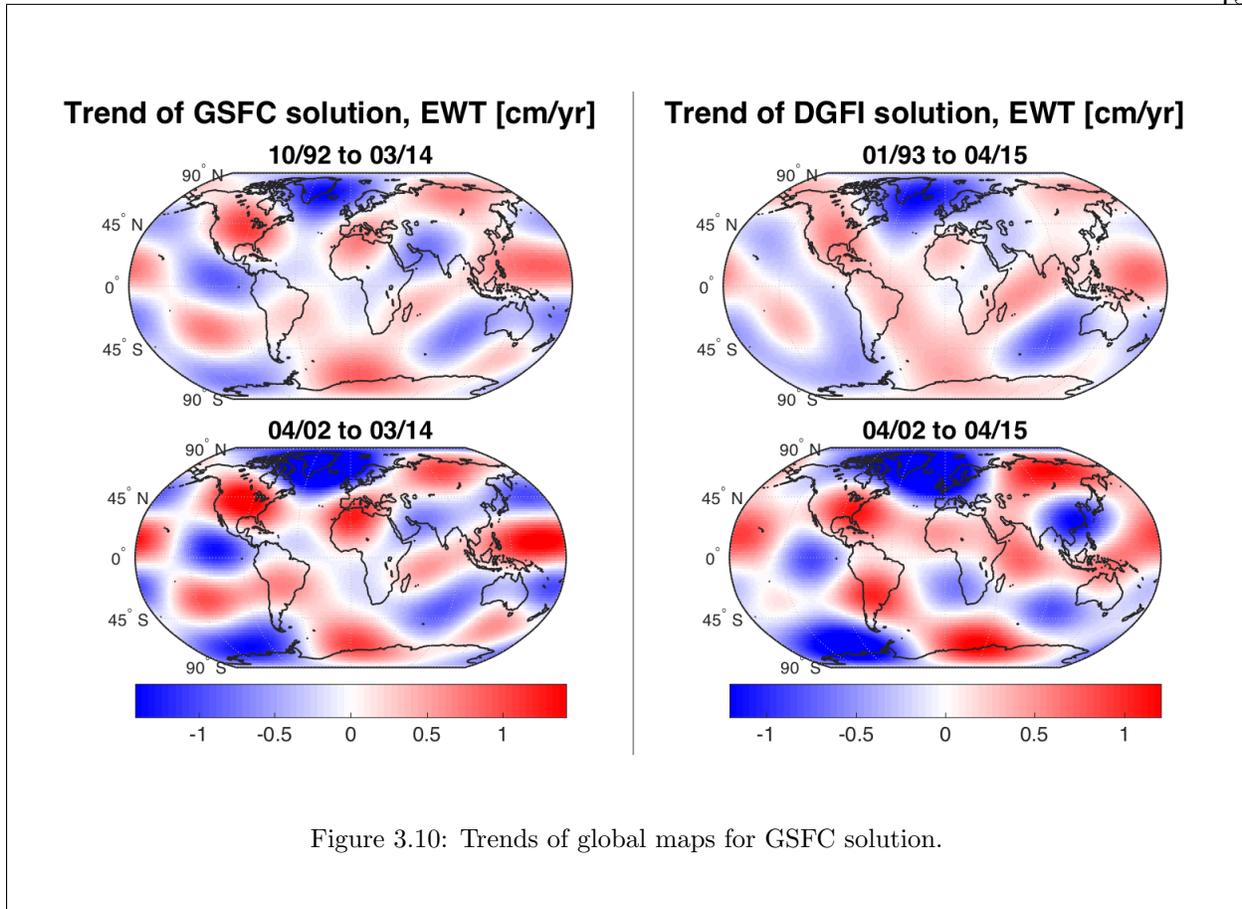
Figure 3.10: Trends of global maps for GSFC solution.

Figures 3.11 and 3.12 illustrate the individual coefficients. It is acceptable to consider GRACE as the "truth" signal, although the GRACE C_{20} coefficient originates from an SLR-based analysis, as mentioned in Section 3.2, so the information is not entirely independent. A comprehensive comparison, both qualitative and quantitative, of the coefficients is limited by the fact that SLR/DORIS-based coefficients are correlated. However, such plots still shed light on the fact that DGFI coefficients contain significantly more noise than their counterparts and that spurious signal in non-GRACE coefficients is especially visible at higher degrees. This is likely due to the lack of DORIS information in the DGFI solutions. Correlations between GRACE and SLR/DORIS coefficients from GSFC are illustrated in Figure 2 of the Supplemental Information in *Lemoine et al.* (2016).

Furthermore, Figure 3.13 shows the difference against the GRACE solutions in an RMS sense. This means that over the GRACE time frame, GRACE maps are subtracted from GSFC
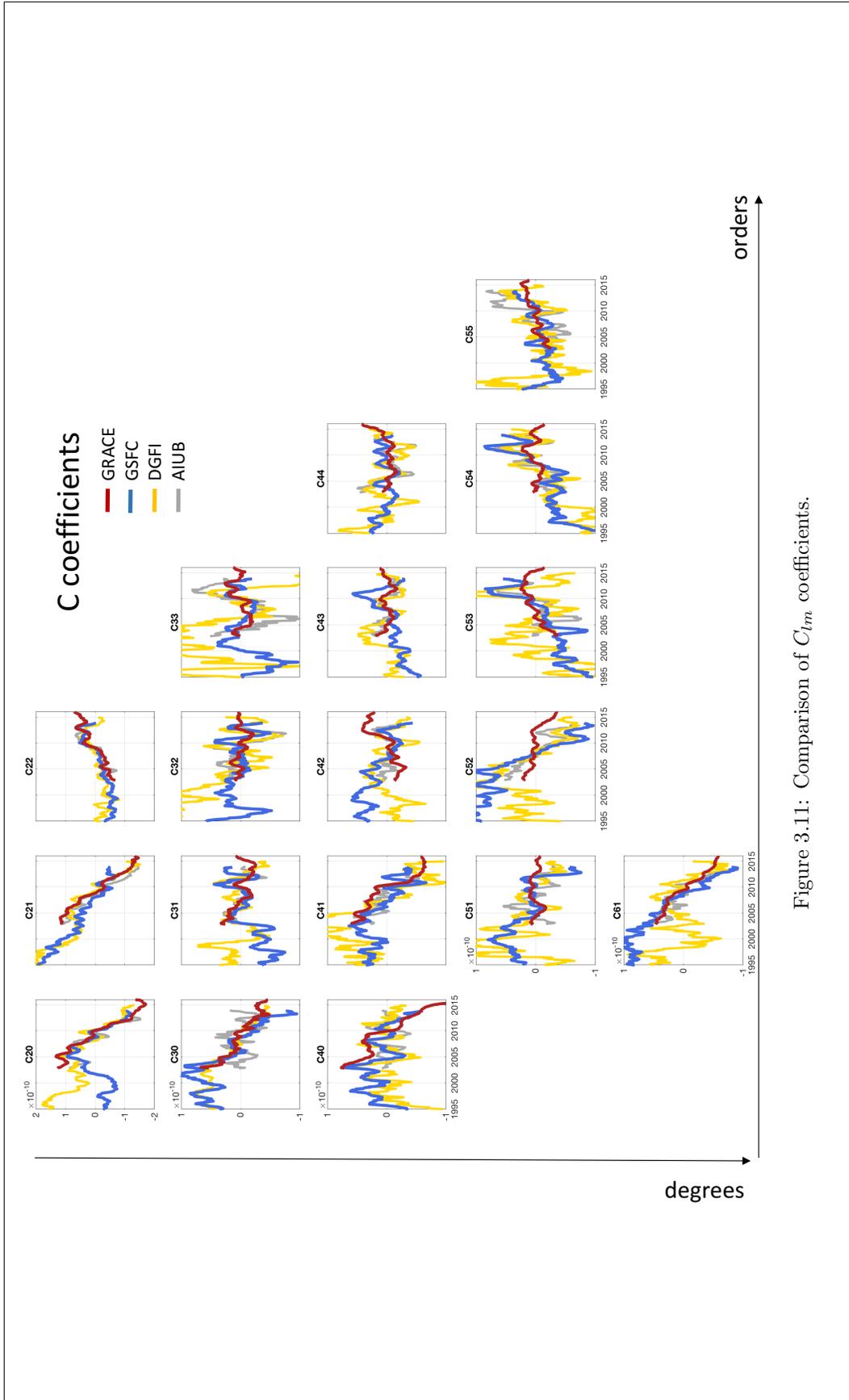
Figure 3.11: Comparison of C_{lm} coefficients.
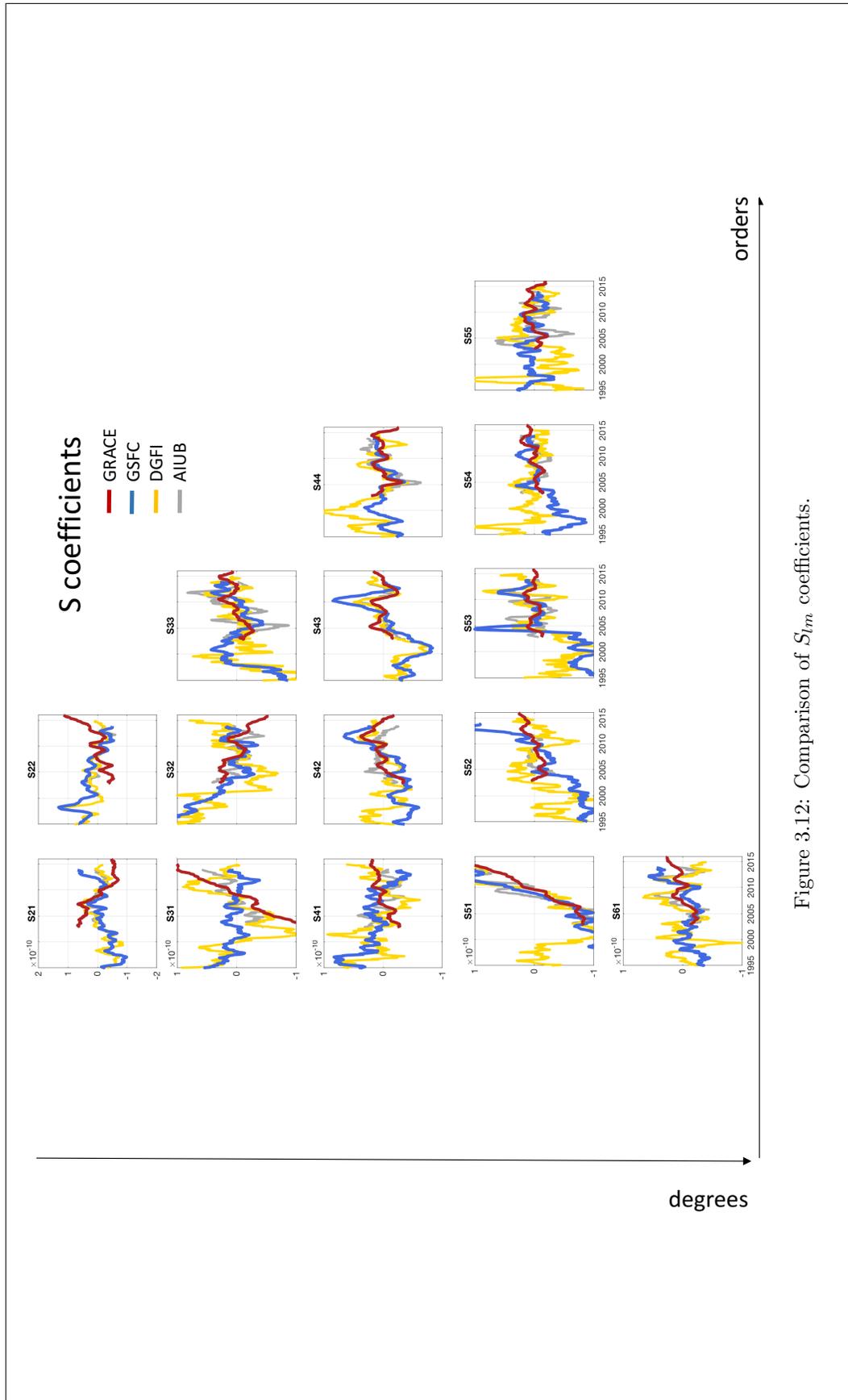
Figure 3.12: Comparison of S_{lm} coefficients.

and DGFI maps; for each grid cell, an RMS is applied to find the equivalent RMS grid cell. Higher RMS therefore indicates that the difference for a particular solution against the GRACE "truth" is highest. Naturally, the comparison is limited to the common coefficients common to GRACE and the lower-resolution ground-based tracking solutions, so the resolution of the maps is limited. The top two plots of Figure 3.13 display comparisons that included the trends for all fields, while the bottom plots show similar comparison without the trend included. They clearly show that the GSFC solution matches best with GRACE over the GRACE interval. The bottom plots provide insight for a comparison without the trend. If the trends captured by the two types of solutions were exactly the same, this would mean the bottom plots match the top plots. However, the GSFC RMS comparisons are greatly reduced; in particular, the discrepancies over the Eastern Pacific and North America are effectively removed. Similarly, a number of discrepancies in the DGFI solutions are removed, but South Africa and Siberia still show discrepancies that are independent of the trend.

Figure 3.13: Comparison of ground-based tracking solutions against GRACE solution. The top plots display comparisons that included the trends for all fields, while the bottom plots show similar comparison without the trend included.
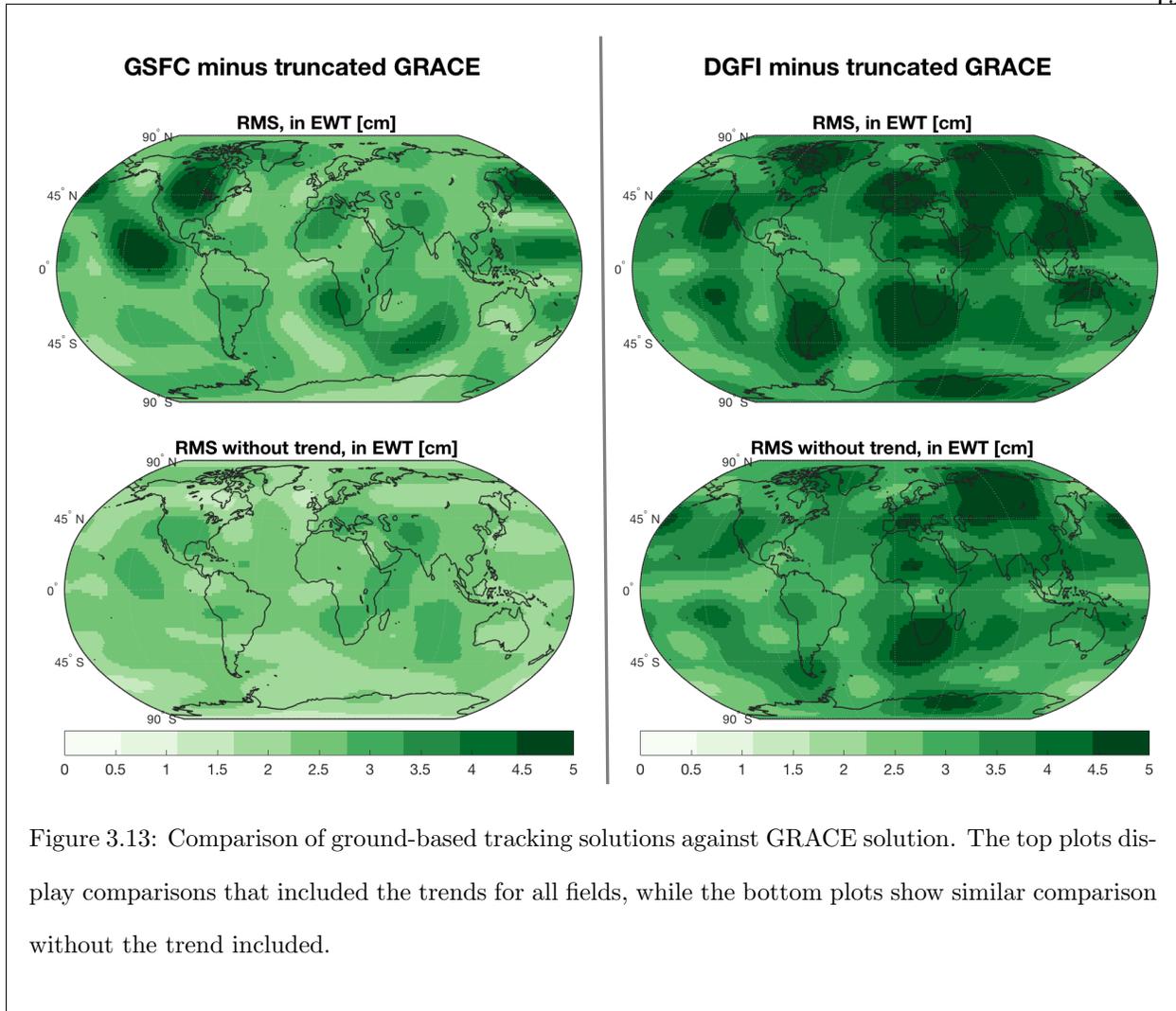
Finally, appendix B shows the difference in correlation and covariance information between GSFC and DGFI.

3.5   Summary

Chapter 3 introduced the two types of gravity solutions that are combined in Chapter 4 to form an extended record of time-variable gravity. Section 3.2 provided an overview of the GRACE solutions and the needed corrections, such as the C_{20} replacement. This overview was brief in its scope owing to the fact that the work presented in this dissertation merely uses the GRACE solutions without seeking to improve them. Section 3.3 presented the solutions that are

derived from ground-based tracking of a constellation of satellites. Two systems and their respective advantages, drawbacks, and measurement types are described: SLR and ranging measurements and DORIS and relative velocity measurements. Additionally, the satellite constellation and influence of parametrization choices are explained. The GSFC solution is described in detail and it is shown that the DORIS contribution is significant in reducing variance and correlations for the solutions. While the current GSFC solution only starts in November 1992, it is also shown that an updated C_{20} solution extending to 1979 can be generated using only LAGEOS-1 tracking observations. However, the quality of this time series is poor before 1983. Other solutions, including from DGFI and AIUB, are presented, along with post-processing strategies designed to ensure that the solutions are consistent in their content and in their format. Finally, Section 3.4 illustrated comparisons between all solutions; while comparisons of coefficients are limited by existing correlations, comparisons of EWT maps show that GSFC match best with equivalent GRACE maps.

Chapter 4

Reconstruction of Longer Time Series of Time-Variable Gravity

4.1   Overview

Combining gravity fields from GRACE and SLR/DORIS relies on one fundamental step: the projection of global gravity field modes onto SLR/DORIS fields (Section 4.2). A notable feature of the proposed approach is that the PCA is applied to GRACE fields in the spectral domain (Section 4.3.1). The projection of these global gravity modes onto SLR/DORIS fields is estimated via a Least Squares Adjustment (LSA) (Section 4.4.1), in which incorporating the information from the SLR/DORIS covariances is necessary given the existing correlations between Stokes coefficients. The solution of this LSA is a set of temporal amplitudes associated with each global gravity mode. The number of modes N_{modes} used for combining GRACE and SLR/DORIS products is justified in Section 4.4.2 (although the determination of this number is not a critical step). The spatial and temporal modes from the previous sections are combined to form the final gravity fields, as described in Section 4.5. Section 4.6 will develop the novel error quantification approach that is necessary for this reconstruction.

4.2   Framework of Reconstruction

In this section, an overview of the Principal Component Analysis (PCA) method is provided and its relation to the reconstruction process. Though a detailed description of PCA and its application for analyzing time-variable gravity products is provided in *Forootan* (2015) and *Preisendorfer*

(1988), and Section 2.3 of this dissertation, the main equations provided below facilitate under-standing of the reconstruction algorithm.

The global time-variable gravity products used here (SLR/DORIS and GRACE) show mass redistribution concentrated mostly over land. Each component possesses its own set of subcomponents that operate at different spatial and temporal scales. The PCA approach is applied here to extract orthogonal (uncorrelated) spatial and temporal patterns that capture the dominant variability in the GRACE fields.

The first step of a PCA is to build a data matrix $\mathbf{X}$ consisting of monthly time series $\mathbf{x}_i$, where i represents the time index ($i = 1, ..., N_{months}$) of the global fields. In this study, the time series $\mathbf{x}_i$ are column vectors each comprised of N_{coeffs} temporally centered Stokes coefficients (i.e., the mean is removed from each row of $\mathbf{X}$).

Then, an auto-covariance matrix $\mathbf{C}$ is built from $\mathbf{X}$ ($\mathbf{C} = \mathbf{X}^T\mathbf{X}/N_{months}$) and decomposed into its eigenvector basis $\mathbf{H}_0$ of size $N_{coeffs} \times N_{months}$. $\mathbf{H}$ represents a reduced version of $\mathbf{H}_0$ and only contains the first N_{modes} dominant modes, where N_{modes} is defined in Section 4.4.2. $\mathbf{H}$ therefore has a size $N_{coeffs} \times N_{modes}$. Columns of this matrix $\mathbf{H}$ are the eigenvectors $\mathbf{h}_k$ ($k = 1, ..., N_{modes}$) of length N_{coeffs}. They are also known as the Empirical Orthogonal Functions (EOFs) and contain the spatial information of the multi-dimensional data matrix $\mathbf{X}$.

To determine the temporal evolution of each EOF $\mathbf{h}_k$, $\mathbf{H}$ is projected onto the data matrix $\mathbf{X}$ (i.e., $\mathbf{Y} = \mathbf{H}^T\mathbf{X}$). The matrix $\mathbf{Y}$ contains the Principal Components (PCs) of size $N_{modes} \times N_{months}$, where the N_{months} entries of each row represent a PC $\mathbf{y}_k$ that is uniquely associated with an EOF by describing its temporal behavior. In other words, over each epoch i, an EOF $\mathbf{h}_k$ is scaled by $\mathbf{y}_k(t_i)$.

An approximation of the original multi-dimensional data $\mathbf{Z}_{Rec}$ is reconstructed from a linear combination of each mode's EOF and its respective PC: $\mathbf{Z}_{Rec} = \mathbf{HY} = \sum_{k=1}^{N_{modes}} \mathbf{h}_k\mathbf{y}_k$. The reconstructed data matrix $\mathbf{Z}_{Rec}$ is a set of time series of Stokes coefficients of size $N_{coeffs} \times N_{months}$.

The key of the study is the fact that the EOFs $\mathbf{H}$ come from GRACE and the PCs $\mathbf{Y}$ from the SLR/DORIS fields. Hence, the reconstruction entails that information from GRACE,

which contains spatial information of high resolution, is combined with temporal information from SLR/DORIS, which offers an additional decade of coverage compared to GRACE.

Analogous reconstruction techniques (i.e., combining two datasets, each with its distinct temporal or spatial resolution advantage) have been applied in sea-level reconstructions, whereby high-resolution and global spatial modes obtained from satellite altimetry are combined with decades of relatively spatially inhomogeneous times series from tide gauges (*Church and White*, 2002; *Hamlington et al.*, 2011; *Ray and Douglas*, 2011), or generally with sea level pressure (*Kaplan et al.*, 2000).

4.3   Determining Spatial Modes

To combine SLR and GRACE products, a PCA is applied to a data matrix of monthly time series of Stokes coefficients.

4.3.1   Choice of Input Data: Stokes or Grids

The use of Stokes coefficients as data contrasts with applying a PCA on a data matrix of grid cells. This choice is motivated by the inability to calculate full-rank covariances matrices in the grid cell approach. Full-rank matrices are necessary in order to compute the temporal modes, as outlined in Section 4.4.1.

There are $N_{coeffs}^{SD} = 33$ coefficients per epoch in SLR/DORIS fields, as opposed to $N_{coeffs}^{G} = 3627$ coefficients for GRACE fields. Each covariance matrix $\mathbf{P}_{stokes}^{j}$ ($j = 1, ..., N_{months}^{SD}$) and its inverse, the weighting matrix $\mathbf{W}_{stokes}^{j}$, are therefore a square matrix of of size 33×33. Mapping Stokes coefficients to a grid of Equivalent Water Thickness (EWT) is straightforward as outlined in (*Wahr et al.*, 1998),' but mapping the weighting matrices of Stokes coefficients from the SLR/DORIS field to the grid space (as required in Section 4.4.1) is hindered by singular matrices.

An EWT gridded field at an epoch i is computed as follows:

$$
\begin{aligned}
EWT(\theta_1, \phi_1, t_i) &= \frac{a\rho_e}{3\rho_w} \sum_{l=0}^{\infty} \sum_{m=0}^{l} \left(\frac{2l+1}{k_l+1} \right) \tilde{P}_{lm}(\cos(\theta_1))(\Delta C_{lm}(t_i)\cos(m\phi_1) + \Delta S_{lm}(t_i)\sin(m\phi_1)) \\
\mathbf{EWT}(t_i) &= [EWT(\theta_1, \phi_1, t_i), EWT(\theta_2, \phi_2, t_i), ..., EWT(\theta_{N_{pix}}, \phi_{N_{pix}}, t_i)] \\
&= \mathbf{Q}\mathbf{z}(t_i)
\end{aligned}
\tag{4.1}
$$

where a is the mean radius of the Earth, ρ_w the density of water, ρ_e the average density of the Earth, θ and ϕ the co-latitude and longitude, respectively, k_l the Love numbers of degree l, and $\tilde{P}_{lm}$ the normalized associated Legendre functions (*Wahr et al.*, 1998). The matrix $\mathbf{EWT}$ contains all spatio-temporal EWT information. The column vector $\mathbf{z}(t_i)$ contains N_{coeffs}^{SD} Stokes coefficients of a monthly SLR/DORIS field and the matrix $\mathbf{Q}$ is the mapping function from spectral domain to grid space. The matrix $\mathbf{Q}$ has a size $N_{pix} \times N_{coeffs}^{SD}$, where N_{pix} is the desired numbers of pixels in the grid. A grid with 5 degree/pixel would translate to 2592 pixels (36×72) and, therefore, a size for $\mathbf{Q}$ of $2592 \times N_{coeffs}^{SD}$.

By standard error propagation, the covariance matrix $\mathbf{P}_{stokes}$ can be converted to EWT grid space as $\mathbf{P}_{grid} = \mathbf{Q}\mathbf{P}_{stokes}\mathbf{Q}^T$. The equivalent weighting matrix $\mathbf{W}_{grid}$ is simply the inverse of $\mathbf{P}_{grid}$. But considering the fact that $\mathbf{P}_{stokes}$ has a rank of N_{coeffs}^{SD}, the propagated $\mathbf{P}_{grid}$ is a square matrix of size N_{pix}, which for $N_{pix} >> N_{coeffs}^{SD}$, is rank-deficient. Two common methods to mitigate this issue of rank-deficiency include reducing the dimensionality of $\mathbf{P}_{stokes}$ and adding a priori information. Reducing the matrix's dimensionality to match the rank of the input data translates to $N_{pix} \leq N_{coeffs}^{SD} = 33$, i.e., a map with 33 pixels. The resolution of such a map is not only unacceptably small for the purposes of this study, but its equivalent $\mathbf{P}_{stokes}$ also still possesses a high condition number (10^{17}) (*Koch*, 1988). Regarding the second method, there is currently no known way to estimate a priori information for covariances of global gravity field coefficients starting in 1992.

4.3.2   Other Approaches: Radial Basis Functions, Regional Kernels, etc.

In addition to PCA alternatives, two additional approaches to building modes were discussed in Section 2.3.3. First, it is possible to force modes by associating distinct spatial modes for each continent and ocean (e.g., a grid with one over Europe and zero everywhere else). This approach has its merits, namely the customization of kernels, but was not pursued in this dissertation because the modes would imply that time-variable gravity signal follows such regionally-constrained behavior, which does not represent the geophysical reality. Second, *Schmidt et al.* (2007) and other studies have developed a technique concentrating information in a non-global basis function framework, namely, regional functions called radial basis functions. However, the fundamental limitation of this approach in the context of combining GRACE-based radial basis functions with SLR/DORIS fields is in the resolution of the SLR/DORIS fields – there simply is not enough information. But RBFs could be pursued when independent solution can resolve a higher number of coefficients.

4.4   Solving for Temporal Modes

4.4.1   Least Squares Adjustment

Generally speaking, it is assumed that the SLR/DORIS-derived PCs (as opposed to the PCs from the GRACE PCA) can be estimated by projecting the EOFs from GRACE onto each SLR/DORIS monthly field via a LSA. The advantage of this projection is that the EOFs are basis functions that represent the physical characteristics of the gravity fields from GRACE. This contrasts with projecting customized spatial patterns onto SLR/DORIS fields, such as distinct fingerprints of continental basins. In that case, one would be forcing basis functions without any direct connection to the physical reality seen by GRACE.

The matrix $\mathbf{Y}_{SD}$ contains this temporal information (the PCs) from SLR/DORIS observations. Each column y_{SD}^{j} represents the principal components of all modes at a specific month j. The vector $\mathbf{y}_{SD}^{j}$ is estimated from a LSA of the truncated GRACE spatial modes $\mathbf{H}_{G}^{trunc}$ (size $N_{coeffs}^{SD} \times N_{modes}$) onto a monthly set of SLR/DORIS coefficients $\mathbf{x}_{SD}^{j}$ (size $N_{coeffs}^{SD} \times 1$) (see below

for further clarification on the meaning of $\mathbf{H}_G^{trunc}$). The observation equation can be described as $\mathbf{x}_{SD}^j = \mathbf{H}_G^{trunc}\mathbf{y}_{SD}^j$ and its equivalent LSA in Eq. 4.2.

$$\mathbf{y}_{SD}^j = \left((\mathbf{H}_G^{trunc})^T\mathbf{W}_{SD}^j\mathbf{H}_G^{trunc}\right)^{-1}\left((\mathbf{H}_G^{trunc})^T\mathbf{W}_{SD}^j\mathbf{x}_{SD}^j\right) \tag{4.2}$$

The weighting matrices are the inverses of the given SLR/DORIS covariances, $\mathbf{W}_{SD}^j$ (size $N_{coeffs}^{SD} \times N_{coeffs}^{SD}$). The reconstruction hinges on these weighting matrices because the SLR/DORIS Stokes coefficients are correlated. Without the covariances, the resulting temporal modes lead to reconstructed gravity fields that are drastically different.

The observation equation is an approximation of the PCA decomposition of the SLR/DORIS fields. Normally, it is noted $\mathbf{X}_{SD} = \mathbf{H}_{SD}\mathbf{Y}_{SD}$. However, $\mathbf{H}_{SD}$ is replaced with $\mathbf{H}_G^{trunc}$. In other words, it is assumed that the cross-correlations between the gravity coefficients over 11/1992 – 04/2014 (the time frame of SLR/DORIS) are the same as those over 04/2002 – 06/2016 (the time frame of GRACE). In the statistical language, the EOF patterns are stationary over 11/1992 – 04/2014. The error of this assumption is estimated in Section 4.6.2.

It is worth mentioning that to estimate the temporal modes $\mathbf{Y}$, the original EOFs $\mathbf{H}_G$ are truncated to match the resolution of the SLR/DORIS fields, as illustrated in Figure 4.1. This means that once the EOF modes are obtained from GRACE observations, they are truncated. This truncation involves removing all Stokes coefficients of degree and order that do not match that of the SLR/DORIS fields to find the associated temporal components (i.e., by reducing the size each $\mathbf{h}_k$ from $N_{coeffs}^G \times 1$ to $N_{coeffs}^{SD} \times 1$). The option of truncating a field provides an opportunity to easily switch between resolutions (e.g., 60x60 field becomes a 5x5 field by simply removing all unwanted Stokes coefficients, and then back to 60x60 by adding the Stokes coefficients back in) and therefore highlights another advantage of keeping the data in spectral domain (Stokes coefficients) instead of grids, with which it is much more complicated to switch resolutions. When truncating Stokes fields, one should note that the orthonormality of EOFs is violated, i.e., $\mathbf{h}_{k_1}^T\mathbf{h}_{k_2} = 0$, but $(\mathbf{h}_{k_1}^{trunc})^T\mathbf{h}_{k_2}^{trunc} \neq 0$. However, our numerical assessment indicates that the truncation from the original GRACE to the SLR/DORIS resolution does not significantly harm the orthogonality. Therefore, this is an

acceptable step and would have no significant influence on the final reconstruction results.
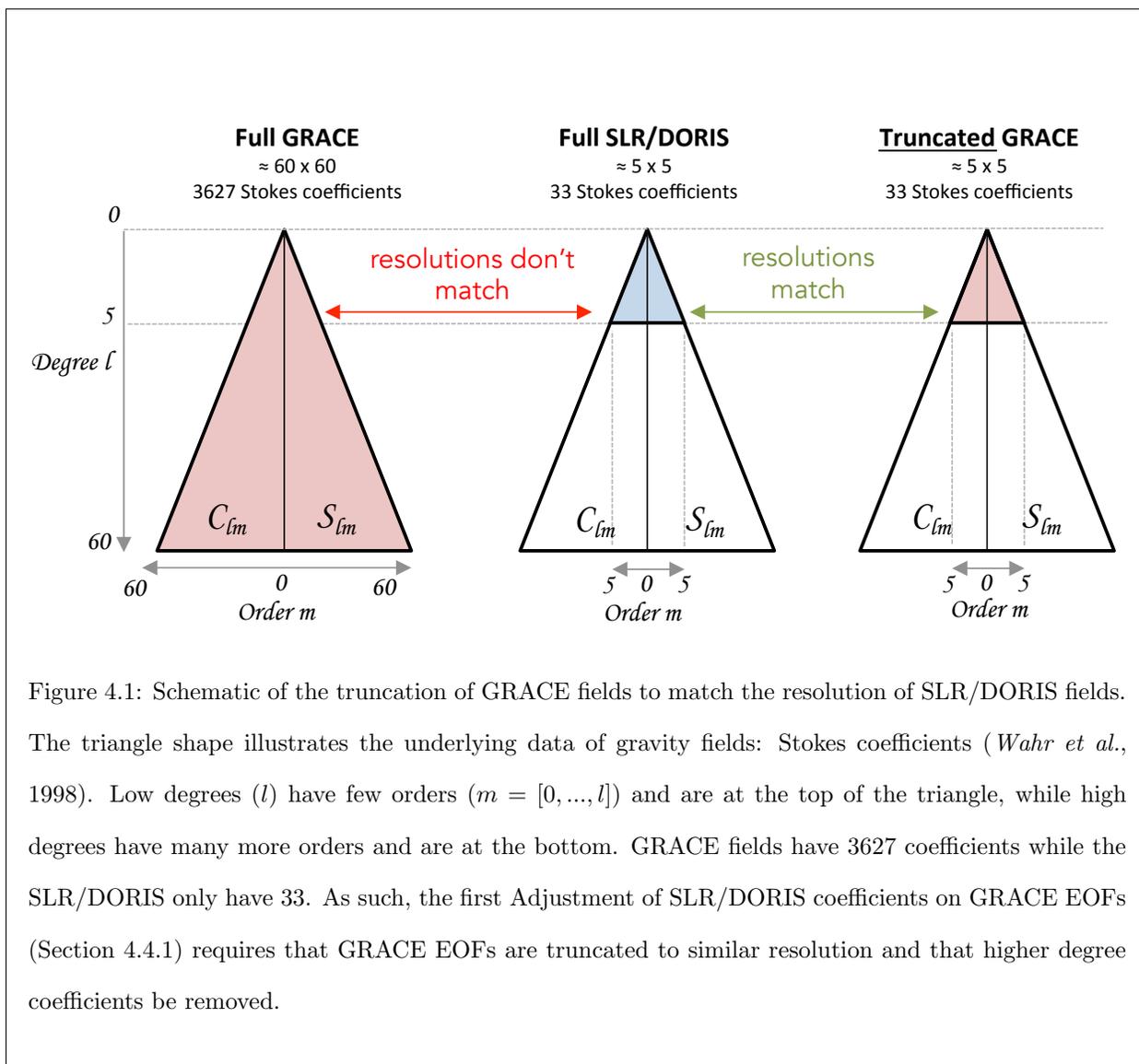
Figure 4.1: Schematic of the truncation of GRACE fields to match the resolution of SLR/DORIS fields. The triangle shape illustrates the underlying data of gravity fields: Stokes coefficients (*Wahr et al.*, 1998). Low degrees (l) have few orders ($m = [0, ..., l]$) and are at the top of the triangle, while high degrees have many more orders and are at the bottom. GRACE fields have 3627 coefficients while the SLR/DORIS only have 33. As such, the first Adjustment of SLR/DORIS coefficients on GRACE EOFs (Section 4.4.1) requires that GRACE EOFs are truncated to similar resolution and that higher degree coefficients be removed.

High-resolution patterns: (1) Obtained from PCA
(3) Used in the reconstruction

Mode 1 - full 60x60 [EWT cm]
Mode 2 - full 60x60 [EWT cm]

Truncation

Mode 1 - truncated [EWT cm]
Mode 2 - truncated [EWT cm]

Low-resolution patterns: (2) Fit onto SLR/DORIS solutions
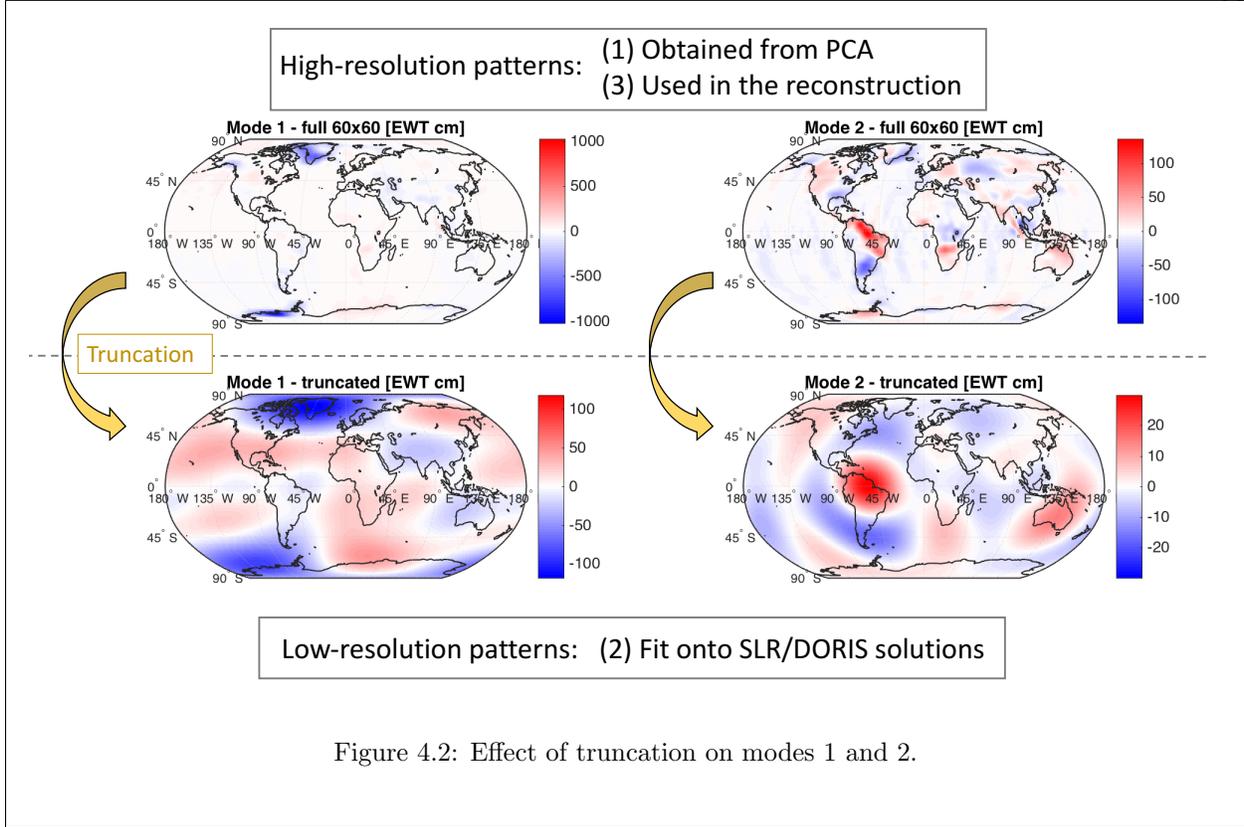
Figure 4.2: Effect of truncation on modes 1 and 2.

The LSA yields a covariance term that contains the information on the errors and cross-correlations of the PCs $\mathbf{y}_{SD}$, $\mathbf{P}_y^j = ((\mathbf{H}_G^{trunc})^T \mathbf{W}_{SD}^j \mathbf{H}_G^{trunc})^{-1}$. The resulting correlations are mostly due to existing correlations in the SLR/DORIS covariances but also, to a lesser extent, from the fact that the columns of $\mathbf{H}_G^{trunc}$ are no longer orthogonal. However, the highest correlations remain under 0.5 and statistically insignificant.

4.4.2   Number of Modes

The number of modes N_{modes} determines how many parameters are solved for in the LSA in Eq 4.2 at each epoch. Each parameter is the temporal amplitude associated with each EOF spatial mode (see Section 4.4.1). In regular PCA methods, the number modes can be selected from dominant-variance rules, sampling error rules such as North's rule of thumb (*North et al.*, 1982), etc. Many of these rules are summarized in *Forootan* (2015). For example, 22 modes suffice to explain 95% of the original variance in the GRACE fields.

However, this study is limited by the ability of the model in the LSA to solve for parameters given the 33 observations per epoch. The model is the EOF matrix ($N_{obs} \times N_{modes}$) and the 33 observations are the SLR/DORIS coefficients. On one hand, when the number of modes solved for is too low (below three), this means that the total global reconstructed fields are only based on two modes. Therefore, independent regional variability is severely limited, which is an issue for this study because the signals in Greenland and Antarctica should be uncorrelated. On the other hand, when the number of modes is too high (above six), the comparison between reconstructed global maps and GRACE maps over similar time frames is clearly worst (i.e., the average RMS of the differences between the maps is higher). The two extremes are balanced by setting $N_{modes} = 4$, although the differences between reconstructions using four through eight modes are not significant.

4.5   The Reconstruction Process: Combining Spatial and Temporal Modes

4.5.1   Combination

The reconstructed global gravity fields $\mathbf{Z}_{rec}$ are obtained by combining the full GRACE spatial modes $\mathbf{H}_G$ ($\neq \mathbf{H}_G^{trunc}$) with the SLR/DORIS-based temporal modes: $\mathbf{Z}_{rec} = \mathbf{H}_G \mathbf{Y}_{SD}$. Figure 4.3 shows the modes.

The matrix $\mathbf{H}_G$ contains spatial information (the EOFs) derived solely from the PCA of the GRACE data matrix $\mathbf{X}$ (hence the "G" subscript). These EOFs reflect the spatial distribution of the geophysical processes that explain most of the variance in the global, time-variable, monthly fields obtained from GRACE between 04/2002 and 06/2016.

Each EOF $\mathbf{h}_k$ is comprised of Stokes coefficients that are evaluated into a global grid of EWT (see left column Figure 4.3). Mode 1 captures a secular trend mainly indicating the mass loss of the polar regions (e.g., *Forootan and Kusche* (2012)), which could be expected because the trend is the largest signal in time-variable gravity fields in which seasonal signals are removed. The three other modes reflect hydrologic signals, such as droughts in northeast Australia (mode 2), as well as residuals from seasonal effects (e.g., the Amazon basin) in several of the modes (*Rodell et al.*, 2004)

and also residuals of stripes, especially observed over Antarctica. The EOFs obtained from a PCA on GRACE products from other processing centers (Jet Propulsion Laboratory (*Watkins and Yuan*, 2014) and GeoForschungsZentrum (*Dahle et al.*, 2013)) yield similar results: a trend mode capturing 65-70% of the variance followed by modes showing variability in land hydrology and residual non-tidal ocean, each capturing 2-8% of the variance. The PCs from GRACE are shown against the PCs from SLR/DORIS in Figure 4.3. There are inherent differences between the two sets, since the GRACE PCs represent a direct output of the PCA process, while the SLR/DORIS PCs are the solved parameters from an inversion of the truncated GRACE EOFs onto SLR/DORIS. As such, the SLR/DORIS PCs contain high-frequency artifacts that can be traced back to the variability in the SLR/DORIS covariances. Nonetheless, there is broad agreement between the two time series: for each mode, most long-wavelength behavior is recovered.

Figure 4.3: The four dominant spatial and temporal patterns from GRACE and SLR/DORIS time-variable gravity data. The global spatial modes (EOFs) from the PCA decomposition of GRACE fields and the percent of variance captured are shown. Right below each global map is its associated normalized temporal modes (PCs) directly from a GRACE PCA (red curve) and from SLR/DORIS (blue curve, see Section 4.4.1).

It is worth mentioning that in order to distribute the variance in a more balanced way, one might rotate the dominant EOFs to derive a new basis, e.g., the "varimax" criterion, which seeks to "maximize the contrast" between the regions containing the high variance via an optimal rotation (*Forootan and Kusche*, 2012). However, the first mode of various Rotated EOF sets still contained the combined signal from Greenland and Antarctica and still dominated the other modes. Therefore, the REOFs were not used to solve the reconstruction but ways to reduce this imbalance

in modes by modifying the matrix $\mathbf{H}_G$ are explored, such as Complex REOFs (which remove the assumption of stationary modes) and various forms of Independent Component Analysis (which use higher-level statistics than just the auto-covariance of the original data) (*Forootan and Kusche*, 2012; *Jolliffe*, 1986; *Richman*, 1986).

The matrix $\mathbf{Y}_{SD}$ contains the temporal information (the SLR-DORIS-derived PCs from the LSA, blue curves in Figure 4.3) from SLR/DORIS observations projected onto the EOFs, as discussed in Section 4.4.1. In Figure 4.3, it is also shown that the PCs from the GRACE-only decomposition (red curve) for comparison.

Figure 4.4 illustrates the global comparison of GRACE fields, considered to be the "truth," against the reconstructed fields, for both the DGFI and GSFC solutions. The RMS comparisons indicates that both sets of reconstructions show similar error patterns over Greenland, Antarctica, the Amazon, and South East Asia of nearly 20 cm EWT. The first two are due to slight differences in trends, but these differences are much smaller than the absolute value of the signal. In the Amazon, the differences are due to poorly isolated seasonal variations, i.e., not properly removed in the pre-analysis seasonal fit. These variations are visible in patterns 2–4 and illustrate the potential for improvement when using PCA alternatives that can capture near-periodic effects with poorly-established periodicities (see Section 2.3.3).

RMS of [GRACE - Reconstruction] for GSFC, EWT [cm]

RMS of [GRACE - Reconstruction] for DGFI, EWT [cm]

Figure 4.4: Comparison of reconstruction over GRACE time frame.
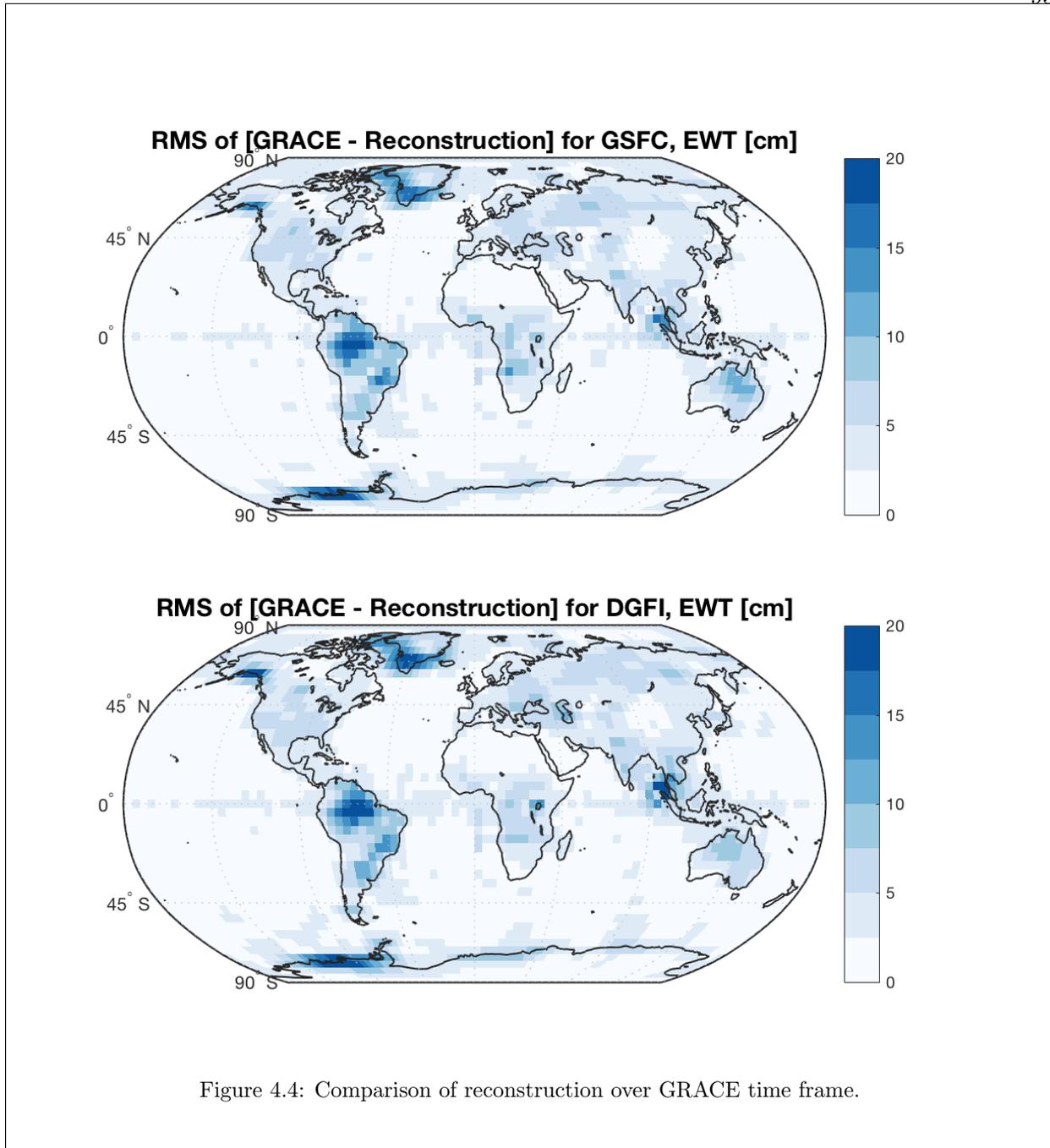
4.5.2 Computing Regional Mass Change Curves

Time series of cumulative mass change of the Greenland and Antarctic ice sheets are obtained by convolving a regional kernel with the reconstructed gravity fields, as outlined in *Swenson and Wahr* (2002), and smoothed by applying a 12-month moving average. It is worth noting that

this 12-month smoothing requires a six-month truncation on both ends of the time series, so the resulting time series span 04/1993 – 11/2013 instead of 11/1992 – 04/2014. In the spatial domain, the regional kernels are global grids with a value of zero outside the region of interest and one within. In the case of Greenland and Antarctica, the contours are simply chosen as the coastlines plus 300 km, which ensures that the land signal is fully captured. This extra area introduces signal from the residual non-tidal ocean signal and is taken into account in the error budget in Section 4.6.4. The conversion of the kernel from the spatial domain to the spectral domain is set to a maximum degree of 60 in order to match the size of the gravity fields with which it is convolved. This necessary cutoff leads to an artificial smoothing of the kernel. This artificial smoothing of the kernel yields an artificial loss of mass that requires compensation via a scaling factor (*Velicogna and Wahr*, 2006a). The scaling factor are also estimated by calculating the ratio of the kernel area in the spatial domain to the kernel area in the spectral domain (see Eqs. 3 and 4 in *Longuevergne et al.* (2010)). For Greenland and Antarctica, the scale factors are 1.3 and 1.0, respectively.

4.6   Error Budget

The total error budget of each mass curve is composed of two broad types of errors: those from the reconstruction process of two different gravity fields and those inherent to satellite-derived, global gravity fields. The first broad type of error (from the reconstruction process, i.e., combining the GRACE EOFs with their associated temporal amplitudes from the LSA of SLR/DORIS fields onto GRACE modes) is further classified in three separate errors called the measurement error, the stationarity assumption error, and the truncation error. The second broad type of error is simply classified as an inherent geophysical error. In total, the four errors in the following sections are treated and illustrate their magnitude as a function of time in Figure 4.5. All errors described here are added in quadrature.
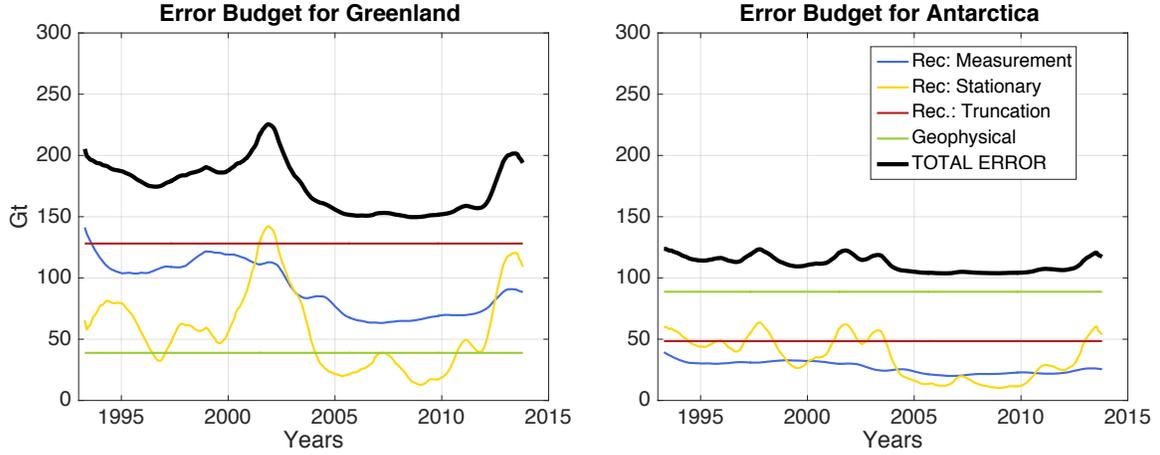
Figure 4.5: Error budget for the Greenland and Antarctic ice sheet mass change reconstruction in Gt. The blue curve denotes the measurement error (Section 4.6.1), the yellow curve the stationary assumption error (Section 4.6.2), the red curve the truncation error (Section 4.6.3), and the green curve the geophysical error (Section 4.6.4). The total error budget is obtained by adding all the errors in quadrature and denoted as the thicker black curve.

4.6.1   Measurement Error

The errors derived from the given SLR/DORIS full covariances represent the measurement error component of the total error budget (blue curve in Figure 4.5). The general full matrix error propagation technique is described in Section 2.4.3. First, the SLR/DORIS covariance at epoch j (size $N_{coeffs}^{SD} \times N_{coeffs}^{SD}$) is propagated to errors in the temporal components: $\mathbf{P}_{\mathbf{y}}^{j} = ((\mathbf{H}_{G}^{trunc})^{T}\mathbf{W}_{SD}^{j}\mathbf{H}_{G}^{trunc})^{-1}$ (see also Eq. 4.2). Second, the covariance matrix of the temporal modes $\mathbf{P}_{\mathbf{y}}^{j}$ (size $N_{modes} \times N_{modes}$) is propagated to errors in the reconstruction step, in which EOFs $\mathbf{H}_{G}$ from GRACE are combined with SLR/DORIS-derived PCs $\mathbf{Y}$, so that $\mathbf{P}_{field}^{j} = \mathbf{H}_{G}\mathbf{P}_{\mathbf{y}}^{j}\mathbf{H}_{G}^{T}$. The third and last step is the propagation of this covariance $\mathbf{P}_{field}^{j}$ into a covariance of mass change in the basin of interest, as described in Eq. (17) in *Swenson and Wahr* (2002). This step uses the re-

constructed Stokes coefficients ΔC_{lm} and ΔS_{lm} to obtain the mass change in a region M^j. Because this operation is a linear combination of the reconstructed Stokes coefficients, it can be written in matrix form, i.e., $M^j = \mathbf{A}\mathbf{z}^j$, where $\mathbf{A}$ is a matrix containing the linear coefficients (size $1 \times N^G_{coeffs}$) and $\mathbf{z}^j$ a column vector of reconstructed Stokes coefficients at epoch j (size $N_{coeffs} \times 1$). Hence, the covariance matrix of the mass calculation is now defined as $\mathbf{P}^j_M = \mathbf{A}\mathbf{P}^j_{field}\mathbf{A}^T$ (size 1×1). This value is the variance in the Greenland and Antarctic ice sheet mass reconstructions that originally came from the SLR/DORIS covariances.

The measurement error evolves in time because the accuracy of the SLR/DORIS fields is dependent on the number of satellites present in the solution and because of the changing quality of the tracking system and of its observations. A notable example is the tracking of Envisat (2002–2014), which strongly influences the solution by reducing the errors and correlations between the SLR/DORIS coefficients. This is due to its relatively low altitude, high inclination, and continuous orbit coverage (*Lemoine et al.*, 2016). The error associated with the Greenland mass change curve ranges between 60 and 140 Gt while the Antarctic error ranges between 30 and 50 Gt. The temporal behavior of this measurement error is similar for Greenland and Antarctica because they are both mostly defined by mode 1, as seen in Figure 4.3. This dependence on mode 1 is carried through the uncertain propagation steps outlined above. Finally, the larger magnitude of Greenland's error compared to Antarctica's is a consequence of its larger signal.

4.6.2   Stationary Assumption Error

The assumption that the GRACE spatial modes $\mathbf{H}_G$ span the SLR/DORIS time frame yields an error that are called the "stationary" assumption error (yellow curve in Figure 4.5). Indeed, this assumption is inherently imperfect because the geophysical processes that dominated over the GRACE time frame are not exactly the same over the SLR/DORIS time frame. To estimate these errors, 30 unique and separate reconstructions are simulated, each using EOFs calculated from a PCA on limited GRACE data. Limited GRACE data means that the GRACE fields do not contain the full set of monthly fields, but rather have a unique pseudo-randomly generated gap. "Pseudo-

randomly" entails that gaps of constrained lengths (between three and six years) and constrained midpoints (between 2006 and 2012) were, other than those two constraints, created randomly. This pseudo-randomness is justified because other more specific families of gaps (with either fixed length, or fixed midpoint, or both, etc.) yielded similar results. The use of simulated gaps seeks to recreate the lack of GRACE data over the SLR/DORIS time frame. For each simulated set of EOFs, the method described in Section 4 is followed and 30 unique mass change curves for the Greenland and Antarctic ice sheets are reconstructed.

These 30 reconstructed mass change curves are then compared to the "truth" mass change curve from a reconstruction using the full GRACE data, denoted as gray lines and a blue line, respectively, in Figure 4.6. To quantify the errors, the residuals (simulated minus truth) are examined, and their mean is plotted in purple in Figure 4.6 and in yellow in Figure 4.5. The Greenland error time series ranges between 10 and 130 Gt, while the Antarctica error time series ranges between10 and 60 Gt. The magnitude is smallest over the GRACE time frame, which is expected because the stationary assumption should inherently be close to valid during the middle years of the GRACE time frame (i.e., EOFs from limited GRACE data should still be similar to the truth EOFs). The variability in the error indicates that certain epochs are particularly sensitive to the choice of EOFs, especially around 2002 and 2014 in Greenland.
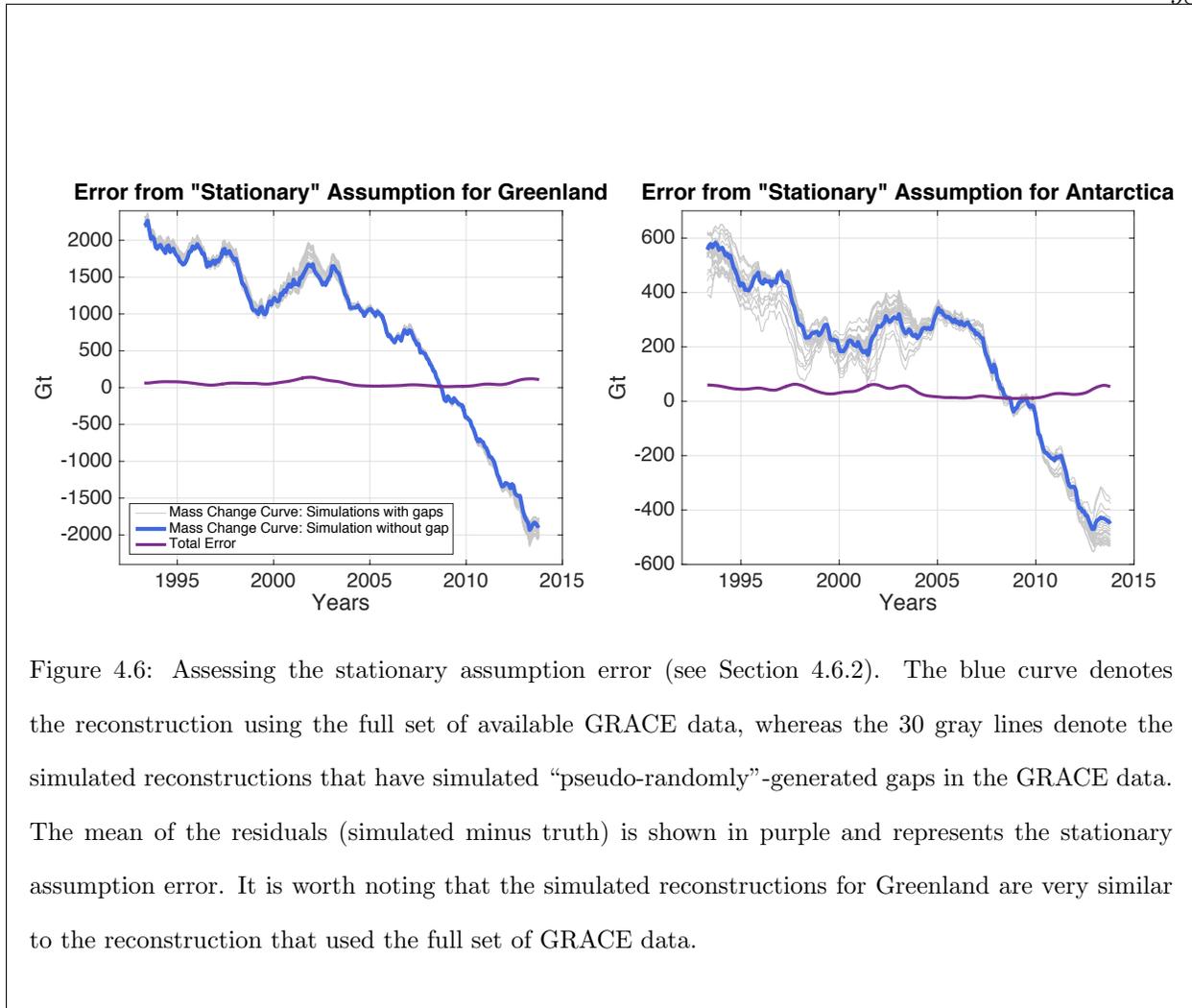
Figure 4.6: Assessing the stationary assumption error (see Section 4.6.2). The blue curve denotes the reconstruction using the full set of available GRACE data, whereas the 30 gray lines denote the simulated reconstructions that have simulated "pseudo-randomly"-generated gaps in the GRACE data. The mean of the residuals (simulated minus truth) is shown in purple and represents the stationary assumption error. It is worth noting that the simulated reconstructions for Greenland are very similar to the reconstruction that used the full set of GRACE data.

Similar results are seen even when only three reconstructions (instead of 30) are used, where each of the three reconstructions cover gaps of similar lengths at the beginning, end, and middle part of the GRACE time frame. In other words, the estimation of this stationary assumption error is robust. It is important to note that this approach only provides a lower bound estimate: Figure 2a in *Rignot et al.* (2011) shows that the Greenland ice sheet had even larger mass balance swings before the GRACE time frame. In fact, this approach is highly limited by the SLR/DORIS fields themselves. It is expected that this error estimation would be more meaningful if other independent SLR, DORIS, or SLR/DORIS fields with full covariances were available for testing.

4.6.3   Truncation Error

The need to truncate GRACE fields to match the low-resolution SLR/DORIS fields in the LSA (see Figure 4.1) is designated as the truncation error (red curve in Figure 4.5). To estimate its magnitude, two types of reconstructions are compared: (1) another set of reconstructed mass change curves using simulated SLR/DORIS fields against (2) the reconstructed mass change curves using the original SLR/DORIS fields. The simulated SLR/DORIS fields are truncated GRACE fields (i.e., using only 33 Stokes coefficients instead of 3627), with covariances that belong to the original SLR/DORIS covariances. These simulated low-resolution fields are fit onto GRACE EOFs to obtain the associated PCs (as described in Section 4.4.1) and, ultimately, mass curves for the Greenland and Antarctic ice sheets over the GRACE time frame. Once again, inspection of the residuals (simulated minus truth) provides a sense of the errors. The resulting standard deviations of the residuals – 128 and 48 Gt for Greenland and Antarctica, respectively – indicate that truncating the fields leads to a larger error for Greenland. This is expected because the Antarctic ice sheet is an relatively isolated signals in contrast to the Greenland. In a truncated, low-resolution, long-wavelength gravity field, Greenland is influenced by its neighboring, dynamic regions (Canadian archipelago, Svalbard, Iceland, etc.). Given the lack of time-dependent bias error over the GRACE time frame, it is assumed that the truncation error is constant over the SLR/DORIS time frame.

4.6.4   Inherent Geophysical Errors

The reconstructed global gravity fields also contain uncertainties that are of geophysical origin and inherent to any GRACE-like data product (*Velicogna and Wahr*, 2013). The major uncertainties stem from GIA trend errors, omission of degree-1 terms, and leakage from non-tidal ocean signals (green curve in Figure 4.5).

Because of the long time scales associated with the viscoelastic nature of the GIA signal compared to GRACE timescales, one can represent the GIA signal as a linear one: $y_{\vec{GIA}} = b_{GIA}\vec{t}$, where the time vector as $\vec{t}$ is defined as covering the time span of the reconstructed fields (size

$N_{months} \times 1$). The error in the Greenland GIA trend is determined by taking the standard deviation of several GIA models: 4 Gt/yr from *A et al.* (2013), 1 Gt/yr from *Peltier et al.* (2015), and 20 Gt/yr from *Khan et al.* (2016). With equal weighting applied to the three models, the standard deviation is $\sigma_{b_{GIA}}^{Gre.} = 10$ Gt/yr. Similarly, for Antarctica, the various GIA trends are: 55 Gt/yr from *Ivins et al.* (2013), 69 Gt/yr from *Peltier et al.* (2015), and 110 Gt/yr for *A et al.* (2013), yielding a standard deviation of $\sigma_{b_{GIA}}^{Ant.} = 29$ Gt/yr. However, the GIA errors are only considered when comparing trends because integrating this error from Gt/yr to Gt leads to an ambiguous choice of reference time (i.e., the integration constant).

The error due to omitting degree-1 terms (C_{10}, C_{11}, and S_{11}) are estimated following *Swenson et al.* (2008). The mass change associated to those time series adds variability with an RMS (Root-Mean-Square) over the Antarctic ice sheet of 68 Gt and over the Greenland ice sheet of 22 Gt. It is assumed that those errors are constant in time, but these are a lower bound estimates, because the omission of degree-1 errors may lead to even larger errors prior to the GRACE period (*Ivins et al.*, 2013).

Similarly, the error due to ocean signal leaking into ice signal is estimated by computing the mass change from the GRACE GAB fields. The GAB fields are the ocean component of the Atmosphere and Ocean De-aliasing Level 1B (commonly referred to as AOD1B) background model (*Flechtner et al.*, 2015; *Dobslaw et al.*, 2013) and zero over land. This signal has an RMS of 57 Gt and 32 Gt over the Antarctic and Greenland ice signal, respectively. Because the GAB fields are removed from the GRACE solutions, only GAB model errors and/or remaining non-tidal ocean signal should influence the GRACE solutions, so this approach provides an upper bound estimate of ocean signal leakage. Finally, it is assumed that those errors are constant in time.

Velicogna and Wahr (2013) list a number of other error sources: errors in the atmosphere background models, hydrology leakage, omission of eustatic ocean, scaling associated with the kernel-averaging step (see Section 4.5.2). These error sources are not considered because their magnitude are much smaller than the other errors presented here. In particular, the error on the scaling coefficient (1.3 for Greenland and 1.0 for Antarctica) originates from errors in the kernels

areas (spectral vs. spatial, see Section 4.5.2); these kernel areas are well constrained, so that the error on the scaling coefficient is negligible. Finally, the errors in GRACE coefficients are not considered because they are significantly smaller than the errors in the SLR/DORIS coefficients.

4.6.5   Comments on the Limits of the Reconstruction

The main limits of the PCA approach are addressed, namely, its possible inadequacy in representing non-stationary processes within the longer SLR/DORIS time frame. By applying PCA, a statistical relationship between the low and high degree Stokes coefficients is established, while considering a shorter GRACE time series. Assume one selects n PCA derived components, which in principle represent an n-dimensional orthogonal sub-space. The orientation of this subspace is optimum in a way that the variance of the projected original GRACE signals is maximum on to the subspace. At this stage, the PCA is an optimum solution, since it does not care whether the variance is originated from a standing waveform, cyclic, or an episodic (e.g., a sudden drought, flood, or sudden earthquake) phenomenon. One should note that PCA is consciously applied here to the global domain of time-variable gravity, which means that the phenomenon of interest should be dominant enough to be reflected in the global PCA modes. The limitations of this assumption have been assessed in Section 4.6.2. It is worth noting, however, that the PCA sub-space is not the best choice to represent the cyclic and episodic variations. For instance, changing the amplitude (modulation) of seasonal and interannual cycles might not be well presented by the PCA derived sub-space. The mixing of variability between PCA modes also limits achieving the best fit in the reconstruction stage. This has been to some extent reduced by removing the seasonal cycles from GRACE time series before applying the PCA. However, an application of non-stationary statistical approaches (*Forootan*, 2015) might improve the reconstruction results.

Another limitation of the reconstruction is its sensitivity to the input data. The final results are influenced by modifications in the input data in both steps of the reconstruction process: the PCA step, in which the spatial modes are defined (Section 4.2), and the LSA step, in which the temporal modes are calculated (Section 4.4.1). The different versions of the GRACE data

(JPL, CSR, or GFZ) do not fundamentally alter the reconstruction. However, adding one of the background products (e.g., GAD) to the GSM component of the GRACE fields will yield mass change curves that differ, especially for intra-annual signals. The discrepancy at the high frequencies explains why the focus here is set on the shorter frequency behavior (interannual and trend behavior). Furthermore, preliminary work shows that using another set of low-degree time-variable gravity solutions has an impact on the reconstruction – neither more negative or positive than the GSFC solutions.

4.7 Summary

In this chapter, the framework for combining two gravity fields of different resolution and time span is presented. This framework is best summarized in three steps. First, the PCA analysis enables the extraction of dominant, high-resolution spatial patterns from GRACE. Several design decisions are discussed, such as the need to use Stokes coefficients instead of grids as input data, which leads to the need for a $1/l$ weighting scheme. The second step entails fitting the spatial patterns onto the lower-resolution, but longer time series of Stokes coefficients from SLR/DORIS. Several modeling decisions are presented, included the truncation of the original GRACE patterns to match the resolution of the SLR/DORIS fields. The Least Squares Adjustment of these two variables – the GRACE patterns and the SLR/DORIS coefficients – yield to the temporal modulation of each pattern, i.e., the Principal Components. Moreover, the number of modes is determined by a trade study, not by usage of typical PCA-based selection rules. Finally, the last step is simply the linear combination of the full patterns and of the PCs. As such, the output of this reconstruction process is a set of monthly global gravity fields that extend over the time of the SLR/DORIS fields.

Furthermore, the error budget for two specific regions, Greenland and Antarctica, is addressed. There are two broad sources of errors: those due to geophysical limitations of time-variable gravity fields and those due to the reconstruction process. In particular, a novel error quantification approach was developed for the three sources of errors from the reconstruction process. The first relates to the propagation of the original SLR/DORIS covariances and is not constant time. The

second pertains to the stationarity assumption, i.e., assessing how constant the GRACE patterns are over the reconstruction, and this error is evidently not constant in time. The third seeks to quantify the error that arises because the patterns are truncated in the second step of the reconstruction. In this case, the error is shown to be approximately constant because it does not deviate significantly over time compared to a "truth" case. Finally, Chapter 7 will shed further light on the regional variability of these errors.

Chapter 4 presented the statistical framework for the reconstruction of fields and Chapters 5, 6, 7 will apply these fields to geophysical applications. As such, while this Chapter 4 touches on the validation of the reconstructed fields, Chapter 5 and 6 go into greater detail in assessing the validity of the fields.

Chapter 5

Time-Variable Gravity in the Cryosphere

5.1   Overview

The output of chapter 4 is a set of reconstructed monthly fields and associated error budget designed specifically for the Greenland and Antarctic ice sheets. The fact that these fields are based on the combination of the dominant patterns from GRACE means that the largest signals, such as Greenland and Antarctica, are best captured. This chapter examines these longer time series of polar ice sheet mass change, which has been an active area of research, as described in Section 5.2. The validity of the reconstructed EWT maps in Greenland and Antarctica is first assessed by comparing them against GRACE-only solutions over the GRACE interval in Section 5.3. Comparing EWT maps sheds light on existing geographic differences between the reconstructions and the GRACE fields. The reconstructed mass change data are then compared against two types of data for Greenland and Antarctica in Sections 5.4 and 5.5, respectively. First, two mass change curves derived only from GRACE fields are used: *Velicogna and Wahr* (2013) and *J. Wahr (personal communication, 2014)*. Second, three independent mass change data are used: Input-Output Method (IOM) data digitized from *Rignot et al.* (2011), IOM from data collected for this dissertation (*Enderlin et al.*, 2014; *Noël et al.*, 2015), and data from an ensemble of methods (*Shepherd et al.*, 2012). The general comparison entails a comparison of trends and a comparison of full mass change curves involving the reconstructed vs. IOM curves.

5.2   Background: How Did the Ice Sheets Melt Prior to GRACE?

Efforts to assess the mass balance of the Greenland and Antarctic ice sheets hinge on a number of different satellite-based data types (InSAR, radar altimetry, gravimetry, etc.) and regional models (surface mass balance, atmospheric pressure, etc.), some with longer time series than others (*Rignot et al.*, 2011; *Shepherd et al.*, 2012; *Velicogna and Wahr*, 2013).

Zonal harmonics also be used as observations and/or constraints to invert for various geodetic parameters: *James and Ivins* (1997) show that polar mass balance estimates are highly sensitive to odd-degree zonal harmonic, while *Tosi et al.* (2005) find that the Greenland and Antarctic ice sheets lose 280 and 60 Gt/yr of ice mass, respectively, using 26 years of secular variations in SLR-derived zonal harmonics (presumably starting soon after the launch of LAGEOS-1). *Matsuo et al.* (2013) employ an SLR-based field of degree and order four to show that SLR tracking provides a consistent benchmark to assess the history of mass variations in Greenland. Similarly, *Cerri et al.* (2013) estimated Greenland mass change solely from DORIS-based tracking solutions. The high-low, satellite-to-satellite, GPS-based tracking data of the Challenging Minisatellite Payload (CHAMP) satellite have been used to extract trends and annual amplitude of mass change in Greenland over CHAMP's lifetime (2000-2010) (*Baur*, 2013; *Weigelt et al.*, 2013). Finally, the recently launched, three-satellite mission Swarm also holds much promise for time-variable gravity studies, as well as other high-low GPS-based approaches (*Sośnica et al.*, 2015; *Zehentner and Mayer-Gürr*, 2015).

In contrast to the studies described above that use uniquely the conventional tracking data, this study seeks to combine SLR and DORIS with GRACE time-variable products. Indeed, the GRACE fields are high spatial resolution but cover a relatively shorter timespan (April 2002 onward) while the SLR/DORIS fields are low spatial resolution but cover a longer timespan (November 1992 onward). By combining these datasets into a single and distinct set of monthly fields, this analysis seeks to overcome their respective shortcomings and extends the time-variable gravity information by a full decade prior to the GRACE period, placing the changes observed by GRACE since April

2002 into a longer-term context. As such, the resulting gravity fields, obtained from the combination of GRACE and SLR/DORIS measurements, provide the first perspective of ice sheet mass change starting in the early 1990s from satellite gravimetry at a resolution higher than degree four.

For this reconstruction to be valid, the GRACE and SLR/DORIS gravity fields have to be processed as similarly as possible. For both fields, the influence of Glacial Isostatic Adjustment (GIA) is then removed via the ICE-6G_C (VM5a) model (*Peltier et al.*, 2015), the mean of the fields over the GRACE timespan, and the annual and semi-annual components of seasonal signals.

5.3   Comparison of EWT Maps

The reconstructed EWT maps are compared to GRACE EWT maps over the GRACE interval, as shown in Figure 5.1. The residuals are examined, i.e., truth EWT maps minus reconstructed maps.

The means of the residuals are small for both regions: less than 0.5 cm EWT when the total change in EWT over the GRACE interval can reach 50 cm. The values of the means are negative in areas that experience high melt (south-eastern and western coast of Greenland and in West Antarctica) (*Velicogna*, 2009; *Rignot et al.*, 2011; *Shepherd et al.*, 2012), but the small values render any particular interpretation of this bias negligible. Overall, the reconstructions show no large systematic discrepancy compared to the truth fields over the GRACE interval. The residual variability reflects the reconstructions' inability to recover short-term changes and is illustrated by the standard deviation of the differences (the middle plot in Figure 5.1). This variability is pronounced along the south-eastern coast of Greenland and West Antarctica.

A customized version of Signal-to-Noise Ratio (SNR) is defined to reflect the ability of a reconstruction to recover the truth signal as opposed to noise. The signal is the maximum range of change in EWT values (e.g., up to 50 cm of loss in areas of Greenland). The noise is the variability of the residuals (the middle column in Figure 5.1), since the means of the residuals are negligible. This SNR measure is skewed towards large values in pixels where the trends are large, but appropriately highlights the areas where the variability in the residuals is large compared to the

signal. Such areas are the north-east coast of Greenland and the interior of Antarctica, where the trend in mass loss is relatively small (*Velicogna*, 2009; *Rignot et al.*, 2011; *Shepherd et al.*, 2012). Overall, the fact that areas of high mass loss contain high SNR values gives us confidence that the reconstructions capture meaningful signal during the GRACE time frame.

Figure 5.1: Quality of reconstructed gravity fields in Greenland (top row) and Antarctica (bottom row). The first two columns show the mean and the standard deviation of the difference between truth EWT maps (GRACE-only) and PCA reconstructions over the GRACE interval. The last column shows the signal-to-noise ratio.
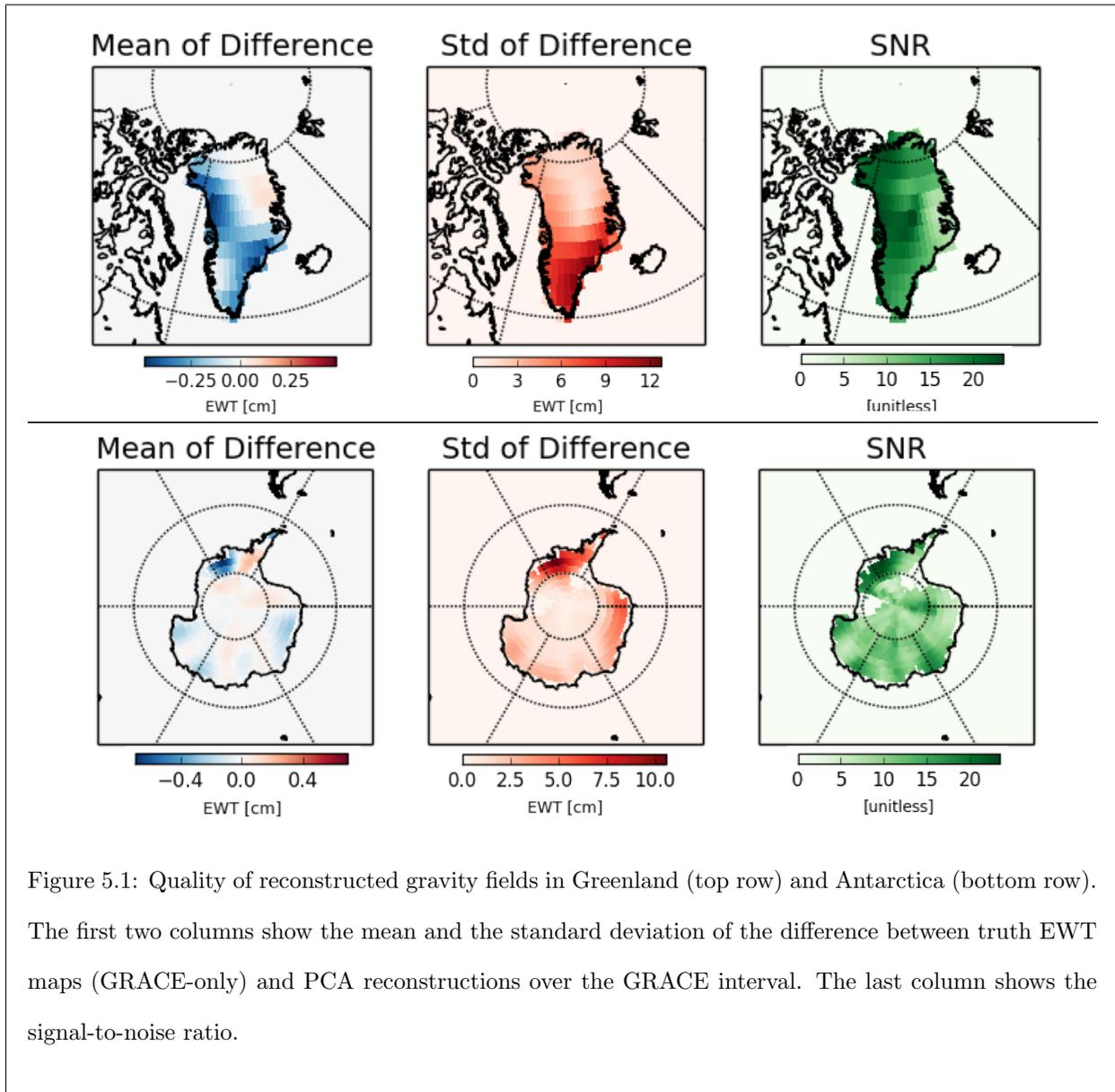
5.4   Greenland Mass Change

Figure 5.2 shows the different mass change curves for the Greenland ice sheet.

First, the reconstruction is assessed, represented as the blue curve in Figure 5.2. With the perspective of an additional decade of data, best-fit trends applied to the reconstructed mass change curve suggests two distinct epochs of approximately linear mass loss prior to and following 2005. From 1993 to 2005, the mass change trend is -70±20 Gt/yr, while the next decade shows a trend of -360±28 Gt/yr. The trend errors are the formal errors of the linear regression.

The transition to a faster rate of mass loss around 2005 is concurrent with an increase in mass loss due to surface meltwater runoff (*van Angelen et al.*, 2014; *Enderlin et al.*, 2014). Independent polar motion data also indicate that rapid ice mass loss is the cause of the observed change in the direction of the mean pole of the Earth (*Chen et al.*, 2013; *Wahr et al.*, 2015). Figure 2 in *Chen et al.* (2013) shows the deviation of the annual mean pole from the long-term trend starting in 2005 using IERS pole motion data. *Wahr et al.* (2015) also discuss this deviation from a long-term (20th century) trend of the mean pole (see Figure 1) and its impact on GRACE C_{21} and S_{21}. On the other hand, it is noted that the mass change of the Greenland ice sheet is influenced by many factors, such as circulation in the North Atlantic (*Seo et al.*, 2015), and that this current interpretation is limited in its scope.

A comparison between the reconstruction and the GRACE-only solution (red curve in Figure 5.2) shows that the reconstruction has higher artificial variability, but overall the GRACE-only curve is within the 1-σ envelope.

Furthermore, the reconstructed mass curve before the GRACE time frame are compared. Despite the lack of independent time-variable gravity data, mass change curves extending back to 1992 from two other approaches are generated. First, the IOM curve generated in this study are computed, shown in black in Figure 5.2. The IOM obtains mass change estimates by subtracting yearly ice discharge across the grounding line (*Enderlin et al.*, 2014) from monthly surface mass balance (SMB) determined from the RACMO2.3 atmospheric model (*Noël et al.*, 2015; *van den Broeke et al.*, 2016). The yearly ice discharge data is divided by 12 to obtain monthly discharge values. One drawback of this simple conversion is that seasonal variations are neglected, but this is acceptable because this study is focused on interannual signals. Furthermore, seasonal changes in

the velocity of Greenland's fast-flowing marine-terminating glaciers, and presumably ice discharge as well, are relatively small (*Moon et al.*, 2014). The SMB data are also filtered in order to remove their seasonal signals, both the annual and semi-annual components. Furthermore, the ice discharge data only start in 2000 and are extrapolated to 1992 using two assumptions: (1) a linear trend from 1996 to 2000 and (2) ice discharge changes of zero from 1992 to 1996, which are common assumptions for the computation of mass loss estimates due to discharge change (*van den Broeke et al.*, 2016; *Enderlin et al.*, 2014). Second, mass balance data from Figure 2a in *Rignot et al.* (2011) are digitized and plotted the integrated values, as seen by the green line in Figure 5.2.

Generally speaking, the three curves match well to each other and all indicate an increase in mass change rate since the early 1990s, even though the reconstruction show larger mass change before 2000. The biggest difference is in the rapid mass loss in 1998 following by a multi-year mass gain. This dip is clearly not observed in the other curves and remains unexplainable. This type of dip (along with smaller variability in 1996, 1997, 2002, and 2003) are associated with the limits of the SLR/DORIS solution that have not been accounted for in the error budget. This highlights the need for independent conventional tracking data to account for the unknown errors in the SLR/DORIS fields that influence the reconstructions, but are not captured in the covariances.

Comparisons of mass change trends from this study and previous analyses are presented in Table 5.1. The *Rignot et al.* (2011) data are not included in this table because the detailed and full time series required for a rigorous fit are unavailable. The comparisons are applied to matching time intervals. Greenland trends for this study's reconstruction are consistently higher than previous analyses by 15-25%. One potential reason for this consistent bias is signal leakage from surrounding melting regions (Baffin island, Ellesmere island, and Iceland) that is absorbed by temporal mode 1 during the process of fitting SLR/DORIS coefficients onto spatial modes, due to resolution difference in the fitting. An earlier study estimates the mass loss in these regions to be 51 ± 17 Gt/yr (*Schrama and Wouters*, 2011) and 42 ± 24 Gt/yr (*Rignot et al.*, 2011). Furthermore, differences in processing (e.g., the recently recommended corrections for C_{21} and S_{21} outlined in (*Wahr et al.*, 2015), which influence the reconstructed Greenland trend by about -10 Gt/yr, but not Antarctica) also likely

lead to discrepancies in estimates of mass loss between the different datasets in Table 5.1. Hence, these two sources of extra loss in mass change could perhaps explain the differences with the other studies. Finally, the trends calculated using the earliest time frame available (1993 – 2000) show higher mass loss by 102 and 78 Gt/yr for the reconstruction as compared to the IOM and the ensemble solution in *Shepherd et al.* (2012), respectively.

Although the mass loss acceleration fit reported in previous studies could also provide a useful metric for these comparisons, such fits as a means for comparison are not used because the acceleration estimates are highly sensitive to the time frames selected (*Wouters et al.*, 2013). For reference, however, the acceleration of the full reconstructed Greenland mass change time series is -24±6 Gt/yr^2. This value represents the quadratic coefficient a, where $M(t) \approx \frac{1}{2}at^2 + bt + c$.

In summary, the magnitude of the Greenland ice sheet balance appears to have increased approximately five-fold after 2005. Despite the lack of independent time-variable gravity data, the reconstruction to two separate IOM approaches are compared. The reconstruction shows higher mass loss before 2000 and presents variability, in particular a large dip in the late 1990s, that is not visible in the IOM curves. However, these comparisons are hindered by a number of assumptions (such as assuming linear mass loss before 2000 and zero changes before 1996 for the extrapolated *Enderlin et al.* (2014) ice discharge) and the fact that data are digitized (Figure 2 in *Rignot et al.* (2011)). The comparison of trends over different time intervals shows that the reconstruction has a higher mass loss rate of between 39-53 Gt/yr over the GRACE interval. Even when taking into account this additional rate, the mass loss from the reconstructions are still higher than the other methods before 1993, suggesting higher mass loss than previously thought in the 1990s.
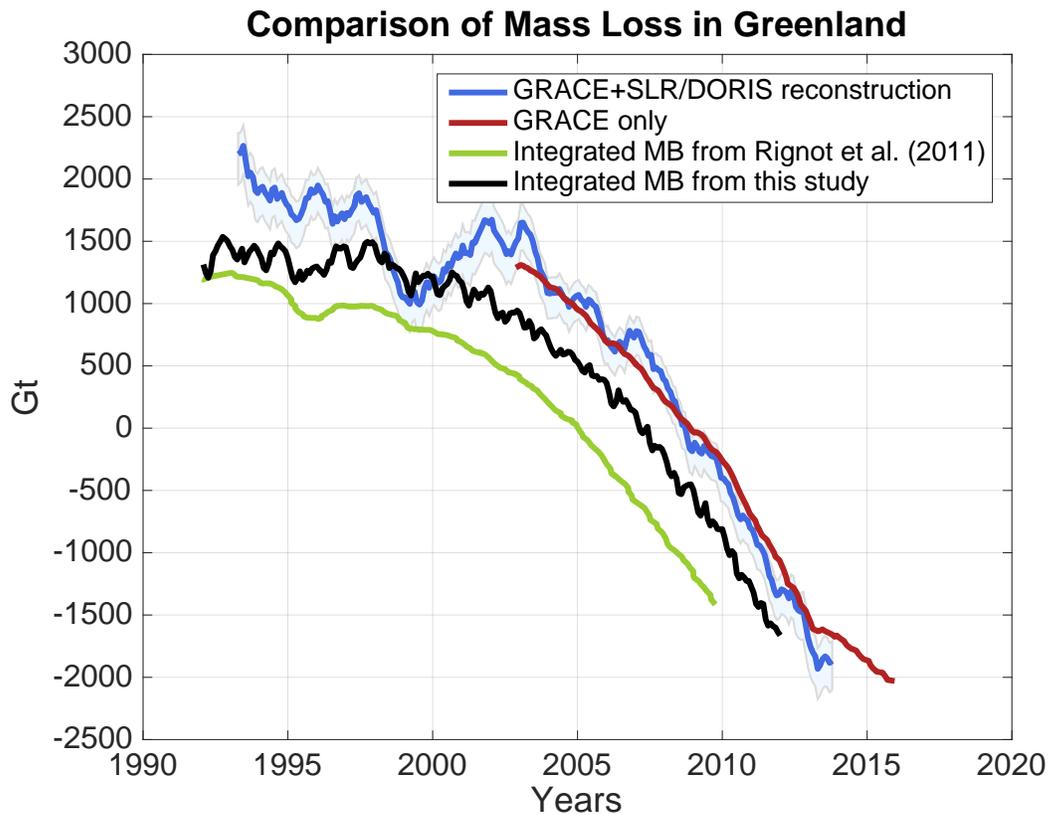
Figure 5.2: Change in Greenland ice sheet mass in Gt. The red curve denotes the mass change from GRACE and the blue curve denotes the mass change from the reconstruction (GRACE+SLR/DORIS). The light blue area shows the 1-σ uncertainty envelope. The green curve shows the integrated mass balance obtained from digitizing Figure 2a in *Rignot et al.* (2011) and the black curve the integrated mass balance obtained from this study. This study's mass balance used surface mass balance from *Noël et al.* (2015) and the ice discharge from *Enderlin et al.* (2014). The black and green curves are each shifted by 400 and 800 Gt to provide a less cluttered view.

5.5   Antarctica Mass Change

Figure 5.3 shows the different mass change curves for the Antarctic ice sheet.

Unlike the Greenland ice sheet, the behavior of the Antarctic ice sheet as a whole is heavily

influenced by interannual variations and counter-balancing regional effects (*van de Berg et al.*, 2006). Although previous analyses found acceleration of mass loss for the entire Antarctic ice sheet (*Velicogna*, 2009; *Rignot et al.*, 2011; *Shepherd et al.*, 2012), the reconstructed mass change suggests three distinct mass change regimes since 1993. Before 2000, the ice sheet lost mass at a rate of -56±28 Gt/yr before being in mass balance from approximately 2000 to 2005 as the ice sheet balance was 20±41 Gt/yr. After 2005, the ice sheet lost mass at almost twice the rate of the earlier mass loss rate of -103±20 Gt/yr. The error on the trend values are large, highlighting the uncertainties that stem from GIA trend errors (see Section 4.6.4).

The GRACE-only mass curve, represented as the red curve in Figure 5.3, is in excellent agreement with the reconstruction and well within its error envelope. The reconstruction are also compared against an IOM curve. The first IOM approach applied in Greenland that used ice discharge data and surface mass balance from atmospheric models (black curve in Figure 5.2) was not reproduced because the *Enderlin et al.* (2014) analysis was restricted to Greenland. Figure 2b from *Rignot et al.* (2011) was digitized to provide perspective prior to 2003. The large trend difference between the two curves is prohibitively large and remains unexplained. Potential explanations for this discrepancy will be explored as part of future work. On one hand, source of uncertainty in IOM include uncertainty in the SMB and uncertainty in discharge caused by bed elevation uncertainty (which can be on the order of tens to hundreds of meters) and/or location of the grounding line (which can influence discharge estimates) (*Enderlin et al.*, 2014). On the other hand, refinements of GIA models will continue to influence the trend of GRACE-based estimates.

The ensemble study from *Shepherd et al.* (2012) shows similar trend numbers to the reconstructions, even before 2003, despite the large error bars. Over the GRACE time frame, the comparisons of trends against other gravimetric analyses that use similar GIA models show strong agreement, as seen Table 5.1.
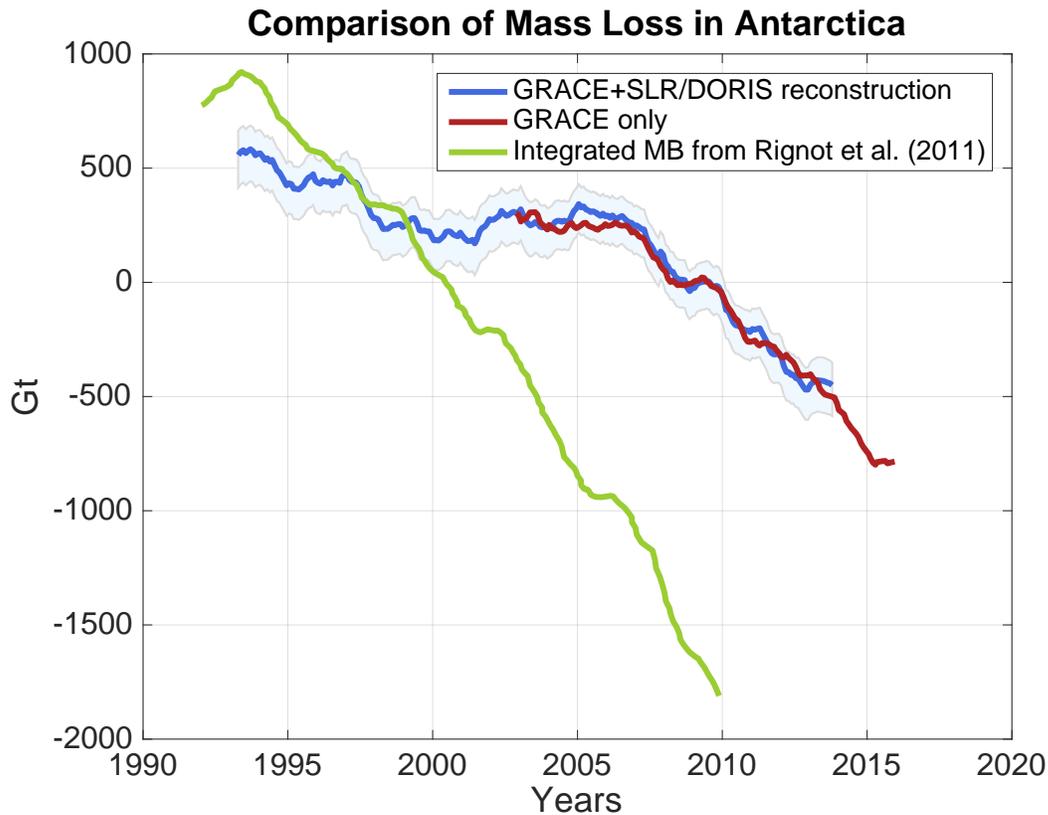
Figure 5.3: Change in Antarctic ice sheet mass in Gt. The red curve denotes the mass change from GRACE and the blue curve denotes the mass change from the reconstruction (GRACE+SLR/DORIS). The light blue area shows the 1-σ uncertainty envelope. The green curve shows the integrated mass balance obtained from digitizing Figure 2b in *Rignot et al.* (2011).

5.6   Summary

In this chapter, mass change curves over Greenland and Antarctica spanning April 1993 to November 2013 are generated from the reconstructed fields presented in Chapter 4. The additional

Table 5.1: Comparison of trend values for the Greenland and Antarctic ice sheet mass change curves over several time frames. The trend fit values are calculated from a least squares adjustment of the time series. The trend errors are the formal errors obtained from the covariance matrix of the linear regression. The 1-σ trend errors are the formal errors obtained from the covariance matrix from the reconstructed mass change curves in the column titled "G+SD" (meaning GRACE+SLR/DORIS). *Velicogna and Wahr* (2013) use GRACE RL05 gravimetry solutions and a combination of the global ICE-5G GIA model and the regional IJ05_R2 GIA model (*Ivins et al.*, 2013); [*personal communication with J. Wahr, 2014*] also uses GRACE CSR RL05 and ICE-6G (*Peltier et al.*, 2015); *Shepherd et al.* (2012) use an ensemble of methods (gravimetry, altimetry, etc.) and a combination of W12a (*Whitehouse et al.*, 2012b) and IJ05_R2 (*Ivins et al.*, 2013) as GIA models. See Section 5.4 for a description of the Input-Output Method results computed in this study.

Name	Timespan	Greenland Trend [Gt/yr]		Antarctica Trend [Gt/yr]	
		Study	Talpe et al. (G+SD)	Study	Talpe et al. (G+SD)
Velicogna et al. (2013)	01/2003 – 11/2012	-258 ± 41	-311 ± 24	-83 ± 49	-80 ± 32
Shepherd et al. (2012)	06/2005 – 12/2010	-263 ± 30	-311 ± 50	-87 ± 43	-98 ± 46
	01/1993 – 12/2011	-142 ± 49	-130 ± 22	-71 ± 53	-30 ± 33
	01/1993 – 12/2000	-51 ± 65	-129 ± 35	-48 ± 65	-54 ± 36
Wahr, John (pers. comm.)	10/2002 – 11/2013	-275 ± 9	-321 ± 22	-78 ± 29	-80 ± 31
Input-Output Method	01/1993 – 12/2011	-136 ± 11	-129 ± 26	-	-
	01/1993 – 12/2000	-27 ± 11	-129 ± 39	-	-
Talpe et al. (GRACE only)	10/2002 – 12/2013	-282 ± 29	-321 ± 22	-76 ± 29	-80 ± 31

decade prior to the GRACE period allows for further interpretation of their mass change behavior in time. The mass change of the Greenland ice sheet can be described by two periods of linear mass loss with the rate of mass loss about five times larger after 2005 than over the 1993 – 2005 time frame. The Antarctic ice sheet appears to have experienced no noticeable mass change in the early 2000s, while experiencing a mass loss rate prior to 2000 that is less than half of the mass loss rate of the late 2000s. However, the validation of the mass change curves is limited by the lack of glaciological data in the 1990s. Moreover, a comparison over the GRACE time frame shows robust agreement for Antarctica and some discrepancies for Greenland, which shows extraneous variability. This study would benefit from further cross-method comparisons. Instead of digitizing results from the IOM curves from *Rignot et al.* (2011), direct access to the data would enable more rigorous comparisons.

While Chapter 5 focused on the dominant, non-seasonal time-variable gravity signals, i.e., the cryosphere, Chapter 6 will explore the validity of the reconstructions for smaller signals.

Chapter 6

Partitioning the Global Water Budget

6.1   Overview

In this chapter, the quality of the reconstructed fields in the spatial domain is assessed. In particular, Section 6.2 addresses the following questions: how do the reconstructions fare in diverse geographical areas and river basins? How are the various errors due to the reconstruction method distributed? How does each mode contribute to regional time series? Section 6.3 leverages the knowledge gleaned from Section 6.2 to a hydrologic application. Indeed, *Reager et al.* (2016) show that the budget of terrestrial water storage (TWS) measured by GRACE has contributed 0.32±0.13 mm/yr to ongoing sea-level rise over the GRACE time frame, i.e., 2002–2014. Can the reconstructed global gravity fields confirm these observations and, furthermore, shed light on the behavior of TWS in the 1990s?

6.2   Regional Reconstructions

Time series of mass change spanning 1993 to 2013 are generated for a number of basins, as described in Section 6.2.1. Based on the information gathered by the regional kernels in Section 6.2.2, three aspects of the reconstructions are then discussed in order to further shed light on their effectiveness, validity, and limitations. First, the errors of the kernels are investigated in Section 6.2.3. Second, Section 6.2.4 assesses the contribution of each mode to the time series. Finally, in Section 6.2.5, the time series from the kernels presented above and additional kernels are compared quantitatively.

6.2.1   Approach

The data used are described in Chapter 3 and the technical approach in Chapter 4. The method used to determine mass change in a specific area follows *Swenson and Wahr* (2002) and the scale factor is determined according to Eqs. 3-4 in *Longuevergne et al.* (2010). Furthermore, the error budget for each area is defined similarly to Section 4.6, but one notable difference is that the lack of geophysical errors inherent to global gravity fields are not accounted for.

The regions selected for generating TWS time series are Africa, Europe, North America, South America, Asia, Australia, and Northern Canada. When combined, these regions represent the total TWS signal outside of Greenland and the Antarctic continent. The kernel outlines were drawn by following the coastlines and generally established land boundaries. The Northern Canada boundary was based on the mascon definition from GSFC (*Luthcke et al.*, 2013). The overlap between the regions is negligible. However, simplifications in creating those kernels led to differences with respect to the true area of the continents. For example, the Asia kernel contains the water mass surrounding Malaysia and Indonesia. Another example is the fact that the designed Africa kernel does not include Madagascar, which is acceptable because Madagascar is in near-hydrologic balance, i.e., it has a small negative trend of 4 Gt as seen on the CCAR mascon site[1] and its area is negligible compared to Africa. On the other hand, Iceland and other high-latitude islands were included in the Europe and Asia kernels because they undergo large interannual changes. While all these simplifications undoubtedly lead to errors in the final reconstructed mass curves, they are not considered significant compared to other errors sources that arise in the reconstruction method.

6.2.2   Resulting Time Series of Mass Change

The following seven figures depict (from left to right): the time series of mass change from the reconstructed, SLR/DORIS-based, and GRACE-based fields; the budget of the errors from the reconstruction process and its evolution in time; and the kernel map. The SLR/DORIS-based time series were included to assess their stand-alone effectiveness. Overall, these illustrations provide a

---

[1] ccar.colorado.edu/grace/

first qualitative overview of the comparisons, but a comprehensive comparison is beyond the scope
of this work.
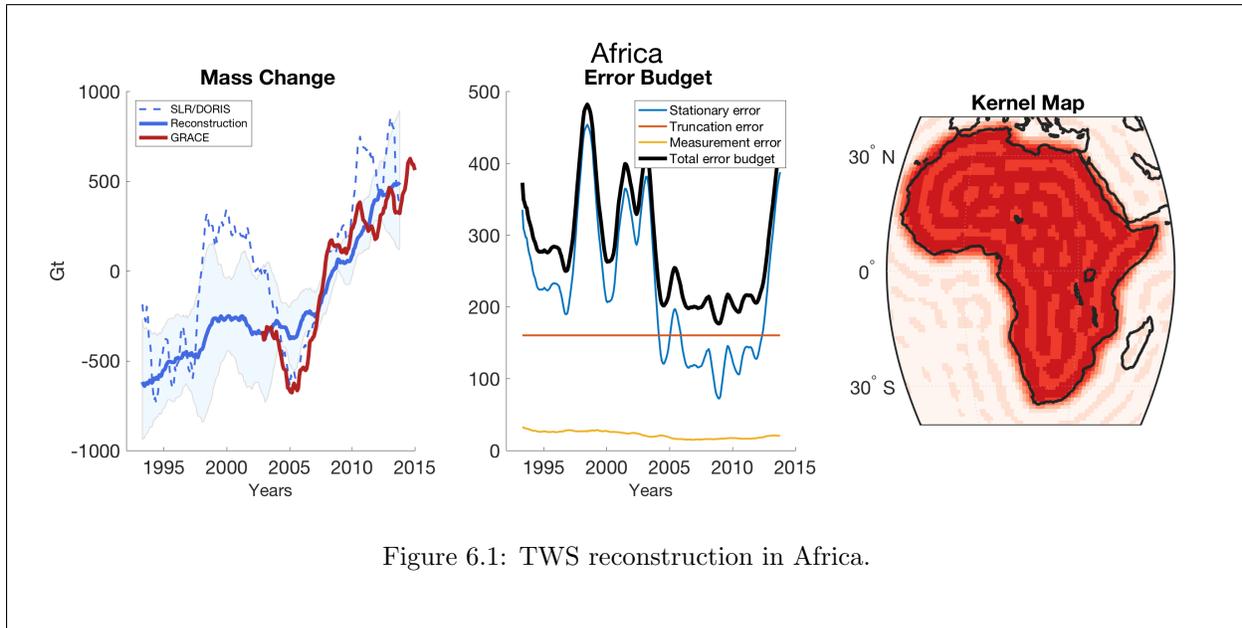
Figure 6.1: TWS reconstruction in Africa.

The African continent has acted as a water sink and has removed up to 1100 Gt of water
mass since 1993. The three time series show a steady increase in mass starting in 2005, but the
drop over 2004–2005 is not captured by the reconstruction. The measurement error is clearly the
smallest, while the truncation and stationarity assumption errors are each about 200 Gt.
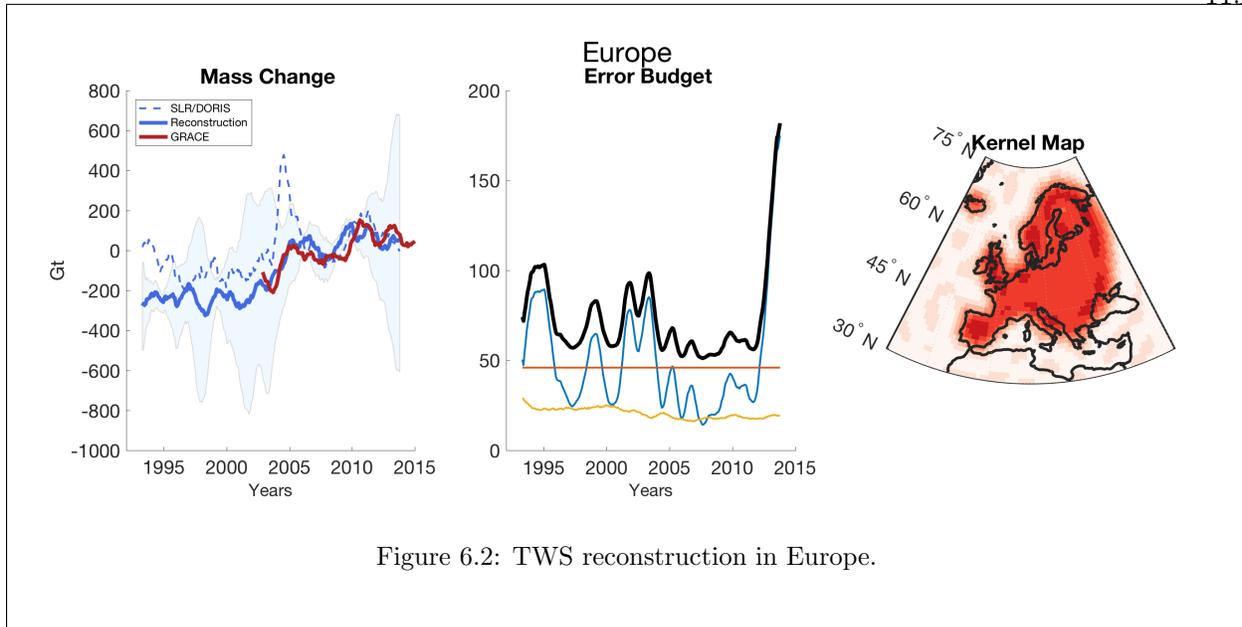
Figure 6.2: TWS reconstruction in Europe.

For the European continental mass, there is a very slight positive trend since 1993. The signal is small, reflecting the fact that Europe has not undergone significant hydrologic changes. Accordingly, the errors are small in magnitude (less than 100 Gt), although they still represent a large portion of the total signal. The spike at the end of the stationary assumption error is a reflection of the impact of the trend on the stationary assumption error determination. In other words, slight differences in trends result in large errors near the end of the time series (see Section 4.6.2). The SLR/DORIS time series shows a large peak around 2005.
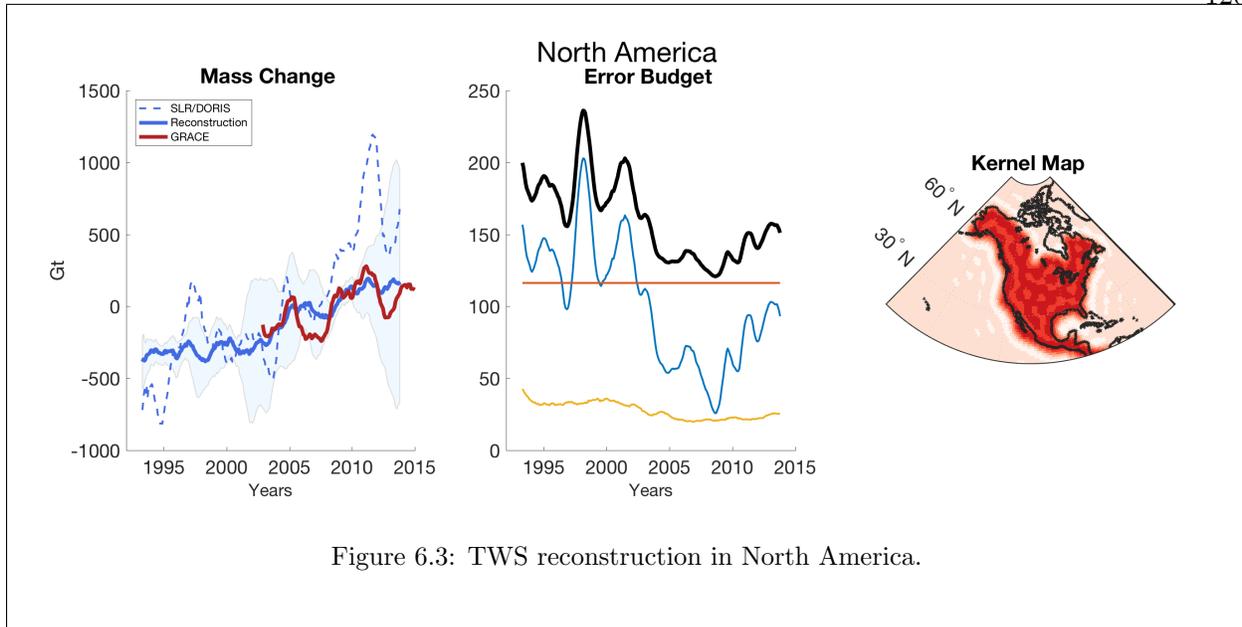
Figure 6.3: TWS reconstruction in North America.

The reconstruction also shows a slightly positive trend in mass from North America. Notably, the contribution from Alaskan glaciers is small and differs from the mascon solution from GSFC (*Luthcke et al.*, 2013). This discrepancy is presumably due to the limitations of the spherical harmonic method, because the coastal location of the Alaskan glaciers inhibits a clear inclusion in the kernel, even though the North America kernel was extended 300 km into the oceans. A peak-through-peak-through cycle over approximately ten years in 2005–2015 is well captured by GRACE, but only somewhat seen in the SLR/DORIS and the reconstructed time series. Just as in the case with Africa, the errors from the stationary assumption and truncation are approximately equivalent in magnitude, although the former has large temporal variations. The measurement error is smallest.
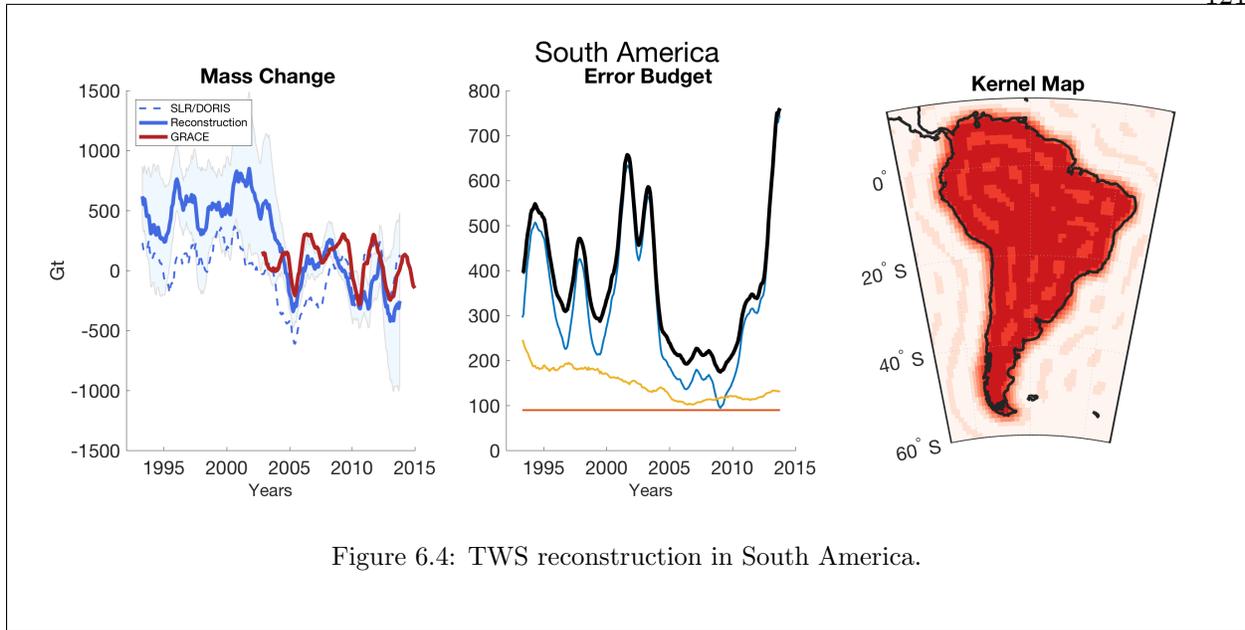
Figure 6.4: TWS reconstruction in South America.

The reconstructed and SLR/DORIS time series of mass change for South America are consistent in the 1990s and both show a 800 Gt drop over 2000–2004. Furthermore, the rebound in 2005 is seen clearly by all gravity solutions, while the drop-rebound in 2010 detected by GRACE is smoothened in the reconstructed time series, and not visible SLR/DORIS. Despite the presence of the Patagonian glaciers, which are losing mass, the trend of the South American mass curve is not significantly negative. The stationary assumption is the largest source of error, which is expected because there are remnant seasonal signals over South America, as seen in the modes in Figure 4.3.
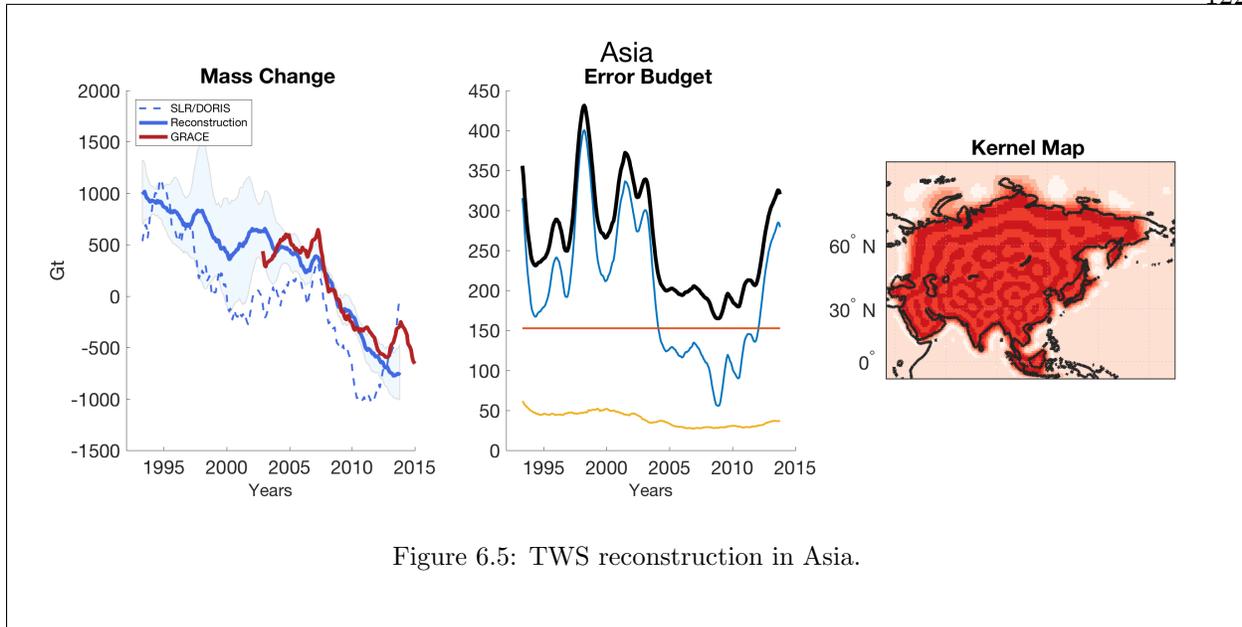
Figure 6.5: TWS reconstruction in Asia.

The behavior of TWS in Asia is dominated by consistent loss, mostly driven by the Himalayan glaciers and the depletion of aquifers in the Middle East (*Reager et al.*, 2016). A few distinct artifacts measured by GRACE, such as the rebound in 2014, are not visible in the two other time series. The errors show similar distribution as for North America and Africa: the measurement error is the smallest while the errors from the truncation and stationary assumption are approximately the same.
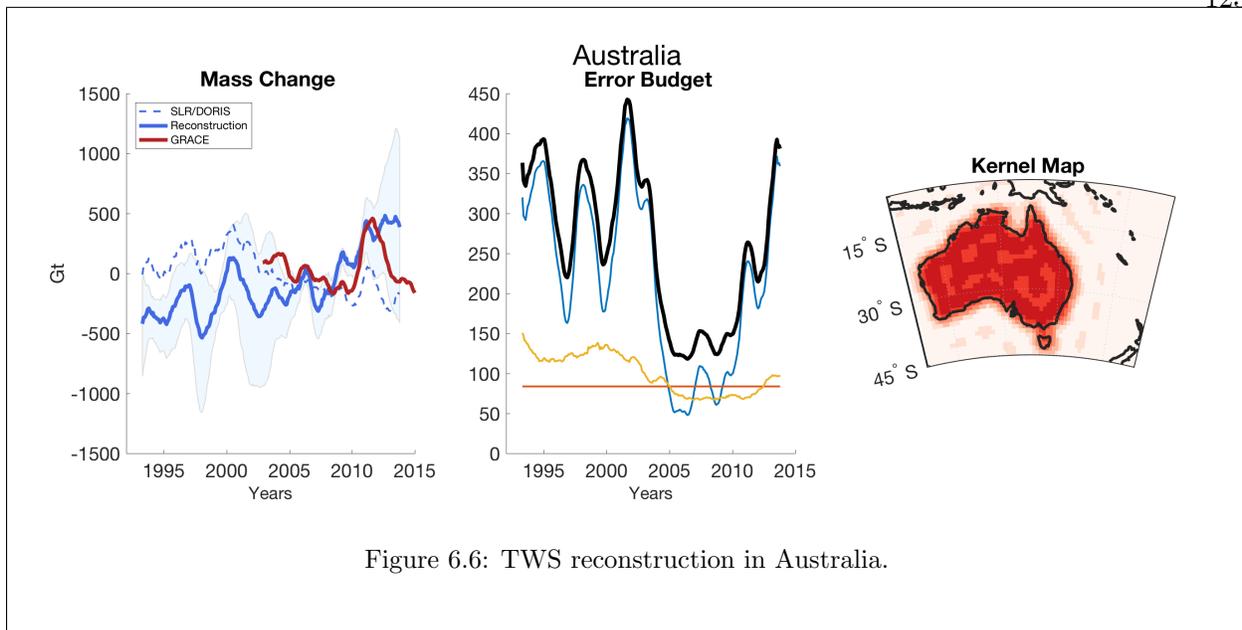
Figure 6.6: TWS reconstruction in Australia.

The reconstruction sees large interannual changes, particularly over 1996–2003, but does not properly capture the 2011 event. Meanwhile, the SLR/DORIS fields detect the 2011 event, but at a much smaller scale than GRACE. For Australia, the measurement error is almost on the same level as the stationary assumption error.
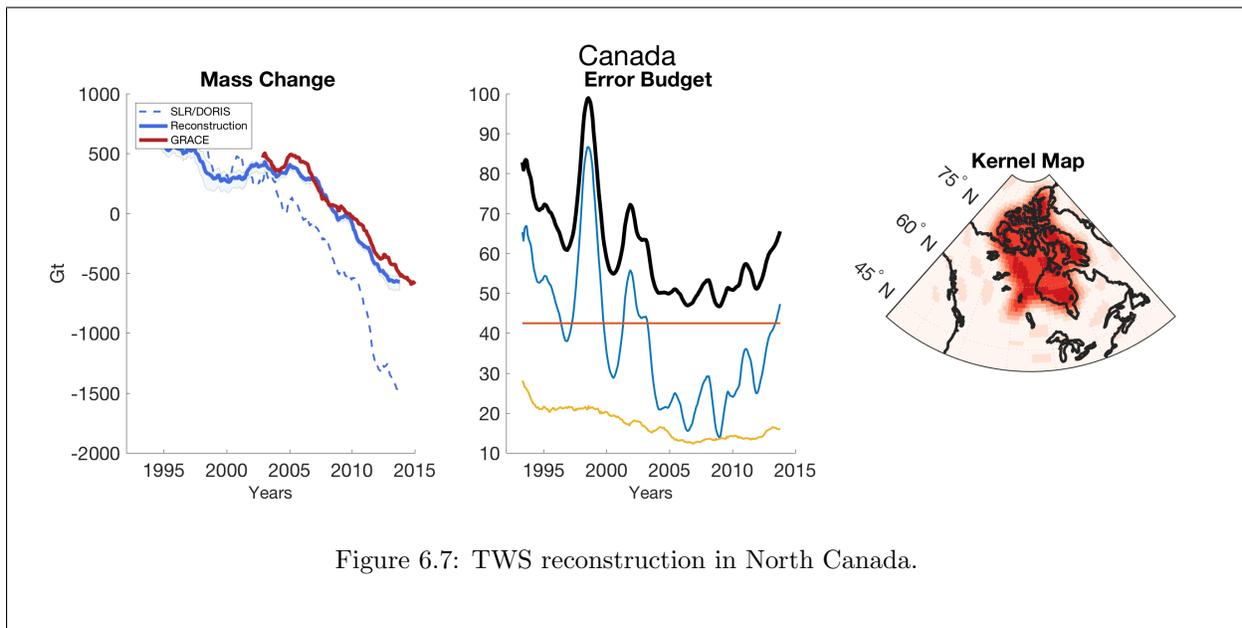
Figure 6.7: TWS reconstruction in North Canada.

Since 2005, North Canada and its archipelago have experienced large ice melts, which is

clearly visible in all time series. The SLR/DORIS and reconstructed fields match well, except that the latter has a larger trend. Despite the fact that the long-term behavior has evolved, the stationary assumption does not dominate the error budget. It is also worth noting that comparisons against the GSFC mascons (*Luthcke et al.*, 2013) yield strong agreement for all areas except for North America where the difference was traced back to the Alaska glaciers.

6.2.3   Error Distribution

In this section, three aspects of the regional reconstructions are examined.

First, the three different types of errors from the reconstruction method are examined to investigate their relative influence. In other words, this section addresses the question: Which errors are largest and why? Section 4.6 describes the design and meaning of each error source that is due to the reconstruction process, as opposed to the geophysical nature of the global gravity fields, e.g., ocean signal leakage. Table 6.1 summarizes the errors for each kernel.

Table 6.1: Partition of error budget by area. The mean and 1-σ variation are shown.

Kernel		Errors [Gt]		
Name	Area [10^6 km^2]	Measurement	Truncation	Stat. Assum.
South America	20	146 ± 33	89 ± 0	322 ± 155
North America	23	28 ± 6	116 ± 0	102 ± 42
Asia	57	39 ± 9	153 ± 0	200 ± 84
Europe	9	21 ± 3	46 ± 0	50 ± 30
Australia	9	100 ± 25	84 ± 0	219 ± 108
Africa	34	22 ± 5	160 ± 0	225 ± 97
Northern Canada	5	17 ± 4	42 ± 0	39 ± 17

First, the measurement error is due to the SLR/DORIS covariances. Their effect on the reconstruction is propagated linearly, as shown in Section 4.6.1. The mean magnitude of these errors is remarkably consistent for all areas as it remains around 20 Gt, except for Australia and South America, where it reaches 100 and 146 Gt, respectively. This is likely not due to any geophysically-meaningful reasons, but rather simply a consequence of the estimation process of SLR/DORIS-based coefficients. However, this discrepancy between Australia, South America, and

the other kernels is large enough that it could warrant a closer examination, including, for example, re-assessing these errors using the DGFI or AIUB solutions. Finally, the temporal evolution is high and reflects the time-variability of the nature of the SLR/DORIS constellation (see Section 3.3.2). The magnitude of the standard deviation is generally consistent across areas in that it weighs between 15 and 25% of the magnitude of the total error signal.

The truncation error stems from the fact that the GRACE fields are truncated when they are fit to the SLR/DORIS fields, as depicted in Figures 4.2 and 4.1 and described in Section 4.6.3. The magnitude of truncation error scales with the geographic isolation of a signal. South America, for instance, is much more isolated than North America, which is near large signal from the Canadian Archipelago and from Greenland. This consideration of isolation carries weight because of the truncation of the modes to fit the SLR/DORIS resolution.

Lastly, the stationary assumption error, which is related to the assumption that GRACE modes are valid over a longer time frame than the GRACE mission, is large over areas that have experienced variability not captured by the reconstruction. The magnitude of these errors are tied to large events found in the GRACE time series. As such, Africa (large drop in 2005), South America (many variations due to remnant seasonal signal), Asia, and Australia (La Niña event) have large stationary assumption errors. On the other hand, Northern Canada (consistent trend drop), Europe (little variation), and North America (regular variability) do not display the errors that can be traced back to this stationary mode assumption. Furthermore, the high standard deviations (40 to 60% of the original signal) highlight the temporal sensitivity of this assumption in comparison to the two other error sources.

6.2.4 Individual Mode Contribution

In previous sections, the errors have been investigated as a function of kernel. The next aspect to investigate is the contribution of each mode to the reconstructed mass change time series. Table 6.2 summarizes the metric selected to quantify contribution: the RMS of each mode's time series with respect to the total time series. It is worth noting that the summation of the RMS

contributions per mode does not add to 100% because of the existing correlations between modes. These correlations arise from the correlations between SLR/DORIS coefficients. Appendix C contains the illustrations of the four EOFs for each kernel. As expected, areas that are mostly driven

Table 6.2: Contribution of each mode by area. The contribution is measured by the RMS of the time series of a mode with respect to the RMS of the total curve.

Name	Mode 1	Mode 2	Mode 3	Mode 4	Total
South America	89.8	3.4	0.1	1.4	94.7
North America	30.9	41.1	67.6	18.7	158.2
Asia	48.0	6.1	35.5	23.4	113.0
Europe	77.7	11.3	6.2	29.0	124.2
Australia	39.6	14.7	55.5	17.4	127.2
Africa	18.8	32.0	24.0	90.6	165.4
Northern Canada	80.7	7.2	12.4	1.7	102.1

by trends, i.e., Asia, North Canada, Africa, have large contributions from mode 1, i.e., over 75%, while other modes never weigh more than 20%. Other areas are better balanced, i.e., Europe, North America, South America, and Australia. But Africa and Australia also show extremely high total contributions of over 150%. It is evident that correlations are problematic for these two areas. Indeed, this dependency means that the behavior of all these areas is driven by similar temporal behavior, which is not a physically reasonable assumption – the African continent does not gain water mass at similar rates as Greenland melts. This raises the possibility of using trend-free EOFs, i.e., a reconstruction approach that first removes the trends from each Stokes coefficient. As such, the emphasis is set on the interannual events rather than the trend behavior.

6.2.5   Quantitative Comparisons

After the assessment of the error distribution and contribution from each mode, the section is concerned with extending comparisons to further basins and the quality of the reconstructions versus signals from only the SLR/DORIS solutions is examined. The river basins chosen are the Upper Mississippi, the Indus, the Yangtze, the Nile, and the Niger. Furthermore, the Sahara, Gulf of Alaska, Black Sea, Zaire, are added with the kernels from the previous sections.

Figure 6.8: Map of river basins.
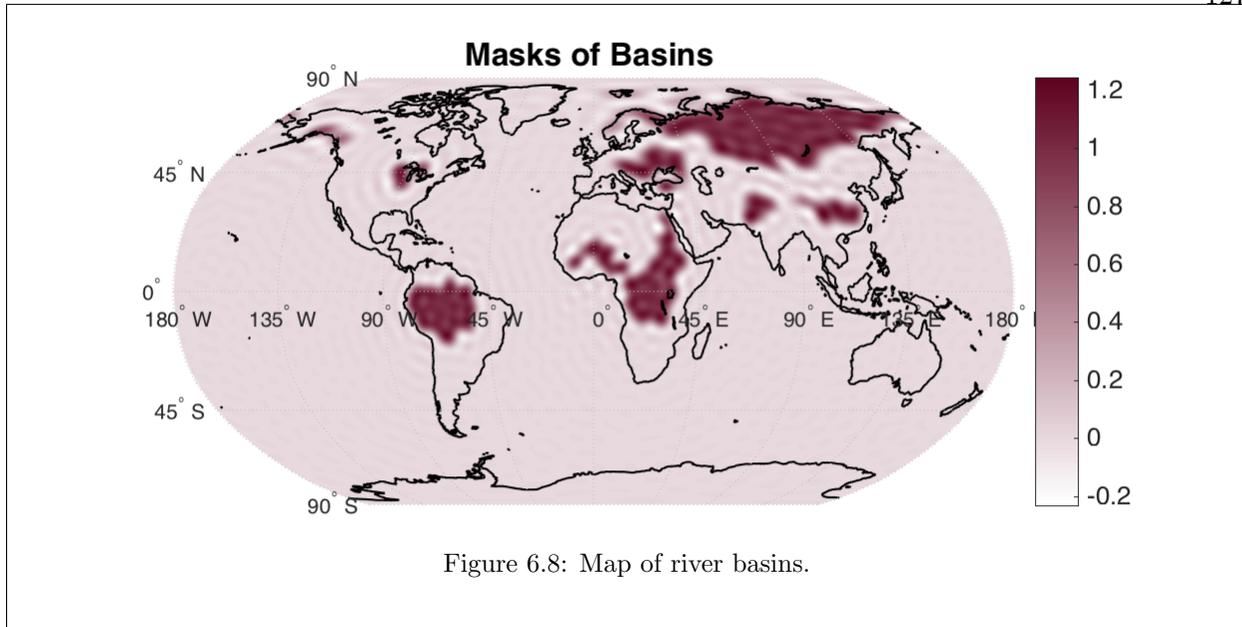
Figure 6.9 shows the metrics while Figure 6.10 illustrates which solution is most effective in matching GRACE as a function of basin. The interannual comparisons rely on a Pearson correlation coefficient, while the trend comparisons rely on the values of a linear regression applied to the time series. It is important to note that occasionally, neither the reconstruction nor the SLR/DORIS time series can be considered valid.

On one hand, a black color-code signals that the SLR/DORIS time series is the only valid comparison, while a blue color-code signals that the reconstruction is the only valid comparison. On the other hand, red or green depicts that neither time series is valid or both are, respectively. Furthermore, the plots sort the results as a function of either the magnitude of the basin signal (top) or the size of the basin (bottom). It is expected that the largest basins, either in size or signal magnitude, would yield better comparisons because the reconstructed fields are inherently most effective with larger basins. Smaller basins, both in size and magnitude, would be expected to match the least well because the reconstruction process tends to overlook small signals in the fitting process. These expectations are met: the largest basins in size and signal tend to compare best. Furthermore, capturing the trend is not as well done as the interannual signal, which suggests that basin trends are easily disrupted compared to GRACE. Naturally, it is possible that the choice
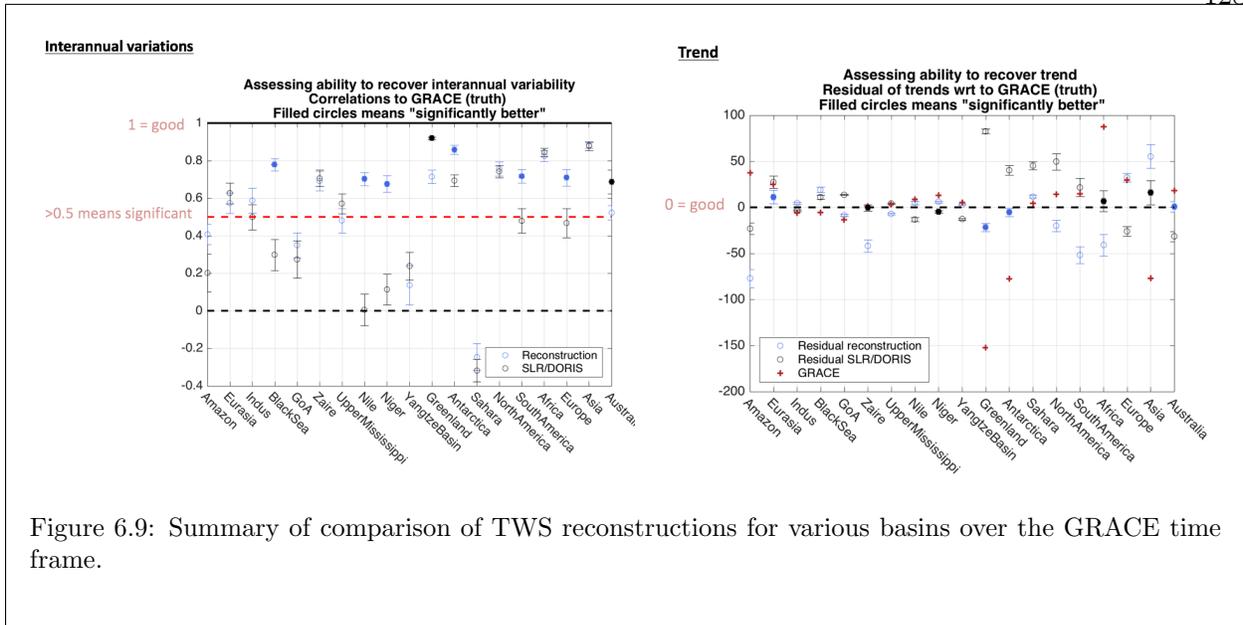
Figure 6.9: Summary of comparison of TWS reconstructions for various basins over the GRACE time frame.

of metric could be improved upon.
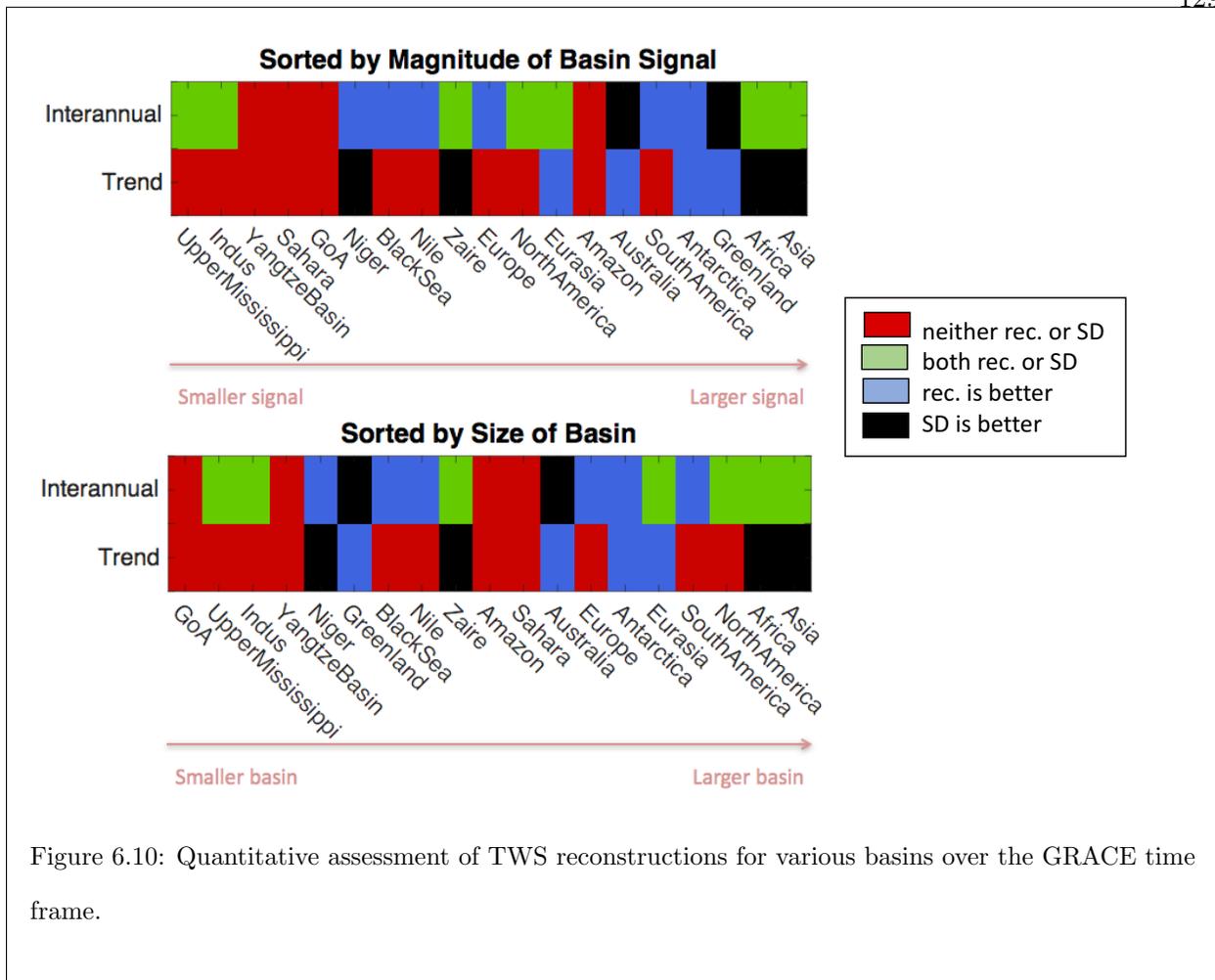
Figure 6.10: Quantitative assessment of TWS reconstructions for various basins over the GRACE time frame.

6.3 Terrestrial Water Storage

Section 6.2 provided perspective on the reconstruction of regional mass curves. This section is concerned with (1) the validity of these fields against an existing hydrologic model and (2) their applicability to a study relating global TWS to sea level.

6.3.1 Comparison Against Global Hydrologic Model

The individual time series presented in Section 6.2.2 are compared to the Global Land Data Assimilation System Version 2 hydrologic model (GLDAS-2) (*Rodell et al.*, 2004). The aim of GLDAS-2 is to provide estimates of water distribution that are not observable globally, such as soil moisture. GLDAS-2 uses the NOAH land surface model (LSM) (*Chen et al.*, 1996) and is

constrained by meteorological forcing fields, e.g., near-surface air temperature, surface pressure, etc., which are based on ground- and space-based observations. The outputs that are relevant for comparisons with GRACE are the summation of the signals from precipitation (rainfall and snowfall), water mass from the canopy, snow layers, and soil moisture up to 2 m. This means that the whole water column cannot be fully represented, because NOAH lacks the water mass below 2 m, i.e., ground water table. Specifically, GLDAS-2.0 is used in this comparison. GLDAS-2.0 differs from GLDAS-2.1 in that it is forced entirely by one consistent meteorological forcing field (*Sheffield et al.*, 2006), while GLDAS-2.1 is constrained by a mix of fields and observations. This difference renders GLDAS-2.0 more climatologically consistent, which enables it to run from 1948 to 2011, while GLDAS-2.1 only starts in 2000 but is delivered consistently and without interruptions on a monthly basis. The primary advantage of GLDAS-2.0 is its ability to study long-term changes, while GLDAS-2.1 hinges on more data assimilation. GLDAS-2.0 also suffers from the limitation of the LSM model, namely, its inability to detect and model hydrological signals at the higher latitudes, for example. GLDAS-2.0 is provided as a grid of spatial resolution 1 degree ($\approx$100 km). Other models exist, such as the publicly available WaterGAP Global Hydrology Model (WGHM), (*Döll et al.*, 2003), but this study was limited to comparison against GLDAS-2.0.

The GLDAS time series are also de-seasoned in similar fashion as the gravimetry reconstructions. The comparisons are shown in Figure 6.11.
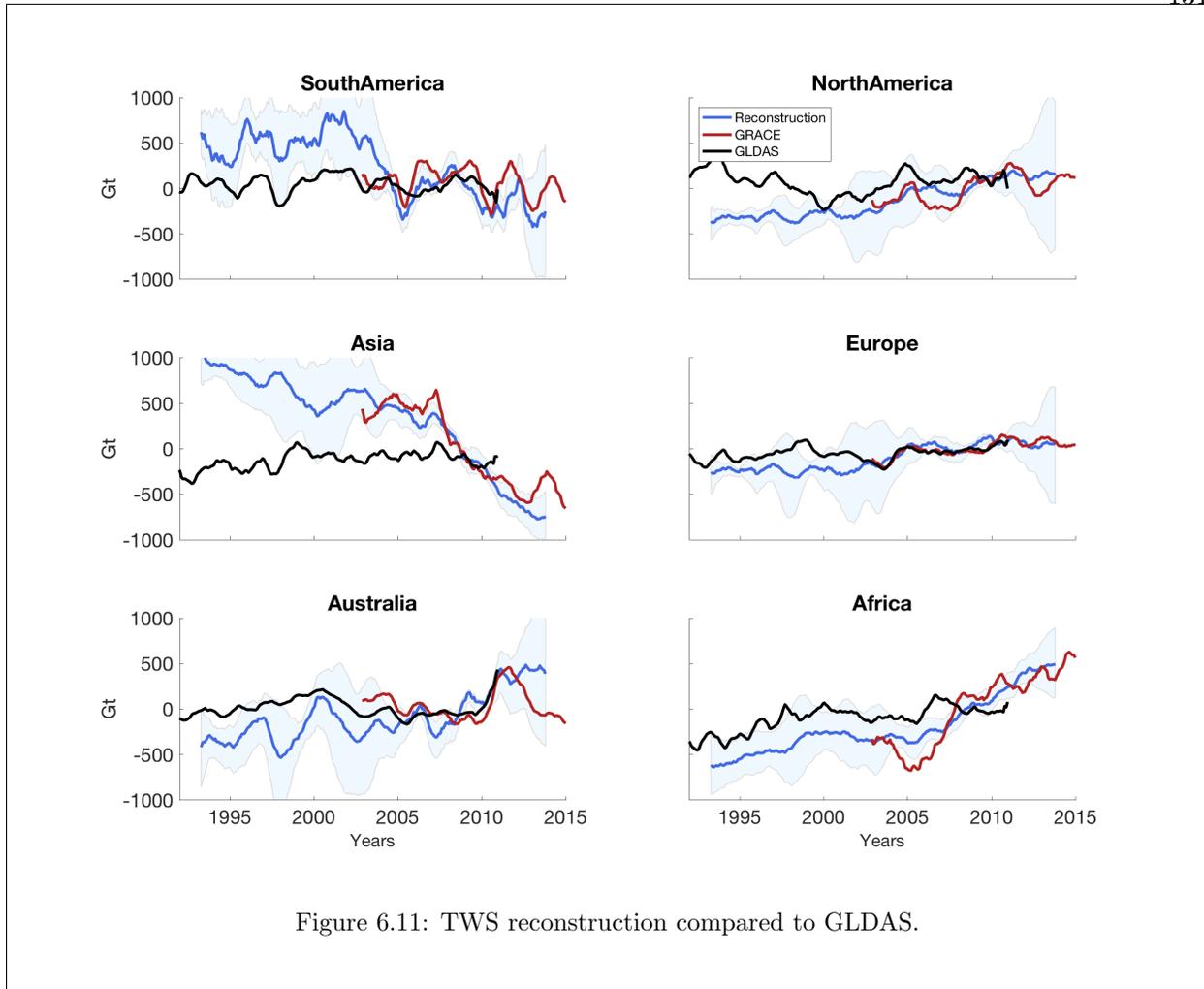
Figure 6.11: TWS reconstruction compared to GLDAS.

The time series of mass change for South America are remarkably consistent in the 1990s, but GLDAS differs in the 2000s and does not capture the large drop in 2002–2005. In North America, however, the 2003–2009 interval shows agreement between GRACE and GLDAS, but GLDAS has a trend before 2000 that is not well captured by the reconstructions. In Asia, the melt of Himalayan glaciers, drying of the Caspian sea and aquifers in the Middle East all induce a large negative trend that is invisible to GLDAS. The comparison in Europe is excellent against GRACE, but not before 2004. This is also the case in Australia, i.e., the reconstructed time series contains large signals over 1995–2000 that are not visible to GLDAS, but comparison over GRACE is strong. Finally, the opposite occurs with the time series of mass change in Africa: GLDAS has an excellent agreement with the reconstruction before 2007 but diverges after. In summary, the long-wavelength and trend

comparisons of GLDAS are worst in areas with high mass loss – South America, North America, and Asia. Furthermore, GLDAS does not necessarily match more with GRACE than with the reconstructions.

6.3.2 How Has Terrestrial Water Storage Contributed to Sea Level Rise?

Terrestrial water storage (TWS) reflects the amount of water stored on continents as part of the global water cycle. Every season, up to 6,000 Gt of water are exchanged between the land, the atmosphere, and bodies of water (*Reager et al.*, 2016). In a perfectly stable global water cycle, long-term trends are inexistent. However, two observations suggest that water is being added to the oceans: (1) the sea level has steadily been rising and (2) the thermal expansion due to increased heat content alone does not explain the full sea level rise (*Chambers and Bonin*, 2012; *Church et al.*, 2013; *Hamlington et al.*, 2011). The mass of water is therefore changing; GRACE measurements allow for the detection of the sources of additional water. For example, it is well established that the melt of the Greenland and Antarctic ice sheets contribute to this seal level rise. But the sea level budget is still not closed, meaning that the remaining portion must be changes in TWS.

Reager et al. (2016) measure this TWS contribution to be 0.32±0.13 mm/yr and further categorize TWS in three components: (1) land glaciers, (2) human-driven TWS, and (3) climate-driven TWS. First, land glaciers simply represent mass change from ice melt from non-polar ice sheets and can be measured directly with GRACE. Second, human-driven TWS reflects changes due to impoundment of water in reservoirs, deforestation, irrigation, extraction of groundwater, etc., and is estimated via models such as AR5 of the IPCC (*Church et al.*, 2013). Lastly, climate-driven TWS therefore represents the last component, i.e., land-based changes minus land glaciers and human-driven TWS. *Reager et al.* (2016) note that changes in climate-driven terrestrial water storage have slowed down the ongoing rise of sea level over the GRACE time period by up to 0.70±0.21 mm/yr.

With these components in mind, the aim of this study is to determine the contribution of the full TWS signal (i.e., the summation of land glaciers, human-driven TWS, and climate-driven

TWS) to sea level rise in the 1990s. Indeed, there are two limitations to further categorizing TWS over the 1990s in three different components. First, the reconstructed fields are not expected to be able to disaggregate land glaciers from human- or climate-driven TWS because of limited spatial resolution compared to GRACE. Second, the human-driven TWS changes determined from models are not necessarily readily available before the GRACE time period, so calculating climate-driven TWS would be difficult. In this section, the focus is therefore on (1) the temporal behavior of the total TWS and (2) trends over 1993–2003 and 2003–2013.

First, the contributions from all continents are added together to illustrate total land water storage contribution to global mean sea level and shown in Figure 6.12. There are two important distinctions to be made about these time series as compared to mass change curves that have been shown previously:

1. the sign of the time series is negative because it represents a mass contribution to the ocean.

2. the value of mass change in Gt is converted to mm of sea level by dividing the time series by 360, since there are approximately 360 Gt of ice for every mm of global sea level change.

Figure 6.12: TWS reconstruction from non-polar ice sheet land mass.
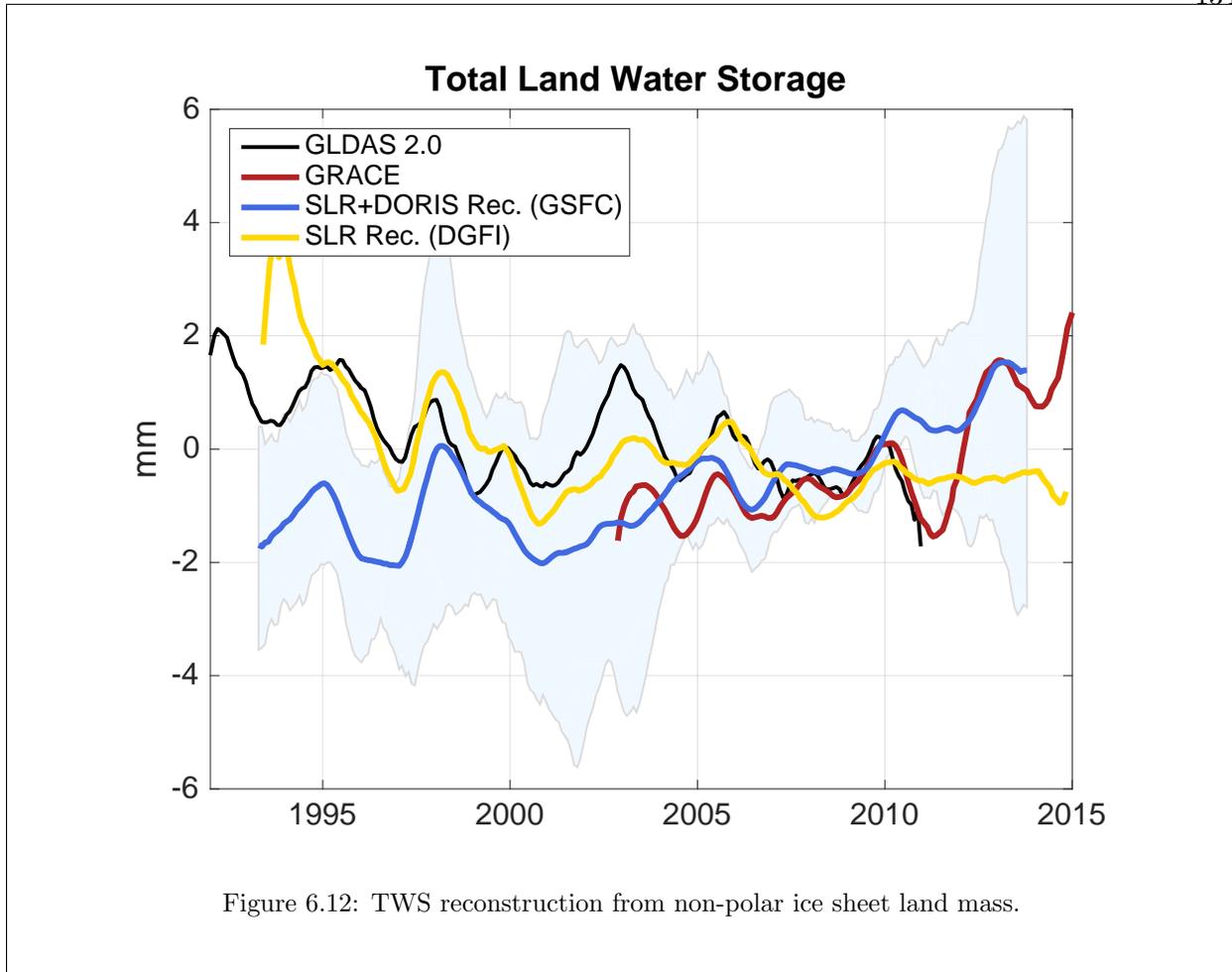
In addition to the GSFC-based reconstructed time series, the figure also shows the DGFI-based reconstruction. Overall, the GLDAS curve shows similar variability but does not have a positive trend because it excludes glaciers and the Canadian archipelago. Both reconstructions also fail to capture the Australian event of 2011, but also show similar behavior to the GSFC solution, except for a trend difference in the 1990s. The comparison against GRACE is otherwise fair and better with the GSFC reconstruction.

Table 6.3 shows the trends of the time series over varying periods. The first two columns display the trend from the reconstructed time series while the last column show GRACE-based estimates. The trend value comes from a least-squares fit and the associated error is the formal error of the covariance from the fit. As mentioned in the previous section, the error budget only reflects the uncertainties from the reconstruction method and does not include geophysical errors

that are inherent to global gravity fields, so the total error budget is lower than it should be. On

Table 6.3: Trend of contribution to sea level from each area. The units are mm/yr. Two different time frames, including one over GRACE, are chosen to highlight any difference before the GRACE mission. The uncertainties are artificially low because the error budget only accounts for uncertainties in the reconstruction process.

Name	Rec. $1993 - 2003$	Rec. $2003 - 2013$	GRACE $2003 - 2013$
South America	-0.15 ± 0.04	0.15 ± 0.05	0.01 ± 0.03
North America	-0.17 ± 0.02	-0.01 ± 0.02	-0.10 ± 0.02
Asia	0.40 ± 0.03	0.29 ± 0.04	0.34 ± 0.03
Europe	-0.01 ± 0.01	-0.03 ± 0.01	-0.06 ± 0.01
Australia	-0.03 ± 0.03	-0.22 ± 0.03	-0.04 ± 0.03
Africa	-0.35 ± 0.04	-0.32 ± 0.04	-0.32 ± 0.03
Northern Canada	0.13 ± 0.02	0.29 ± 0.02	0.26 ± 0.01
Total non-ice sheet	-0.18 ± 0.08	0.14 ± 0.08	0.09 ± 0.06
Greenland	0.33 ± 0.04	0.81 ± 0.03	0.71 ± 0.02
Antarctica	0.10 ± 0.01	0.22 ± 0.01	0.19 ± 0.01
Total ice sheet	0.43 ± 0.04	1.03 ± 0.03	0.90 ± 0.02

one hand, during the GRACE interval, the areas of high positive sea level contribution over the GRACE time period are Asia, South America, and Northern Canada, which is expected because of the loss of mass in land glaciers. But the North American continent, which also possesses significant glaciers in Alaska, does not show mass loss with the reconstructed time series. On the other hand, the African and Australian continents have contributed negatively to sea level according to the reconstructions. As pointed out previously, the reconstruction does not adequately capture the 2011 event in Australia, which was ultimately a one-time event instead of a trend.

Most relevantly, the most significant changes between the two decades for the reconstructed time series is in South America, which reversed its contribution by 0.30 mm/yr: from absorbing up to 0.15 mm/yr over 1993–2013 to contributing 0.15 mm/yr. North America and Northern Canada have both also contributed an additional 0.16 mm/yr over 2003–2013 compared to the decade before.

The two ice sheets both show a large increase in sea level contribution over the GRACE time frame. Chapter 5 concerns itself exclusively with this effect, and it was shown that the Greenland time series is slightly steeper as compared to the GRACE presumably because mode 1 contained

signal from the Canadian Archipelago and because of the C_{21} and S_{21} correction. It is evident that the computed trend from the ice sheets is smaller than the truth trend. The lack of geocenter terms explains most of the discrepancy, because degree-1 terms will contribute up to 0.20 mm/yr to sea level.

In summary, the reconstructed time series show that the ice sheets have increased in their contribution to the rise in sea level between the first and second decade of 1993–2013. However, while the TWS also appears to have contributed in the second decade by 0.14 ± 0.08 mm/yr (compared to 0.09±0.06 mm/yr using GRACE time series), during the first decade the contribution was -0.18±0.08 mm/yr. As such, this may indicate that TWS cycle undergoes significant interannual changes over two decades, unlike the polar ice sheets, which contribute in a consistent manner to sea level rise.

6.4   Summary

This chapter sought to assess the spatial quality of the reconstructions by first examining regional time series of mass change and then determining their contribution to sea level rise over two decades.

First, Section 6.2 illustrated the reconstructed time series of mass change for various continental basins. The error budget that arises from the reconstruction method is also analyzed, along with its evolution in time. In particular, it is shown that the measurement error is largest in areas where the SLR/DORIS covariances have the most significant errors, the truncation error scales with the geographic isolation of the basin and is constant, and, lastly, the stationary assumption error is largest over areas that contain variability not captured by the reconstruction. Furthermore, in areas with high trends, namely Africa, North America, and Asia, mode 1 is the dominant contribution, while other areas, such as Europe and South America, have a more balanced distribution of modes.

Second, Section 6.3 assessed the regional reconstructed time series in the context of hydrology. Indeed, the use of hydrologic models allows for validation of the fields in the 1990s, when GRACE-

only estimates (considered to be "truth") did not exist. However, the global hydrologic model used was GLDAS-2.0 and was limited in its ability to capture time-variable record of hydrology for several reasons, including the fact that it contains little data at high latitudes and does not see changes in the full water column (i.e., not below 2 m). Despite the limitations, some areas are shown to compare better, especially in areas with high data quality and low trend, e.g, Europe. Finally, an analysis of the trends of the reconstructed time series indicate that TWS has contributed positively to sea level rise since 2003, but negatively over 1993–2003, suggesting interdecadal variability. This finding is unique in that hydrologic models such as GLDAS-2.0 are not able to measure the entire water table and, hence, arrive to such findings.

To address the lack of proper validation data before GRACE, altimetry products over inland seas, such as the Caspian or Black sea, could serve as comparisons. Furthermore, a significant limitation is the lack of degree-one coefficients, which reflect the offset between the Earth's center-of-figure and center-of-mass. Using estimates from *Swenson et al.* (2008) show that the geocenter coefficients alone influence trends by up to 0.20 mm/yr. However, there is no public record of geocenter coefficients in the longer-term reconstruction and adding coefficients from separate analyses is technically invalid. Another potential source of improvement is a better definitions of the kernels. Lastly, the error budget could be ameliorated by incorporating geophysical errors and exploring the use of an ensemble SLR solution to better constrain errors.

Chapters 5 and 6 presented scientific applications of the reconstructions based on continuous GRACE-like data. But gaps in such high-resolution fields are likely to exist in the near future because the GRACE mission will end before the launch of GRACE Follow-On. As such, Chapter 7 examines the influence of such gaps.

Chapter 7

Detecting Meaningful Signals over Short Gaps

7.1   Overview

In this chapter, a second application of the reconstruction method presented in Chapter 4 is presented. Namely, the influence of gaps in a time series of GRACE-like data on the reconstructed fields is assessed. In particular, one real-life application is examined: the upcoming multi-month gap between GRACE and its successor mission, GRACE Follow-On (GFO). As such, this work seeks to determine the effectiveness of capturing meaningful data when GRACE data are not available by simulating gaps in GRACE data and recreating the reconstruction methods with the full set of time-variable gravity solutions from SLR/DORIS. In other words, can the reconstructed fields be used as a proxy over this GRACE – GFO gap?

Section 7.2 reviews previous work seeking to address the bridging-the-gap problem. In Section 7.3, the setup of the simulations, i.e., the gaps and the approaches, is presented. The effects of the gaps and approaches on the global reconstructions are analyzed. The resulting global gravity fields are shown in Section 7.4. Specifically, their ability in capturing trends and interannual effects are assessed, and reconstructions over Greenland and trend-free reconstructions over Australia are shown. Finally, in Section 7.5, the effectiveness of this technique in bridging the gap is discussed, along with the general advantages and weaknesses of these reconstructed gravity fields.

7.2   Background: The Upcoming GRACE – GRACE Follow-On Gap

As of December 2016, the GRACE mission is expected to come to an end in June or July 2017 after more than 15 years of operations (*Webb et al.*, 2016). While battery issues have long limited the efficacy of the GRACE mission, its end will most likely occur when the two satellites disintegrate as they enter the denser portions of the atmosphere. As of September 2016, the altitude of the GRACE satellites was approximately 350 km and decreasing by about 94 m per day (*Witkowski and Massman*, October 5 - 7, 2016).

Its successor mission, GRACE Follow-On (GFO), is slated to launch on a SpaceX Falcon-9 rocket from Vandenberg Air Force Base, California sometime between December 2017 and February 2018 (*Tapley et al.*, October 5 - 7, 2016). The gap in high-resolution time-variable gravity is therefore expected to last at least eight months, and perhaps much longer depending on the launch schedule.

Many geophysical disciplines rely on the continuous record of time-variable gravity products (see Section 1.5) and would, therefore, be hindered by a gap between GRACE and GFO. A number of studies have shown that meaningful gravity signals can be captured from the inversion of conventional tracking data of satellites. The conventional tracking data in *Matsuo et al.* (2013) comes from Satellite Laser Ranging (SLR) spanning 1993 to 2013. Furthermore, *Weigelt et al.* (2013) use high-low satellite-to-satellite (hl-SST) tracking data, whereby the Challenging Minisatellite Payload (CHAMP) mission is tracked using its Global Positioning System (GPS) receivers. *Baur* (2013) validates these time-variable gravity fields by comparing the mass change over the Greenland ice sheet against GRACE results. While the CHAMP mission came to an end in September 2010 and could therefore not cover the GRACE – GFO gap, this approach successfully illustrates the possibility of using hl-SST to assess surface mass changes independently of GRACE. In another study, *Encarnacao et al.* (2016) employed GPS tracking of the three-satellite Swarm mission. Independent precise orbit determination (POD) solutions from three processing centers (Astronomisches Institut – Universität Bern (AIUB) in Bern, Switzerland; Astronomical Institute in the Czech Re-

public (*Bezděk et al.*, October 5-7, 2016); Institute of Geodesy in Graz, Austria) were combined to generate a single, global gravity field up to degree and order 12 ($\approx$1,700 km spatial resolution). This averaging ensured that weaknesses from individual solutions and their respective approaches in POD (celestial mechanics, acceleration, and short-arc, respectively) were reduced. A direct comparison with GRACE K-Band Ranging results showed a difference of 2-4 mm in geoid height over ten months. All in all, conventional tracking data of satellites has been shown to deliver meaningful gravity results, but are significantly lower in resolution than the GRACE fields.

Instead of using satellite tracking data, *Peralta-Ferriz et al.* (2016) exploited complementary ocean bottom pressure (OBP) data. As such, they focused on reconstructions of OBP in the Arctic Ocean in the absence of GRACE. They show that two predictors (North Pole OBP and wind-OBP) are able to explain 50% of the total variance of the Arctic OBP seen from GRACE. But this approach does not resolve global changes in time-variable gravity.

To overcome these limitations, this study utilizes the enhancement of global fields from conventional tracking data by including GRACE information. As such, the reconstructed global gravity fields contain high-resolution spatial patterns from GRACE (resolution of $\approx$330 km) instead of only relying on coarse ($\approx$3000 $-$ 4000 km resolution) fields. In summary, this approach relies on projecting high-resolution patterns from GRACE onto longer time series of global time-variable gravity. Therefore, this approach can also investigate the influence of gaps.

7.3   Framework of Simulations

This study entails applying the reconstruction method from Chapter 4 in order to combine (1) a number of simulated GRACE fields and (2) the original SLR/DORIS fields described in Chapter 3. Section 7.3.1 describes the reconstruction approach. Section 7.3.2 discusses how the gaps are designed and the influence of the design decisions.

7.3.1   Reconstruction Approaches

Two approaches for the reconstructions are pursued. The first approach retains the trend of the GRACE and SLR/DORIS fields and is therefore exactly the same approach as presented in Chapter 4. The second approach removes the trend from each Stokes coefficient before the reconstruction process. This trend-free approach mitigates the primary problem of the first approach, in which the first spatial EOF mode captures nearly 70% of the original variance because the trend is the largest signal. The second approach consequently yields a set of modes that are well balanced and allow the expression of several modes in the final reconstructed fields, instead of one dominant mode as seen in the first approach.

The data are fundamentally the same, except when the trend is removed in the second approach. Furthermore, it is worth noting that it is assumed that the content of the time-variable gravity information from GRACE and GFO is the same. Hence, any potential systematic difference between GRACE and GFO, such as different instrument calibrations, for instance, are not taken into account. The error from this assumption is assumed to be negligible.

7.3.2   Gap-building Approaches

A GRACE – GFO gap is simulated by (1) removing consecutive months in the original GRACE record, (2) defining the first leg of the original GRACE record as "full GRACE" data, and (3) defining the second leg of the original GRACE record as the "GFO" data. Step (1) involves removing consecutive months from the original GRACE record. The choice of length and center point of such gaps is justified in the following paragraph. In other words, are the modes obtained from GRACE data with a gap influenced by (1) when the gap occurs or (2) how long should the gap be?

Figure 7.1 illustrates how the length of a gap influences the modes. This influence is quantified by correlating the new EOFs derived from GRACE fields with a gap against EOFs derived from GRACE fields without a gap, i.e., the "truth."
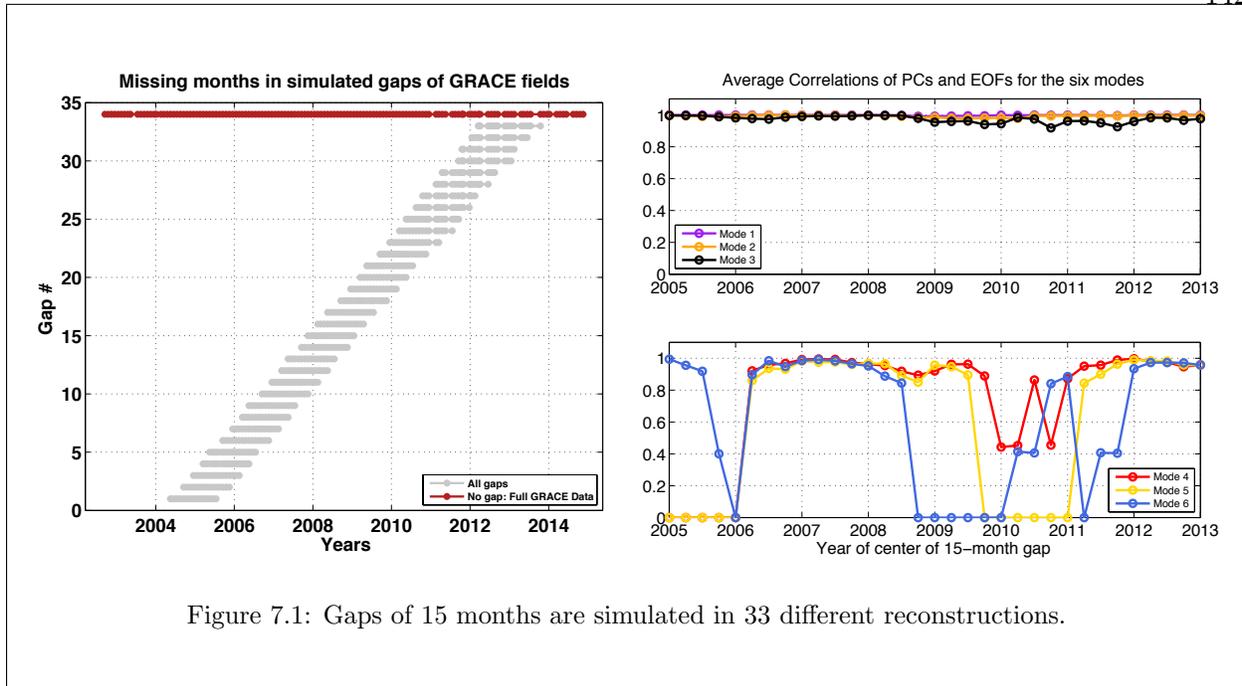
Figure 7.1: Gaps of 15 months are simulated in 33 different reconstructions.

The absolute value of the correlations between each mode and its "truth" version are shown as a function of gap. Modes 1-3 are shown on the plot at the top right and Modes 4-6 are shown on the plot at the bottom right. Modes 1-3 match the "truth" modes regardless of when the gap occurs. Modes 4-6 match well around 2007, but not around 2010. Hence, the influence of gap is non-existent for top three modes and depends on time period for remaining three modes. Two different regimes emerge: the 2006 – 2009 regime is high-correlation and there are low changes in gravity; the 2009 – 2011 regime is low-correlation and there are high changes in gravity. Figure 7.2 illustrates the second case, when the gaps change in length instead of their center point. The two regimes are based on the previous case study, where it was shown that a center point in 2007 would be a high-correlation regime (i.e., little influence of the gaps on the top six modes), whereas 2010 was a low-correlation regime (i.e., large influence on the modes 4-6).
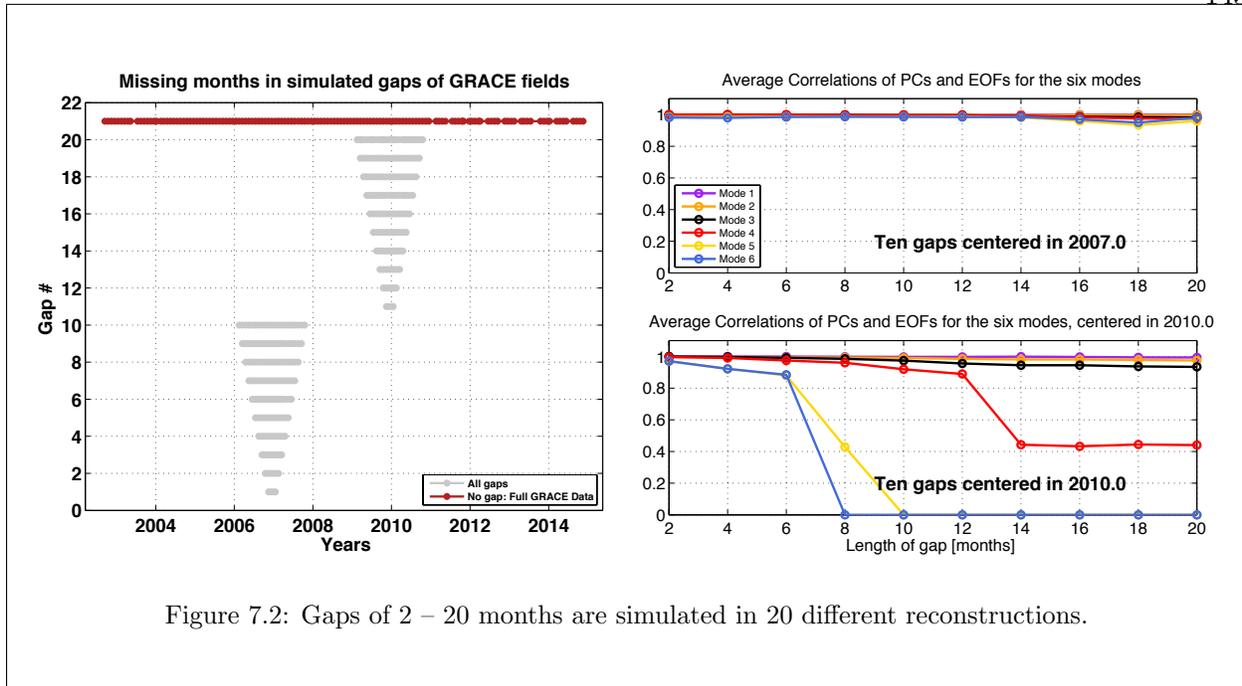
Figure 7.2: Gaps of 2 – 20 months are simulated in 20 different reconstructions.

The absolute value of the correlations between each mode and its "truth" version are shown as a function of number of months in the gap. The high-correlation regime is shown in bottom left in Figure 7.2 while the low-correlation is shown in bottom right. The correlations of the modes in the high correlation regime are all close to 1 for all lengths of gaps. The last three modes in the low-correlation regime become uncorrelated when gaps become longer than 6 months. The length of gaps only influences low-correlation regimes. Based on these findings, these two case studies suggest that the choice of gap settings will not greatly influence the reconstructions, so creating gaps that are customizable for the point of a specific study is acceptable.

Gaps relevant for the GRACE – GFO gap problem are designed as follows: while the real gap will likely not extend beyond eight months, six unique gaps of 12 consecutive months are simulated (see Figure 7.3).

Figure 7.3: Gaps used for the bridging simulation.
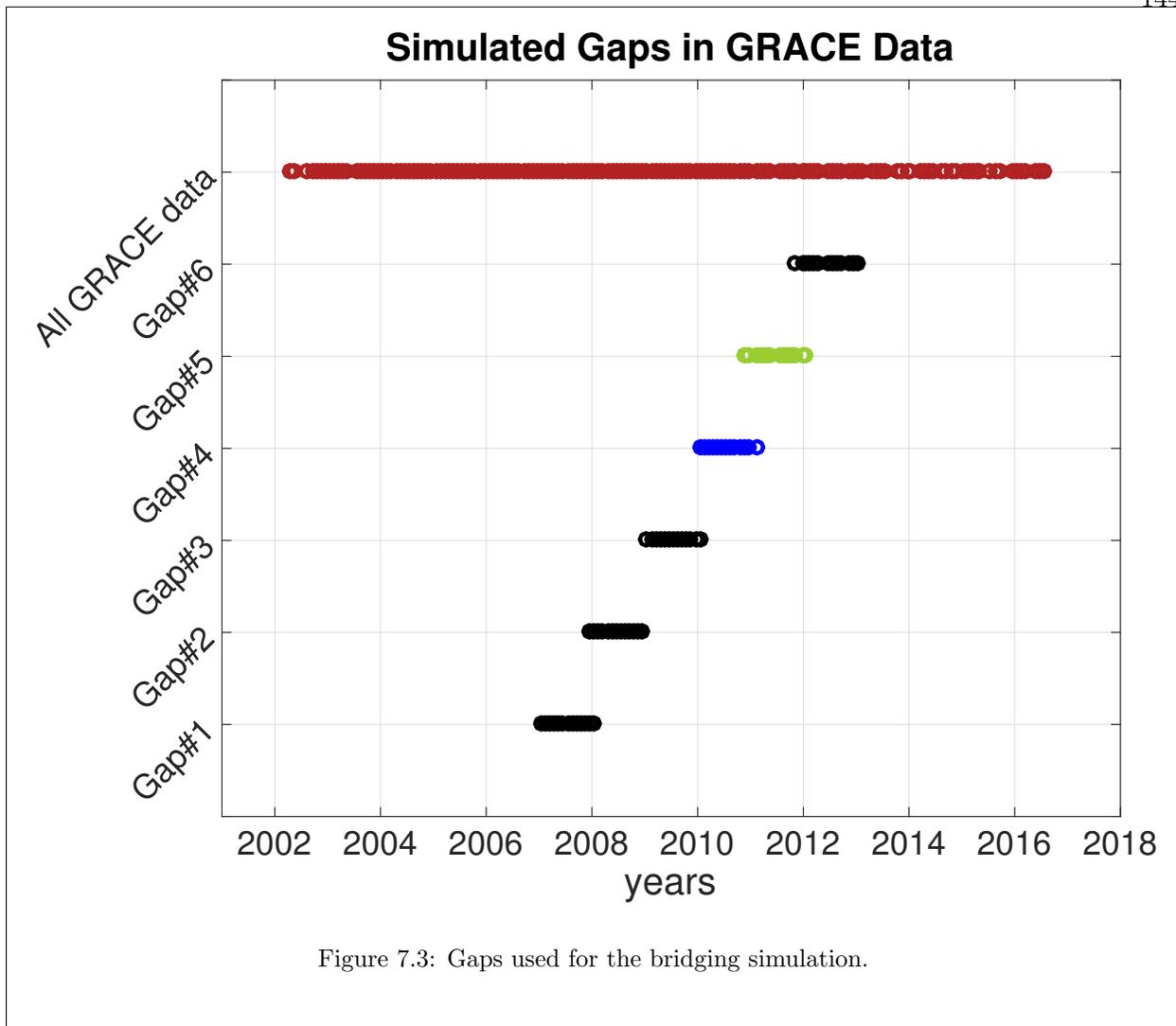
In particular, two simulated gaps stand out because major events happened during them. The 2012 gap was characterized by a record melt of the Greenland ice sheet (*Nghiem et al.*, 2012; *Tedesco et al.*, 2013). Second, 2011 was marked by a major anomaly in terrestrial water storage over Australia (*Boening et al.*, 2012; *Fasullo et al.*, 2013). Therefore, these two years and their associated simulated gaps provide benchmarks to see whether this reconstruction method could capture such events, even without GRACE data. The next section evaluates the impact of these gaps on the EOF modes.

7.4   Influence of Gaps on Reconstructions

The influence of the gap on the reconstruction process described above is shown in Figure 7.4. The EOFs and PCs from the cases with gaps are correlated against the nominal case without gaps (see two subplots in the left column of Figure 7.4). If the gaps had no influence at all, the correlations would be one and the spread would be zero. But because each case with its specific gap yields a set of EOFs and PCs that are different than the non-gap case and other gap cases, the correlations are lower and different. We see that for higher modes, the gaps have a larger influence and therefore the correlations are lower, albeit still well above 0.7, except for mode 4 of the regular approach. Furthermore, the distribution of variance remains similar, which shows the limited effect a six-month gap can have.

Figure 7.4: Influence of gaps on EOFs.
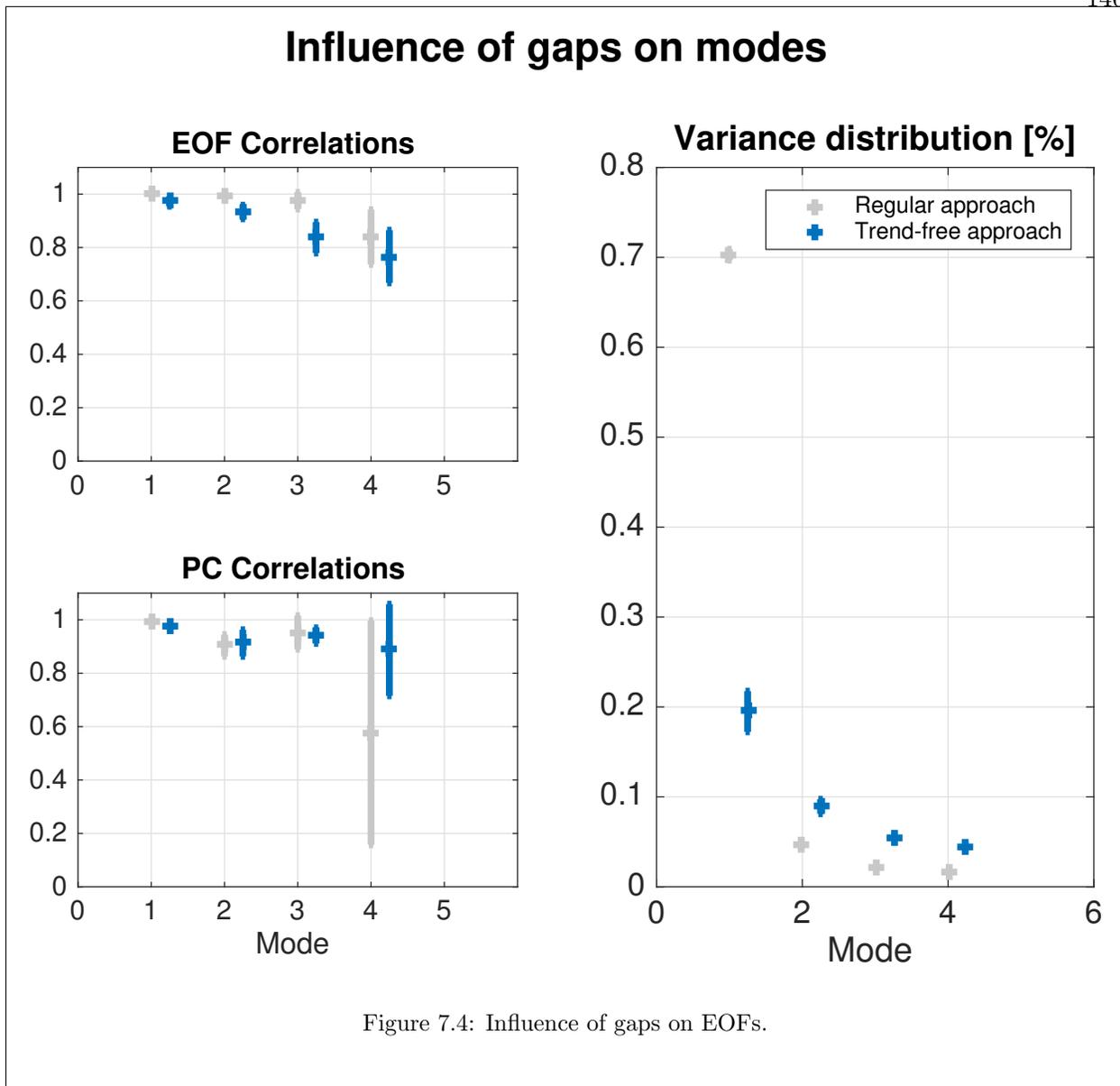
This indicates that the gaps of 12 months are not long enough to fundamentally alter both the spatial component (EOFs) and temporal components (PCs from LSA) of the reconstructions.

Shown below are cases for Greenland and Australia – these are two relevant examples for the two approaches. The mass change curves were computed using the *Swenson and Wahr* (2002) kernel-averaging techniques.

In the case of Greenland, the trend in the GRACE fields was kept because the main interest of the polar ice sheet behavior pertains to long-wavelength behavior. The mass curves for all cases

are depicted in Figure 7.5.

Figure 7.5: Influence of gaps on Greenland. The different gaps are shown in Figure 7.3; each gap covers twelve months and is centered between 2007.5 and 2012.5.
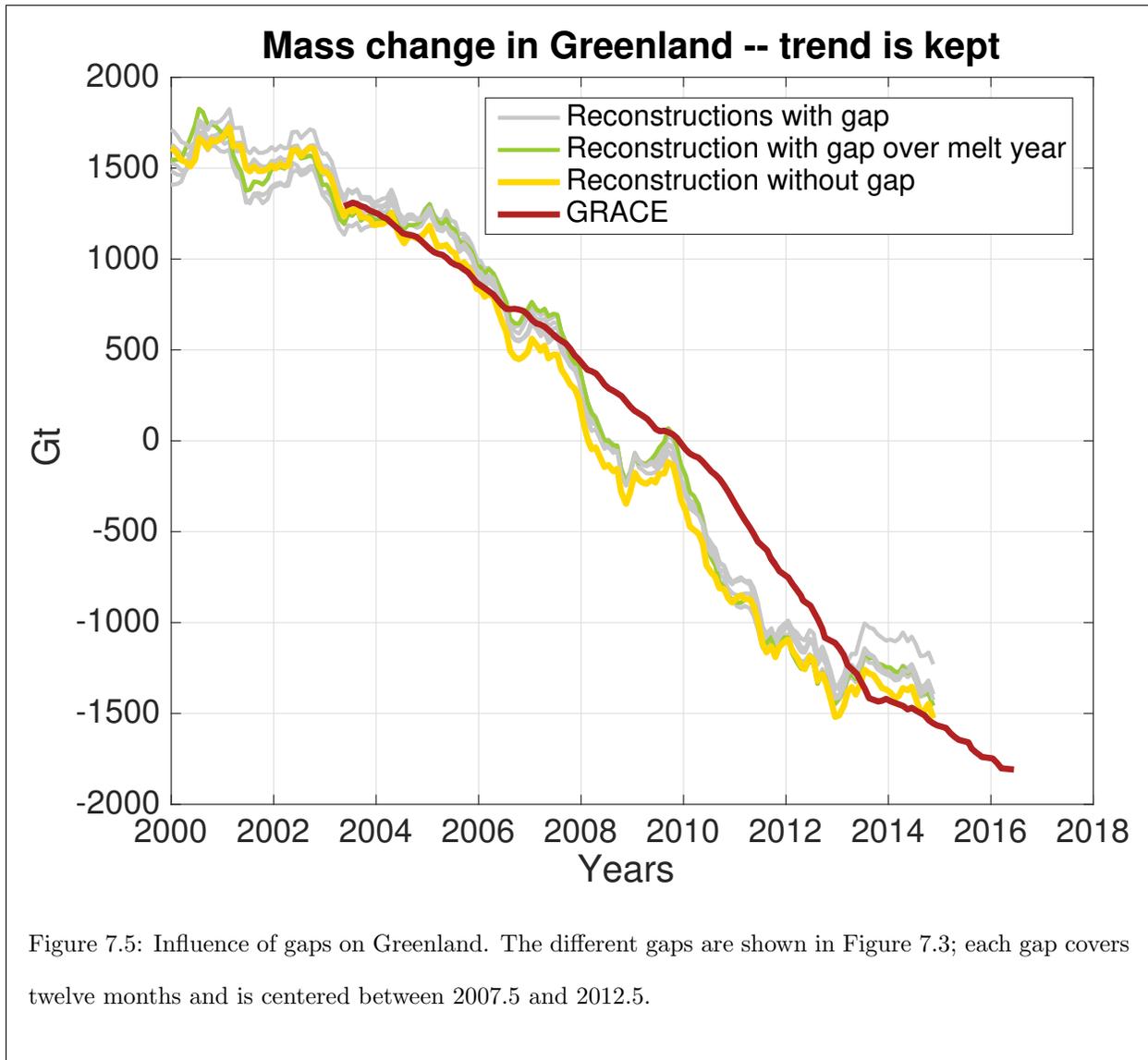
It is clear from the gaps have little influence on the final mass changes. This is expected from Section 7.4, in which it was shown that the gaps do not have a significant influence on the top three modes. Because mode one is the largest contributor to high-trend areas such as Greenland, it makes sense that all the reconstructions which contain gaps ultimately yield highly similar curves, even when the gap is over a high melt year (denoted as the green curve).

On the other hand, how do reconstructions with gaps behave when the trends are discarded?

This relates to the second approach mentioned in Section 7.3.1. In that case, mass change over Australia is examined because it has a large event in 2012, as shown in Figure 7.6. However, even with a gap in GRACE data in 2012, the resulting mass curves are similar for all cases, except for one of the reconstructions that shows a much lower peak of mass change in 2011. Overall, this behavior suggests that the gaps do not, once again, change the modes and subsequent mass change curves.

Figure 7.6: Influence of gaps on Australia. The different gaps are shown in Figure 7.3; each gap covers twelve months and is centered between 2007.5 and 2012.5
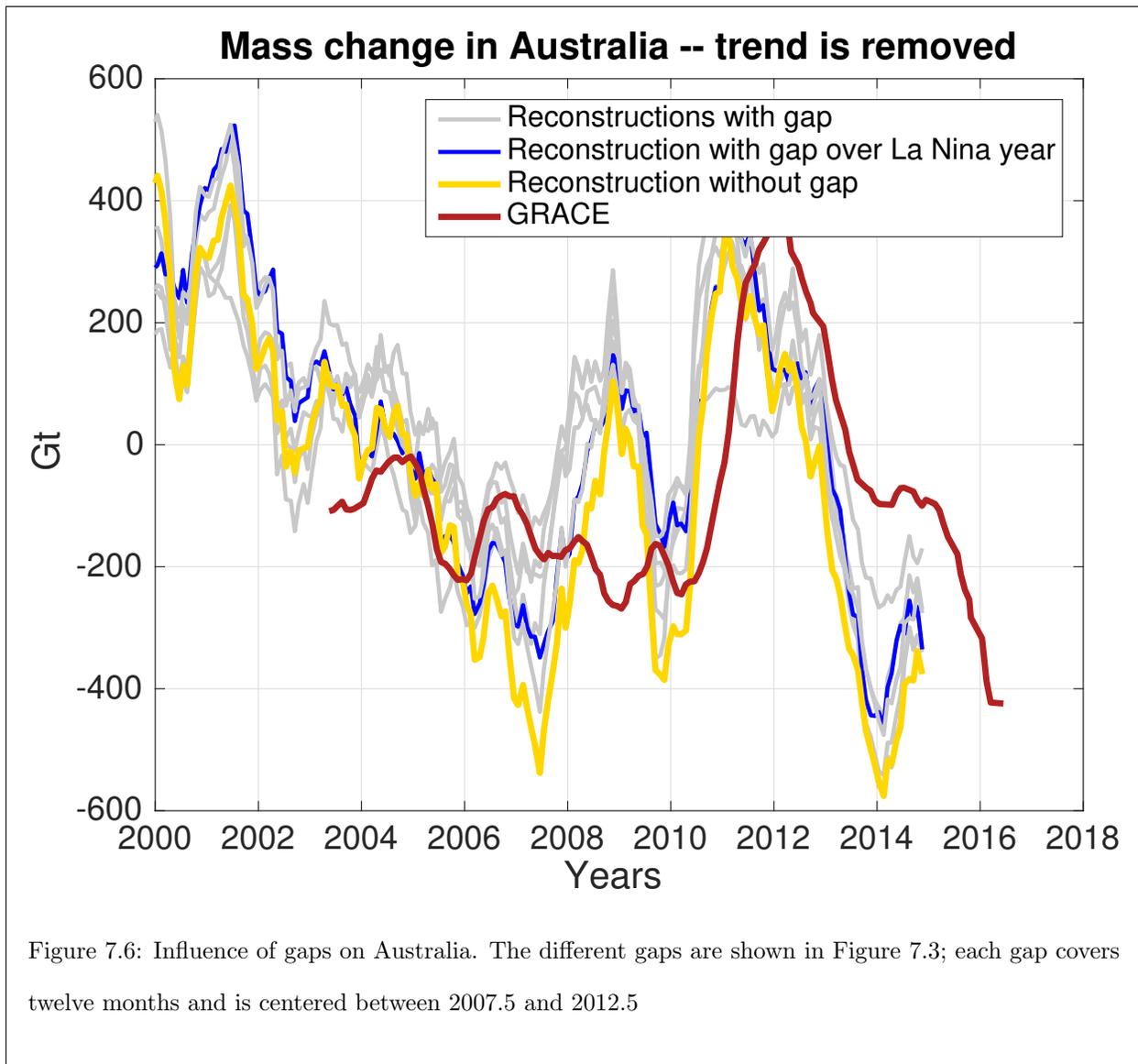
The Greenland and Australia examples indicate that the simulated gaps do not significantly

influence mass change curves, even when the gaps occur over significant years (i.e., large melt Greenland in 2012 and La Niña in 2013 over Australia).

Lastly, Figure 7.7 illustrates how this technique would be employed for one particular gap case over several regions. However, further work is needed to first understand the influence of the gap on the GRACE-based modes themselves before focusing on the interpretation of the gap-filling time series.

Figure 7.7: Gap scenarios for four different regions.
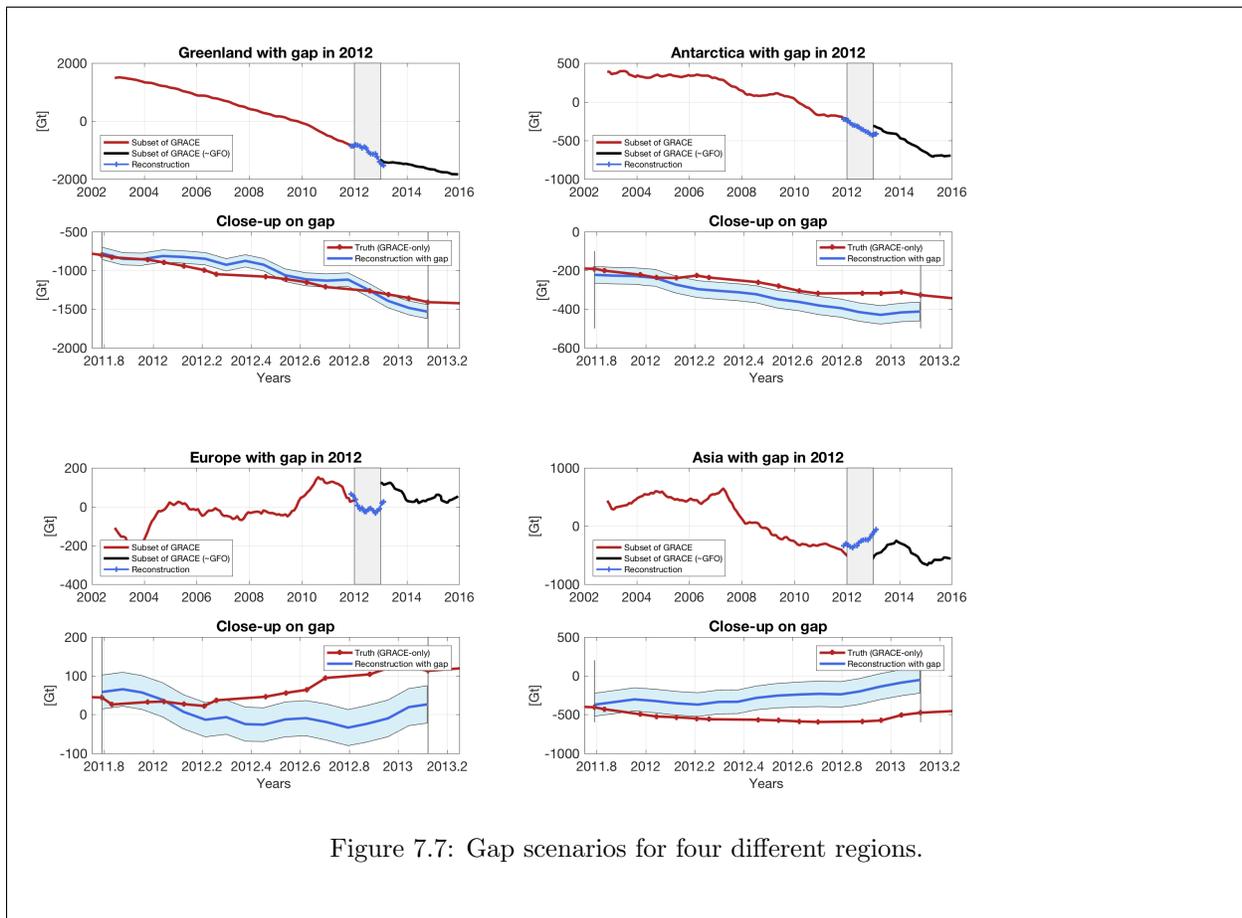
7.5   Summary

The fundamental question that is addressed in this chapter is the following: if major changes in time-variable gravity occur during the GRACE – GFO gap, is the reconstructed method able to capture these changes? Possible future notable changes in time-variable gravity include the large

ice melt at the poles through the summer of 2017. Gaps are created to simulate the lack of GRACE – GFO data; the choice of gaps is informed by the fact that the length and center points do not greatly influence the top three modes of the PCA decomposition of GRACE fields. In fact, cases studies with the Greenland and Australia mass change curves over the GRACE time span indicate the differences due to gaps are significantly smaller than due to the errors of the methods.

Future work would seek to answer the following question: how long would a gap need to be in order to be recovered? Furthermore, a crucial aspect of the bridging-the-gap problem relies on the availability and frequent delivery of the complementary gravity solutions. To this day, none of the centers involved in generating solutions from conventional tracking data are able to produce new solutions over a short interval, but have indicated that their framework will be modified to enable global delivery with short turnaround. Ideally, this delivery time would compare with the GRACE delivery time of about one to two months.

Chapter 8

Conclusion

8.1   Summary

In this dissertation, the gravity fields from GRACE are combined with the longer gravity solutions from conventional tracking data in order to extend the record of high-resolution time-variable gravity. Since the LAGEOS-1 and Starlette satellites were first used to detect changes in the C_{20} coefficient (*Yoder et al.*, 1983), an incrementally higher number of Stokes coefficients have been resolved. Using SLR tracking data of several satellites, the other four degree two coefficients (C_{21}, C_{22}, S_{21}, and S_{22}) were resolved in the 1980s (*Cheng et al.*, 2011). By the 1990s, weekly gravity fields of degree and order four ($l = 4$) could be solved for (*Lemoine et al.*, 2010; *Matsuo et al.*, 2013), as well as degree and order ten for constrained solutions with GPS-based, high-low satellite-to-satellite tracking starting in 2000 (*Baur*, 2013). The GRACE mission revolutionized the state of time-variable gravity starting in 2002 by producing monthly fields of spatial resolution of approximately 330 km (d/o 60) – an order of magnitude better than prior. There is therefore a dramatic disconnect in the spatial resolution of the gravitational fields between the GRACE era and pre-GRACE. This disconnect is addressed and mitigated in this study: the fifteen years of GRACE information provide an opportunity to complement and improve the low-resolution fields from at least the 1990s (Chapter 3). As such, the information from these high-resolution fields is extended to time periods that are not covered by GRACE by fitting spatial patterns onto low-resolution fields (Chapter 4). No other high-resolution gravity field has been produced outside of the GRACE timeframe and the outcome of this dissertation, i.e., more than two decades of monthly global

gravity fields, is a unique set of information that can be applied to advance various geophysical disciplines (Chapters 5, 6, and 7).

Chapter 3 discusses the gravity solutions. First, the corrections commonly applied to GRACE solutions are described, followed by an in-depth description of the conventional tracking data. The two tracking systems, SLR and DORIS, possess their own advantages and drawbacks. On one hand, data from SLR extend over longer time spans but can suffer from poor geographical coverage. On the other hand, DORIS data only start in 1990 and are generally more prone to errors in correction models, but they are very important contributors that allow for the adjustment of higher degree terms ($l > 4$) in the GSFC solution. The set of satellites that are tracked have a varied set of orbits, which allows for a better de-correlation of the gravitational coefficients. Indeed, a pair of satellites with similar design and altitude will still detect highly complementary information when they are placed at different inclinations – such as LAGEOS-1 and -2. The solutions that are solved for using this tracking data consist of weekly sets of up to 33 Stokes coefficients. One solution is examined in greater detail – the GSFC solution and its full associated covariances. The solutions are clearly influenced by the evolving satellite constellation, in particular, satellites that collect many measurements, e.g., Envisat. Envisat is tracked by the two systems, SLR and DORIS, so its addition and removal from the solutions are clearly visible in the covariance information. Furthermore, it is shown that the altimetry satellites contribute more to reducing the error of the solutions than the SPOT satellites. Moreover, the GSFC approach is used to generate a time series of J_2 back to the 1980s using LAGEOS-1. However, the sole use of LAGEOS-1 before 1983 is inadequate because the resolved C_{20} time series shows spurious signal. Lastly, solutions from AIUB and DGFI are examined and also show characteristics of an evolving satellite constellation even though they only use SLR-based tracking data. Post-processing is needed to render the content of the three solutions consistent, which includes re-arranging covariances, interpolating the time series over similar time steps, and normalizing Stokes coefficients.

Chapter 4 describes the combination of the high-resolution GRACE fields with the conventional tracking data. The combination involves first finding the dominant spatial pattern of the

season-free GRACE fields. These patterns are the outcome of a Principal Component Analysis (PCA) and therefore are the eigenvectors of the covariance matrix of the GRACE data. The GRACE data matrix is composed of the Stokes coefficients that are weighted by $1/l$ to homogenize the information content. This weighting scheme is analogous to weighting grid-based data by $\cos(\phi)$, where ϕ is the latitude, to minimize the influence of the polar areas. The need to use Stokes coefficients is due to the mathematical impossibility of translating the SLR/DORIS covariances from Stokes coefficients to the grid cells, because increasing the dimensions of covariances without additional information leads to singular matrices. Furthermore, fitting these high-resolution patterns is limited on the low-resolution SLR/DORIS fields, so they are truncated to have matching resolution. The fitting process, through least-squares, yields a set of temporal amplitudes for each pattern. The final reconstruction of the global reconstructed fields is obtained by a linear combination of the full fields with their associated temporal amplitudes. The error of the reconstruction method is estimated by examining three types of errors: the uncertainties associated with the original SLR/DORIS covariances, the error from the stationarity assumption, and the error from the truncation assumption.

The reconstructed fields are used for three main scientific applications. First, the primary goal was to determine longer wavelength behavior of the polar ice sheets described in Chapter 5. It is shown that the Greenland ice sheet has melted at a rate five times smaller over the 1990s compared to the 2000s, while the Antarctic ice sheet has undergone three main phases, including a period of zero mass change around the 2000s. A common problem of these reconstructed time series is the lack of independent validation in the 1990s. However, there are two possible ways to validate the fields. First, validation comes from an input-output model built using surface mass balance and ice discharge data. Second, a comparison is applied by digitizing the results of radar-based estimates of mass change from *Rignot et al.* (2011).

The second application of the reconstructed gravity fields pertains to partitioning the budget of terrestrial water storage (TWS) as described in Chapter 6. Indeed, while TWS does not yield a time-variable gravity signal that is as large as the polar ice sheets, GRACE measurements have

still been able to decisively advance knowledge of the field: *Reager et al.* (2016) show that the contribution to sea level rise from land not associated with polar ice sheets reaches 0.32 ± 0.13 mm/yr over the GRACE time frame. The reconstructed fields are used to build time series for the contribution from each continental area to sea level rise. A comparison against GRACE-only estimates show fairly strong agreement in areas that are mostly driven by mode 1, but lower agreement in areas that have undergone events not well captured in the truncated version of the modes, such as Australia, which captured a large amount of water in 2010–2011 (*Fasullo et al.*, 2013). Overall, the sum of non-polar ice sheet areas yields a time series of sea level rise in the 1990s that does not resemble the trend-like contribution of the 2000s. However, the large error bars inhibit a clear interpretation.

Finally, the third application of the reconstructed gravity fields involves bridging the upcoming gap between GRACE and GRACE Follow-On and is presented in Chapter 7. This situation is simulated by removing a year of data in the GRACE fields. A year-long gap does not significantly alter the first three modes of the PCA decomposition on GRACE fields, which reduces the ability of the reconstruction to recover meaningful change over a gap.

8.2   Outlook and Future Applications

While the framework for combining the two types of fields has been put in place and has already been applied to shed light on geophysical applications, future avenues of research can be explored. In particular, three types of possible improvements stand out: the refinement of the combination method, and in particular the definition of the spatial patterns; the scientific interpretation of the applications of the reconstructed time-variable gravity fields; and the push for more consistent and longer gravity solutions that stem from conventional tracking data.

The first possible improvement pertains to the refinement of the combination method. The combination method, which seeks to use high-resolution patterns from GRACE and temporal amplitudes from SLR/DORIS, consists of a choice of basis functions that is the backbone to the study. The influence of these decisions could be examined quantitatively. The use of "next-level"

basis functions have the potential to improve the reconstructions, namely, the use of ICA could further de-couple Greenland and Antarctica from mode 1. Multi-channel singular spectrum analysis, as applied in *Rangelova et al.* (2010) could also remove the remnant seasonal signals found in some coefficients and that is visible in the Amazon. It is also possible that the reconstructions would be improved by leaving the seasonal signals in all gravity fields, although it might take away from other interannual signals of interest. Furthermore, implementing temporal constraints to the least-squares adjustment would smooth the resulting temporal modes.

The second possible improvement relates to scientific interpretation. Indeed, a major obstacle for the validation of these gravity fields pertains to the acquisition of data that (1) are independent of GRACE and (2) extend over timeframes that are longer than GRACE. This means improving comparisons of ice sheet mass balance before GRACE, as well as hydrological models that capture the full water column in the 1990s. Improvement of the TWS comparisons includes, for example, adding degree-one terms or altimetry-based comparisons of inland seas. However, these degree-one coefficients would have to be estimated in parallel to the other time-variable gravity coefficients, because current estimates are limited to the GRACE time series (*Swenson et al.*, 2008).

The third possible improvement deals with the original tracking data. While SLR/DORIS solutions are delivered with full covariances, the use of independently-generated solutions would shed light on possible unknown errors. Preliminary work collecting solutions from different centers (DGFI and AIUB) show systematic differences that are likely due to differing background models. These differences therefore call for a convergence of processing standards, yielding reconstructions that are more similar and with differences that are easier to understand. Furthermore, the delivery of these solutions is currently relatively slow and gravity reconstructions over a current gap would greatly benefit from a faster delivery of the solutions.

Finally, the reconstructed fields could be used for future applications. One example is their inclusion in an ensemble of hydrologic models, as recently proposed by Prof. E. Forootan in a 2017 Natural Environment Research Council (NERC, United Kingdom) proposal [*personal communication with E. Forootan, 2017*]. Another example relates to Precise Orbit Determination (POD). POD

applications could benefit from higher-resolution, time-variable gravity fields before the GRACE mission. For altimetry satellites, the goal is to obtain an accuracy in the radial component of the orbit of 1 cm over the 10-day repeat cycle and 0.1 mm/yr in order to properly support altimetry work. Figure 10 in *Couhert et al.* (2015) shows that using the 10-day GRGS solutions (*Bruinsma et al.*, 2010) instead of a d/o 50 GRACE+LAGEOS field with annual, semiannual, and drift modeled reduces the variability of the radial orbit error (in an RMS sense) by 2-3 mm over the Envisat time frame (2002–2012). Table 6 in *Couhert et al.* (2015) also states that long-term, global errors from time-variable gravity are a significant component of the error budget and on the order of 0.1 mm interannually and 0.1 mm/yr. *Lemoine et al.* (2010) indicate that the usage of geophysical models representing time-variable gravity (e.g., hydrology from GLDAS/Noah or atmospheric models from NCEP) present radial differences in the Jason-1 orbit of up to 6 mm in an RMS sense over January 2003 to January 2005. Preliminary work has indicated that a framework is already in place to compare the two types of fields and that the reconstructed fields compare well with GRGS fields (*Bruinsma et al.*, 2010) for the Jason-2 altimetry satellite time series (cycles 2–215) [*personal communication with A. Smith, 2015*]. Overall, the reconstructed fields presented in this dissertation could contribute to reducing errors in the radial component of POD for altimetric satellites, especially before the GRACE time period. *Rudenko et al.* (2012) provide orbit information for re-analysis of altimetry results that are used over 1993–2010 in *Ablain et al.* (2015); specifically, annual and semi-annual variations up to d/o 50 from EIGEN-GL04S-ANNUAL gravity field model were applied, as well as drift terms in the low-degree zonal coefficients (*Lemoine et al.*, 2007). Adding time-variable gravity information obtained from this dissertation that can complement the annual, semi-annual, and drift information would surely improve the next re-analysis of the altimetry satellites over the 1993–2000 time frame.

8.3   Concluding Remarks

This dissertation presents a framework for combining different types of time-variable gravity fields and resulted in a new set of high-resolution, global gravity fields that is longer by ten years.

The global nature of these fields enables them to shed light on various geophysical disciplines, especially those with the largest signals, namely, the cryosphere and terrestrial water storage, although not yet oceanography. Furthermore, this project has given another impetus for centers that generate time-variable gravity solutions using SLR, DORIS, and GPS observations to coordinate their processing. As more and more data types provide perspective on the connection between time-variable gravity and the Earth system, this framework provides an example for a combination of data that leverages the strengths of each gravity field, while also providing a rigorous assessment of the errors that arise in the reconstruction process.

Bibliography

A, G., J. Wahr, and S. Zhong (2013), Computations of the viscoelastic response of a 3-D compressible Earth to surface loading: an application to Glacial Isostatic Adjustment in Antarctica and Canada, *Geophys. J. Int.*, *192*(2), 557–572.

Ablain, M., et al. (2015), Improved sea level record over the satellite altimetry era (1993–2010) from the Climate Change Initiative project, *Ocean Sci.*, *11*(1), 67–82.

Adhikari, S., and E. R. Ivins (2016), Climate-driven polar motion: 2003–2015, *Sci. Adv.*, *2*(e1501693).

Appleby, G., J. Rodríguez, and Z. Altamimi (2016), Assessment of the accuracy of global geodetic satellite laser ranging observations and estimated impact on ITRF scale: Estimation of systematic errors in LAGEOS observations 1993–2014, *J. Geod.*, *90*(12), 1371–1388.

Bail, K. L., F. Lemoine, and D. Chinn (2010), GSFC DORIS contribution to ITRF2008, *Adv. Space Res.*, *45*(12), 1481–1499, doi:10.1016/j.asr.2010.01.030.

Baur, O. (2013), Greenland mass variation from time-variable gravity in the absence of GRACE, *Geophys. Res. Lett.*, *40*, 4289–4293, doi:10.1002/grl.50881.

Bettadpur, S. (2012), *UTCSR Level-2 processing standards document (For Level-2 Product Release 0005)*, pp. 327–742, University of Texas at Austin, Austin.

Bezděk, A., J. Sebera, J. T. Encarnacao, and J. Klokočník (October 5-7, 2016), Time-variable gravity from GPS tracking of Grace and Swarm, in *GRACE Science Team Meeting*.

Bloßfeld, M., H. Müller, M. Gerstl, V. Štefka, J. Bouman, F. Göttl, and M. Horwath (2015), Second-degree Stokes coefficients from multi-satellite SLR, *J. Geod.*, *89*(9), 857–871.

Boening, C., J. K. Willis, F. W. Landerer, R. S. Nerem, and J. Fasullo (2012), The 2011 La Niña: So strong, the oceans fell, *Geophys. Res. Lett.*, *39*(L19602).

Boergens, E., E. Rangelova, M. G. Sideris, and J. Kusche (2014), Assessment of the capabilities of the temporal and spatiotemporal ICA method for geophysical signal separation in GRACE data, *J. Geophys. Res.-Sol. Ea.*, *119*(5), 4429–4447.

Bonin, J., and D. Chambers (2016), Measuring two decades of ice mass loss using GRACE and SLR, in *American Geophysical Union Fall Meeting, San Francisco, California, 12-16, 2016*.

Bonin, J. M., and D. P. Chambers (2013), Uncertainty estimates of a GRACE inversion modelling technique over Greenland using a simulation, *Geophys. J. Int.*, *194*, 212–229.

Bruinsma, S., J.-M. Lemoine, R. Biancale, and N. Valès (2010), CNES/GRGS 10-day gravity field models (Release 2) and their evaluation, *Adv. Space Res.*, *45*(4), 587–601, doi: 10.1016/j.asr.2009.10.012.

Cazenave, A. (2006), How Fast Are the Ice Sheets Melting?, *Science*, *314*, 1250.

Cerri, L., J. M. Lemoine, F. Mercier, N. P. Zelensky, and F. G. R. Lemoine (2013), DORIS-based point mascons for the long term stability of precise orbit solutions, *Adv. Space. Res.*, *52*, 466–476, doi:10.1016/j.asr.2013.03.023.

Chambers, D. P., and J. A. Bonin (2012), Evaluation of Release-05 GRACE time-variable gravity coefficients over the ocean, *Ocean Sci.*, *8*, 859–868.

Chambers, D. P., C. A. Mehlhaff, T. J. Urban, D. Fujii, and R. S. Nerem (2002), Low-frequency variations in global mean sea level: 1950–2000, *J. Geophys. Res.–Oceans*, *107*(C4).

Chambers, D. P., J. Wahr, M. E. Tamisiea, and R. S. Nerem (2010), Ocean mass from GRACE and glacial isostatic adjustment, *J. Geophys. Res.*, *115*(B11415).

Chao, B. F. (2016), Caveats on the equivalent water thickness and surface mascon solutions derived from the GRACE satellite-observed time-variable gravity, *J. Geod.*, *90*, 807–813.

Chen, F., K. Mitchell, J. Schaake, Y. Xue, H.-L. Pan, V. Koren, Q. Y. Duan, M. Ek, and A. Betts (1996), Modeling of land surface evaporation by four schemes and comparison with FIFE observations, *J. Geophys. Res.–Atmos.*, *101*(D3), 7251–7268.

Chen, J. L., C. R. Wilson, and J. S. Famiglietti (2007), Attenuation effect on seasonal basin-scale water storage changes from GRACE time-variable gravity, *J. Geod.*, *81*, 237–245.

Chen, J. L., C. R. Wilson, and K.-W. Seo (2009), S2 tide aliasing in GRACE time-variable gravity solutions, *J. Geod.*, *83*(7), 679–687, doi:10.1007/s00190-008-0282-1.

Chen, J. L., C. R. Wilson, J. C. Ries, and B. D. Tapley (2013), Rapid ice melting drives Earth's pole to the East, *Geophys. Res. Lett.*, *40*, 2625–2630, doi:10.1002/grl.50552.

Cheng, M., J. C. Ries, and B. D. Tapley (2011), Variations of the Earth's figure axis from satellite laser ranging and GRACE, *J. Geophys. Res.*, *116*, B01,409, doi:10.1029/2010JB000850.

Cheng, M., B. D. Tapley, and J. C. Ries (2013), Deceleration in the Earth's oblateness, *J. Geophys. Res.-Sol. Ea.*, *118*, 740–747, doi:10.1002/jgrb.50058.

Church, J. A., and N. J. White (2002), A 20th century acceleration in global sea-level rise, *Geophys. Res. Lett.*, *33*, L01,602, doi:10.1029/2005GL024826.

Church, J. A., N. J. White, R. Coleman, K. Lambeck, and J. X. Mitrovica (2004), Estimates of the regional distribution of sea level rise over the 1950–2000 period, *J. Climate*, *17*(13), 2609–2625.

Church, J. A., et al. (2013), Sea level change, in *Climate Change 2013: The Physical Science Basis. Contribution of Working Group I to the Fifth Assessment Report of the Intergovernmental Panel on Climate Change*, PM Cambridge University Press.

Couhert, A., et al. (2015), Towards the 1 mm/y stability of the radial orbit error at regional scales, *Adv. Space Res.*, *55*(1), 2–23.

Cox, C. M., and B. F. Chao (2002), Detection of a large-scale mass redistribution in the terrestrial system since 1998, *Science*, *297*(5582), 831–833.

Crowley, J. W., J. X. Mitrovica, R. C. Bailey, and M. E. Tamisiea (2006), Land water storage within the Congo Basin inferred from GRACE satellite gravity data, *Geophys. Res. Lett.*, *33*(L19402).

Dach, R., U. Hugentobler, P. Fridez, M. Meindl, et al. (2007), Bernese GPS software version 5.0, *Astronomical Institute, University of Bern*, *640*, 114.

Dahle, C., F. Flechtner, C. Gruber, D. König, R. König, G. Michalak, and K. H. Neumayer (2013), *GFZ GRACE Level-2 processing standards document for level-2 product release 0005*, Helmholtz-Zentrum Potsdam, Deutsches GeoForschungsZentrum, Potsdam, Germany., scientific technical report str12/02–data, revised edition. ed.

Ditmar, P., and L. Xianglin (2008), Gravity field modeling on the basis of GRACE range-rate combinations, in *VI Hotine-Marussi Symposium on Theoretical and Computational Geodesy*, pp. 17–22, Springer.

Dobslaw, H., F. Flechtner, I. Bergmann-Wolf, C. Dahle, R. Dill, S. Esselbom, I. Sagsen, and M. Thomas (2013), Simulating high-frequency atmosphere-ocean mass variability for dealiasing of satellite gravity observations: AOD1 RL05, *J. Geophys. Res.–Oceans*, *118*, 3704–3711.

Döll, P., F. Kaspar, and B. Lehner (2003), A global hydrological model for deriving water availability indicators: model tuning and validation, *J. Hydrology*, *270*(1), 105–134.

Dunn, C., et al. (2003), The instrument on NASA's GRACE mission: Augmentation of GPS to achieve unprecedented gravity field measurements, in *Proceedings of the 15th International Technical Meeting of the Satellite Division of The Institute of Navigation (ION GPS 2002)*, pp. 724–730.

Eicker, A., M. Schumacher, J. Kusche, P. Döll, and H. M. Schmied (2014), Calibration/Data Assimilation Approach for Integrating GRACE Data into the WaterGAP Global Hydrology Model (WGHM) Using an Ensemble Kalman Filter: First Results, *Surv. Geophys.*, *35*, 1285–1309.

Encarnacao, J. T., et al. (2016), Gravity fields models derived from Swarm GPS data, *Earth, Planets Space*, *68*, 127.

Enderlin, E. M., I. M. Howat, S. Jeong, M.-J. Noh, J. H. van Angelen, and M. R. van den Broeke (2014), An improved mass budget for the Greenland ice sheet, *Geophys. Res. Lett.*, *41*, 866–872, doi:10.1002/2013GL059010.

Famiglietti, J. S., and M. Rodell (2013), Water in the Balance, *Science*, *340*(6138), 1300–1301.

Fasullo, J. T., C. Boening, F. W. Landerer, and R. S. Nerem (2013), Australia's unique influence on global sea level in 2010–2011, *Geophys. Res. Lett.*, *40*, 4368–4373.

Flechtner, F., H. Dobslaw, and E. Fagiolini (2015), *AOD1B Product Description Document for Product Release 05*, GFZ German Research Centre for Geosciences.

Forootan, E. (2015), Statistical signal decomposition techniques for analyzing time-variable satellite gravimetry data, Ph.D. thesis, Universität Bonn.

Forootan, E., and J. Kusche (2012), Separation of global time-variable gravity signals into maximally independent components, *J. Geod.*, *86*, 477–497, doi:10.1007/s00190-011-0532-5.

Forootan, E., and J. Kusche (2013), Separation of deterministic signals using independent component analysis (ica), *Studia Geophysica et Geodaetica*, *57*(1), 17–26.

Gardner, A. S., et al. (2013), A Reconciled Estimate of Glacier Contributions to Sea Level Rise: 2003 to 2009, *Science*, *340*(6134), 852–857.

Goiginger, H., et al. (2011), The combined satellite-only global gravity field model GOCO02S, in *Geophys. Res. Abstr.*, vol. 13, p. 571.

Gruber, T., R. Rummel, and R. Koop (2006), How to use GOCE level 2 products, in *Proceedings of the 3rd international GOCE user workshop. ESA-ESRIN, Frascati, Italy*, pp. 6–8.

Haberkorn, C., M. Bloßfeld, J. Bouman, M. Fuchs, and M. Schmidt (2014), Towards a Consistent Estimation of the Earth's Gravity Field by Combining Normal Equation Matrices from GRACE and SLR, *IAG Symp. Ser.*, pp. 1–7.

Hamlington, B. D., R. R. Leben, R. S. Nerem, W. Han, and K.-Y. Kim (2011), Reconstructing sea level using cyclostationary empirical orthogonal functions, *J. Geophys. Res.*, *116*, C12,015, doi:10.1029/2011JC007529.

Han, D., and J. Wahr (1995), The viscoelastic relaxation of a realistically stratified earth, and a further analysis of postglacial rebound, *Geophys. J. Int.*, *120*, 287–311.

Han, S.-C., C. K. Schum, M. Bevis, C. Ji, and C.-Y. Kuo (2006), Crustal Dilatation Observed by GRACE After the 2004 Sumatra-Andaman Earthquake, *Science*, *313*(5787), 658–662.

Hannachi, A. (2007), Pattern hunting in climate: a new method for finding trends in gridded climate data, *Int. J. Climatol.*, *27*, 1–15, doi:10.1002/joc.1375.

Harig, C., and F. J. Simons (2012), Mapping Greenland's mass loss in space and time, *Proc. Natl. Acad. Sci. U.S.A.*, *109*(49), 19,934–19,937.

Hoare, M. R. (2005), *The Quest for the True Figure of the Earth*, Ashgate Publishing Company.

Hofmann-Wellenhof, B., and H. Moritz (2005), *Physical Geodesy*, SpringerWienNewYork.

Humphrey, V., L. Gudmundsson, and S. I. Seneviratne (2016), Assessing Global Water Storage Variability from GRACE: Trends, Seasonal Cycle, Subseasonal Anomalies and Extremes, *Surv. Geophys.*, *37*, 357–395.

Ivins, E. R., T. S. James, J. Wahr, E. J. O. Schrama, F. W. Landerer, and K. M. Simon (2013), Antarctic contribution to sea level rise observed by GRACE with improved GIA correction, *J. Geophys. Res.-Sol. Ea.*, *118*, 3126–3141.

James, T. S., and E. R. Ivins (1997), Global geodetic signatures of the Antarctic ice sheet, *J. Geophys. Res.*, *102*(B1), 605–633, doi:10.1029/96JB02855.

Jekeli, C. (1981), *Alternative Methods to Smooth the Earth's Gravity Field*, Geodetic and GeoInformation Science, Department of Civil and Environmental Engineering and Geodetic Science, The Ohio State University.

Jekeli, C. (2009), Potential Theory and Static Gravity Field of the Earth, in *Treatise on Geophysics – Geodesy*, ISBN: 978-0-444-53460-6, chap. 2, pp. 11–42, Elsevier.

Johnson, B. (2009), NOAA Project to Measure Gravity Aims to Improve Coastal Monitoring, *Science*, *325*, 5939, doi:10.1126/science.325_378.

Johnson, G. C., and D. P. Chambers (2013), Ocean bottom pressure seasonal cycles and decadal trends from GRACE Release-05: Ocean circulation implications, *J. Geophys. Res.–Oceans*, *118*, 4228–4240.

Jolliffe, I. T. (1986), *Principal Component Analysis*, Springer, New York. ISBN:9780387954424.

Jolliffe, I. T. (2002), *Principal Component Analysis, Second Edition*, Springer, New York. ISBN:0387954422.

Kaiser, H. F. (1958), The varimax criterion for analytic rotation in factor analysis, *Psychometrika*, *23*(3), 187–200.

Kaplan, A., Y. Kushnir, and M. A. Cane (2000), Reduced Space Optimal Interpolation of Historical Marine Sea Level Pressure: 1854-1992, *Bull. Amer. Meteor. Soc.*, *13*, 2987–3002.

Kaula, W. M. (1966), *Theory of Satellite Geodesy*, Dover Publications, Inc. ISBN:0486414655.

Keay, J. (2000), *The Great Arc*, Harper Collins Publisher.

Khan, S. A., et al. (2016), Geodetic measurements reveal similarities between post-last Glacial Maximum and present-day mass loss from the Greenland ice sheet, *Science Advances*, *2*(9), e1600,931–e1600,931, doi:10.1126/sciadv.1600931.

Kim, K.-Y., B. Hamlington, and H. Na (2015), Theoretical foundation of cyclostationary EOF analysis for geophysical and climatic variables: concepts and examples, *Earth-Science Reviews*, *150*, 201–218.

Kleinherenbrink, M., R. Riva, and Y. Sun (2016), Sub-basin-scale sea level budget from satellite altimetry, Argo floats and satellite gravimetry: a case study in the North Atlantic Ocean, *Ocean Sci.*, *12*, 1179–1203.

Klinger, B., T. Mayer-Gürr, S. Behzadpour, M. Ellmer, A. Kvas, and N. Zehentner (2016), Towards a new ITSG-GRACE release: improvements within the processing chain, in *EGU General Assembly Conference Abstracts*, vol. 18, p. 11547.

Koch, K. R. (1988), *Parameter estimation and hypothesis testing in linear models*, Springer, New York. ISBN:9783540652571.

Koenig, L. (2010), Polar Airborne Observations Fill Gap in Satellite Data, *Eos*, *91*(38), 333–334.

Kusche, J., R. Schmidt, S. Petrovic, and R. Rietbroek (2009), Decorrelated GRACE time-variable gravity solutions by GFZ, and their validation using a hydrological model, *J. Geod.*, *83*(10), 903–913.

Kusche, J., B. Uebbing, R. Rietbroek, C. K. Schum, and Z. H. Khan (2014), Sea level budget in the Bay of Bengal (2002–2004) from GRACE and altimetry, *J. Geophys. Res.–Oceans*, *121*, 1194–1217.

Landerer, F. W., D. N. Wiese, K. Bentel, C. Boening, and M. M. Watkins (2015), North Atlantic meridional overturning circulation variations from GRACE ocean bottom pressure anomalies, *Geophys. Res. Lett.*, *42*, 8114–8121.

Lemoine, F., N. Zelensky, D. Chinn, B. Beckley, and J. Lillibridge (2006), Towards the GEOSAT follow-on precise orbit determination goals of high accuracy and near-real-time processing, in *AIAA/AAS Astrodynamics Specialist Conference and Exhibit*, p. 6402.

Lemoine, F., et al. (2010), Towards development of a consistent orbit series for TOPEX, Jason-1, and Jason-2, *Adv. Space Res.*, *46*(12), 1513–1540.

Lemoine, F. G., D. S. Chinn, N. P. Zelensky, and J. W. Beall (2014), Time-Variable Gravity Solutions from 1993-2014 from SLR and DORIS data, Abstract G23A-0472, in *American Geophysical Union Fall Meeting, San Francisco, California, December 15-19, 2014.*

Lemoine, F. G., D. S. Chinn, N. P. Zelensky, J. W. Beall, and K. L. Bail (2016), The development of the GSFC DORIS contribution to ITRF2014, *Adv. Space. Res.*, doi:10.106/j.asr.2015.12.043.

Lemoine, J.-M., and H. Capdeville (2006), A corrective model for Jason-1 DORIS Doppler data in relation to the South Atlantic Anomaly, *J. Geod.*, *80*(8), 507–523.

Lemoine, J.-M., S. Bruinsma, S. Loyer, R. Biancale, J.-C. Marty, F. Perosanz, and G. Balmino (2007), Temporal gravity field models inferred from GRACE data, *Adv. Space Res.*, *39*(10), 1620–1629.

Long, D., B. R. Scanlon, L. Longuevergne, A. Y. Sun, D. N. Fernando, and H. Save (2013), GRACE satellite monitoring of large depletion in water storage in response to the 2011 drought in Texas, *Geophys. Res. Lett.*, *40*, 3395–3401, doi:10.1002/grl.50655.

Longuevergne, L., B. R. Scanlon, and C. R. Wilson (2010), GRACE Hydrological estimates for small basins: Evaluating processing approaches on the High Plains Aquifer, USA, *Water Resour. Res.*, *46*, W11,517.

Lorenz, E. N. (1956), *Empirical orthogonal functions and statistical weather prediction*, Massachusetts Institute of Technology, Department of Meteorology.

Luthcke, S. B., H. J. Zwally, W. Abdalati, D. D. Rowlands, R. D. Ray, R. S. Nerem, F. G. Lemoine, J. J. McCarthy, and D. S. Chinn (2006), Recent Greenland Ice Mass Loss by Drainage System from Satellite Gravity Observations, *Science*, *314*, 1286–1289.

Luthcke, S. B., A. A. Arendt, D. D. Rowlands, J. J. McCarthy, and C. F. Larsen (2008), Recent glacier mass changes in the Gulf of Alaska region from GRACE mascon solutions, *J. Glaciol.*, *54*(188), 767–777.

Luthcke, S. B., T. J. Sabaka, B. D. Loomis, A. A. Arendt, J. J. McCarthy, and J. Camp (2013), Antarctica, Greenland and Gulf of Alaska land-ice evolution from an iterated GRACE global mascon solution, *J. Glaciol.*, *59*(216), 613.

Maier, A., S. Krauss, W. Hausleitner, and O. Baur (2012), Contribution of satellite laser ranging to combined gravity field models, *Adv. Space Res.*, *49*(3), 556–565.

Makowski, J. K., D. P. Chambers, and J. A. Bonin (2015), Using ocean bottom pressure from the Gravity Recovery and Climate Experiment (GRACE) to estimate transport variability in the southern Indian Ocean, *J. Geophys. Res.–Oceans*, *120*, 4245–4259.

Matsuo, K., B. F. Chao, T. Otsubo, and K. Heki (2013), Accelerated ice mass depletion revealed by low-degree gravity field from satellite laser ranging: Greenland, 1991-2011, *Geophys. Res. Lett.*, *40*, doi:10.1002/grl.50900.

Mayer-Gürr, T., S. Behzadpour, M. Ellmer, A. Kvas, B. Klinger, and N. Zehentner (2016), ITSG-Grace2016 - Monthly and Daily Gravity Field Solutions from GRACE, doi: 10.5880/icgem.2016.007.

McLeish, M., and S. Ferguson (2016), Examples of AIRGrav Vector Gravity Data and Comparison with Ground Truth, in *2016 Airborne Gravimetry for Geodesy Summer School*.

Milne, G. A., J. L. Davis, J. X. Mitrovica, H.-G. Scherneck, J. M. Johansson, M. Vermeer, and H. Koivula (2001), Space-Geodetic Constraints on Glacial Isostatic Adjustment in Fennoscandia, *Science*, *291*(5512), 2381–2385, doi:10.1126/science.1057022.

Misra, P., and P. Enge (2011), *Global Positining System: Signals, Measurements, and Performance*, Ganga-Jamuna Press.

Moon, T., I. Joughin, B. Smith, M. R. van den Broeke, W. J. V. de Berg, B. Noël, and M. Usher (2014), Distinct patterns of seasonal Greenland glacier velocity, *Geophys. Res. Lett.*, *41*, 7209–7216, doi:10.1002/2014GL061836.

Morrow, E., J. X. Mitrovica, M. G. Sterenborg, and C. Harig (2013), A Test of Recent Inferences of Net Polar Ice Mass Balance based on Long-Wavelength Gravity, *Bull. Amer. Meteor. Soc.*, *26*, 6535–6540, doi:10.1175/JCLI-D-13-00078.1.

Nerem, R. S., and J. Wahr (2011), Recent changes in the Earth's oblateness driven by Greenland and Antarctic ice mass loss, *Geophys. Res. Lett.*, *38*, L13,501, doi:10.1029/2011GL047879.

Nerem, R. S., C. Jekeli, and W. M. Kaula (1995), Gravity field determination and characteristics: Retrospective and prospective, *J. Geophys. Res.*, *100*(B8), 15,053–15,074.

Nghiem, S. V., D. K. Hall, T. L. Mote, M. Tedesco, M. R. Albert, K. Keegan, C. A. Shuman, N. E. DiGirolamo, and G. Neumann (2012), The extreme melt across the Greenland ice sheet in 2012, *Geophys. Res. Lett.*, *39*(L20502).

Noël, B., W. J. van de Berg, E. van Meijgaard, P. K. Munneke, R. S. W. van de Wal, and M. R. van den Broeke (2015), Summer snowfall on the Greeland Ice Sheet: a study with the updated regional climate model RACMO2.3, *The Cryosphere Discuss.*, *9*, 1177–1208, doi:10.5194/tcd-9-1177-2015.

North, G. R., T. L. Bell, R. F. Cahalan, and F. J. Moeng (1982), Sampling errors in the estimation of Empirical Orthogonal Functions, *Bull. Amer. Meteor. Soc.*, *110*, 699–710.

O'Leary, D. (1948), *How Greek Science Passed to the Arabs*, Routledge.

Otsubo, T., R. A. Sherwood, G. M. Appleby, and R. Neubert (2015), Center-of-mass corrections for sub-cm-precision laser-ranging targets: Starlette, Stella and LARES, *J. Geod.*, *89*(4), 303–312.

Pavlis, D. E., J. Wimert, and J. J. McCarthy (2015), *GEODYN II system description, Vol. 1–5*, SGT Inc., Greenbelt, MD.

Pearlman, M. R., J. J. Degnan, and J. M. Bosworth (2002), The international laser ranging service, *Adv. Space Res.*, *30*(2), 135–143.

Peltier, W. R., D. F. Argus, and R. Drummond (2015), Space geodesy constrains ice age terminal glaciation: The global ICE-6GC (VM5a) model, *J. Geophys. Res.-Sol. Ea.*, *120*, 450–487, doi: 10.1002/2014JB011176.

Peralta-Ferriz, C., J. H. Morison, and J. M. Wallace (2016), Proxy representation of Arctic ocean bottom pressure variability: Bridging gaps in GRACE observations, *Geophys. Res. Lett.*, *43*, 9183–9191.

Petit, G., and B. Luzum (2010), *IERS Conventions (2010), IERS Technical Note No. 36*, Verlag des Bundesamts fuer Kartographie und Geodaesie.

Preisendorfer, R. (1988), *Principal component analysis in meteorology and oceanography*, Elsevier, Amsterdam. ISBN:0444430148.

Quinn, K. J., and R. M. Ponte (2012), High frequency barotropic ocean variability observed by GRACE and satellite altimetry, *Geophys. Res. Lett.*, *39*(L07603).

Ramillien, G., A. Lombard, A. Cazenave, E. R. Ivins, M. Llubes, F. Remy, and R. Biancale (2006), Interannual variations of the mass balance of the Antarctica and Greenland ice sheets from GRACE, *Glob. Planet. Change*, *53*, 198–208.

Rangelova, E., W. Van der Wal, M. Sideris, and P. Wu (2010), Spatiotemporal analysis of the grace-derived mass variations in north america by means of multi-channel singular spectrum analysis, in *Gravity, geoid and earth observation*, pp. 539–546, Springer.

Rangelova, E., M. Sideris, and J. Kim (2012), On the capabilities of the multi-channel singular spectrum method for extracting the main periodic and non-periodic variability from weekly GRACE data, *J. Geodyn.*, *54*, 64–78.

Ray, R. D., and B. C. Douglas (2011), Experiments in reconstructing twentieth-century sea levels, *Prog. Oceanogr.*, *91*, 496–515, doi:10.1016/j.pocean.2011.07.021.

Reager, J. T., A. S. Gardner, J. S. Famiglietti, D. N. Wiese, A. Eicker, and M.-H. Lo (2016), A decade of sea level rise slowed by climate-driven hydrology, *Science*, *351*.

Reigber, C., et al. (2005), *Earth gravity field and seasonal variability from CHAMP*, pp. 25–30, Springer.

Richman, M. (1986), Rotation of principal components, *Int. J. Climatol.*, *6*, 293–335, doi: 10.1002/joc.3370060305.

Ries, J., and M. Cheng (2014), Satellite laser ranging applications for gravity field determination, in *Proceedings from the 19th international workshop on laser ranging, Annapolis*.

Rignot, E., I. Velicogna, M. van den Broeke, A. Monaghan, and J. T. M. Lenaerts (2011), Acceleration of the contribution of the Greenland and Antarctic ice sheets to sea level rise, *Geophys. Res. Lett.*, *38*, L05,503, doi:10.1029/2011GL046583.

Rodell, M., et al. (2004), The Global Land Data Assimilation System, *Bull. Amer. Meteor. Soc.*, *85*(3), 381–394.

Rudenko, S., M. Otten, P. Visser, R. Scharroo, T. Schöne, and S. Esselborn (2012), New improved orbit solutions for the ERS-1 and ERS-2 satellites, *Adv. Space Res.*, *49*(8), 1229–1244.

Sakumura, C., S. Bettadpur, and S. Bruinsma (2014), Ensemble prediction and intercomparison analysis of GRACE time-variable gravity field models, *Geophysical Research Letters*, *41*(5), 1389–1397, doi:10.1002/2013gl058632.

Schmeer, M., M. Schmidt, W. Bosch, and F. Seitz (2012), Separation of mass signals within GRACE monthly gravity field models by means of empirical orthogonal functions, *J. Geodyn.*, *59*, 124–132.

Schmidt, M., M. Fengler, T. Mayer-Gürr, A. Eicker, J. Kusche, L. Sánchez, and S.-C. Han (2007), Regional gravity modeling in terms of spherical base functions, *J. Geod.*, *81*(1), 17–38.

Schmidt, M., F. Seitz, and C. K. Schum (2008), Regional four-dimensional hydrological mass variatins from GRACE, atmospheric flux convergence, and river gauge data, *J. Geophys. Res.*, *113*(B10402).

Schrama, E. J. O., and B. Wouters (2011), Revisiting Greenland ice sheet mass loss observed by GRACE, *J. Geophys. Res.*, *116*, B02,407, doi:10.1029/2009JB006847.

Seo, K.-W., D. E. Waliser, C.-K. Lee, B. Tian, T. Scambos, B.-M. Kim, J. H. van Angelen, and M. R. van den Broeke (2015), Accelerated mass loss from Greenland ice sheet: Links to atmospheric circulation in the North Atlantic, *Global Planet. Change*, *128*, 61–71, doi: 10.1016/j.gloplacha.2015.02.006.

Sheffield, J., G. Goteti, and E. F. Wood (2006), Development of a 50-year high-resolution global dataset of meteorological forcings for land surface modeling, *J. Climate*, *19*(13), 3088–3111.

Shepherd, A., et al. (2012), A Reconciled Estimate of Ice-Sheet Mass Balance, *Science*, *338*, 1183, doi:10.1126/science.1228102.

Sobel, D. (1995), *Longitude: The True Story of a Lone Genius Who Solved the Greatest Scientific Problem of His Time*, Walker.

Sośnica, K., A. Jäggi, U. Meyer, D. Thaller, G. Beutler, D. Arnold, and R. Dach (2015), Time variable Earth's gravity field from SLR satellites, *J. Geod.*, *89*(10), 945–960.

Stammer, D., and et al. (2014), Accuracy assessment of global barotropic ocean tide models, *Rev. Geophys.*, *52*, 243–282.

Sutterley, T. C., I. Velicogna, E. Rignot, J. Mouginot, T. Flament, M. R. van den Broeke, J. M. van Wessem, and C. H. Reijmer (2014), Mass loss of the Amundsen Sea Embament of West Antarctica from four independent techniques, *Geophys. Res. Lett.*, *41*, 8421–8428.

Swenson, S., and J. Wahr (2002), Methods for inferring regional surface-mass anomalies from Gravity Recovery And Climate Experiment (GRACE) measurements of time-variable gravity, *J. Geophys. Res.*, *107*(B9), 2193, doi:10.1029/2001JB000576.

Swenson, S., and J. Wahr (2006), Post-processing removal of correlated errors in GRACE data, *Geophys. Res. Lett.*, *33*, L08,402, doi:10.1029/2005GL025285.

Swenson, S., D. Chambers, and J. Wahr (2008), Estimating geocenter variations from a combination of GRACE and ocean model output, *J. Geophys. Res.*, *113*, B08,410, doi:2007JB005338.

Talpe, M. J., R. S. Nerem, F. G. Lemoine, E. Pilinski, D. Chinn, and R. E. Riva (2013), Extending the record of time-variable gravity, Poster G23A-0776, in *2013 Fall Meeting, American Geophysical Union, San Francisco, CA, 9-13 Dec., 2013.*

Talpe, M. J., R. S. Nerem, F. G. Lemoine, R. E. Riva, E. Pilinski, and D. Chinn (2014), Mass loss in Greenland and Antarctica from 1993 to 2013 determined from a combination of GRACE, SLR, and DORIS data, Talk G3.2-13168, in *2014 Spring Meeting, European Geosciences Union, Vienna, Austria, 27 April - 2 May, 2014.*

Talpe, M. J., R. S. Nerem, F. G. Lemoine, and F. Landerer (2015a), Ice sheet melt in Greenland over 1993 - 2014 from time-variable gravity, in *2015 Climate Days Conference, Ilulissat, Greenland, 2-5 June, 2015.*

Talpe, M. J., R. S. Nerem, F. G. Lemoine, and M. Blossfeld (2015b), Bridging the Potential Gap in Polar Ice Sheet Melt Estimates between GRACE and GRACE Follow-On using SLR/DORIS Data, Poster G31B-1117, in *2015 Fall Meeting, American Geophysical Union, San Francisco, CA, 14-18 Dec., 2015.*

Talpe, M. J., R. S. Nerem, F. G. Lemoine, and M. Blossfeld (2016a), Influence of SLR Solutions on Reconstructions of Polar Ice Sheet Melt from Time-Variable Gravity using GRACE, Poster EART-118, in *ESA Living Planet Symposium, Prague, Czech Republic, 9-13 May, 2016.*

Talpe, M. J., R. S. Nerem, F. G. Lemoine, E. Forootan, and M. Blossfeld (2016b), Extending the record of terrestrial water storage (TWS) from time-variable gravity, Poster G13B-1101, in *2016 Fall Meeting, American Geophysical Union, San Francisco, CA, 12-16 Dec., 2016.*

Talpe, M. J., R. S. Nerem, F. G. Lemoine, E. Forootan, M. Schmidt, E. M. Enderlin, and F. W. Landerer (2017), Ice mass change in Greenland and Antarctica between 1993 and 2013 from satellite gravity measurements, *J. Geod.*, pp. 1–16, doi:10.1007/s00190-017-1025-y.

Tamisiea, M. E., E. W. Leuliette, J. L. Davis, and J. X. Mitrovica (2005), Constraining hydrological and cryospheric mass flux in southeastern Alaska using space-based gravity measurements, *Geophys. Res. Lett.*, *32*(L20501).

Tapley, B. D., S. Bettadpur, M. Watkins, and C. Reigber (2004a), The gravity recovery and climate experiment: Mission overview and early results, *Geophys. Res. Lett.*, *31*, L09,607, doi:10.1029/2004GL019920.

Tapley, B. D., B. E. Schutz, and G. H. Born (2004b), *Statistical Orbit Determination*, ISBN: 0-12-683630-2, Elsevier Academic Press.

Tapley, B. D., F. Flechtner, C. Boening, and S. Bettadpur (October 5 - 7, 2016), GRACE Mission: Status and Prospects, in *GRACE Science Team Meeting*, Postdam, Germany.

Tavernier, G., et al. (2006), The International DORIS Service: Genesis and early achievements, *J. Geod.*, *80*(8-11), 403–417.

Tedesco, M., X. Fettweis, T. Mote, J. Wahr, P. Alexander, J. E. Box, and B. Wouters (2013), Evidence and analysis of 2012 Greenland records from spaceborne observations, a regional climate model and reanalysis data, *The Cryosphere*, *7*(615-630).

Tosi, N., R. Sabadini, and A. M. Marotta (2005), Simultaneous inversion for the Earth's mantle viscosity and ice mass imbalance in Antarctic and Greenland, *J. Geophys. Res.*, *110*, B07,402, doi:10.1029/2004JB003236.

Touboul, P., E. Willemenot, B. Foulon, and V. Josselin (1999), Accelerometer for CHAMP, GRACE and GOCE space missions: Synergy and evolution, *B. Geofis. Teor. Appl.*, *40*, 321–327.

Vallado, D. A. (2007), *Fundamentals of Astrodynamics and Applications*, Space Technology Libary and Microcosm Press.

van Angelen, J. H., M. R. van den Broeke, B. Wouters, and J. T. M. Lenaerts (2014), Contemporary (1960-2012) Evolution of the Climate and Surface Mass Balance of the Greenland Ice Sheet, *Surv. Geophys.*, *35*, 1155–1174, doi:10.1007/s10712-013-9261-z.

van de Berg, W. J., M. R. van den Broeke, C. H. Reijmer, and E. van Meijgaard (2006), Reassessment of the Antarctic surface mass balance using calibrated output of a regional atmospheric climate model, *J. Geophys. Res.*, *111*, D11,104, doi:10.1029/2005JD006495.

van den Broeke, M. R., E. M. Enderlin, I. M. Howat, P. K. Munneke, B. Y. P. Noël, W. J. van de Berg, E. van Meijgaard, and B. Wouters (2016), On the recent contribution of the Greenland ice sheet to sea level change, *The Cryosphere*, *10*, 1933–1946, doi:10.5194/tc-10-1933-2016.

van der Meijde, M., R. Pail, R. Bingham, and R. Floberghagen (2013), GOCE data, models, and applications: A review, *Int. J. Appl. Earth Obs. Geoinf.*, *35*, 4–15, doi:10.1016/j.jag.2013.10.001.

Vaníček, P., and E. Krakiwsky (1986), *Geodesy: The Concepts*, Elsevier Science Publishers.

Velicogna, I. (2009), Increasing rates of ice mass loss from the Greenland and Antarctic ice sheets revealed by GRACE, *Geophys. Res. Lett.*, *36*, L19,503, doi:10.1029/2009GL040222.

Velicogna, I., and J. Wahr (2006a), Measurements of Time-Variable Gravity Show Mass Loss in Antarctica, *Science*, *311*, 1754–1756, doi:10.1126/science.1123785.

Velicogna, I., and J. Wahr (2006b), Acceleration of Greenland ice mass loss in spring 2004, *Nature*, *443*, 329–330.

Velicogna, I., and J. Wahr (2013), Time-variable gravity observations of ice sheet mass balance: Precision and limitations of the GRACE satellite data, *Geophys. Res. Lett.*, *40*, 3055–3063, doi: 10.1002/grl.50527.

Velicogna, I., T. C. Sutterley, and M. van den Broeke (2014), Regional acceleration in ice mass loss from Greenland and Antarctica using GRACE time-variable gravity data, *Geophys. Res. Lett.*, *19*, doi:10.1002/2014GL061052.

von Storch, H., and F. W. Zwiers (1999), *Statistical Analysis in Climate Research*, Cambridge University Press.

Wahr, J. (1986), *Geodesy and Gravity: Class Notes*, Samizdat Press.

Wahr, J., M. Molenaar, and F. Bryan (1998), Time variability of the Earth's gravity field: Hydrological and oceanic effects and their possible detection using GRACE, *J. Geophys. Res.*, *103*(B12), 30,205–30,229, doi:10.1029/98JB02844.

Wahr, J., R. S. Nerem, and S. Bettadpur (2015), The pole tide and its effect on GRACE time-variable gravity measurements: Implications for estimates of surface mass variations, *J. Geophys. Res.-Sol. Ea.*, *120*(6), 4597–4615, doi:10.1002/2015JB011986.

Wang, L., C. K. Schum, F. J. Simons, B. Tapley, and C. Dai (2012), Coseismic and postseismic deformation of the 2011 Tohoku-Oki earthquake constrained by GRACE gravimetry, *Geophys. Res. Lett.*, *39*(L07301).

Watkins, M., and S. Bettadpur (2000), The GRACE mission: Challenges of using micron-level satellite-to-satellite ranging to measure the Earth's gravity field, in *International Symposium on Space Dynamics*.

Watkins, M. M., and D.-N. Yuan (2014), *JPL Level-2 Processing Standards Document*, Jet Propulsion Laboratory, California Institute of Technology, Pasadena, CA.

Watkins, M. M., D. N. W. and. D.-N. Yuan, C. Boening, and F. W. Landerer (2015), Improved methods for observing Earth's time variable mass distribution with GRACE using spherical cap mascons, *J. Geophys. Res.-Sol. Ea.*, *120*, 2648–2671.

Webb, F., M. M. Watkins, F. Flechtner, F. W. Landerer, and L. Grunwaldt (2016), Current Status of the GRACE Follow-On Mission, in *American Geophysical Union Fall Meeting, San Francisco, California, 12-16, 2016.*, G11C-05.

Weigelt, M., T. van Dam, A. Jäggi, L. Prange, M. J. Tourian, W. Keller, and N. Sneeuw (2013), Time-varity gravity signal in Greenland revealed by high-low satellite-to-satellite tracking, *J. Geophys. Res.*, *118*, 3848–3859, doi:10.1002/jgrb.50283.

Whitehouse, P. L., M. J. Bentley, and A. M. L. Brocq (2012a), A deglacial model for Antarctica: geologic constraints and glaciological modelling as a basis for a new model of Antarctic glacial isostatic adjustment, *Quat. Sci. Rev.*, *32*, 1–24.

Whitehouse, P. L., M. J. Bentley, G. A. Milne, M. A. King, and I. D. Thomas (2012b), A new glacial isostatic adjustment model for Antarctica: calibrated and tested using observations of relative sea-level change and present-day uplift rates, *Geophys. J. Int.*, *190*, 1464–1482.

Witkowski, M., and F.-H. Massman (October 5 - 7, 2016), Status GRACE Mission Operations, in *GRACE Science Team Meeting*.

Wouters, B., and E. Schrama (2007), Improved accuracy of GRACE gravity solutions through empirical orthogonal function filtering of spherical harmonics, *Geophysical Research Letters*, *34*(23).

Wouters, B., D. Chambers, and E. J. O. Schrama (2008), GRACE observes small-scale mass loss in Greenland, *Geophys. Res. Lett.*, *35*(L20501).

Wouters, B., J. L. Bamber, M. R. van den Broeke, J. T. M. Lenaerts, and I. Sasgen (2013), Limits in detecting acceleration of ice sheet mass loss to climate variability, *Nat. Geosci.*, *6*, doi:10.1038/NGEO1874.

Wu, X., and M. B. Heflin (2015), A global assessment of acceleration in surface mass transport, *Geophys. Res. Lett.*, *42*, 6716–6723.

Wu, X., J. Ray, and T. van Dam (2012), Geocenter motion and its geodetic and geophysical implications, *J. Geod.*, *58*, 44–61.

Xu, Z., E. J. O. Schrama, and W. van der Wal (2015), Optimization of regional constraints for estimating the Greenland mass blance with GRACE level-2 data, *Geophys. J. Int.*, *202*, 381–393, doi:10.1093/gji/ggv146.

Yoder, C., J. Williams, J. Dickey, B. Schutz, R. Eanes, and B. Tapley (1983), Secular variation of Earth's gravitational harmonic J2 coefficient from Lageos and nontidal acceleration of earth rotation, *Nature*, *303*(5920), 757–762.

Zehentner, N., and T. Mayer-Gürr (2015), SST-hl: Time variable gravity from multiple non-dedicated satellites, in *EGU General Assembly Conference Abstracts*, vol. 17, p. 10613.

Appendix A

Modeling Choices for Gravity Field Estimation

Table A.1: Goddard Space Flight Center (GSFC), Deutsches Geodätisches Forschungsinstitut (DGFI), and Astronomisches Institut Universität Bern (AIUB).

General Type	Specific Name	GSFC	DGFI	AIUB
Technique specific	Number of Stokes coefficients	33	33	33
	Arcs [days]	monthly	weekly	monthly
	Solution	d/o 5 - $C_{50} + C_{61} + S_{61}$	d/o 5 - $C_{50} + C_{61} + S_{61}$	constrained d/o 10
	Time span	Nov. 1992 – April 2014	Jan. 1993 – March 2015	March 2002 – April 2014
A *priori* information	A priori station coordinates	ITRF2008 and SLRF2008	SLRF2008	SLRF2008
	range/time biases for SLR	?	ILRS recommendations	IRLS recommendations
	Fixed station coordinates	?	Yes	No, solved for with constraints
	Atmo. gravity (gravity)	?	S1/S2 atmospheric tides	AOD products
	Atmo. gravity (loading)	?	Ray & Ponte 2003 from GGFC	Ray & Ponte 2003 from GGFC
	Solid Earth tides	IERS2003	IERS2010	IERS2010
	Ocean tides (load. + gravity)	GOT4.8	FES2004	FES2004
	Ocean pole tide (load. + gravity)		Desai 2002 up to d/o 10	Desai 2002 up to d/o 10
	Static gravity model	GOCO2S	EIGEN6S	Internal GRACE-derived solution
	C_{21} and S_{21}	IERS2010	IERS2010	IERS2010
	Lunar gravity	?	Konopliv01 to d/o 10	Only GM term
	Ephemerides	?	DE421	DE405
Non-grav. orbit pert.	Solar radiation			
	Sat. drag coefficient			
	Earth albedo			
	Atmosph. & Thermo.			
	Thermal diss.			
	Non-conserv. force mod.	Sat. specific macromodels	same	same
EOP	LOD	?	Daily offsets at 12h	Constrained daily offsets
	Terrestrial mean pole	IERS2010	IERS2010	
	EOF	?	Daily offsets at 0h	Daily offsets + drift

Appendix B

Variance Comparison between GSFC and DGFI
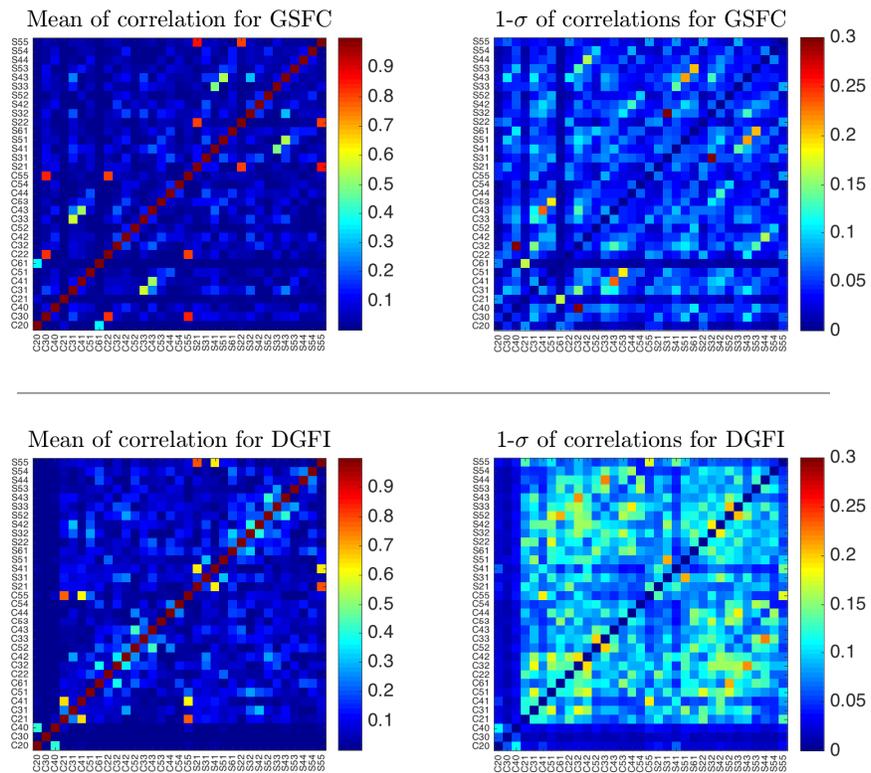
Figure B.1: Correlation information for GSFC solution.
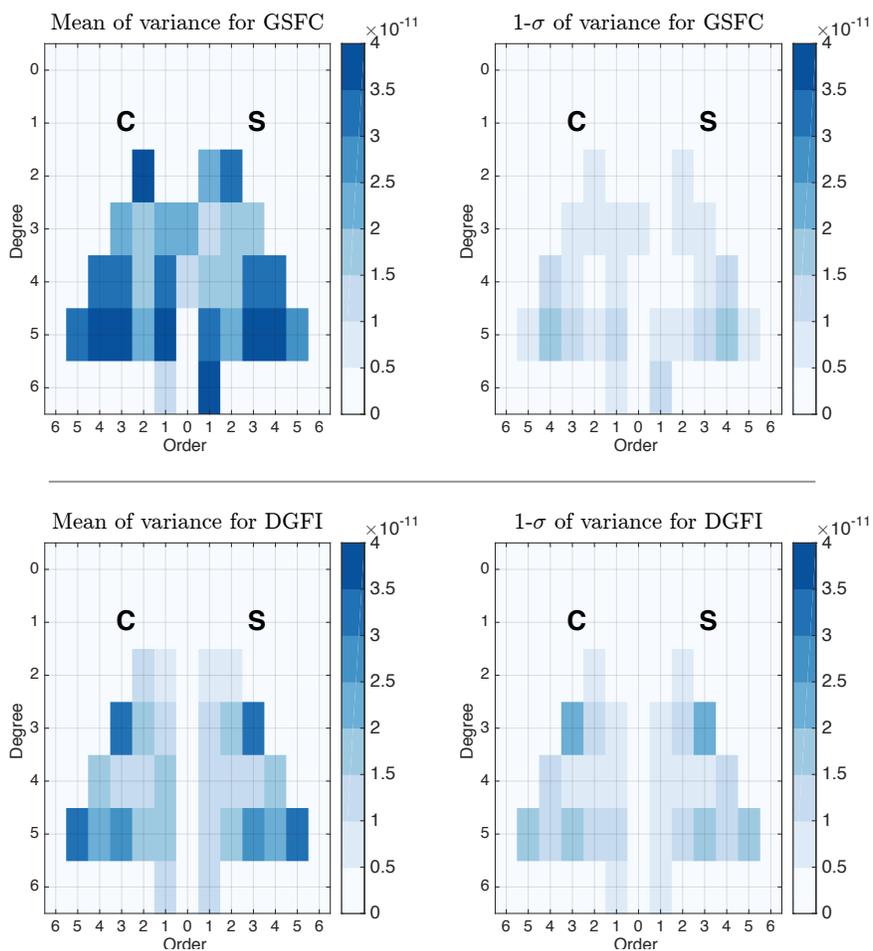
Figure B.2: Correlation information for GSFC solution.

Appendix C

Spatial Modes Per Region
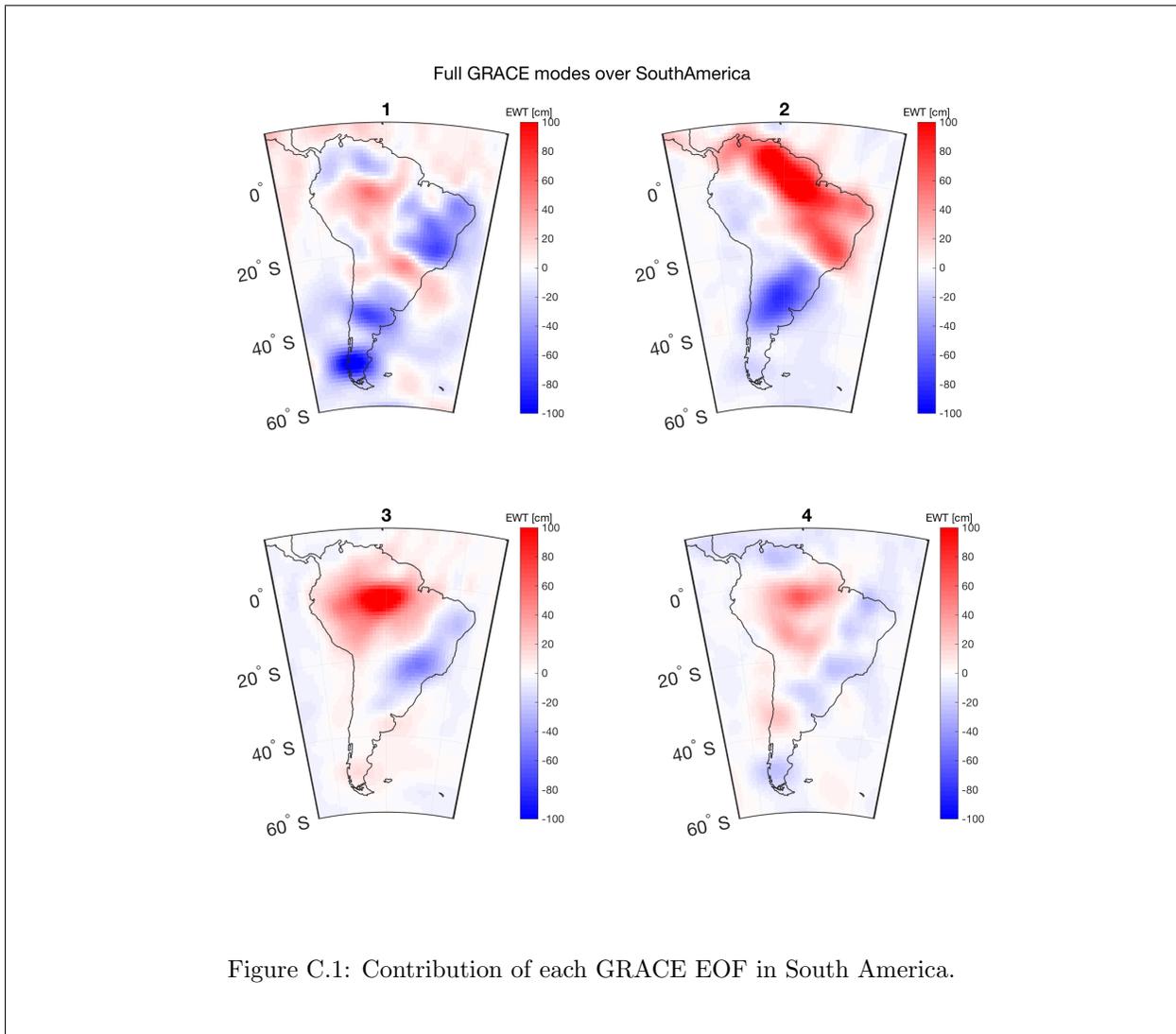
Figure C.1: Contribution of each GRACE EOF in South America.
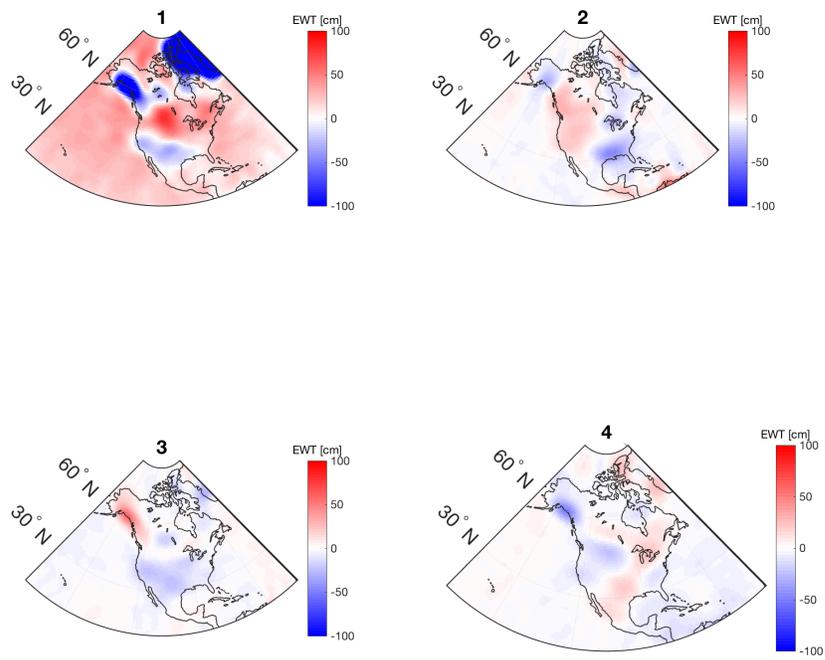
Figure C.2: Contribution of each GRACE EOF in North America.
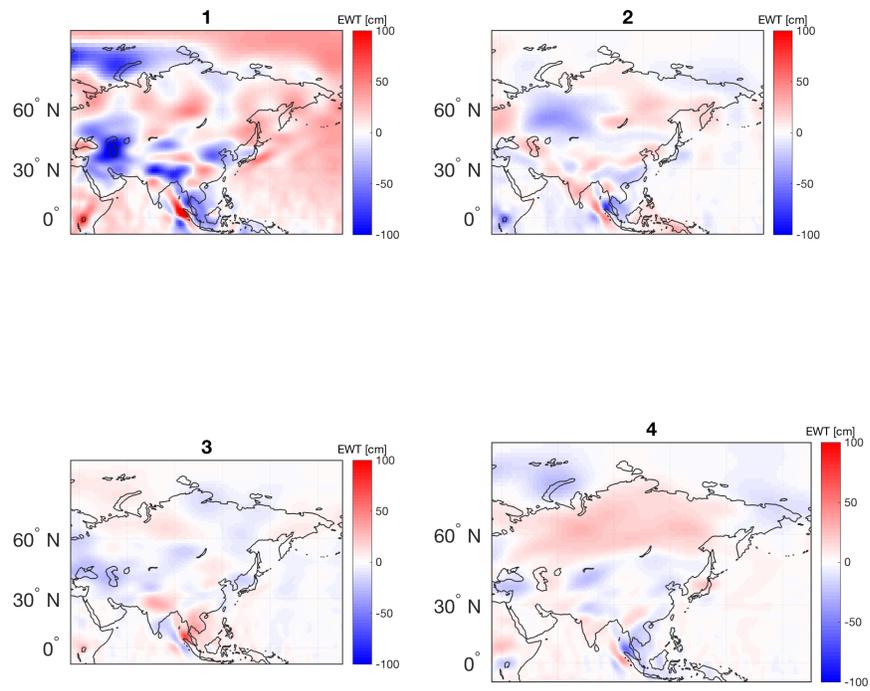
Figure C.3: Contribution of each GRACE EOF in Asia.
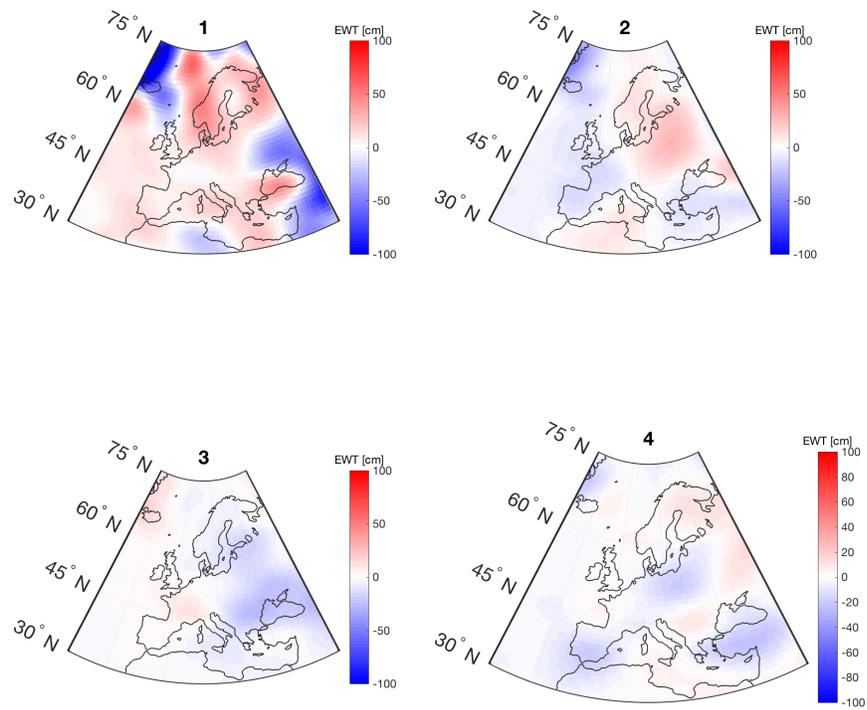
Figure C.4: Contribution of each GRACE EOF in Europe.
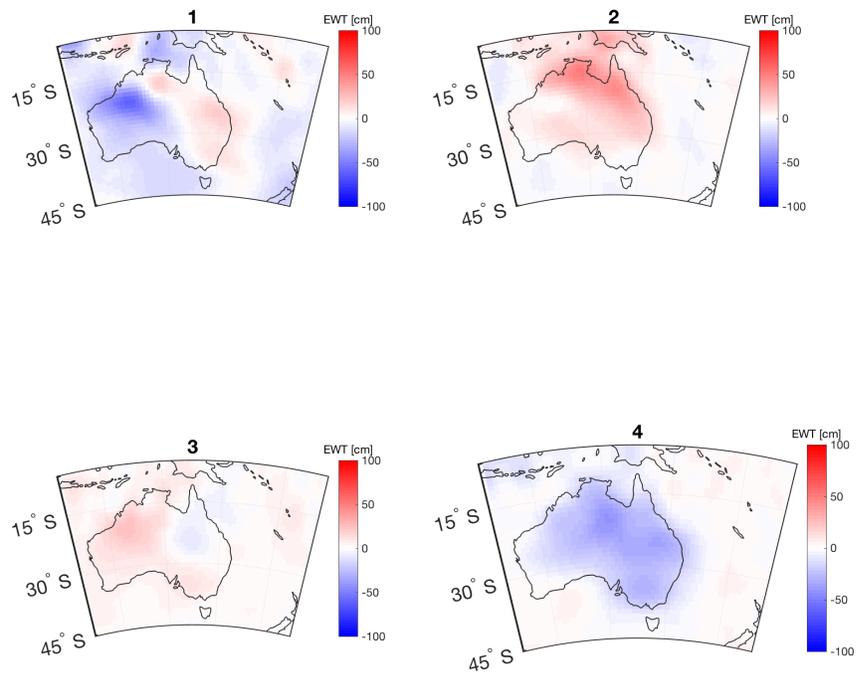
Figure C.5: Contribution of each GRACE EOF in Australia.
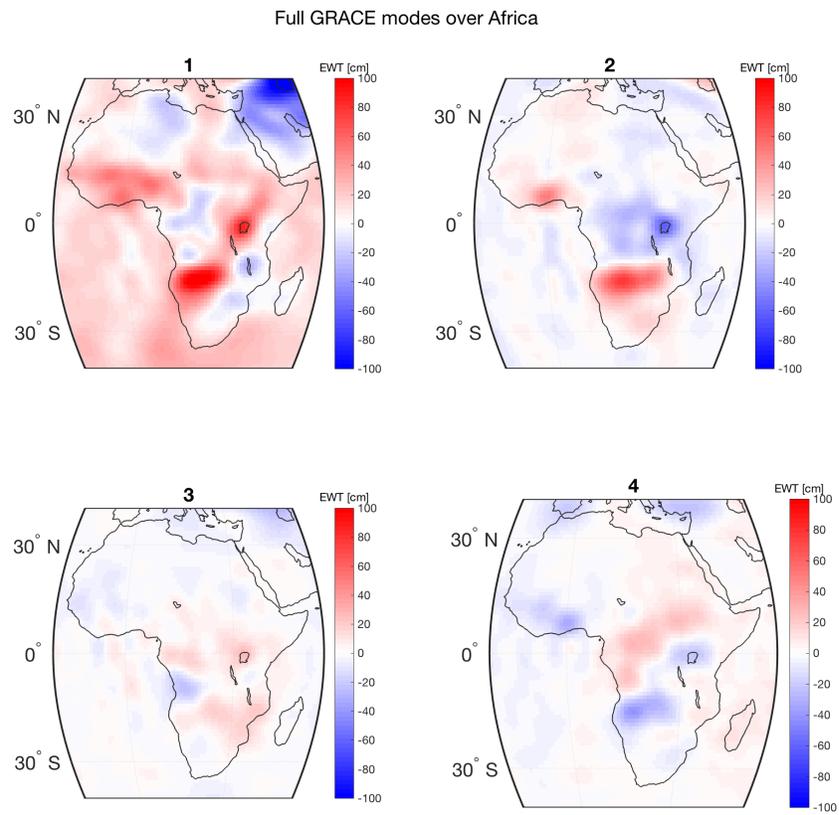
Figure C.6: Contribution of each GRACE EOF in Africa.